Analysis of GEM Properties and Development of a GEM Support Structure for the ILD Time Projection Chamber

by

Lea Hallermann

Analysis of GEM Properties and Development of a GEM Support Structure for the ILD Time Projection Chamber

Dissertation

zur Erlangung des Doktorgrades
des Department Physik
der Universität Hamburg

vorgelegt von

Lea Hallermann

aus Nürnberg

Hamburg
2010

Gutachter der Dissertation:	Prof. Dr. Rolf-Dieter Heuer Dr. Philip Bechtle
Gutachter der Disputation:	Prof. Dr. Joachim Mnich Dr. Philip Bechtle
Datum der Disputation:	22.03.2010
Vorsitzender des Prüfungsausschusses:	Dr. Georg Steinbrück
Vorsitzender des Promotionsausschusses:	Prof. Dr. Joachim Bartels
Dekan der MIN Fakultät:	Prof. Dr. Heinrich Graener
Leiterin des Department Physik:	Prof. Dr. Daniela Pfannkuche

Kurzfassung

Im Konzept des International Large Detector (ILD), der für den International Linear Collider (ILC) entwickelt wird, ist eine Zeitprojektionskammer (englisch: TPC) als Spurkammer vorgesehen. Solche Gasdetektoren müssen mit Verstärkungsstrukturen versehen werden, um die Ladung, die von geladenen Teilchen durch Ionisation erzeugt wird, zu vervielfachen. In der ILD TPC werden zu diesem Zweck Micro Pattern Gas Detectors (MPGDs) eingesetzt werden. In der vorliegenden Arbeit werden Eigenschaften spezieller MPGDs, nämlich von Gas Electron Multipliern (GEMs), analysiert. Effektive Verstärkung und Energieauflösung von GEM Folien verschiedener Hersteller werden verglichen, wobei ein gutes Verständnis dieser Größen erlangt wird. Dies gelingt durch die Interpretation der Ergebnisse anhand von geometrischen Parametern der GEMs. Erstmals wurden im Rahmen dieser Arbeit Höhenprofile von GEM Folien vermessen und ihr Einfluß auf dE/dx Messungen und die Driftfeld-Qualität untersucht. Die Ergebnisse unterstreichen die Notwendigkeit von möglichst flach installierten GEMs in TPCs. Zu diesem Zweck wurde eine neue Methode zur Montage von GEM Folien entwickelt, um Flachheit zu garantieren und gleichzeitig eine große Auslesefläche, wie in der ILD TPC, mit möglichst geringem Materialaufwand zu instrumentieren. Die neue Installationsmethode wurde in einem TPC Prototypen getestet, mit dem Daten von kosmischen Myonen aufgezeichnet wurden. Der Einfluss der neuen Struktur auf die Spurrekonstruktion, die Einzelpunktauflösung, die Rekonstruktionseffizienz und dE/dx Messungen werden quantifiziert. Unter der Berücksichtigung einiger Konstruktionsbedingungen kann die neue Montagemethode für GEM Folien in der ILD TPC verwendet werden.

Abstract

In the concept of the International Large Detector (ILD), developed for the International Linear Collider (ILC) a Time Projection Chamber (TPC) is envisaged as main tracking detector. Such gaseous detectors have to be equipped with amplification devices in order to enlarge the amount of charge, which is set free by ionization caused by traversing charged particles. Micro Pattern Gas Detectors (MPGDs) will be used in the ILD TPC as amplification stage. In this thesis, Gas Electron Multipliers (GEMs) – one specific MPGD species – are analyzed concerning various properties. Effective gains and energy resolutions are compared for GEM foils produced by different manufacturers. A good understanding of these observables is obtained by interpretation of the results with the help of geometrical parameters. Height profile measurements of GEM foils have been performed for the first time and the impact of non perfect flat GEMs is analyzed, especially on dE/dx determination and drift field quality. The results emphasize the need of a flat installation of GEMs in TPCs. As a consequence, a new mounting device has been developed to ensure flatness and to provide a method to cover large readout areas, as in the ILD TPC, by introducing the least possible amount of dead material into the detector. The developed structure has been tested in a TPC protoype, taking cosmic muon data. The influence of the mounting on track reconstruction, single point resolution, tracking efficiency and dE/dx measurements is quantified. The developed mounting is applicable in a large scale TPC, if some design considerations are taken into account.

Contents

Chapter 1

Introduction

In fall 2009 the Large Hadron Collider (LHC) went in operation. It represents the first step towards the so-called terascale. At these energies around 1 TeV, new particles are expected to be found. On the one hand the long searched Higgs boson, which should have – due to theoretical and experimental constraints – a mass between 115 GeV and about 200 GeV. On the other hand, new physics beyond the standard model is expected to occur at the terascale energies as well. Consequently, the LHC is built as a discovery machine and has to be complemented by the construction of a high precision electron positron collider, which is able to measure for instance the Higgs mechanism in all detail.
The International Linear Collider (ILC) is the most advanced proposal for such a collider. The current design contains linear electron and positron accelerators of a length of 15 km each, colliding the beams in one single interaction region, where two detectors are operated in a so-called push-pull configuration. The International Large Detector (ILD) represents one of two validated concepts for a multipurpose detector to be built for the ILC.
The ILD is dedicated to precision physics measurements, which require a complete event reconstruction and in particular an excellent jet energy resolution. Hence, a particle flow concept is planned for the ILD, for which a highly efficient tracking system is crucial. As main tracking detector for the ILD, a Time Projection Chamber (TPC) is planned, since the pattern recognition abilities provide an excellent tracking efficiency and the small amount of material needed for such a gas detector fulfill the stringent requirements of the particle flow concept. The excellent momentum resolution of a TPC allows for example very precise Higgs recoil mass measurements. Charged particles traversing a TPC, ionize the gas inside and produce free electrons, which are drifted in electric and magnetic fields to the readout structures at the anodes. In front of the readout, an amplification stage is necessary, which multiplies the electrons in order to produce a detectable amount of charge. The amplification devices are planned to be Micro Pattern Gas Detectors (MPGDs), which are available in two main species, Micro Mesh Gas Amplifiers (MicroMEGAS) and Gas Electron Multipliers (GEMs).

The subject of this thesis, is the analysis of GEM foil properties and the development of a support structure for GEMs, to be used in the ILD TPC. The impact of this structure on the track reconstruction is analyzed. The effective gains of GEMs produced by different manufactures are measured in a dedicated assembly. The results are compared and interpreted based on the different geometrical and material parameters. In addition, a measurement of energy resolutions is presented.
The flatness of GEM foils, used in TPC prototypes, is measured for the first time and the impact of non perfect flat GEMs on dE/dx resolution, single point resolution and drift field quality is analyzed. A new method for the mounting of GEM foils is proposed and the influence of the support structure on hit reconstruction and efficiency, in particular the single point resolution, is analyzed. In addition, the impact on dE/dx measurements and tracking efficiency is estimated.
The content of this thesis is organized as follows. At first, an introduction to the standard model of particle physics and the ILC design is given. In the ILC chapter a short overview about TPCs and MPGDs is presented, before in the subsequent chapters detailed descriptions of TPC principles and GEM foils follow. A dedicated chapter outlines the physics motivation for the GEM studies of this thesis. Afterwards the comparative effective gain and energy resolution measurements are presented, as well as the flatness analysis. The description of the new GEM mounting is followed by the studies of the impact of this support structure. Finally, a summary of the presented work and conclusions are given.

Chapter 2

Standard Model of Particle Physics

The whole knowledge about elementary particles and "whatever holds the world together in its inmost folds" [Goe10] is summarized in the standard model of particle physics. It was developed during the second half of the 20th century and successfully withstood any experimental challenges up to now. The standard model contains fermions – particles with spin one half – and bosons – particles with integer spin – and their antiparticles. It describes three fundamental forces, namely the strong, the electromagnetic and the weak force, which are mediated by exchange bosons. The fermions are subdivided into leptons and quarks. Both types are organized in three generations with increasing mass, indicated by the size of the circles in figure 2.1, though not to scale. Exact values for the masses can be found in [PDG08]. In the standard model, neutrinos are assumed to be massless. However, since the observation of neutrino oscillations [SNO02, SKam98], it is known that they have to have non-zero mass, even if no direct measurements of their mass eigenstates have been performed up to now and only upper limits of the masses are determined

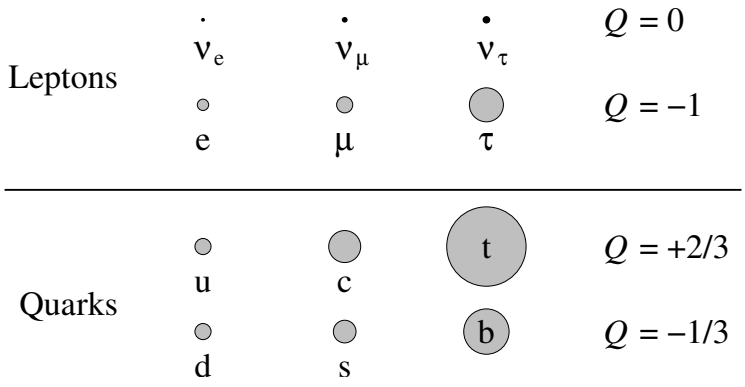

Figure 2.1: Fermionic content of the standard model. Q denotes the charge of leptons and quarks [Vog08].

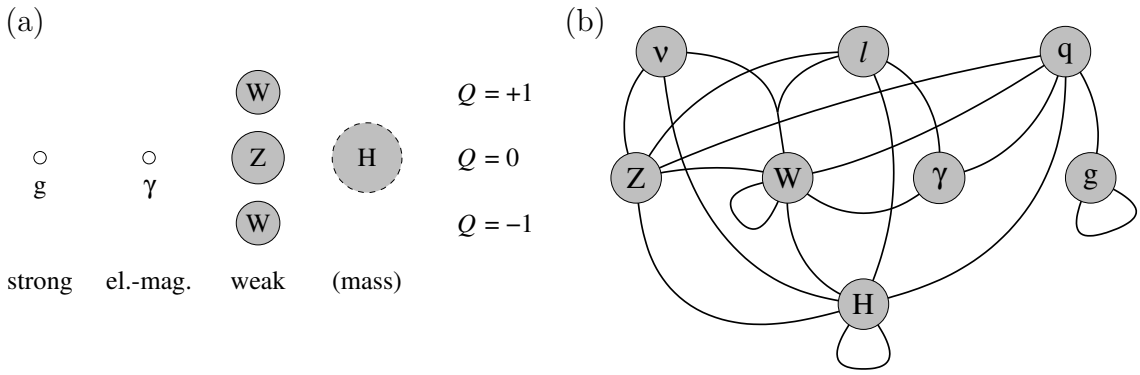

Figure 2.2: (a) Gauge bosons and Higgs particle with their charge Q [Vog08].
(b) Interactions and couplings in the standard model [Vog08].

[PDG08]. The fundamental forces are mediated by the spin one gauge bosons depicted in figure 2.2(a). The electromagnetic force is carried by massless photons and the strong force by massless gluons. In contrast, W and Z bosons – acting as exchange particles of the weak force – are quite heavy with a mass of 80.4 GeV or 91.2 GeV respectively [PDG08]. To explain their mass, the Higgs mechanism was introduced, which is explained in the next section. The Higgs boson, which is part of this mechanism, is the "most wanted" particle in modern high energy physics. Up to now only exclusion limits on its mass have been determined by the Large Electron Positron collider (LEP), the Tevatron experiments and the Stanford Large Detector (SLD). The combined result is shown in figure 2.3 [LEP09].
An overview of the possible couplings and self couplings between the standard model particles is illustrated in figure 2.2(b). Mathematically the standard model is represented by a relativistic quantum field theory with an underlying local gauge symmetry [Kak93]:

$$\mathrm{SU(3)_c} \times \mathrm{SU(2)_L} \times \mathrm{U(1)_Y}, \tag{2.1}$$

where $\mathrm{SU(3)_c}$ describes the quantum chromodynamic (QCD) with its three color charges [FGML73]. $\mathrm{SU(2)_L} \times \mathrm{U(1)_Y}$ is the symmetry of the electroweak theory [Gla61, SW64, Wei67], where the generator of $\mathrm{SU(2)_L}$ is the weak isospin and the weak hypercharge acts as generator of $\mathrm{U(1)_Y}$.

2.1 The Higgs

Since the Higgs particle is the only missing part of the standard model and the LHC is optimized and built for the Higgs discovery, but not for precise measurements of its mass and quantum numbers, a major motivation for a linear lepton collider is given by Higgs precision physics. Hence, a short introduction into the Higgs mechanism and an outlook to possible measurements at the International Linear Collider (ILC) are presented in this section, although other parts of the standard model are

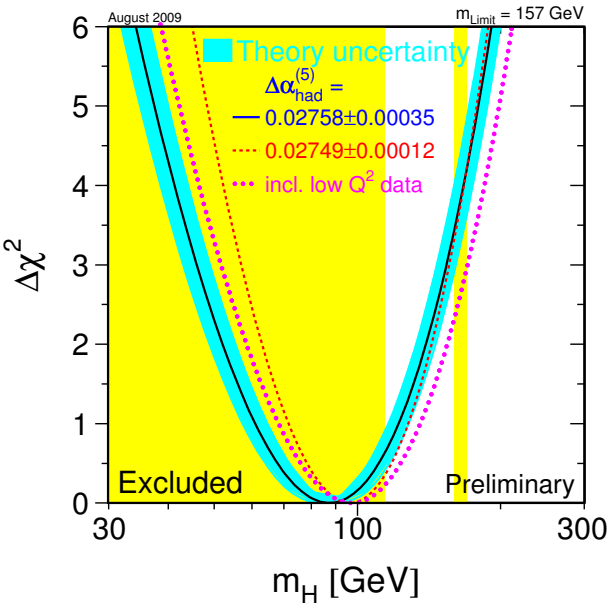

Figure 2.3: Higgs mass exclusion limit, determined by a combined effort of SLD, LEP and Tevatron experiments [LEP09].

not described in this depth.
In the standard model the explicit mass terms of gauge bosons and fermions break local gauge invariance. To solve this problem a dynamic gauge invariant mass generation was proposed in 1964 [Hig64b, Hig64a, EB64, GHK64]. In this solution, particles gain their mass through an interaction with the Higgs field. This field is a scalar isospin doublet with four degrees of freedom of the following form:

$$\phi = \frac{1}{\sqrt{2}} \begin{pmatrix} \phi_1 + i\phi_2 \\ \phi_3 + i\phi_4 \end{pmatrix} = \begin{pmatrix} \phi^+ \\ \phi^0 \end{pmatrix}. \tag{2.2}$$

The Klein-Gordon Lagrangian density can be written as:

$$\mathcal{L} = \frac{1}{2}(\partial_\mu \phi)(\partial^\mu \phi) - V(\phi), \tag{2.3}$$

where $V(\phi)$ denotes the potential of the Higgs field, which is $SU(2)_L$ symmetric. This potential:

$$V(\phi) = \mu^2 \phi^\dagger \phi + \lambda(\phi^\dagger \phi)^2 \tag{2.4}$$

has – as most important characteristic – a non-zero ground state. $\lambda > 0$ is needed to ensure, that the potential goes to infinity for $\phi \to \pm\infty$. With a choice of $\mu^2 < 0$, the minimum for the potential lies not at zero, but at:

$$\phi_{min} = \sqrt{\frac{-\mu^2}{\lambda}} = v. \tag{2.5}$$

Every possible ground state breaks the $SU(2)_L$ symmetry, while the potential itself is still symmetric. Such a behavior is called spontaneous symmetry breaking. Three degrees of freedom of the Higgs field are absorbed into the longitudinal polarization of the massive gauge bosons, while the fourth stands for the Higgs mass. In the Lagrangian, effective mass terms for the gauge bosons with fixed couplings occur. The masses of the bosons are given by:

$$m_\gamma = 0, \tag{2.6}$$

$$m_W = \frac{1}{2} \cdot g \cdot v, \tag{2.7}$$

$$m_Z = \frac{1}{2} \cdot v \cdot \sqrt{g^2 + g'^2}, \tag{2.8}$$

where g and $g^{'}$ are the coupling constants of $SU(2)_L$ and $U(1)_Y$ respectively. The Z and W Boson masses are not independent, but related via the Weinberg angle Θ_W, which describes the gauge boson mixing:

$$m_W = m_Z \cdot \cos\Theta_W. \tag{2.9}$$

The ratio of W and Z mass was measured precisely at the LEP experiments [L397, LEP93], where also the scattering of longitudinal polarized W bosons is measured. This process would violate the unitarity bound without the introduction of a Higgs with a mass smaller than roughly 1 TeV [L303].
The coupling of the Higgs field to the fermions is described by the Yukawa coupling λ_f:

$$m_f = \lambda_f \frac{v}{\sqrt{2}}. \tag{2.10}$$

These couplings, or the proportionality of the masses to the couplings, have to be measured precisely in order to clarify, whether one single isospin doublet is able to explain all gauge boson masses and the Higgs mechanism is realized in nature in the proposed form. In addition, a possibly found Higgs particle has to be tested, whether it corresponds to the one described in the standard model Higgs mechanism. For these measurements, an absolute branching ratio for Higgs production has to be determined. This is only possible at the ILC, where model independent mass measurement of the Higgs can be performed with the Higgs-strahlung process $e^+e^- \longrightarrow HZ$. By the measurement of its cross section $\sigma(HZ)_{meas}$ and a measurement of an arbitrary decay, which can be chosen according to the sensitivity of the detector, the branching ratio can be determined:

$$BR(H \to X) = \frac{[\sigma(HZ)BR(H \to X)]_{meas}}{\sigma(HZ)_{meas}} \tag{2.11}$$

The leading order Feynman graph of the Higgs-strahlung process can be seen in figure 2.4(a). Given that the center of mass energy is known very precisely, the clean signature of muonic Z boson decays can be used to measure the recoil mass

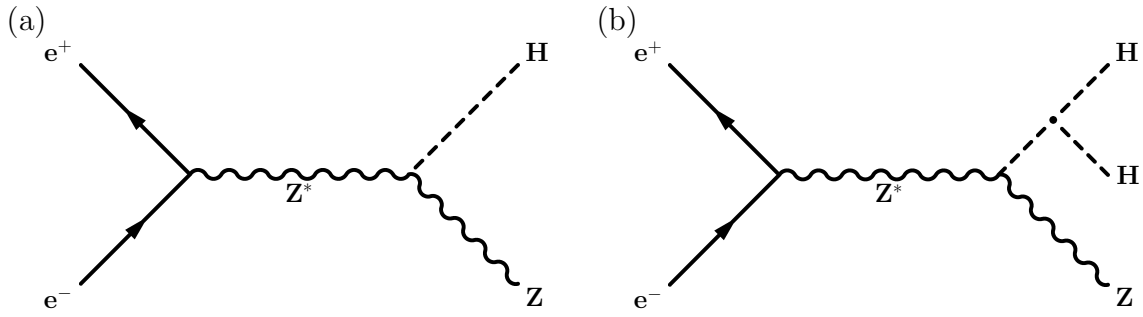

Figure 2.4: Feynman diagram of (a) Higgs-strahlung and (b) double Higgs-strahlung.

of the Higgs, independent from the decay channel of the Higgs particle itself. More details about the requirements for ILC detectors, which are needed to reconstruct such kind of events precise enough can be found in section 7.4.
Another part of the Lagrangian are trilinear couplings of the Higgs boson, which describe the self-interaction and the mass generation of the Higgs boson. These can also be measured at the ILC with the help of double Higgs-strahlung $e^+e^- \longrightarrow ZHH$, shown in figure 2.4(b).

2.2 The Successes

The whole standard model has been very successful over the past decades. It made many predictions, which were later on experimentally confirmed. One of the first successes of the early standard model was the discovery of the Ω^- baryon in 1964 [B+64]. Already three years earlier, the existence of the Ω^- was predicted by Gell-Mann as missing particle – consisting of three strange quarks – in the context of the "eightfold way". The discovery was a strong confirmation of the validity of the quark model [GM64]. In the same year, the observation of CP violation in the Kaon system [CCFT64] made the introduction of a third quark generation in the CKM matrix essential [KM73]. CP violation can only be explained with a complex phase in this matrix, which describes the quark mixing of three generations. However, at that time only three quarks were discovered: up, down and strange. The measurement of Kaon branching ratios led to the prediction of a fourth quark. In the processes $K^0_L \longrightarrow \mu^+\mu^-$ and $K^+ \longrightarrow \mu^+\nu_\mu$, a strong suppression of the first process could not be explained theoretically without the assumption of the charm quark [GIM70]. Including this quark in the theory, a destructive interference of Feynman box diagrams occurs, which explains the suppression of the first process. After some years, in 1974 the so-called "November Revolution of Particle Physics" was caused by the experimental observation of a narrow resonance at a mass of 3.1 GeV, the J/ψ meson [SLAC74, BNL74]. This resonance was identified as a bound $c\bar{c}$ state, proving the existence of the searched quark flavor.
The first experimental evidence of gauge bosons was made in the year 1979 at

PETRA in Hamburg. Three jet events in electron positron collisions led to the interpretation, that one of these jets originates from a gluon [PLUTO79, JADE80, TASSO80]. The electroweak theory, as formulated in the sixties [Gla61, SW64, Wei67], predicted three heavy gauge bosons. These bosons, called W^+,W^- and Z^0, have not been observed before 1983. In order to find these particles, the existing super proton synchrotron at CERN was converted to a proton anti-proton collider. With their collisions the energy range was enlarged enough to detect W and Z bosons [UA183a, UA183b].
With LEP the era of high precision tests of the standard model started, many of the results can be found in [LEP04]. Of particular importance was the measurement of Z^0 decay widths and triple gauge boson couplings. The visible and invisible Z^0 decay widths can be used to determine the number of neutrinos. The results constrains the number of lepton generations in the standard model to three. In addition, the observation of triple gauge boson couplings were able to describe the shape of the measured $e^+e^- \longrightarrow W^+W^-$ cross section and confirmed the validity of the standard model. Although the standard model was not intended to describe such exotic couplings, it turned out that these can be calculated within the existing formalism.
In 1995 the top quark was observed at the Tevatron [D095, CDF95] as most recent, however not really surprising, discovery of predicted particles. The only missing particle of the standard model content is the Higgs boson.

2.3 The Shortcomings

Despite the fact that all precision measurements performed up to now in high energy physics laboratories can be explained by the standard model, some severe problems make extensions of the model necessary. A selection of these shortcomings is given in the following.
Cosmological observations, like galaxy motion measurements, give one of the most striking arguments for the incompleteness of the standard model. Only a small fraction of the energy content – around 5 % – in the universe can be explained with standard model particles. The rest consists of so-called dark matter and dark energy of unknown origin [WMAP09].
A theoretical shortcoming of the model is the hierarchy problem. The mass generation of the Higgs particle itself shows divergent loop contributions as higher order corrections. If the standard model is valid up to the Planck scale ($\Lambda \approx 10^{19}\,\mathrm{GeV}$), the natural scale for the Higgs mass would be this Λ, since the corrections to Higgs mass are:

$$\Delta m_H^2 \sim \Lambda^2. \tag{2.12}$$

The problem occurs due to the extremely large difference of the weak and the natural cut-off, namely the Planck scale. The tremendous Higgs masses could only be canceled by a very precise fine-tuning of parameters. Such solutions, where fine-tuning is needed, are not impossible but disfavored in high energy physics.

Another blemish of the standard model – more an aesthetic problem – is that the unification of couplings of all forces does not work in the standard model, even on high energies. With the unification of the weak and the electromagnetic force due to spontaneous symmetry breaking, a first step towards unification was made. But an extension of the model is needed to achieve unification of the couplings of electroweak and strong force at high energies.
As last argument in this incomplete list, the integration of gravity – or the theory of space-time respectively – into the standard model shall be mentioned. Gravity can be experienced in everyday life but is not part of the model in its current state. The coupling strength of gravity is extremely small compared to the other three forces. Hence, gravity is always neglected in particle physics experiments. The problem is, that the theory of gravity is not quantized and cannot be renormalized. However, a complete theory of particle interactions should describe all forces in order to stay valid up to very high energies.
Some possible extensions of the standard model – for example the famous supersymmetry (SUSY) [FF77, DRW81] – are able to solve many of these shortcomings. In SUSY models, each standard model particle gets a supersymmetric partner with a spin shifted by one half. So bosons gain a fermionic partner and vice-versa. These models provide a candidate for dark matter – the so-called lightest supersymmetric particle (LSP). In addition, the hierarchy problem can be solved due to additional contributions to the Higgs mass by SUSY particles with opposite spin statistics, which cancel the large corrections. Also the unification of couplings is possible in SUSY models and even the involvement of gravity is possible via interpretation of supersymmetric theories as local symmetry.

2.4 The Next Step

The Large Hadron Collider (LHC) [B$^+$04] is the current step to the terascale and to solutions for at least some of the problems mentioned above. The Higgs is awaited to be found in the proton proton collisions as well as supersymmetric particles, provided that supersymmetry is existing. Whether SUSY or another model is realized in nature, in any case new physics is expected to appear in the terascale region. For example, the above mentioned violation of the unitarity by scattering of longitudinally polarized W bosons, has to be avoided, either by a Higgs particle or another new mechanism. If the Higgs exists, some particles – maybe sparticles predicted by SUSY – have to be at the terascale in order to solve the hierarchy problem of the Higgs mass. In addition, the unification of couplings, should become visible at the terascale. The strength of the coupling constants as functions over the energy, needs to develop a kink in the terascale region in order to unify at the Planck scale.
The high energy physics community agrees that beyond the LHC a new lepton collider is needed to complete and define the results of the large hadron collider more precisely [LHC-LC06]. The International Linear Collider (ILC) [ILC07] is the most

advanced project aiming in that direction. Different scenarios for the future research in high energy physics are thinkable. The most favored one is, that the Higgs will be found at the LHC and precision measurements will be performed at the ILC. It will be possible only at the ILC to determine the spin, the couplings and other parameters to clarify, whether really a standard model Higgs was found at the LHC. In addition, SUSY measurements and searches for other models like large extra dimensions can be performed at the ILC. More details about this project are described in the next chapter.

Chapter 3

International Linear Collider

This chapter explains why the next high energy physics collider should be a linear lepton collider. It introduces the international linear collider project and its subsystems. A section about the international large detector briefly presents the particle flow approach and the detector design with an emphasis on time projection chambers and the therein used amplification devices, since they are the main topic of this thesis.

3.1 A Linear Lepton Collider

In the past, both hadron and lepton colliders contributed equally to the level of understanding achieved in particle physics. Therefore a lepton collider is the logical successor of the LHC, which is built as discovery machine, while the ILC will be a precision instrument. The differences in both concepts are originating from the accelerated particles. At the LHC the high mass of the colliding protons is used to reach high center of mass energies, whereas the ILC profits from the relatively clean environment of a lepton collider. Electrons and positrons are elementary particles, while protons posses a substructure. This yields an unknown initial state at the LHC, since type and fractional momentum of the interacting partons cannot be chosen. Also the parton polarization is not defined and strong interactions of the protons lead to high QCD background, which requires selective triggers for the experiments. In addition, the so-called underlying event occurs due to multiple parton parton scattering and beam remnant interactions. Finally, the detector components and materials have to be radiation hard.
In the case of lepton colliders the initial state energy and the polarization are well known and adjustable. Since no underlying event occurs and electrons and positrons only participate in electroweak interactions, the standard model background is low, therefore trigger-less running is possible. The requirements for radiation hardness are smaller with respect to the LHC, which allows for high precision detectors with low material budgets.
To increase the energy in lepton collisions to a level well above the one of LEP, a

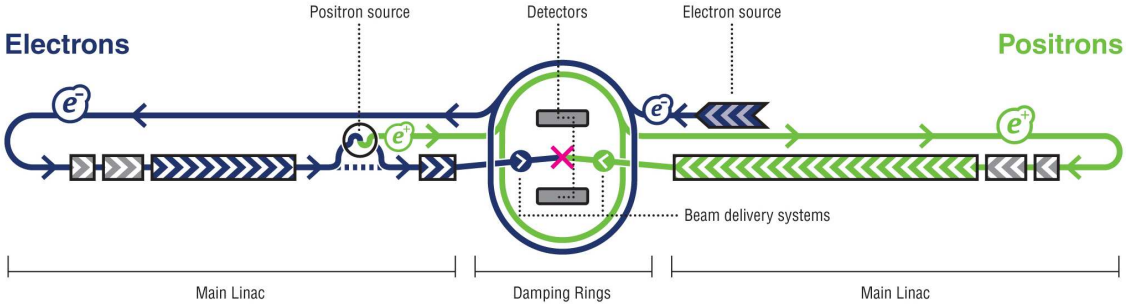

Figure 3.1: International linear collider baseline design [ILC07].

linear collider will be needed. The energy loss due to synchrotron radiation ΔE_{syn} emitted by accelerated particles with mass m in a ring accelerator can be described like:

$$\Delta E_{syn} \sim \frac{E^4}{R \cdot m^4}. \tag{3.1}$$

E denotes the beam energy and R the radius of the accelerator. The fact, that the loss increases with the fourth power of the beam energy and decreases only linearly with the radius, would make a future lepton ring collider unacceptable large and expensive.
Consequently the ILC will collide leptons after acceleration in a linear machine. The base line design is described in the following section. More details can be found in [ILC07].

3.2 Machine Design

The center of mass energy of the ILC is designed to be 200-500 GeV with an upgrade option to 1 TeV. Electrons and positrons are accelerated over a total length of 15 km each and are delivered to the interaction region. A design luminosity of $\mathcal{L} = 2 \cdot 10^{34}\,\mathrm{cm}^{-2}\mathrm{s}^{-1}$ yields in the first four years of operation an integrated luminosity of $\int \mathcal{L}\mathrm{dt} = 500\,\mathrm{fb}^{-1}$. The principles of all major parts are given in the following with a list of the beam parameters in the end. An overview sketch of the baseline design of the ILC is shown in figure 3.1, where the whole chain from the sources over the damping rings into the main linear accelerators and via the beam delivery system to the Interaction Point (IP) is illustrated. In addition to electron positron collisions, electron electron or photon photon options are under study as well as running at the Z^0 pole in the so-called Giga Z mode.

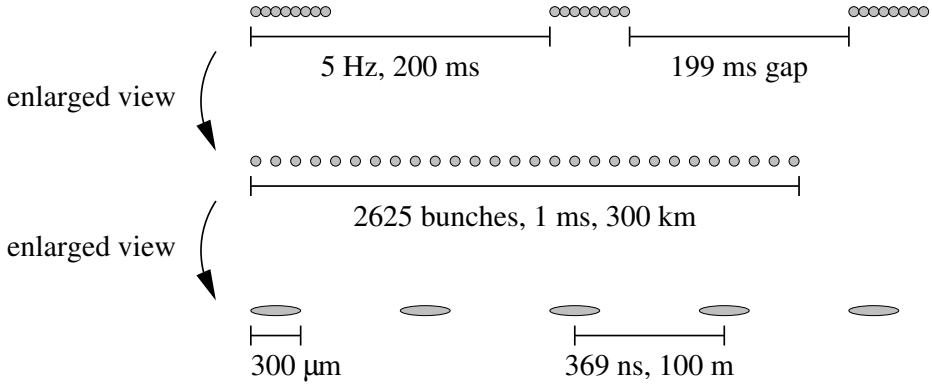

Figure 3.2: Illustration of the ILC bunch structure. In the top row three bunch trains are shown. The middle row depicts the structure of one train. On the bottom parameters of single bunches are illustrated [Vog08].

3.2.1 Particle Sources

In a linear collider all beam parameter tuning and acceleration have to take place on the way through the accelerator to the interaction point, since the particles are passing only once through the structures. Therefore it sets stringent requirements on the particle sources. This means, the number of particles per bunch provided by the sources has to be large – of the order of $2 \cdot 10^{10}$. Even more important is a low emittance to increase the luminosity and achieve highly polarized beams. A polarization of 80 % for the electrons and 30-60 % for the positrons is the design goal for the ILC to be able to suppress standard model processes and enrich cross sections of processes beyond the standard model. More details about the benefit of beam polarization can be found in [MP+08].
Particles are not delivered in continuous beams at colliders. Instead they appear in so-called bunches, which are caused by the acceleration in cavities. The bunch structure envisaged for the ILC is illustrated in figure 3.2. It is organized in bunch trains with a frequency of 5 Hz. The train itself is 1 ms long and consists of 2625 bunches, followed by a gap of 199 ms. This gap is needed due to rise and decay times of the accelerating fields in the cavities and for the damping, which needs a time of the order of this gap.
A laser-driven photo injector serves as electron source. It uses circular polarized photons to produce polarized electrons. The positron source is located in the main electron linear accelerator (linac) and uses electrons with roughly 150 GeV. They are shot through an undulator and produce photons with 10 GeV. The latter are converted in positrons with the help of a thin target. In order to polarize these positrons, a helical undulator is used.

3.2.2 Damping Rings

An important performance parameter of accelerators is the luminosity. In order to achieve high luminosity, the particles per bunch and the number of bunches have to be maximized. In addition, the emittance, which describes the phase space volume occupied by the beam, has to be as small as possible. Damping rings are used to reduce the emittance of the electron and positron beam.
At the ILC they are designed to operate at a beam energy of 5 GeV. The preaccelerated beams are fed into the damping rings where they emit synchrotron radiation in dedicated wiggler magnets caused by the accelerated motion on a circular path. The energy is afterwards restored in the acceleration cavities, but only in longitudinal direction, which significantly reduces the emittance.
The whole process takes of the order of some milliseconds. Since every bunch train with its 300 km length is treated as a whole, strong demands are put on the damping rings and the kicker magnets. The bunch train has to be wind up in the ring, in consequence the gaps in between the single bunches are filled with additional bunches and are reduced to a few nanoseconds. Hence, the kicker magnets are required to be able to operate with rise times of a few nanoseconds in order to feed and extract the bunches to and off the damping rings. In the ILC reference design report the damping ring were planed with a circumference of 6.7 km [ILC07], but considerations for smaller rings with a circumference of about 3 km are made [O$^+$08]. In order to save money, both damping rings – for electrons and positrons – are positioned in a single tunnel in the middle of the accelerator.

3.2.3 Main Linacs

After the extraction from the damping rings both beams are transferred to the Ring To Main Linac (RTML), which leads the particles to the far ends of the main linacs. Each main linac is about 11 km long and instrumented with about 7500 "cold" superconducting nine-cell cavities, developed within the TESLA (TeV-Energy Superconducting Linear Accelerator) project [TESLA01b]. They are operated at a frequency of 1.3 GHz and are designed to provide an average acceleration of 31.5 MV/m. In figure 3.3, the yield of 22 industrially produced cavities, tested at JLab and DESY is shown. The results are obtained by so-called first-pass tests, which means the first test under standard conditions, where no system problems occurred [Gin09]. It can be seen, that up to now 40 % of the nine-cell cavities meet the ILC design goal. In [Bar09] it is mentioned, that until mid of the year 2010 a yield of 50 % shall be reached, which seems to be possible. The cavities are organized in modules, one radio frequency unit supplies a group of 26 cavities in three super conducting modules [ILC07]. The acceleration in the linac has to preserve the low emittance of the bunches, which requires a precise orbit control via a beam monitor system and higher order modes of the cavities have to be under control. In addition, the linac has to be operated without introducing a jitter to the beams. Otherwise it could

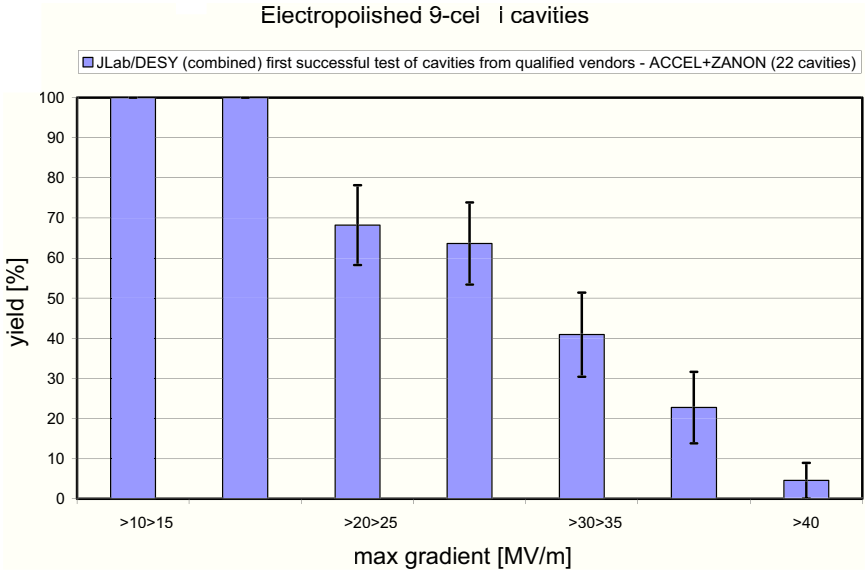

Figure 3.3: Cavity yield of 22 industrially produced cavities, tested at JLab and DESY [Gin09].

happen, that the beams miss each other on the IP. At the end of the main linacs a beam energy of 250 GeV per beam is reached.
With the Free electron LAser Hamburg (FLASH) a 260 m long test facility for the ILC cavities exists, where research and development for the acceleration structures is performed [FLA10]. The same cavities will also be used in the XFEL (X-ray Free Electron Laser) project, currently build at DESY Hamburg. This new accelerator will have a length of 3.4 km [XFEL10].

3.2.4 Beam Delivery System and Interaction Region

The Beam Delivery System (BDS) is meant to provide the best achievable conditions for the interaction. Therefore, collimators scrape off the beam halo and a 5 m thick magnetized muon shield reduces the number of halo muons. In addition, beam diagnostic and monitoring systems are installed as part of the BDS as well as an upstream polarimeter. In the last part of the BDS the final focussing quadrupoles, which reach close to the interaction region, are installed.
Since the BDS is a very complex and expensive component, the decision was made to deliver the beams to only one interaction region, where two movable detectors are placed. In this so-called push-pull concept one detector will take data, while the other one is able to be maintained in the parking position. The position will be changed on a regular basis. However, this new concept yields many technical challenges and a large development effort is needed to be able to realize such a push-pull option.
In order to simplify the extraction of the beams from the detectors and according to

beam parameter	nominal value	
bunch population	2×10^{10}	
number of bunches	2625	
linac bunch interval	369	ns
RMS bunch length	300	µm
normalized horizontal emittance	10	mm·mrad
normalized vertical emittance	0.04	mm·mrad
RMS horizontal beam size	640	nm
RMS vertical beam size	5.7	nm

Table 3.1: Selected nominal beam parameters at the IP for the ILC [ILC07].

beam dump issues a crossing angle of 14 mrad between the two beams is planned. Such a crossing angle would significantly reduce the cross section for collisions, because the geometric overlap of the bunches become smaller due to their elliptical shape. To recover the full luminosity a technique called crab crossing is developed. The single bunches are kicked sideways shortly before they reach the interaction point to maximize the geometrical overlap of the two colliding bunches.

3.2.5 Beam Parameters

The most important nominal beam parameters at the IP, as planned for the design luminosity and a center of mass energy of 500 GeV, are summarized in table 3.1. The parameters are a result of optimization studies, trying to involve different technology challenges. For example, beam instability and kicker hardware constraints in the damping rings, beam current, power and especially pulse length limitations in the cavities of the main linacs, emittance preservation and background control.
More important than the technological requirements are the physics processes, which will be observable at the ILC. The whole machine is designed for high precision measurements of the Higgs mechanism and possible beyond standard model scenarios. In figure 3.4 a set of cross sections of expected processes as a function of the center of mass energy at the ILC is shown. Especially the Higgs boson, here the Higgs-strahlung depicted by HZ is shown, and supersymmetric processes, like slepton or chargino production, are of interest. The advantage of the ILC is, that the background is moderate compared to the LHC backgrounds.

3.3 International Large Detector

At the ILC, precision measurements to investigate the Higgs mechanism in detail and to study new physics – be it SUSY or something else – will be performed. In order to exploit the full physics potential of the ILC, detectors of unprecedented precision equipped with state of the art technologies are needed. A detailed description of

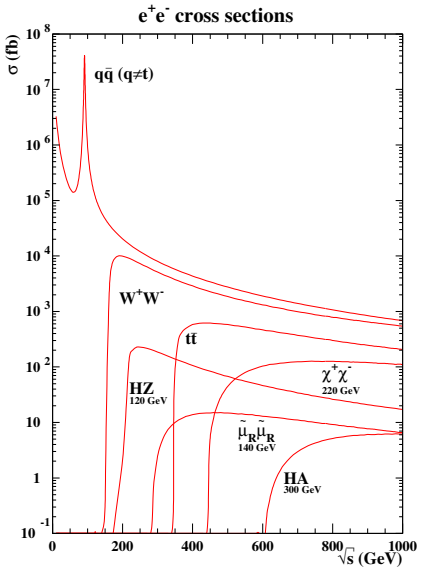

Figure 3.4: Expected cross sections as a function of the center of mass energy at the ILC [God06].

requirements for the detectors defined by the physics program of the ILC can be found in [ILC07]. Many of the physics processes are identified by a hadronic final state. Hence, a new concept called particle flow is introduced in order to provide the necessary jet energy resolution of $\Delta E/E \approx 3-4\,\%$ for jets below 100 GeV [LOI09]. With it, the separation of W and Z jets can be achieved, which is needed for Higgs physics. For Higgs recoil mass studies and low multiplicity events, a very good momentum resolution and a large angular coverage with high efficiencies of the tracking system are required. More details about such studies can be found in section 7.4. Another important detector performance parameter is the flavor tagging ability by means of the lifetime signatures of particles. This requires a very precise and efficent vertex detector and is for example necessary to measure branching ratios of Higgs decays into b, c and τ signatures.
In 2009, three concept groups submitted so-called Letters Of Intent (LOI) to the International Detector Advisory Group (IDAG). The three mentioned collaborations are International Large Detector [ILD09] – merged from GLD and LDC in summer 2007, Silicon Detector [SiD09] and the fourth concept [4th09]. In late summer 2009 the ILD and SiD concepts were validated by the IDAG [IDAG09] and are encouraged to provide a technical design report of their detectors until the year 2012.
In this section the ILD concept is briefly introduced, concentrating on the tracking system, in particular on the TPC with its amplification structures, as they are the subject of the studies presented in this thesis.
A sketch of the ILD is shown in figure 3.5. In this figure, the onion-like structure around the interaction point is visible, which is typical for 4π multi purpose detectors in high energy physics. The coordinate system is indicated, with the z axis pointing

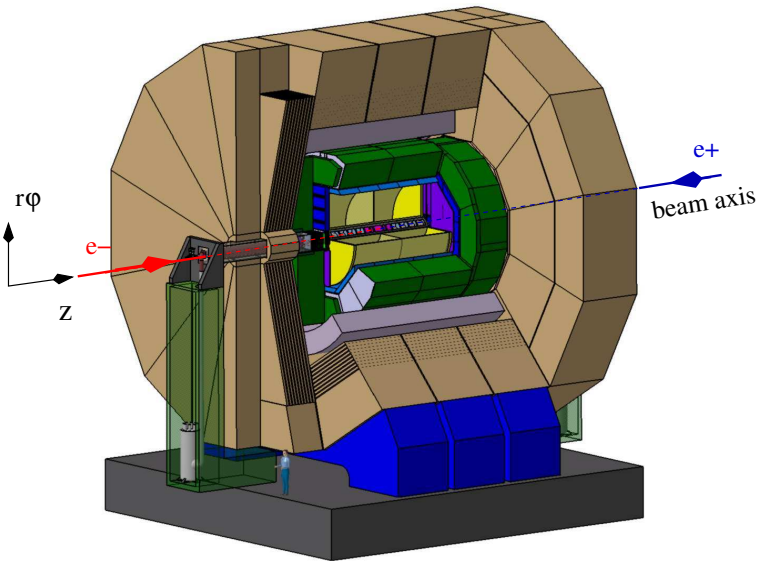

Figure 3.5: Sketch of the international large detector. The main parts are the TPC (yellow) wrapping the vertex and silicon detectors. The TPC is surrounded by the calorimeters in blue and green, which are located inside the magnet coil. The return yoke (brown) instrumented as muon detector is completing the detector [LOI09].

in the electron beam direction, perpendicular to the rϕ plane, where r denotes the radius and ϕ the azimuthal angle. The polar angle θ is defined with respect to the positive z axis.

3.3.1 Particle Flow Concept

The whole ILD layout is designed for the particle flow concept. This approach aims to use the best available measurement to reconstruct full four momentum vectors of all particles coming from the interaction region. For this purpose all sub-detectors are used instead of relying only on calorimeter information. The momentum of charged particles is measured in the tracking system, it translates via $E^2 = p^2 + m^2$ into energy. The mass is assumed to be negligible at typical ILC energies. If a track is measured in the tracking detector, a matching energy deposition in the calorimeter is searched and removed from the calorimetric information, in order to avoid double counting. Photons – not causing a signal in the tracking system – are identified in the electromagnetic calorimeter (ECAL). Muons are treated with the help of a so-called minimum ionizing particle finder and the muon detector inside the iron return yoke. Finally, the hadronic calorimeter (HCAL) can be used exclusively for precision measurements of neutral mesons and hadrons. A jet energy in the particle flow concept is composed of energies of all individual particles contained in the jet. The crucial part in the particle flow algorithm is the correct assignment of calorimeter hits to reconstructed tracks. Therefore, a sophisticated separation method for close-by clusters in the calorimeter is needed. Two problems can occur, missing

energy and double counting. In the first case, a neutral hadron is accidentally not separated from an energy deposition originating from a charged particle. Since the energy for this charged particle is determined in the tracking system, the energy of the neutral hadron will be missed. The other scenario, which should be avoided is double counting. This happens, if a shower produced by a charged particle is split and a part of it is misidentified as neutral particle. The energy of the latter cluster is counted twice, since it is already measured in the TPC. Hence, the performance of the particle flow depends on detector resolution and the reconstruction algorithms. For the realization of such a particle flow concept, the tracking detectors need an excellent momentum resolution, while the calorimeters have to be highly granular for good separation of particles in jets. In [LOI09] an energy resolution of $\Delta E/E \approx 3-4\,\%$ for jets below 100 GeV is mentioned as design goal. This number is equivalent to $\sigma/E = 30\%/\sqrt{E}$ for the calorimetric system. Currently energy resolutions of $\sigma/E = 17\%/\sqrt{E}$ in the ECAL and $\sigma/E = 49\%/\sqrt{E}$ in the HCAL are reached with prototypes. In addition, a very good spatial resolution of the calorimeters is required in order to separate clusters from each other. Excellent transverse and lateral granularity is a new challenge for calorimetry research and development. The achievable energy resolution for a jet is the squared sum of energy resolutions of all sub-systems and a so-called confusion term, weighted with energy fractions:

$$\frac{\sigma_{\text{jet}}}{E} = f_{\text{ch}} \cdot \frac{\sigma_{\text{tracker}}}{E} \oplus f_{\gamma} \cdot \frac{\sigma_{\text{ECAL}}}{E} \oplus f_{\text{h}^0} \cdot \frac{\sigma_{\text{HCAL}}}{E} \oplus \sigma_{\text{confusion}}. \tag{3.2}$$

In average f_{ch} accounts for 60 % of the jet particles, while f_{γ} is about 30 % and 10 % of a jet consist of neutral hadrons (f_{h^0}). On a single event basis, fluctuations of these values can be very large. The confusion term summarizes all systematic uncertainties related to the double counting and missing energy effect. In order to provide a sufficient resolution, this contribution has to be as small as possible. In addition to the requirements mentioned above, a good hermeticity of the detector and a low material budget of the tracking system is crucial, since conversions and multiple scattering in front of the calorimeters have to be minimized, in order to avoid energy loss.

3.3.2 Detector Layout

This section describes the design of the ILD detector and its sub-detectors in more detail, a complete description can be found in [LOI09]. Figure 3.6 is showing a schematic side view of one of the quadrants of the detector.
As vertex detector, either five single or three double layers of silicon pixel detectors are used. They are installed around the interaction point and approach it down to a distance of 15 mm. This sub-detector is important for flavor tagging and the measurement of tracks with very low momenta, which are not able to reach the main tracker. Key parameters are an outstanding single point resolution of the order of 3 µm and a very low material budget.

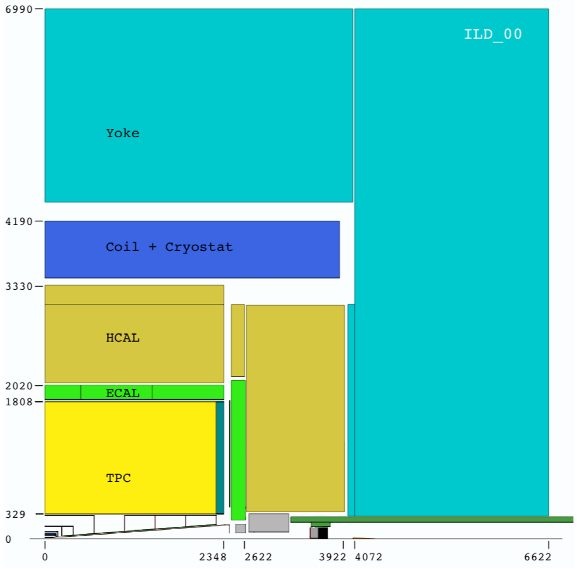

Figure 3.6: Side view of one quadrant of the ILD detector model with its subdetector systems. In the forward region the FTD, ETD, LumiCAL, LHCAL and BeamCAL are shown in addition to the labeled components [LOI09].

The vertex detector is surrounded by the tracking system. In the case of the ILD, a TPC is planned as main tracking detector. The TPC performance is supported by auxiliary tracking systems, more details can be found in the next section about the ILD tracking system.
The calorimeters are subdivided in an electromagnetic and a hadronic system. As electromagnetic part serves a tungsten-silicon sampling calorimeter with small Moliere radius and 24 radiation lengths X_0. The cell size is of the order of $1 \times 1\,\mathrm{cm}^2$ and 30 active layers are used. For the detection of hadrons a steel sampling calorimeter is planned with either scintillating tiles with optical readout or resistive plate chambers as sensitive layers. The mean free path is five interaction lengths λ and the cell size is about $3 \times 3\,\mathrm{cm}^2$. The hadronic calorimeter (HCAL) contains 48 active layers.
Luminosity measurement is done in the so-called LumiCAL. It measures Bhabha-scattered electrons and positrons and is built similar to the ECAL. The LumiCAL adds calorimetric information for polar angles down to 40 mrad. The BeamCAL made of tungsten-silicon or even tungsten-diamond is another sampling calorimeter, measuring down to 5 mrad. It has to stand a lot of radiation through beam induced background and uses those particles to determine parameters of bunch crossings. It can also be used as feedback and control for the beam delivery system. The last component is the LHCAL, which serves as an extension of the HCAL down to very small θ.
A superconducting solenoid coil providing a magnetic field of 3.5 Tesla contains all inner parts of the detector. The design is similar to the CMS (Compact Muon

Solenoid experiment at LHC) coil [CMS08]. An iron yoke returns the field lines and is additionally used as muon detector with resistive plate chambers and as tail catcher for the HCAL.

3.3.3 Tracking System at ILD

The tracking system of the ILD is composed of a TPC as main tracker and the vertex detector, two silicon detectors in- and outside the TPC (SIT & SET) and the forward and the endcap tracking discs (FTD & ETD). All components are described briefly in the following and a short introduction to TPCs can be found in the next section. Chapters 4 and 6 are dedicated to the principles of gaseous detectors, TPC design, track reconstruction and particle identification in TPCs and design goals for the ILD TPC.
The Silicon Inner Tracking (SIT) consists of two cylindrical layers of silicon strip detectors positioned in the gap between vertex detector and TPC. With the help of the SIT, the linking efficiency of tracks from vertex to TPC can be enlarged and the reconstruction of secondary vertices of long lived particles can be improved with the additional hits. The Silicon Envelope Tracker (SET) adds another space point for tracks outside the TPC and in front of the ECAL in the barrel region. With the help of these reference points the main tracker can be aligned and track reconstruction inside the TPC can be understood in detail. SIT and SET provide for example a possibility to monitor field distortions inside the TPC, because large inhomogeneities would cause a discrepancy of the reference points and the reconstructed tracks of the TPC. The silicon system improves the achievable momentum resolution and allows for time stamping, which can be used to disentangle overlaid events in the TPC.
Seven Forward Tracking Discs (FTD) with pixel sensors on the inner three discs and strip sensors on the outer four discs are part of the ILD design. They are located between beam tube and TPC and allow track measurements down to polar angles of 100 mrad. Between TPC and ECAL endcaps the Endcap Tracking Discs (ETD) can be found. They ensure good momentum resolution for tracks with a short path length inside the TPC and improve matching between charged tracks and clusters identified in the calorimetric system.

3.3.4 Time Projection Chamber

The concept of Time Projection Chambers (TPC) – as invented in the 1970s [Nyg74] – is introduced here, while a more sophisticated description of the basic physics processes and details of the working principle follows in the next chapter.
A TPC is a gas filled cylinder as illustrated in figure 3.7. It is used for tracking of charged particles and is based on ionization principles. In order to provide an electrical field in the drift region, on the cathode a negative high voltage of the order of 10-50 kV – depending on the drift length of the chamber – is applied. A charged particle passing the chamber ionizes the gas inside the volume and the

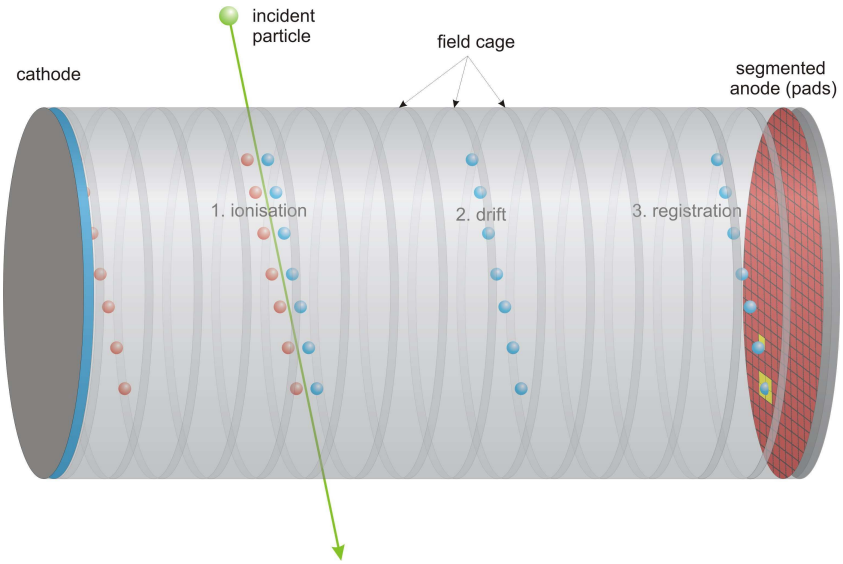

Figure 3.7: Time projection chamber principle [Sch06].

resulting primary electrons drift in the electric field towards the anode. Since a direct detection of these electron clouds is not possible due to the small amount of charge, an amplification stage is installed in front of the anode. The anode itself is instrumented and the charge is detected here as two dimensional projection of the track. As readout device, analog as well as digital techniques are used. The z coordinates of the track hits are reconstructed by means of drift time measurements. If the drift velocity v_D of electrons in the gas is known, the z coordinate can be reconstructed via:

$$z = v_D \cdot (t_1 - t_0), \tag{3.3}$$

where t_1 is the arrival time at the anode, while t_0 denotes the time of the particle passage, given by the beam collision time or in the case of prototypes by an external trigger.
Parallel to the electrical field a magnetic field is applied. It bends tracks of charged particles due to Lorentz forces. The resulting curvature allows for measurement of particle momenta. In addition, a magnetic field reduces the diffusion of the charge cloud on its way to the anode, which ensures a good single point resolution.
In order to determine precise results with a TPC, a good homogeneity of E and B field is required. Otherwise tracks cannot be reconstructed at their original positions. To ensure reliable operation conditions, like a constant drift velocity and constant gain, a precise monitoring and control of the gas and high voltage parameters is needed as well.

3.3.5 Micro Pattern Gas Detectors

The drifting primary electrons have to be amplified before they can be read out at the anode plane. In the past, proportional wires – thin metal wires supplied with high voltage – have been used as amplification stage in gaseous detectors. The wires attract the drifting electrons and due to the strong electrical field, the electrons are amplified shortly before they reach the wire surfaces. In TPCs a wire plane was installed in front of the anode and the signals on the wires as well as the induced signal on the pad plane were read out. Due to four aspects these wire planes are not able to fulfill the ILD requirements. First of all, the spatial resolution is limited by the width of the induced signal on the pad plane and the distance of the wires. The strong electrostatic forces do not allow to place them with less than 1 mm distance, which does not allow to reach the ambitious goals for the ILD TPC. A second problem occurs near the wires, where the electrical field of the wire and the outer magnetic field cause $\overrightarrow{E} \times \overrightarrow{B}$ effects, which distort the electron propagation of tracks with small dip angles, causing a track direction almost parallel to the wires. The third drawback is the mechanical mounting of the wires, which is needed to provide sufficient tension. This structure introduces a lot of dead material into the detector. A fourth problem is that wire structures are normally operated with a gating plane to reduce the backdrift of ions produced during the amplification process. These ions drift towards the cathode and distort the drift field. Hence, they have to be prevented to drift back into the sensitive volume. For this purpose, a plane of gating wires is built in between the sense wires and the drift region. This plane consists of wires, which are set in between the events on alternating potentials in order to close the gate. Then all field lines end on the gating wires and the ions are caught on the gate and cannot enter the drift volume. During the readout phase of an event, the wires are set on equal potentials to open the gate. The switching of the gate will not be possible for trigger-less running at the ILC, since the time between the bunch crossings is too short. Only in between the bunch trains a switching would be possible, which does not help much.
Therefore, nowadays Micro Pattern Gas Detectors (MPGD) are used as amplification devices, not only in TPCs but in all kinds of gaseous detectors. In principle, MPGDs are made of metalized foils with holes. The primary electrons are guided through the holes by electrical fields. Potentials are applied such across the devices, that the resulting field strengths are able to multiply the electrons via gas amplification. MPGDs are able to meet the ambitious demands for an ILC detector. Although they have not been used in large scale TPCs for collider experiments up to now, MPGDs are envisaged for the ILD TPC. The existing two sub-species are introduced in the next two sections.

MicroMEGAS

Micro Mesh Gas Amplifiers (MicroMEGAS) were invented in 1995 [GRRC96]. They consist of a few microns thin metal mesh with a pitch of the holes of 20-50 µm. This

(a) (b)

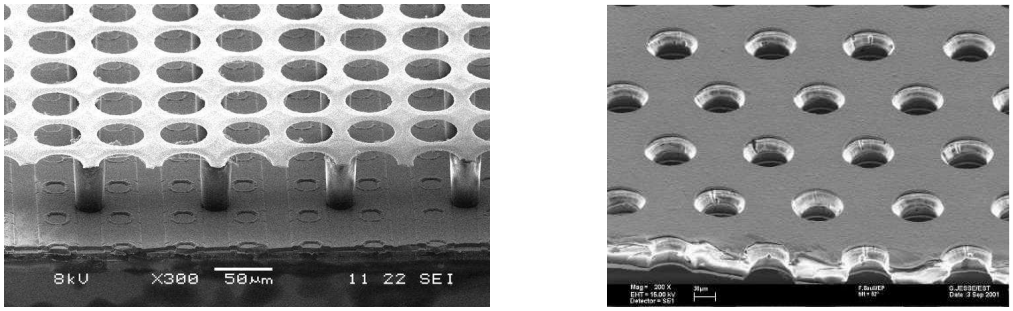

Figure 3.8: Micro pattern gas detectors. Pictures of (a) an InGrid MicroMEGAS with a hole diameter of 30 µm [Che09] and (b) a GEM foil with an outer hole diameter of 70 µm [GDD10a].

mesh foil is held by small pillars above an anode plane. A picture of a special kind of MicroMEGAS – a so-called InGrid – is shown in figure 3.8(a). InGrids are directly built on top of a silicon wafer and the holes are aligned with the readout pixels. The complete production process and performance studies of InGrids can be found in [Che09].
Mesh and anode of MicroMEGAS build a parallel plate capacitor. Since they have a distance of about 100 µm, strong electrical fields in the gap of the order of 50 kV/cm can be reached by applying some hundred volts at the mesh. The gas amplification takes place in the gap between anode and mesh and reaches a strength of about 10^4. The field configuration produces a funnel shape of the field lines through the holes. Therefore electrons, which are following the field lines, are pulled into the amplification region. Typical multiplication factors possible with MicroMEGAS are of the order of 10^4. This measure is normally called gain and specifies the number of electrons produced per primary particle. The ion backflow of MicroMEGAS is of the order of one percent for drift fields larger than a few ten volts per centimeter. Only for lower fields, the fraction of back drifting ions can be reduced to the per mill level [Che09].

Gas Electron Multipliers

A short introduction of Gas Electron Multipliers (GEMs) is given here, while a detailed description can be found in chapter 5. In 1996 Fabio Sauli introduced GEMs as a new amplification structure [Sau97]. A picture of a GEM is shown in figure 3.8(b). It consists usually of a copper plated polyimide substrate with a total thickness of 60 µm. Double conical holes are etched into the foil with a pitch of 140 µm. Across the two copper surfaces a voltage difference of about 350 V is applied resulting in a strong electrical field inside the holes. As a consequence the gas amplification takes place inside the GEM holes and the gain is of the order of up to 10^3 per GEM.

GEMs are typically used in so-called stacks, which means that two or three foils are installed on top of each other with small gaps of a few millimeters. This is done to reach effective gains of the order of 10^4. Advantages of such a stack compared to a single GEM foil are firstly the smaller discharge probability due to less stress on the individual GEMs. With two or three GEMs a certain amplification factor can be reached with less voltage across the GEMs compared to the voltage needed across one single GEM. The second benefit of a GEM stack is the number of available free parameters. $2 \cdot \mathrm{N_{GEM}} + 1$ parameters – three GEM voltages and four field strengths in the case of a triple GEM stack – can be adjusted to reach envisaged effective gains and ion backflow fractions, as described in section 5.6.

Chapter 4

Time Projection Chamber Principles

A basic introduction to Time Projection Chambers (TPCs) has already been given in the last chapter. As mentioned, a TPC is a gas filled cylinder, therefore the next section deals with the gas choice and the design of a cylindrical field cage for a TPC. The general principle of a TPC consists of charge production due to ionization – described in section 4.2 – followed by the drift of the charge over large distances – see section 4.3 – while suppressing the diffusion – described in section 4.3.2. The amplification of the drifting electrons is presented in the same section. Since in this thesis Gas Electron Multipliers (GEMs) are used as amplification stage, the defocussing in this stage and the subsequent read out of the charge signals is described in section 6.3, within a chapter dedicated to GEM TPCs.

4.1 Main Ingredients

A TPC field cage consist of a barrel with two electrodes as endcaps, the cathode and the anode. In applications for large scale detectors – like the ILD – the chamber is usually built symmetrically with two anodes and one cathode in the middle – near the interaction point, as shown in figure 4.1. Tracks produced in particle collisions are in average distributed more or less isotropically around the interaction point, therefore such a symmetric and nearly hermetic arrangement is used at collider experiments. At the cathode, a negative high voltage is applied in order to create a drift field for the electrons. These electrons are released by charged particles due to ionization of the counting gas. At the anodes, the read out of the charge and time signal takes place.

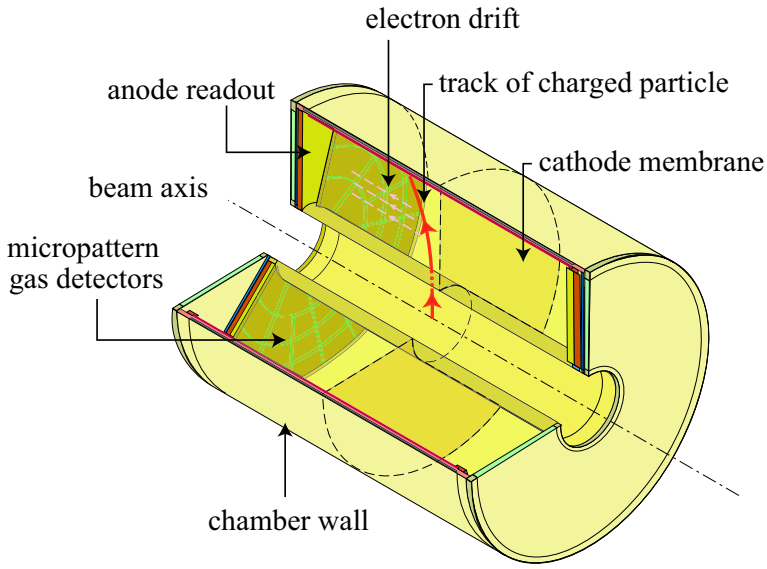

Figure 4.1: Schematic layout of the ILD TPC [LOI09].

4.1.1 Field Cage

The homogeneity of the electrical field is of particular importance for the TPC operation. Only a homogeneous field without distortions is able to avoid $\vec{E} \times \vec{B}$ effects, which influence the track reconstruction. To obtain the best possible field quality, mechanical precision, an external shielding and, more important, field strips are introduced (cf. figure 6.1 on page 51). The strips are installed parallel to the electrodes and reduce the potential stepwise from cathode to anode. The equidistant strips are made of copper carried by an polyimide foil. These field strips are connected via a resistor chain. At DESY, a special design of field strips together with mirror strips has been developed to obtain a better field quality for a large TPC prototype. The mirror strips are mounted on the backside of the substrate foil in the gaps of the field strips. More details about the electrical design and the consequences for the field quality are presented in [Sch09].

4.1.2 Gas

A proper choice of the gas is crucial for the performance of a TPC. The gas has to provide good signal production and transportation capabilities and a sufficient gas gain in the amplification structure has to be achievable. Noble gases are often used – preferably argon – since they require relative low ionization energies, are chemically inert and have only few degrees of freedom. The latter fact provides that all deposited energy causes ionization and no rotation or vibration states are excited.
In addition, so-called quencher gases are part of the mixture with a fraction of $5-10\,\%$. Such gases, like methane, carbon dioxide or isobutane, catch the photons,

which are released inside the amplification stage. These photons would be able to ionize further gas molecules and therewith produce additional free electrons. Rotation and vibration states of the quencher gas dissipate the photon energy.
Optimization of gas mixtures for TPC operation is a wide field with many parameters to consider. Only some of these parameters are mentioned here, more details can for example be found in [Gru99] or [A$^+$06]. The drift velocity v_D of electrons in the gas is crucial for a fast read out of the drift region, but at the same time the velocity has to be stable against small variations of the drift field. Another aspect is the longitudinal diffusion, which has to be small in order to obtain a good z resolution and the attachment coefficient of the gas mixture has to be small as well in order to guarantee that only few electrons are lost during the drift. For a good spatial resolution, a small diffusion in the drift area and large defocussing inside the amplification stage are required in order to reach a sufficient charge sharing (cf. paragraph 6.3.2). To ensure a good momentum resolution, the multiple scattering and conversion probability inside the gas has to be small. For dE/dx measurements it is important to maximize the total number of released electrons per length unit. Finally, the gas should not be aggressive in order to protect the detector material during long term operation.

4.2 Ionization

Gaseous detectors work on the basis of ionization. Traversing particles release electrons from the gas molecules. These electrons carry the information, that is used for track reconstruction. The ionization process and the additional benefit of particle identification due to dE/dx measurements in the TPC are presented here.

4.2.1 Primary Ionization and Delta Electrons

A charged particle traversing a gas volume interacts with the gas molecules and releases primary electrons. This interaction can be interpreted as single virtual photon exchange [AC80]. If the energy transferred to the released electron is larger than the ionization energy of the gas W_I, secondary electrons are set free due to inelastic collisions of the primary electron and the gas molecules. The secondary electrons form clusters, spatially correlated to the primaries. The number of primary electrons n_e produced in a specific gas, is roughly proportional to the mean atomic number $\overline{Z}$ of the gas molecules. The uncertainty on the number of primary electrons is given by the Fano factor F, which is dependent on the gas molecules [Fan47]:

$$\sigma_{n_e} = \sqrt{n_e \cdot F}. \tag{4.1}$$

The total number of ionization electrons n_{tot} is given by the ratio of the total energy deposit ΔE and the ionization energy W_I [LW92]:

$$n_{tot} = \frac{\Delta E}{W_I}. \tag{4.2}$$

gas	mean atomic number $\overline{Z}$	ionization potential I [eV]	ionization energy W_I [eV]	number of primary e^- n_e [cm^{-1}]	number of total e^- n_{tot} [cm^{-1}]	Fano factor F
He	2	24.6	41	4.8	7.8	0.17
CH_4	10	13.1	28	26.5	53.0	0.26
Ar	18	15.8	26	24.3	94.0	0.21
CO_2	22	13.7	33	36.5	91.0	0.33
Kr	36	14.0	24	22.0	192.0	0.19
Xe	54	12.1	22	44.0	307.0	0.15

Table 4.1: Ionization gas parameters for gases used in TPCs. Given are the averaged atomic number, the ionization potential and energy, the number of primary and total electrons per centimeter [LW92] and the Fano factor [Che09].

W_I is in this case larger than the ionization potential I of the gas, since some energy is transformed into excitations of gas molecules and into kinetic energy of the remaining ion and the released electron. In argon, 24 primary electrons are produced per centimeter. Together with the secondary electrons in total 94 electrons per centimeter are emitted. A summary of ionization parameters of different gases can be found in table 4.1.
Most of the clusters along a track consist of up to ten electrons, but occasionally the initial particle transfers a very large amount of energy to one single electron. These so-called delta electrons are able to travel up to several centimeters in an arbitrary direction, ionizing other gas molecules on their way. In argon, such delta electrons form clusters of about 100 electrons and occur in average every ten centimeters. Hence, the ionization on small scales can be very inhomogeneous. Therefore, tracks with a sufficient length – about half a meter – have to be used for the determination of a mean cluster size or average ionization.

4.2.2 Energy Loss and Particle Identification

Particles can be identified with the help of their momenta and their specific energy loss. A TPC is able to measure both and to perform therewith a complete particle identification. The average specific energy loss of a particle crossing matter and causing ionization is described by the Bethe-Bloch formula [Bet33]. It is based on three assumptions: first, the transfer of energy does not change the direction of flight of the ionizing particle, second, the gas molecules are at rest and third, the ionizing particle is much heavier than an electron. A modified version of the Bethe-Bloch formula – which makes the dE/dx behavior directly readable – can be written as function of the particle velocity β and the charge number Q:

$$\left\langle \frac{dE}{dx} \right\rangle = \xi \frac{Q^2}{\beta^2}[K + \ln Q^2 + \ln\gamma^2 - \beta^2 - \delta(\beta\gamma)]. \tag{4.3}$$

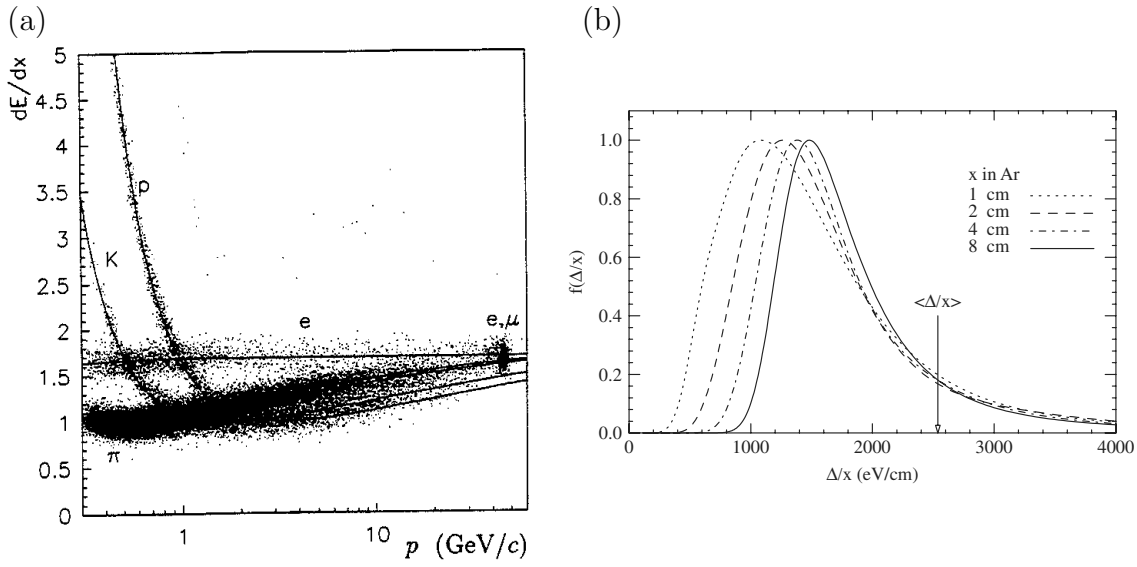

Figure 4.2: (a) Specific energy loss over particle momenta measured in the ALEPH TPC [ALEPH95]. The curves are determined with the Bethe-Bloch equation. (b) Straggling functions $f(\Delta/x)$ as function of the energy loss Δ/x of a particle with $\beta\gamma = 3.6$ traversing argon of different thickness [Bic06].

In this equation K is representing a constant and ξ the electron density of the gas, while $\delta(\beta\gamma)$ denotes the density function, first introduced by Fermi. This correction accounts for polarization effects due to the electrical field of the relativistic particle. The energy loss as a function of $m\beta\gamma = p$, shown in figure 4.2(a) with ALEPH TPC data [ALEPH95], can be subdivided in three regions. At low momenta and therefore non-relativistic velocities a decrease with $1/\beta^2 \sim 1/p^2$ – causing large ionization – is visible. For momenta corresponding to three to four times the mass of the particle, a minimum is reached, followed by the relativistic rise proportional to $\ln(\gamma^2)$ or $\ln(p^2)$. The relativistic rise is an effect of the deformed electrical field of the ionizing particle, leading to an increase of the transverse component of the field. A saturation is reached for very large values of $\beta\gamma$ at the "Fermi plateau". There the relativistic rise ends and the energy loss becomes independent from $\beta\gamma$. The most interesting physics processes at lepton colliders involve particles in the region of relativistic rise, where the energy loss difference of different particle types is small, $\mathcal{O}(10\,\%)$. Hence, the resolution of dE/dx measurements has to be at the level of a few percent only, in order to give a handle for particle identification in this momentum regime.
By measuring hit charges, using correction algorithms and applying the truncated mean method, which is described in section 7.5, the energy loss of a track can be determined. With the additional information of the momentum – calculated from the track curvature – the particle can be identified with the help of the Bethe-Bloch diagram.

4.2.3 Energy Straggling

The probability density functions of the energy loss are called straggling functions. Only averaged dE/dx values are described by the Bethe-Bloch formula. The energy loss of a single particle traversing matter is a highly statistical process. The resulting distribution of dE/dx depends on the thickness of the absorber via the central limit theorem. For a thick absorber, providing enough statistics due to many collisions, a Gaussian shape develops for the energy loss distribution. The absorber thickness in TPCs is defined by the gas and the pad height on the readout structure, usually of the order of 5-7 mm. This can be assumed as thin absorber and instead of a Gaussian, a Landau distribution is developing due to delta electrons gaining much energy and forming the tail of the function. The transition from thin to thick absorbers can be described by the Vavilov model, which yields distributions between Gauß and Landau [Bic06]. In figure 4.2(b) straggling functions f(Δ/x) as function of the energy loss for different absorber thickness are shown. They are derived for particles with $\beta\gamma = 3.6$ traversing x = 1, 2, 4 and 8 cm of argon. Additionally depicted is the mean energy loss $< \Delta/\mathrm{x} >$.

4.3 Drift

Electrons released during the ionization process are drifting influenced by electric and magnetic fields towards the anode. They are forming clouds, which undergo diffusion. The drift velocity and the diffusion process is described in the following, as well as the influence of the fields and the amplification process.

4.3.1 Drift Velocity

The velocity $\overrightarrow{v}$ of an electron under the influence of an electrical and magnetic field is described by the Langevin equation [LW92]:

$$\mathrm{m}\frac{\mathrm{d}\overrightarrow{v}}{\mathrm{dt}} = \mathrm{e}\overrightarrow{E} + \mathrm{e}(\overrightarrow{v} \times \overrightarrow{B}) + \overrightarrow{Q}(\mathrm{t}). \tag{4.4}$$

Here, $\overrightarrow{E}$ and $\overrightarrow{B}$ represent the fields, e is the electron charge and $\overrightarrow{Q}(\mathrm{t})$ denotes a time dependent noise term, which describes the stochastic scattering with gas molecules. A stationary solution for the velocity $\overrightarrow{v_D} = \langle\overrightarrow{v}\rangle$ averaged over $\mathrm{t} \gg \tau$ exists, where τ denotes the mean time between collisions:

$$0 = \left\langle \mathrm{m}\frac{\mathrm{d}\overrightarrow{v}}{\mathrm{dt}} \right\rangle = \mathrm{e}\overrightarrow{E} + \mathrm{e}(\overrightarrow{v_D} \times \overrightarrow{B}) - \frac{\mathrm{m}}{\tau}\overrightarrow{v_D}. \tag{4.5}$$

In this equation the noise is approximated as friction term: $\overrightarrow{Q}(\mathrm{t}) \rightarrow -\mathrm{m}\overrightarrow{v_D}/\tau$. With the help of the electron mobility $\mu = \mathrm{e}\tau/\mathrm{m}$, the drift velocity without magnetic field can be written as $\overrightarrow{v_D} = \mu\overrightarrow{E}$.

In order to get an expression for the drift velocity in the case of a non vanishing magnetic field, the cyclotron frequency $\overrightarrow{\omega} = \mathrm{e}\overrightarrow{B}/\mathrm{m}$ is plugged in equation 4.5 and the result is:

$$\overrightarrow{v_D} = \mu\overrightarrow{E} + \tau\overrightarrow{v_D} \times \overrightarrow{\omega}, \tag{4.6}$$

with μ and τ depending on gas properties. In order to solve this for the drift velocity, the equation can be transformed. Additionally using $\widehat{\mathrm{E}}$ and $\widehat{\mathrm{B}}$ as unit vectors in direction of $\overrightarrow{E}$ and $\overrightarrow{B}$ the equation can be written as follows:

$$\overrightarrow{v_D} = \frac{\mu \mathrm{E}}{1 + \omega^2\tau^2} \cdot \left[\widehat{\mathrm{E}} + \omega\tau\widehat{\mathrm{E}} \times \widehat{\mathrm{B}} + \omega^2\tau^2(\widehat{\mathrm{E}} \cdot \widehat{\mathrm{B}})\widehat{\mathrm{B}}\right]. \tag{4.7}$$

As a consequence of this equation, electrons follow rather the magnetic field lines, since for a large magnetic field – leading to large $\omega\tau$ – the last term in equation 4.7 becomes dominant. Positive ions are much heavier than electrons, that yields a very small value for $\omega\tau$ and accordingly the ions follow the electrical field.
In a TPC, the electric and magnetic fields are parallel, which means that the second term in equation 4.7 with the cross product vanishes and the last term can be written as $1 \cdot \widehat{\mathrm{B}} = \widehat{\mathrm{E}}$, since $(\widehat{\mathrm{E}} \cdot \widehat{\mathrm{B}})$ equals one for parallel fields. The result is a simplified version of equation 4.7:

$$\overrightarrow{v_D} = \frac{\mu \mathrm{E}}{1 + \omega^2\tau^2}\widehat{\mathrm{E}}(1 + \omega^2\tau^2) = \mu\overrightarrow{E} = \overrightarrow{v_D}(\overrightarrow{B} = 0). \tag{4.8}$$

This equation shows that a parallel alignment of the fields is mathematically the same as an absence of the magnetic field.
The drift velocity is influenced via the electron mobility μ by gas mixture parameters like pressure or water content. In figure 4.3, the drift velocity is shown as a function of the drift field for two different gas mixtures used in TPCs [Lux05]. The shape of the drift velocity curve is explained by the Ramsauer effect [Sau77]. For this explanation, the cross section for a collision of an electron with a gas molecule is used, which is anti proportional to the drift velocity, since less collisions yield a faster drift. In general, the cross section decreases with the increase of the kinetic energy of the electron. But Ramsauer observed a minimum in the collision cross section for particles with a de Broglie wave length of the order of the dimension of the gas molecules. The molecules become permeable for such electrons, which reach at this point a local maximum of the drift velocity.
In a TPC the drift velocity has to be large in order to read out the detector in a reasonable time. In addition, an insensitivity to small fluctuations of the field is required. Therefore, the settings are chosen to obtain a drift velocity near the peak, since in the regions of steep slope the dependence on the field fluctuations would be large.

4.3.2 Diffusion

The reconstructed position of the original ionization process is smeared, since the drifting electrons undergo diffusion on their way to the anode. This influences the

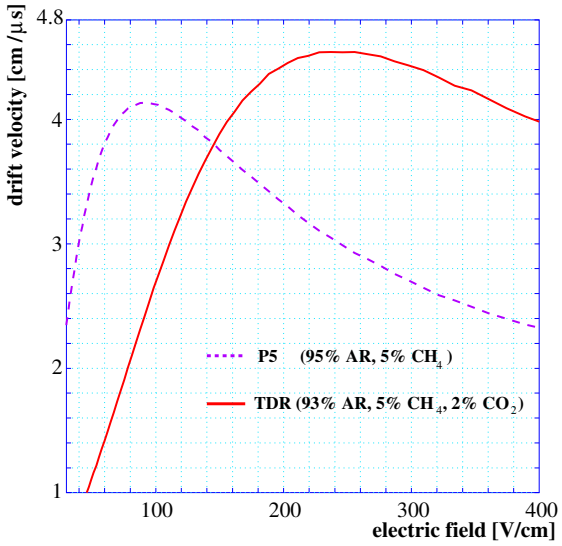

Figure 4.3: Simulated drift velocity as a function of the electric field. Shown are functions for two gas mixtures (P5 and TDR) typically used in TPCs [Lux05].

spatial resolution and needs to be understood. In the field-free case depicted by an index 0, the diffusion is caused by thermic energy and is isotropic. The mean velocity in all directions can be described with the help of the Boltzmann constant k, the gas temperature T and the mass of the electrons m_e:

$$v = \sqrt{\frac{8kT}{\pi m_e}}. \tag{4.9}$$

The probability for no interaction of an electron with the gas molecules during the time t is given by $\frac{1}{\tau}\exp(-t/\tau)$. With λ as free mean path, the expansion in any fixed direction after the first collision is given by the spread δ_0 of the electron cloud [LW92]:

$$\delta_0^2 = \frac{1}{3}\int_0^\infty \frac{dt}{\tau}\exp\left(-\frac{t}{\tau}\right)\cdot\left(\lambda\frac{t}{\tau}\right)^2 = \frac{2}{3}\lambda^2. \tag{4.10}$$

After a long time ($t \gg \tau$) and many collisions (t/τ) the width of the charge cloud has grown to:

$$\sigma_0^2(t) = \delta_0^2\cdot\frac{t}{\tau} = \frac{2}{3}\lambda^2\frac{t}{\tau}. \tag{4.11}$$

Using the width, the general diffusion coefficient is defined as $\widetilde{D} = \frac{\sigma^2(t)}{2t}$ or in absence of a field:

$$\widetilde{D}_0 = \frac{\sigma_0^2(t)}{2t} = \frac{1}{3}\frac{\lambda^2}{\tau} = \frac{1}{3}v\lambda. \tag{4.12}$$

The last transformation in this equation is made due to the correlation $v = \lambda/\tau$. More often another definition is used for the diffusion coefficient. The width of the

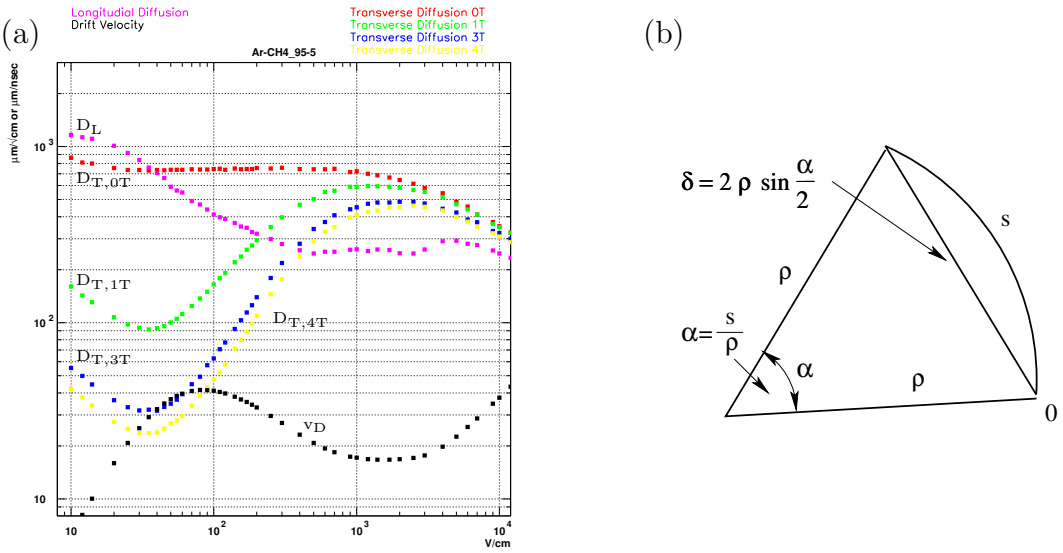

Figure 4.4: (a) Simulation of longitudinal and transverse diffusion for P5 gas (95 % argon – 5 % methane). In addition the drift velocity is shown [Gas09]. (b) Sketch of mean transverse velocity and transverse electron distance δ in a magnetic field [Jan08].

charge cloud σ_D is then defined as:

$$\sigma_D = D\sqrt{L}, \tag{4.13}$$

where L denotes the drift length and D is related to the above defined diffusion coefficient $\widetilde{D}$ via $D = \sqrt{2\widetilde{D}/v_D}$.

Influence of Electrical Field

With an applied electrical field the movement of the electrons is a superposition of the thermal and the by the field caused motion. In argon, the outer electrical field dominates already at low field strengths. Therefore, the diffusion is not isotropic anymore and the longitudinal and transversal diffusion have to be distinguished since the energy and velocity distribution is different parallel and perpendicular to the field. In figure 4.4(a), simulated longitudinal and transverse diffusion coefficients for P5 gas (95 % argon – 5 % methane) are shown [Gas09]. The drift velocity is also plotted. For the transverse diffusion, four different values for the magnetic field are assumed. The impact of the magnetic field on the diffusion is explained in the next section.

Influence of Magnetic Field

With an applied magnetic field along the direction of the drift the transverse diffusion changes, while the longitudinal coefficient stays the same. The reason is the

Lorentz force perpendicular to the magnetic field, which causes a transverse particle movement on a circular arc. In this context the squared mean transverse velocity is defined as $v_T^2 = 2/3 \cdot \lambda^2/\tau^2$ [LW92], the radius of the arc is given by $\rho = v_T/\omega$ as sketched in figure 4.4(b). The transverse distance (secant in figure 4.4(b)) can be calculated as $2\rho \cdot |\sin(s/2\rho)|$. With $s = v_T \cdot t$, the spread of the charge distribution after the first collision can be written analog to equation 4.10:

$$\delta^2(B) = \frac{1}{2}\int_0^\infty \frac{dt}{\tau} \exp\left(-\frac{t}{\tau}\right) \cdot \left(2\rho \sin\frac{v_T \cdot t}{2\rho}\right)^2 = \frac{1}{2}\frac{\tau^2 v_T^2}{1+\omega^2\tau^2}. \tag{4.14}$$

For a given time t, after many collisions, the spread is:

$$\sigma^2(B,t) = \frac{t}{2}\frac{\tau v_T^2}{1+\omega^2\tau^2} = t\frac{\widetilde{D}_0}{1+\omega^2\tau^2}, \tag{4.15}$$

which results for the transverse diffusion coefficient in:

$$\widetilde{D}_T(B) = \frac{\widetilde{D}_0}{1+\omega^2\tau^2}. \tag{4.16}$$

It can be seen, that the transverse diffusion is reduced by a factor $\frac{1}{1+\omega^2\tau^2}$ in comparison to the field-free case $\widetilde{D}_0$. In figure 4.4(a), this fact is visible. The larger the field, the lower the diffusion coefficient.

4.3.3 Gas Amplification

Due to their acceleration in a high enough electric field, drifting primary electrons are able to gain a sufficient amount of energy to ionize gas molecules releasing secondary electrons. Primary and secondary particles are accelerated further and ionize additional molecules triggering an avalanche process. The occurrence of this effect starts at high fields of about 10 kV/cm. The developing number of electrons N can be calculated via:

$$N(x) = N_0 \cdot e^{\alpha x} \tag{4.17}$$

where x denotes the distance and α the so-called Townsend coefficient. α describes the ionization probability per unit length and is depending on the gas mixture and the electric field strength. The gain factor describes the ratio of electrons before (x_0) and after (x_f) the avalanche process. The amplification area of a TPC is operated in the proportional mode, where the number of measured electrons is proportional to the primary electrons. in this case the gain G is defined as follows:

$$G = \frac{N(x_f)}{N(x_0)} = \exp\left(\int_{x_0}^{x_f} \alpha(x)dx\right). \tag{4.18}$$

The Townsend coefficient is defined as a function of x since in an inhomogeneous electric field α becomes dependent on the position x.

Chapter 5

Gas Electron Multipliers

Gas electron multiplier (GEM) foils have already been briefly introduced in section 3.3.5. They are used as electron amplification device in TPCs and are the main subject of the studies presented in this thesis. This chapter describes the working principle and the key parameters of standard GEMs produced at CERN. All values mentioned here are valid for standard CERN GEMs, while in chapter 8, foils produced by other manufacturers are introduced and the differences to CERN GEMs are described.
GEMs consist of a copper clad polyimide substrate with microscopic holes etched into it. The geometry is shown in figure 5.1(a) and is explained in some detail in the following section. For the operation of GEMs, different potentials are applied on the upper and lower surface. The surfaces build a parallel plate capacitor, since they are not electrically connected. With a voltage of a few hundred volts across the GEM, field configurations as depicted in figure 5.1(b) are possible. Due to the concentration of field lines, the electrons follow no longer the magnetic field lines but are forced into the holes. There, the electric field becomes strong enough that the electrons are multiplied due to gas amplification. Details of this processes are described in the subsequent paragraphs.

5.1 Geometrical Parameters of GEMs

Polyimide foil is used as substrate for GEMs, since it is a good insulator with a low outgassing rate. The insulation is needed for the working principles of a GEM, as the two conductive surfaces have to be electrically separated. Outgassing has to be avoided in a detector environment to ensure stable operation conditions. The thickness of the polyimide is typically 50 µm, while the copper metalization is 5 µm thick. In figure 5.1(a) all dimensions of GEMs are illustrated. The double conical shape of the holes is a consequence of the manufacturing process. The inner diameter in the middle of the foil is 50 µm and the outer diameter in the copper surface of the GEM is 70 µm. In addition to the hole diameters, the so-called pitch is

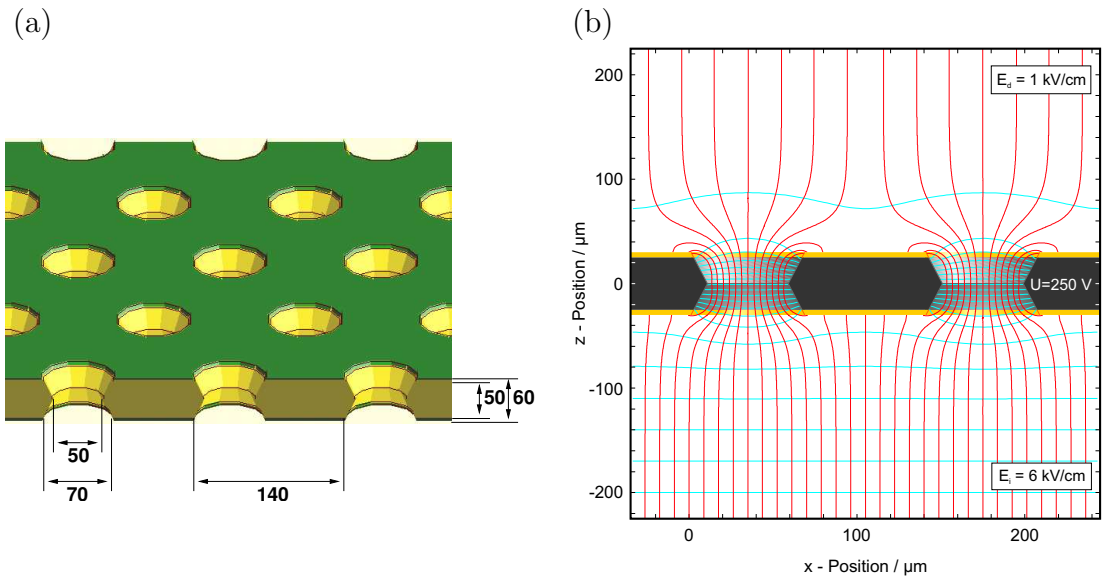

Figure 5.1: (a) Sketch of GEM geometry. The measures correspond to standard CERN GEMS and are given in micrometers. The inner and outer hole diameters are depicted as well as the pitch and the substrate and complete thickness [Web03]. (b) Simulated field settings of a GEM with an applied voltage of 250 V [Sob02, Sch06].

very important to characterize GEMs. The pitch denotes the distance from center to center of two neighboring holes. The holes are arranged in a triangular way, staggered from row to row. The ratio of pitch p to hole diameter d defines the optical transparency τ_{opt} of a GEM:

$$\tau_{opt} = \frac{\pi d^2}{2\sqrt{3}p^2}. \tag{5.1}$$

For a standard CERN GEM the optical transparency is $\tau_{opt} = 0.23$. However, more important is the electrical transparency, which depends on the ratio of the applied fields on upper (E_{top}) and lower side (E_{bottom}) of the GEM structure. The electrical transparency is often called collection efficiency [B+99]. The ratio of the external field to the field inside a GEM hole is called f in the following:

$$f = \frac{E_{ext}}{E_{hole}} \tag{5.2}$$

With the right choice of f, τ_{opt} and voltage across the GEM, the electrical transparency can be close to unity. Only the value of f, where the efficiency starts to decrease is dependent on the optical transparency. A higher τ_{opt} allows for higher drift fields, visible in figure 5.2, where the normalized electron transparency as a function of the field ratio f is shown. The measurements presented in this figure are described in [B+99].
The hole shape influences the behavior of the GEMs as well. In section 8.4.2, characteristics of GEM types with different hole shapes are compared.

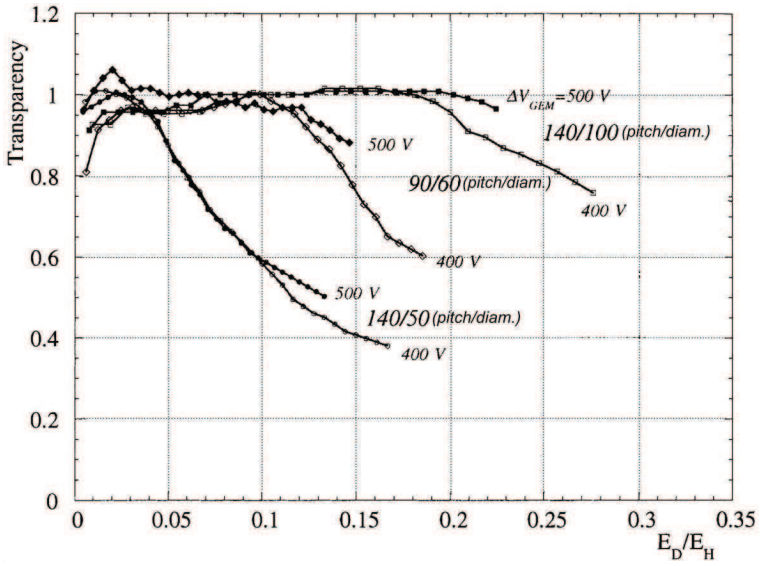

Figure 5.2: Normalized electron transparency over the ratio f of external and hole field. Three different GEM types (given are pitch/hole diameter) and two different voltages across the GEMs are depicted. A detailed description can be found in [B$^+$99].

5.2 Charge Transfer and Amplification

The charge transfer mechanism through GEMs describes the effective electron amplification process and is therefore called effective gain. It factorizes and its components – often called transfer coefficients – and their meanings are described in the following. In [Sob02] a parametrization of transfer coefficients describing the processes in GEMs is given. It has been derived using simulations with the finite element program Maxwell [Max09]. The parametrization has been experimentally confirmed in [Lot06]. For this purpose, the transfer coefficients were parametrized depending on the currents on the different electrodes, which are measurable in a TPC prototype.

5.2.1 Effective Gain

The effective gain of a GEM foil can be written as the product of the charge transfer coefficients. In equation 5.3, C denotes the previously introduced collection efficiency, while G describes the gas gain inside the GEM hole and X the extraction efficiency:

$$G_{\text{eff}} = C \cdot G \cdot X. \tag{5.3}$$

The gain G inside a single GEM is the multiplication factor caused by the gas amplification and dependent on the field inside the GEM hole. In figure 5.3, all factors of the effective gain are illustrated and G equals three in picture (b). The

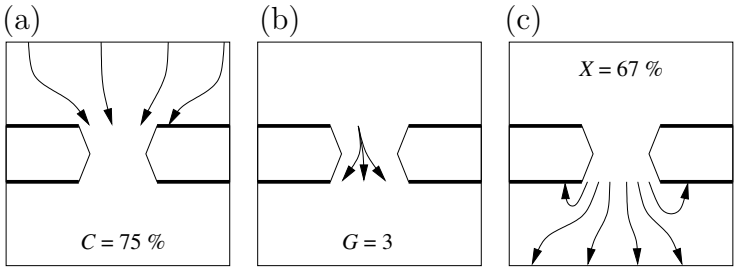

Figure 5.3: Illustration of effective GEM gain factors. From left to right: collection efficiency C, gain G in GEM hole and extraction efficiency X. The used values are only chosen for illustration and are not related to physically relevant values [Vog08].

depicted values are only chosen for a clear representation, but have nothing to do with physical relevant values for the charge transfer coefficients.

5.2.2 Hole Field

Important for the gain G is the field inside the GEM holes. With conventional methods, it is not possible to measure this field directly due to the small dimensions of the holes. But the simple geometry allows for calculations of the field strength. Hence, simulation results from [B+99] are used to illustrate the electric field in GEM holes. Figure 5.4 shows the electric field along a path perpendicular to the GEM surface through the center of a GEM hole. The voltage applied across the GEM is 500 V and the fields outside the GEM on both sides are 6 kV/cm. Visible are curves for different hole diameters from 10 - 100 µm. The narrower the hole, the stronger the field, which develops in the middle of the hole. For the 100 µm hole an additional computation was made assuming that the field E_{bottom} below the GEM – on the right side in the diagram – has a strength of 10 kV/cm. The result is shown as dashed line and indicates a dependence on the applied outer fields. This means that the environmental field settings above (E_{top}) and below (E_{bottom}) have an impact on the gain inside the GEMs. With narrower holes higher gains are achievable, because the field inside is higher, assuming the same voltage between the GEM surfaces.
The parametrized hole field strength E_{hole} is given by the flux through the central cross section area of the hole. The resulting formula [Sob02]:

$$E_{hole} = a \cdot U_{GEM} + b \cdot (E_{top} + E_{bottom}) \tag{5.4}$$

contains the two geometry dependent parameters a and b and is valid for all hole shapes. In the case of standard CERN GEMs they are measured to be $a = 142.9\,\mathrm{cm}^{-1}$ and $b = 0.062$ [Sob02]. The dependence on the applied fields above and below the GEMs is weak, since b is small.

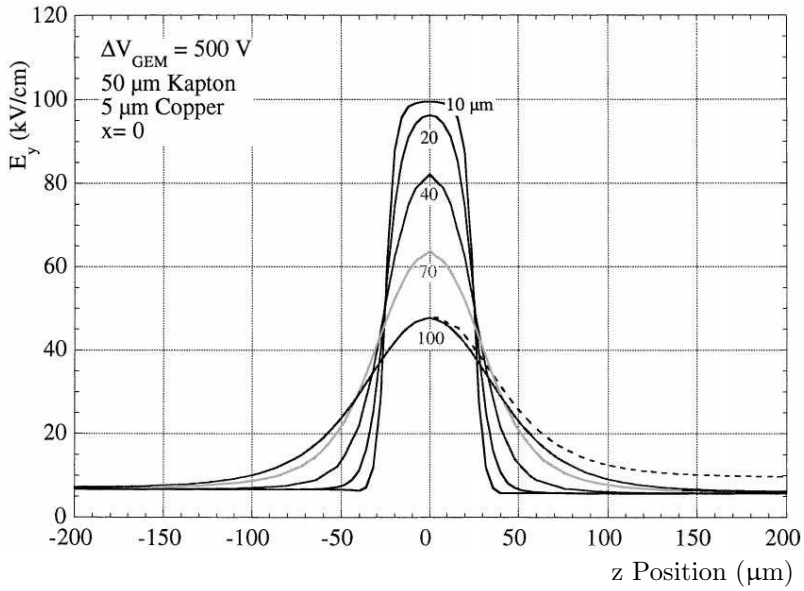

Figure 5.4: Simulated electrical field inside a GEM hole computed along a line through the center of the hole. Fields for different hole diameters are plotted over z – perpendicular to the GEM surface. $z = 0$ corresponds to the middle of the GEM foil [B+99].

5.2.3 Collection Efficiency

The collection efficiency C – or electrical transparency – denotes the fraction of all electrons in the beginning (N_{start}), which are actually collected into the hole ($N_{collected}$):

$$C = \frac{N_{collected}}{N_{start}}. \tag{5.5}$$

This is illustrated in figure 5.3(a). It describes the ratio of electrons collected into the hole, here three out of four, which do not end upon the GEM surface.
In [Sob02] the collection efficiency is parametrized depending on the ratio of the external and the hole field. With $f = E_{ext}/E_{hole}$ and $r, s \in \mathbb{R}^+$ as free parameters it can be written as:

$$C(f) = \begin{cases} 1 & \text{for } f \leq r^{1/s} \\ r \cdot f^{-s} & \text{for } f > r^{1/s}. \end{cases} \tag{5.6}$$

For small values of the field ratio f, the collection efficiency is one (cf. figure 5.5). At higher values of f, the collection efficiency starts to decrease following the proportionality in equation 5.6. For standard CERN GEMs the values of the free parameters are given by $r = 0.19$ and $s = 0.52$ [Sob02].

5.2.4 Extraction Efficiency

The extraction efficiency X takes into account, how many electrons are able to leave the hole without being collected onto the lower surface. In figure 5.3(c), X is 67 %

since four out of six electrons are extracted. A definition of the extraction efficiency can be given like:

$$X = \frac{N_{extracted}}{N_{produced}}, \tag{5.7}$$

where $N_{extracted}$ denotes the number of electrons extracted from the GEM without being absorbed and $N_{produced}$ is the number of electrons produced inside the GEM hole.
The ratio of extraction and collection efficiency can be formulated using a model of electrical flux through a GEM hole [Sob02]:

$$\frac{X}{C} = \frac{\phi_{ext}}{\phi_{hole}} = \frac{E_{ext} \cdot A_{ext}}{E_{hole} \cdot A_{hole}}. \tag{5.8}$$

ϕ_{ext} stands for the flux describing the extraction efficiency, which leaves the hole and flows to an outer electrode. With ϕ_{hole} the collection efficiency can be described. It depicts the ratio of the flux, which is collected into the hole. The ratio of the external surfaces to the area of the hole A_{ext}/A_{hole} can be interpreted as the inverse optical transparency $1/\tau_{opt}$, while the ratio of the fields is denoted by f [Sob02]:

$$\frac{X}{C} = \frac{1}{\tau_{opt}} \cdot f. \tag{5.9}$$

With the help of this formula and $r, s \in \mathbb{R}^+$ as free parameters the parametrization of the extraction efficiency is given by [Sob02]:

$$X(f) = \begin{cases} \frac{1}{\tau_{opt}} \cdot f & \text{for } f \leq r^{1/s} \\ \frac{r}{\tau_{opt}} \cdot f^{1-s} & \text{for } f > r^{1/s}. \end{cases} \tag{5.10}$$

A validation of the parametrizations of the charge transfer coefficients is shown in figure 5.5. Good agreement between the simulated values and the parametrization curves as formulated in equations 5.6 and 5.10 is visible.
In order to achieve high effective gains, the field ratio f is typically chosen between 0.03 and 0.05, so that the collection efficiency is still 100 %, while the extraction efficiency is as large as possible.

5.3 GEM Stacks

To use GEM foils in stacks, either in a double or triple GEM setup as illustrated in figure 5.6, is advantageous in many terms. Most important is the ability to achieve high gains with a low discharge probability, since every single GEM is less strained. A second characteristic is the intrinsic ion gating, which can be reached with appropriate voltage settings. The topmost GEM in such a stack collects many of the back drifting ions on its lower surface and prevents them from reaching back

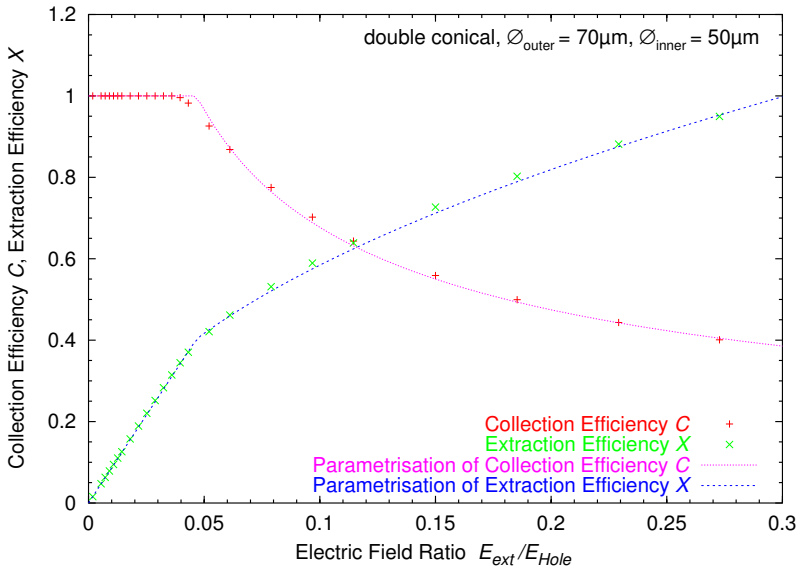

Figure 5.5: Simulated collection and extraction efficiencies as a function of the field ratio $f = E_{ext}/E_{hole}$. The parametrization curves match the simulated values [Sob02, Lot06].

into the drift region. All GEMs in a stack work almost independent from each other and an alignment is not needed due to diffusion and defocussing. The naming scheme used in this thesis numbers the foils in the order of the passage of electrons coming from the drift region. The topmost GEM is called GEM I and the one closest to the anode GEM II or GEM III, depending whether a double or a triple GEM stack is used. The electrical field in between two GEMs is called transfer field, while the field between last GEM and anode is the induction field. A GEM stack can be either operated via a voltage divider or, more flexible, with the help of a multichannel power supply.

5.4 Total Effective Gain

The total effective gain of a GEM stack can be written as product of the effective single GEM gains. The index i is used for the "i-th" GEM in a stack:

$$G_{eff,total} = \prod_{i=1}^{N_{GEMs}} G_{eff,i} = \prod_{i=1}^{N_{GEMs}} C_i \cdot G_i \cdot X_i. \tag{5.11}$$

The total effective gain is identical to the ratio of the number of electrons collected on the anode to the number of primary electrons before the first GEM. With the help of the applied voltages and field settings the total effective gain can be adjusted to match the dynamic range of the electronics. For different readout systems different effective gains are needed. For example, a chip readout needs more electrons than a pad plane. Normally $G_{eff,total}$ is of the order of some thousand to a few ten

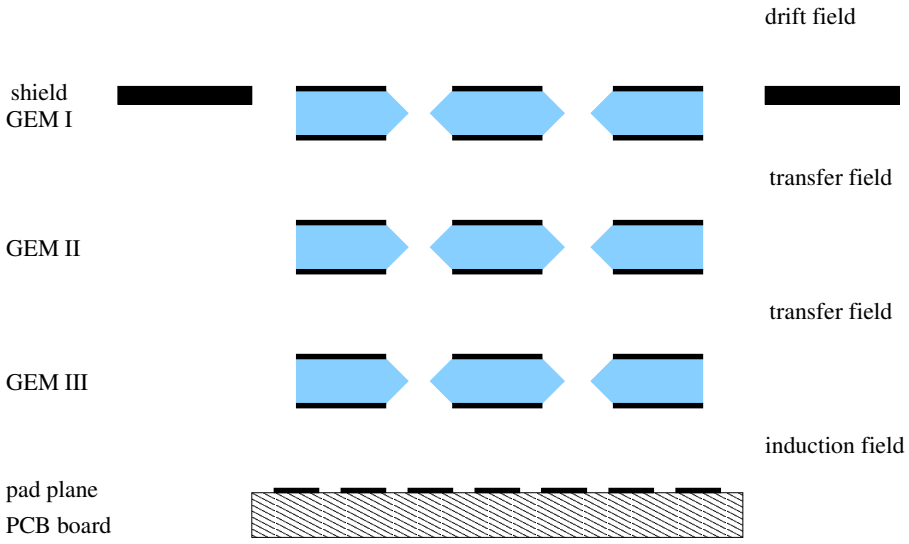

Figure 5.6: Sketch of a GEM stack. The numbering scheme is illustrated and the naming conventions for the fields are given.

thousand. The effective gain increases exponentially with the voltage applied across the GEM and linearly with the strength of the fields in a reasonable range of the field strengths. Narrower holes cause a higher gain, because the field strength inside the holes is higher at the same voltage settings.

5.5 Discharge Probability

A discharge in gas is initiated, when the exponent in equation 4.17 on page 36 reaches $\alpha x \approx 20$, or in other words the gain in equation 4.18 becomes larger than 10^8. This limit is known as Raether criterion [Leo94]. At this limit a so-called streamer breakdown takes place, which is characterized by a narrow bright plasma formed by an electron avalanche. The plasma has a small resistance causing a flow of current and with it a discharge.
The probability for a transition from proportional amplification mode to discharge depends on many different factors. Temperature, humidity and gas flow play a role. For a given effective gain, the discharge probability depends on the amount of charge carriers, their density and their spatial distribution. This yields a dependence on the angle of tracks produced by heavy ionizing particles.
In GEMs, discharges occur usually between both copper surfaces of a single foil. This has to be avoided, since the proportionality between primary ionization and signal is lost in case of a discharge. However, GEMs are capable to withstand several of those discharges but rarely discharges occur, which cause damages of the foils. Conductive carbon fibers or even copper connections through GEM holes can be produced by such so-called trips. GEM foils with connected electrodes, develop a

finite resistance and are unusable. But typically only a temporary excess of current occurs and a trip protection of the power supply avoids severe damage. Discharges can also be propagated through the structure and are problematic, if they hit the anode surface. Hence, direct discharges onto the readout device have to be avoided. The energy of the primary discharge is proportional to the energy stored in the GEM. This energy depends on the capacitance, which can be reduced by sectoring one of the copper surfaces of the GEM. In addition, the probability for the propagation of a primary discharge through the whole structure is influenced by the energy of the first discharge and the strength of the induction field. An induction field below 5 kV/cm provides stable operation conditions in argon based gases.
In order to reduce the charge density, a stack of two or three GEMs can be used. Inside this structure the charge cloud gets spread due to defocussing and for operation at the same effective gain the individual GEM foils do not have to withstand the same high voltage as a single GEM. Multiple structures permit gains, which are one order of magnitude larger compared to a single GEM. Optimal settings concerning discharge prevention for a double GEM structure are obtained with a 5-10 % larger voltage across GEM I than across GEM II [B$^+$02]. With this settings, the second GEM, which has to deal with more electrons due to the amplification, is protected from discharging. Also in a triple GEM stack a small asymmetry in voltages across the single GEMs is advantageous. Variations of 10 % from the first to the other two foils ($+--$) helps to avoid discharges. Even better is a setting with GEM II on a certain voltage and the first one with 10 % more and the last GEM with 10 % less applied voltage ($+0-$). The probability for discharges in cascaded GEMs – predominantly in the closest to the anode – depends on the primary ionization density and the total effective gain.
The discharge probability is not the only matter for GEM setting optimization, another example leading to different results is the ion backdrift reduction, which is described in the next section.

5.6 Ion Backdrift

Not only electrons but also the corresponding positive charged ions are produced during the amplification process. They travel along the electric field lines in the opposite direction as the electrons. Therefore, ions are traveling back into the drift volume of the TPC, where they cause distortions in the drift field and are able to catch signal electrons. The homogeneity of the electrical field is important for a precise track reconstruction, therefore all sources of distortions should be avoided. MPGD devices offer intrinsic possibilities to provide ion suppression. The ion backdrift behavior of GEM foils is described in the following.
In principle, the definitions of collection and extraction coefficients defined in equations 5.5 and 5.7 are also valid for ions. But in the case of the extraction process a distinction has to be made for ions. The term in equation 5.7 can be interpreted

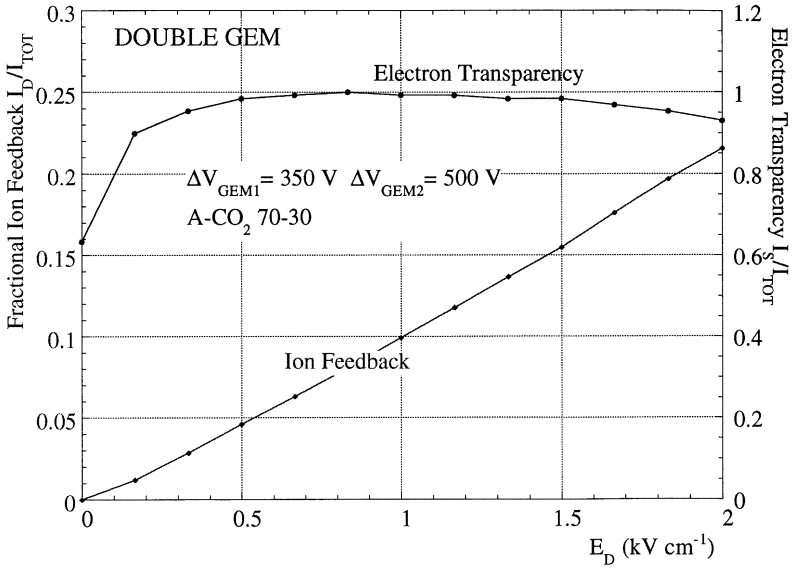

Figure 5.7: Ion feedback fraction and electron transparency (collection efficiency) of a double GEM structure as a function of the applied drift field [B+99].

as so-called primary extraction efficiency X^+_{prim} for ions [K+03]. It describes the extraction of ions produced in this very GEM. The produced ions are spread across the entire hole diameter, since the ionization process takes place in the complete hole cross section. While ions, which were produced in a previous GEM and are collected into a second GEM, can be found exclusively in the hole center. Reason for this is, that ions follow the electric field lines exactly and experience only negligible diffusion due to their high mass. The field lines either end on the surface of the GEM or they are running through the center of the holes. For these previously produced ions the secondary extraction efficiency X^+_{sec} is defined as:

$$X_{sec} = \begin{cases} \frac{X_{top}}{X_{bot}} & \text{for } X_{top} < X_{bot} \\ 1 & \text{for } X_{top} > X_{bot} \end{cases} \tag{5.12}$$

with X_{top} and X_{bot} being the primary extraction efficiencies on the top and bottom side of the GEM. Both depend on the field settings. The secondary extraction takes place on the upper side of the GEMs pointing into the direction of the drift volume. By choosing adequate field settings the secondary extraction and with it the ion backdrift can be suppressed. One handle to reduce the ion backdrift is for example the applied drift field. Figure 5.7 compares the fractional ion feedback and the electron transparency for a double GEM stack. The curves were determined with the help of measurements of the current. For the ion feedback the smallest possible value is desirable, while the transparency or collection efficiency respectively has to be close to 100 %. At a drift field of about 250 V/cm the ion feedback is only 2 %, while the electron transparency is still above 90 %. For drift fields below 200 V/cm the electron transparency starts to drop. By reducing the voltage across the topmost

	prototype TPC	ILD TPC (simulation)
drift field	200 V/cm	240 V/cm
voltage across GEM I	218 V	330 V
transfer field I	6000 V/cm	4000 V/cm
voltage across GEM II	330 V	340 V
transfer field II	120 V/cm	100 V/cm
voltage across GEM III	350 V	350 V
induction field	8000 V/cm	7000 V/cm

Table 5.1: Voltage and field parameters of a triple GEM stack for minimal ion backdrift. The effective gain for the settings, which were measured in a prototype TPC is 3233 [Lot06]. The ILD TPC settings are results of simulation studies [Kra08].

GEM the ion feedback fraction can be even further suppressed, since the production of ions in the GEM closest to the drift volume is reduced. Since the drift field is given by other TPC requirements, the field settings described above are usually realized by a triple GEM stack. Here, the topmost transfer field is adjusted to suppress the ion backdrift according to the conclusion above.
With settings as shown in table 5.1, ion backflow fractions of the order of two per mill are achievable at an effective gain of about $3 \cdot 10^3$. These adjustments are a result of optimization studies performed with the effective gain parametrization in order to minimize the ion backdrift of a triple GEM stack. Measurements with a GEM TPC prototype, using this settings, showed the expected behavior [Lot06].
The drift velocity of ions is much smaller than the velocity of electrons, due to the higher mass of the ions. This small drift velocity causes the formation of so-called ion discs at the ILC, since the ions produced during one bunch train are moving from the front of the amplification structures through the chamber. These discs distort the homogeneity of the drift field with their significant space charge. These distortions cause variations of the drift velocity of electrons and make z coordinate reconstruction very difficult.
In order to avoid this, different techniques for ion backdrift suppression can be used. A gating grid was often used in combination with wire amplification structures, for example in the ALEPH TPC [C$^+$86]. This gate is built as an additional layer of wires, which is operated on the drift potential according to the z location of the grid during the read out of an event. In between the events the gate is closed with the help of alternating high voltages applied on the wires. In this case the field lines end on the wires and the back drifting ions are not able to enter the drift region of the chamber. At the ILC such a gating scheme is not easily applicable due to the trigger-less running and the bunch train structure with its high rate of bunch crossings. But GEMs can also be used at the ILC to reduce the ion backdrift. In [Kra08], details and simulation studies of the influence of ion discs on the spatial resolution are presented. The voltage settings, which were found to be optimal for ion backdrift suppression are also mentioned in table 5.1.

Chapter 6

TPC Research and Gas Electron Multiplier TPCs

In this chapter an insight into the world-wide TPC research and development for a linear collider is given and the envisaged performance parameters for an ILD TPC are presented. Some specialties of GEM based TPCs are explained and the TPC prototypes used at DESY are introduced as well as the employed data reconstruction techniques.

6.1 LCTPC R&D Strategy

The invention of MPGD devices in the 1990s triggered research studies all around the world. They found first applications in high energy physics in the HERA-B and COMPASS experiments at DESY and CERN [HERA-B00, A$^+$02]. In addition, at the end of the 1990s efforts started to develop strategies and methods to use MPGDs in a linear collider TPC as amplification devices. For this purpose several groups built small TPC prototypes and started studies for readout techniques in combination with GEMs and MicroMEGAS.
In the year 2007, the Linear Collider TPC collaboration (LCTPC) was founded. A memorandum of agreement [LCTPC09] defines the goals, the function and the members of the collaboration. In this memorandum, a strategy for the further research activities is described. The goal of the LCTPC collaboration is the development of a TPC for a linear collider detector. The ongoing and future studies are organized in three phases.

Demonstration Phase

This phase has started already some years ago, before the official formation of the LCTPC collaboration. It comprises the effort of groups in the Americas, Asia and Europe to build small prototypes with diameters of the order of 30 cm. This work was meant to show the applicability of MPGD devices in time projection chambers.

Of particular interest was, whether the requirements in an ILC environment can be fulfilled. Several studies concerning gas mixtures, voltage and field settings, readout design and chamber production were performed. The goal was to understand charge transfer coefficients and with it the complete amplification process, as well as to reach a good single point resolution and to reduce the ion feedback. Results of these studies can be found in [K$^+$04, KLM$^+$05, Lot06, Jan08, Gas09].

Consolidation Phase

As a first joint project of the LCTPC collaboration, the so-called Large TPC Prototype (LP) was developed. Main topics for the consolidation phase is the research work – described in the following – with this new chamber. First, the production of the field cage and the endplate itself have to be investigated, in particular the reduction of the material budget of the walls. The development of large amplification and readout structures including electronics are a second topic. Third, the analysis of tracks with a large number of space points is subject of recently performed research work. In addition, track reconstruction algorithms and correction procedures can be tested with the LP. And finally, measurements in a slightly inhomogeneous magnetic field and studies of the resulting track distortions can be performed.
The layout and the field cage of the LP are shown in figure 6.1. It fits with its diameter of 77 cm into an one Tesla magnet currently operated at the DESY testbeam facility. A dedicated endplate was designed at Cornell University [Pet09]. The LP is able to house up to seven readout modules, which can be equipped independently in order to test different readout techniques.
All preliminary studies, design considerations, a description of the production and the commissioning phase including quality monitoring of the LP can be found in [Sch09]. The walls of the chamber have to be on the one hand mechanically and electrically stable and gas tight, but on the other hand the radiation length has to be as small as possible. Therefore composite materials are used. The wall of the barrel is made of sandwiched honeycomb paper with glass fiber as stabilizing layers. On the inner side an insulating foil carrying the field strips and their mirror strips is installed. One wall accounts for 1.24 % X_0, which is close to the ILD design goal. This goal is defined in the letter of intent as 4 % of a radiation length for the complete TPC [LOI09]. Summing up inner and outer walls and taking the gas into account with 1 % X_0, only a small step is missing, assuming that the design can be applied to the ILD TPC field cage. This is not clear, since the chamber will be significantly larger than the LP and therefore the mechanical and electrical requirements are harder, due to the dimensions and the higher cathode voltage, which will have to be used for the longer drift field. A possibility to reduce the radiation length further could for example be the replacement of the copper field strips by aluminum.
The production and survey of the field cage showed some problems with the alignment of the z axis compared to the outer walls and with it the field strips [Sch09].

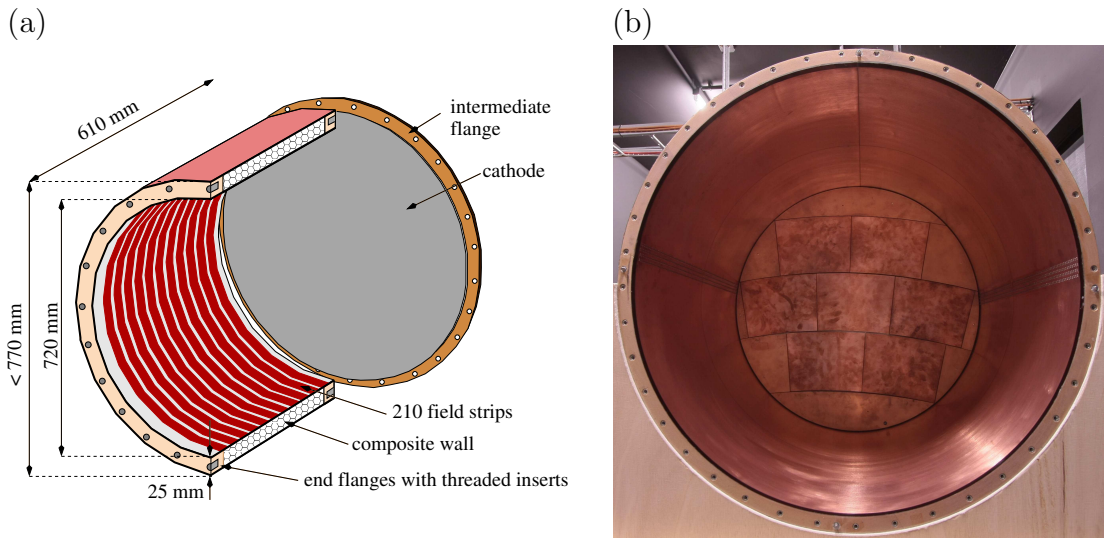

Figure 6.1: (a) Layout [Sch09] and (b) photograph of the LP field cage [Sch09].

Further studies have to be performed to optimize the production process in order to recover the envisaged drift field quality, which is distorted by the tilted axis.

Design Phase

This phase is dedicated to the engineering design of a TPC for the final detector. Results of the demonstration and consolidation phase will allow for technology decisions, which can be considered for the planning of a large scale TPC. First steps into this direction have been made with considerations about material and design of endplates for the ILD TPC.

6.2 TPC Performance Parameters

In the letter of intent for the ILD detector [LOI09], a list of performance goals for the ILD TPC is given, which are summarized in table 6.1. The parameters are key features of a tracking detector and the goals are formulated footing on the experience made during extensive R&D work in the LCTPC collaboration and on experiences made with existing large scale TPCs. In chapter 7, the ambitious requirements will be motivated by the physics analyses planned for the ILC. An important point is, that the TPC – as the whole ILD detector – has to be operated in a trigger-less environment.
In the scope of this thesis in particular the abilities concerning single point and dE/dx resolution are of importance.

parameter	design goal
size (outside dimensions)	$\varnothing = 3.6\,\mathrm{m}$ $\mathrm{L} = 4.3\,\mathrm{m}$
momentum resolution (3.5 T)	
TPC only	$\delta(1/p_T) \leq 9 \cdot 10^{-5}/\mathrm{GeV/c}$ ($\times$ 0.4 if IP incl.)
SET+TPC+SIT+VTX	$\delta(1/p_T) \leq 2 \cdot 10^{-5}/\mathrm{GeV/c}$
solid angle coverage	$\lvert\cos\theta\rvert \lesssim 0.98$ (10 pad rows)
TPC material budget	$\sim 0.05\,X_0$ to outer field cage in r $\sim 0.15\,X_0$ for readout endcaps in z
number of pads/time buckets	$\sim 1{\cdot}10^6/1000$ per endcap
pad size/number pad rows	$\sim 1\,\mathrm{mm} \times 4 - 6\,\mathrm{mm}/ \sim 200$
single point resolution	
in rϕ:	$\sigma_{\mathrm{point}} < 100\,\mu\mathrm{m}$ (average over sensitive length, modulo track ϕ angle)
in rz:	$\sigma_{\mathrm{point}} \approx 0.5\,\mathrm{mm}$ (modulo track θ angle)
2-hit resolution	
in rϕ:	$\sim 2\,\mathrm{mm}$ (modulo track angles)
in rz:	$\sim 6\,\mathrm{mm}$ (modulo track angles)
dE/dx resolution	$\sim 5\,\%$
performance ($p_T > 1\,\mathrm{GeV/c}$)	$> 97\,\%$ efficiency for TPC only $> 99\,\%$ all tracking
background robustness	full efficiency with 1 % occupancy, simulated in [Pet07]
background safety factor	chamber will be prepared for 10$\times$ worse backgrounds at the linear collider start-up

Table 6.1: Performance goals and design parameters for a linear collider TPC as part of the ILD with standard electronics [LOI09].

6.3 Gas Electron Multiplier TPCs

This thesis deals with GEMs as amplification devices in TPC prototypes, therefore some more explanations about GEM TPCs are given in this section. First, the production of GEM foils is described. Second, the defocussing inside a GEM amplification stage is explained and third, signal readout techniques are introduced.

6.3.1 Production of GEM Foils

GEM foils and their production process were developed at CERN [Sau97]. The substrate foil is first clad with a thin copper layer of 5 µm on both surfaces. Subsequently, a photo lithographic method is used to etch the holes into the foil. For this purpose a photosensitive layer is applied and the foil is exposed with light through a mask. During the following etching procedure the copper is removed only at the exposed areas. Another step is needed to etch the holes through the polyimide layer. The whole procedure is applied from both sides of the foil and the holes are etched in two half steps from both directions, hence a good alignment of the masks is required. This manufacturing process explains the double conical shape of the standard GEM holes. Of particular importance is the accuracy of the etching. No sharp copper edges, which could cause sparking, or metal fragments inside the holes can be allowed.

6.3.2 Defocussing in the Amplification Stage

The drift of the primary electrons is followed by the amplification in the GEM stack. Here, only the defocussing is explained, which describes the diffusion between the GEMs in the amplification stage. The diffusion respectively defocussing constant differs from the constant in the drift area due to the different electric fields. The transfer fields of the order of 1.5 kV/cm in between the GEMs and the induction field of about 3 kV/cm between the last GEM and the readout are much higher than the drift field with values of 90-250 V/cm depending on the used counting gas. These high fields in the amplification stage together with an appropriate choice of gas and voltage settings of about 300-400 V across each GEM cause a high defocussing constant σ_0 valid for all electrons. This validity for every primary electron can be explained since electron clouds of all tracks – wherever the particle went through the chamber – have to travel the same distance through the amplification stage and experience therefore the same broadening. The total width of the charge cloud at the readout plane is given by a function depending on the drift length z:

$$\sigma_{\mathrm{charge}}(\mathrm{z}) = \sqrt{\mathrm{D_T^2} \cdot \mathrm{z} + \sigma_0^2}. \tag{6.1}$$

A comparison of the transverse diffusion coefficient $\mathrm{D_T}$ and the defocussing constant σ_0 for settings as used in this thesis can be found in table 6.2. The values were simulated in the DESY TPC group [Jan08]. The considered gas mixture is P5

B [T]	D_T [$\sqrt{\text{mm}}$]	σ_0 [mm]
1	0.0495	0.477
2	0.0269	0.436
4	0.0139	0.375

Table 6.2: Simulated diffusion and defocussing constants for different magnetic fields in P5 gas. The fields are assumed to be: $E_{drift} = 92\,V/cm$, $E_{transfer} = 1.5\,kV/cm$ and $E_{induction} = 3\,kV/cm$ [Jan08].

gas (95 % argon – 5 % methane), which is used for the measurements presented in chapter 10. For the determination of the transverse diffusion a drift field of 92 V/cm was assumed. The experimental assembly of GEMs is described in chapter 5. The simulation used 1.5 kV/cm for the transfer fields and 3 kV/cm for the induction field. The negative impact of the defocussing on the single point resolution due to broadening is much less than the influence of the diffusion. This can be explained by the fact, that the electrons are amplified in the first GEM and with it the statistic is increased significantly. Hence the smearing of the average position of a charge cloud is less important after the first amplification than in the drift region.
A theoretical limit for the single point resolution can be determined by some considerations about diffusion and defocussing. To obtain the precision of a Gaussian mean value, the width σ is divided by the square root of the number of samples, $\sqrt{n}$. In the case of the resolution the number of samples in the drift region is $n_{primary}$, while for the amplification stage the number of detected electrons on the pad plane $n_{detected}$ is assumed. This simplification overestimates the achievable resolution, since that much electrons exist only in the last stage in front of the anode. In the first two stages of a three GEM stack less electrons are present. Therefore, the following formula describes a limit of the best achievable single point resolution depending on the drift distance z:

$$\sigma_{limit}(z) = \sqrt{\frac{D_T^2 \cdot z}{n_{primary}} + \frac{\sigma_0^2}{n_{detected}}}. \tag{6.2}$$

The defocussing is able to minimize the systematic effect caused by the so-called pad response function [Jan08], by maximizing the charge sharing between neighboring pads. Therefore, the maximization of the defocussing constant is an additional parameter – like a small diffusion constant – for gas mixture optimization.

6.3.3 Signal Readout

The charge signals produced in the chamber are read out at the anode endplate. The subsequent steps, performed in the front end electronics, are preamplification, shaping and digitization. At the end of the readout chain, storage and of course analysis of the data follow. For analysis, a pattern recognition algorithm is applied. The reconstruction performs either first a track finding and afterwards a fitting pro-

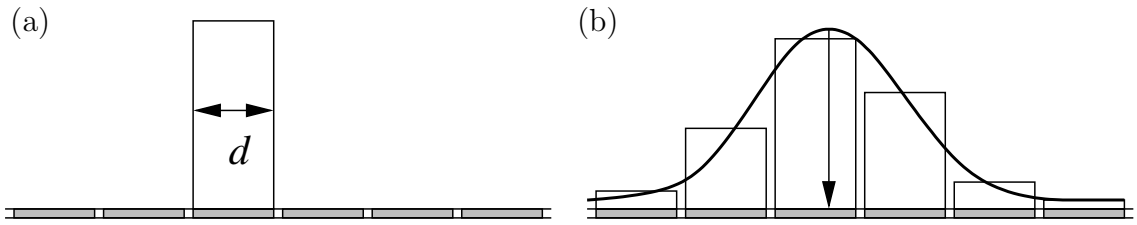

Figure 6.2: Illustration of charge sharing. (a) With a signal on one single pad, the spatial information is not better than the pad width d with an uncertainty of $\mathrm{d}/\sqrt{12}$. (b) The determination of a more precise position is sketched for a signal broadened due to defocussing [Vog08].

cedure [Die06, Jan08], or a combined method like a Kalman filter [Kal60]. These procedures are based on the pad-wise information. A description of the data reconstruction will be given at the end of this chapter.
In order to achieve a good spatial resolution, a charge sharing between a few pads is needed as illustrated in figure 6.2. Only then a spatial information on scales smaller than the pad width is calculable with the help of weighting methods. To generate charge signals, which are spread over more than one pad, either defocussing (in the case of GEMs) or a resistive foil on top of the anode (in MicroMEGAS assemblies) are needed.
The ADC (Analog to Digital Converter) information of every pad is read out in a series of time steps, whose length is given by the readout frequency of the electronics. The information of the time bin can be translated into a z position with the help of the drift velocity $\mathrm{v_D}$. Only the arrival time is measured at the anode, for the determination of the drift time the collision time has to be known. For this purpose collider and detector clock have to be synchronized and a time stamping of the inner track detectors is required. Then the drift time can be calculated. Finally, physical measures – like momentum and dE/dx information – are extracted of the reconstruction of the particle tracks.

Pad Planes

One method to collect the amplified charge information is to use a pad plane. Such a readout plane consists of a printed circuit board with a copper surface divided in small pads with a size of the order of few square millimeters. The pad plane in figure 6.3(a) – used in the DESY medium size prototype – has pads of $1.27 \times 7\,\mathrm{mm}^2$. These measures describe the pitch. A pitch gives the size of the pad together with the gap to the next pad, for example from the bottom left corner of one pad to the bottom left corner of the adjacent pad, including the gap. Pad planes are used with staggered or non-staggered layout, since these reflect the two most extreme alignments that could be realized in a pad plane layout at the final ILD detector. In the case of staggered layout the pads of adjacent rows are shifted by half a pitch, on a non-staggered pad plane the pads are exactly aligned over all rows.

(a) (b)

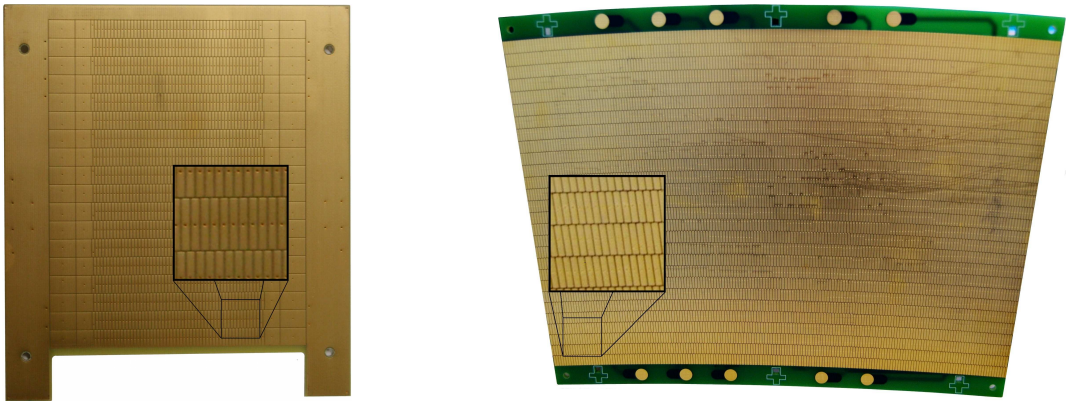

Figure 6.3: (a) Pad plane of a medium size TPC prototype at DESY. The copper pads are of the size: $1.27 \times 7\,\mathrm{mm}^2$, one row consists of 48 pads and 18 rows are available. (b) Pad plane for the large prototype, built at Tsinghua University.

One of the pad planes used for the large prototype TPC is depicted in figure 6.3(b). The pads on this readout surface are trapezoidal and build sections of concentric pad rows if many modules are placed besides each other.

Chip Readout for a Digital TPC

In the last years studies towards a digital TPC have been performed [B+08]. The concept is to drift individual electrons under very low diffusion conditions towards a digital readout. The diffusion coefficient in a magnetic field of 4 T is of the order of $D_T = 0.002\sqrt{\mathrm{mm}}$ for such a TPC, which is about a factor seven smaller than the value mentioned in table 6.2. At the anode, the single electrons are detected with a high efficiency and precise time information on microscopic pixels. With this approach effects of gain fluctuations can be reduced and in addition a better particle identification may become possible, since single electron cluster become visible and cluster counting could be performed [Hau06].
The most recent CMOS chip, used for the readout of digital TPCs, is called TimePix chip and consists of 256×256 pixels each covering a surface of $55 \times 55\,\mu\mathrm{m}^2$ [L+07]. A pixel fires if a charge signal produced by electron clusters exceeds a certain threshold. On board of the chip are a preamplifier-shaper, two discriminators, a 14-bit counter and the communication logic. The specialty of the TimePix chip is that the pixels can be operated in a second operation mode. In this TIME mode the pixels measure the arrival time. Usually every second pixel is operated in this mode, while the others are measuring the charge.
The main difference between digital and analog TPCs is the readout technique. In an analog chamber, the amplitudes of a broad charge signal – widened through diffusion and defocussing – is used to determine the track position and dE/dx information. While in the digital TPC only binary information on tiny pads is used to count single

electron clusters, which gives the possibility to measure the primary ionization and to identify particles via cluster counting excluding signals from delta electrons.

6.4 TPC Prototypes at DESY

Besides the mentioned LP, smaller time projection chambers were built and used at DESY before. They serve different purposes like charge transfer process or effective gain measurements or gas and single point resolution studies. The work described in this thesis uses results acquired with two of them, which are introduced in the following.

6.4.1 Small TPC Prototype

A small chamber was built at DESY to study charge transfer processes [Voi04]. This TPC has a diameter of 25 cm and is operated with a drift length of 20 mm, it is shown in figure 6.4(a). Inside the chamber, on top of the cathode, a ^{55}Fe source can be mounted in order to produce tracks. The chamber is operated with a double GEM stack, shown in figure 6.5(a), and read out by an unsegmented copper anode. As counting gas the TDR mixture of 93 % argon, 5 % methane and 2 % carbon dioxide is used. The applied fields are – if nothing different mentioned – 250 V/cm for the drift region, 1.5 kV/cm as transfer field and 3 kV/cm for the induction gap. Voltages across GEMs vary and are described in chapter 8, where the usage of the chamber for comparative measurements of GEM foils produced by different manufacturers is presented. A preliminary version of results of these studies are presented in the diploma thesis [Bec08].

6.4.2 Medium Size TPC Prototype

The medium size TPC prototype can be seen in figure 6.4(b). It has a sensitive length of 67 cm and a diameter of 27 cm and was built to measure the single point resolution as a function of the drift length [Lux05]. The prototype was used in a magnet available at DESY, which is able to produce magnetic fields up to 5 Tesla. Results of these studies are summarized in [Die06, Jan08].
This prototype was used for studies with grid GEMs developed in the scope of this thesis and shown in figure 6.5(b). Some more details about the measurement conditions are given in the following. The TPC has a sensitive volume of $10 \times 10 \times 67\,\mathrm{cm}^3$ and is for the grid GEM studies equipped with a staggered pad plane (cf. figure 6.3(a)). The readout pad pitch is of the size of $1.27 \times 7\,\mathrm{mm}^2$. 512 electronics channels were read out by an ALEPH DAQ system, ten complete pad rows of 48 pads each are analyzed. As counting gas the P5 mixture (95 % argon and 5 % methane) was used and the drift field was set to 90 V/cm, while the GEMs were used with voltages between 320 V and 325 V. Fields of 1.5 kV/cm were applied in the 2 mm wide transfer distances. While a field of 3 kV/cm is used in the 3 mm wide induction

(a) (b)

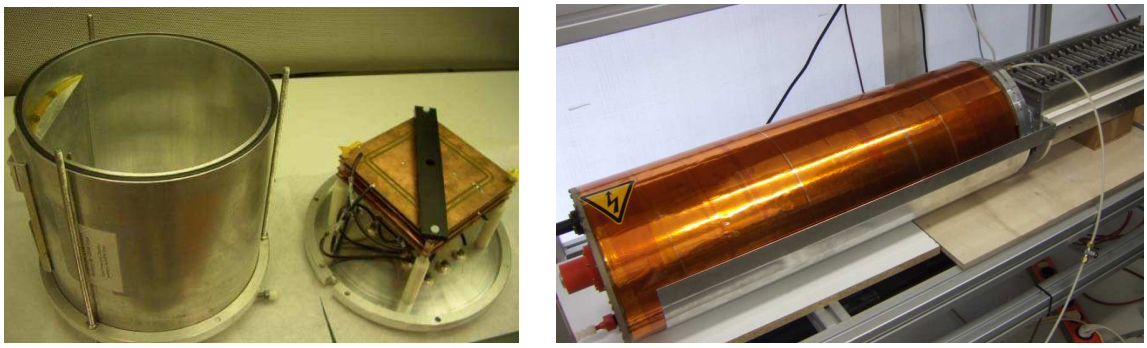

Figure 6.4: (a) Small TPC prototype, on the left the chamber is visible, on the right the inner assembly with the cathode and the source mounting on top of it is shown. (b) Medium size prototype [Die09].

(a) (b)

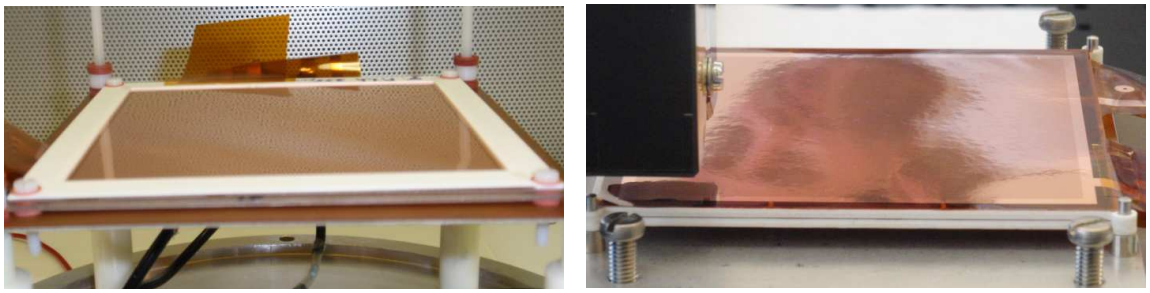

Figure 6.5: (a) Double GEM stack with frames for small TPC prototype. (b) GEM setup with grid as support structure, used in medium size prototype at DESY. The picture shows the stack during a height profile measurement.

region. For the analysis, cosmic muons data sets were taken. A trigger system – consisting of two scintillator paddles above and below the magnet equipped with photo multipliers – started the data acquisition, when coinciding signals were measured.
The readout electronics is based on ALEPH technology [Bow95] and had to be modified in order to match the requirements of a prototype GEM TPC [BGJW04]. It consists of time-integrating preamplifier with a shaping taking place afterwards. The next step is the digitization done by Flash Analog Digital Converters (FADCs) working with a sampling rate of 12.5 MHz, which results in time bins of 80 ns length. The data is read out by a fast intelligent controller and afterwards stored in the lcio (linear collider in- and output) format.

6.5 Data Reconstruction

In this section, a brief introduction to data reconstruction and single point resolution, as used within this thesis, is given. Measurements taken with the medium size TPC prototype at DESY are reconstructed using the program MultiFit, which was developed in the scope of a diploma thesis at DESY [Jan04] and is described in detail in [Die06, Jan08]. The used coordinate system is sketched in figure 6.6(a). Some more variables, which are important for the reconstruction, are shown in figure 6.6(b). Geometrical parameters of tracks are the intercept in x, which denotes the x coordinate of the entrance point of the track into the sensitive area. The inclination angle ϕ, defined in the xy-plane and with respect to the perpendicular. The slope of the track fit in the xy-plane is described by slope x and the curvature by the variable κ.
MultiFit is able to reconstruct tracks based on pad-wise charge measurements, collected with a pad plane as shown in figure 6.3(a). The reconstruction is divided in three steps. First, the pad-wise charge information from different time bins is combined to so-called pulses. With the help of a cluster finder, these pulses are reconstructed row-wise to hits, which describe three dimensional space points of charge. Second, a track finding algorithm is applied, which combines the hits to tracks. And third, the tracks are fitted with different hypotheses.

6.5.1 Track Fitting Methods

Two different track fitting approaches are available within MultiFit. First, a χ^2 fit of a straight or curved track hypothesis to the hits can be performed. For this method a hit reconstruction taking the pad response into account is provided. This pad response function (PRF) has to be considered, since the center of gravity method for determination of the x position of a hit produces incorrect results for charge depositions smaller than a few pads, as illustrated in figure 6.7. Many hits are reconstructed towards the middle of a readout pad. Therefore a correction for the

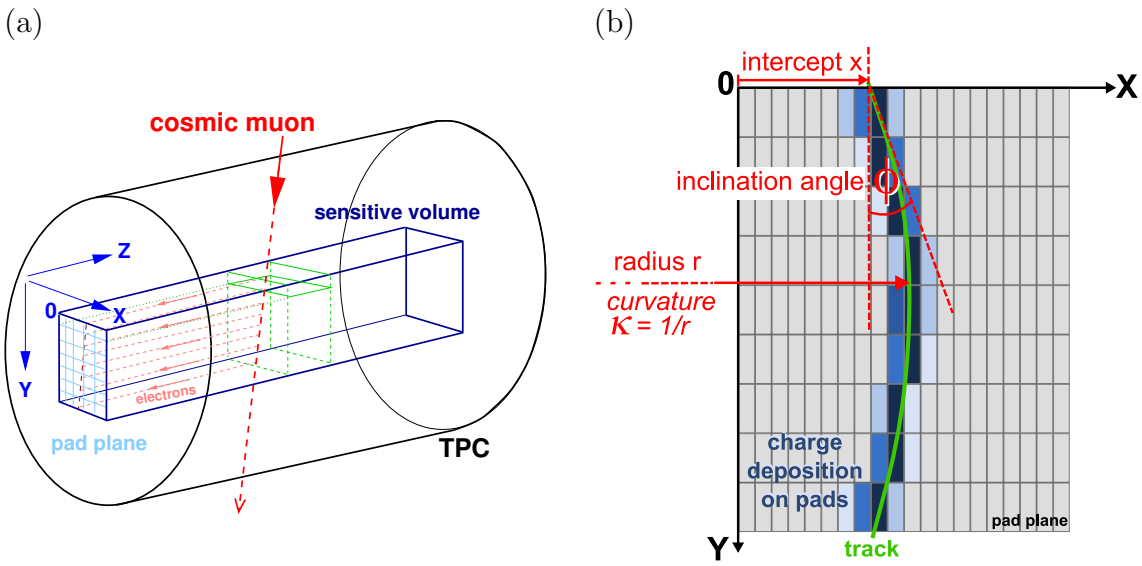

Figure 6.6: (a) MultiFit coordinate system with sketch of TPC prototype [Die06]. (b) Reconstruction variables [Die09].

PRF has to be applied. Further details about the pad response correction and its implementation into MultiFit can be found in [Die06, Jan08].
The second method for track fitting is called global fit method, which is footing on a likelihood function maximization. This method fits a model of a Gaussian charge cloud to the deposited charges on the whole pad plane at once. Here, the width σ of the charge cloud can be treated as free parameter during the fit, or it can be fixed to a value that is calculated according to the diffusion.
If nothing else is mentioned, the standard method for track fitting used in this thesis, is the χ^2 minimization with pad response correction.

6.5.2 Single Point Resolution with Geometric Mean Method

The hits of a track are spread around the true track position following a Gaussian distribution. The width of this distribution describes the single point resolution. In TPC prototype conditions, neither an external reference exist, which could be used to obtain the true track position, nor a sufficient number of hits is available to determine a robust fit, which could serve as reference for the true position. Hence, the so-called geometric mean method is used. This method allows a determination of the single point resolution without external reference and with only a small number of available rows or hits respectively.
In order to understand the geometric mean method, two terms have to be introduced, which are sketched in figure 6.8(a). First the residual, which is the distance of a hit to the track fit, performed without taking this very hit into account. The second perception is called distance and describes the spacing between the hit and the track

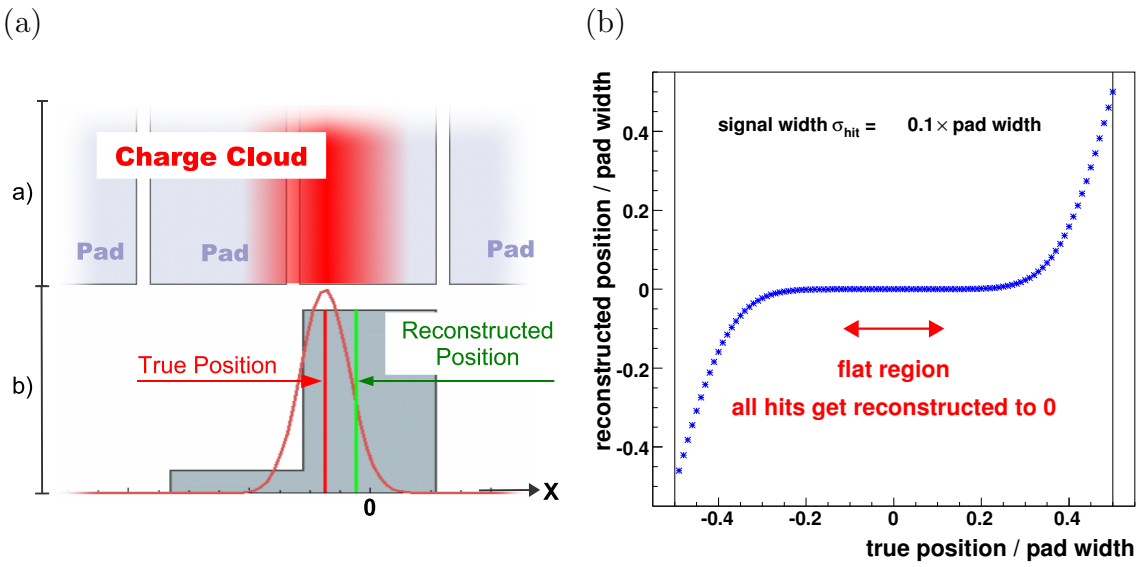

Figure 6.7: Illustration of the pad response. (a) True and reconstructed position of a narrow charge signal [Die06], (b) reconstructed position as function of the true position, normalized to the pad width [Die06].

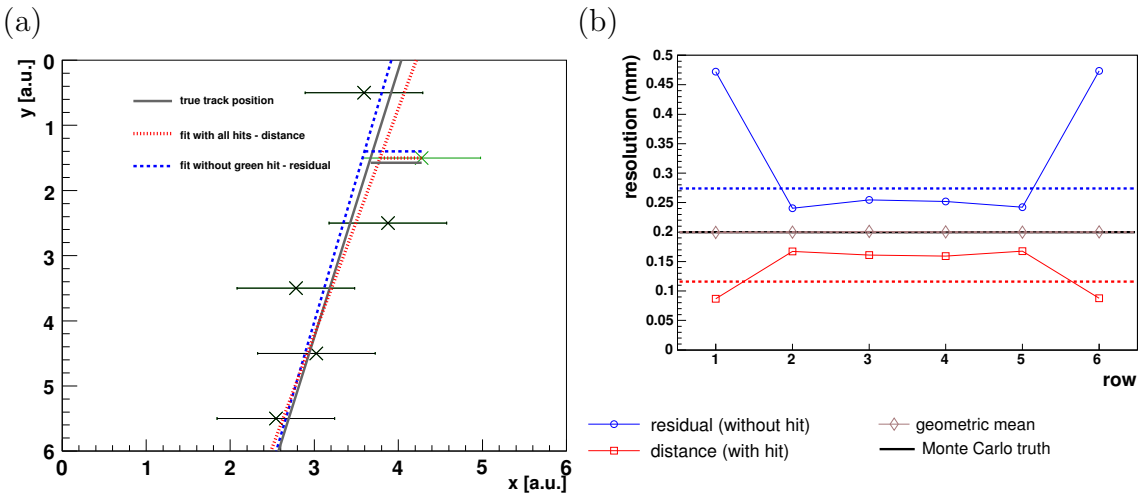

Figure 6.8: Geometric mean method. (a) Sketch of distance and residual [Jan08], (b) simulation study of single point resolution with geometric mean method [Jan08].

fit obtained with all hits used for the fitting process. Using the residuals for the resolution calculation, a larger width will be determined compared to a calculation using the distances. The combination of both methods via the geometric mean yield a robust estimation of the single point resolution:

$$\sigma_{\mathrm{x}} = \sqrt{\sigma_{\mathrm{residual}} \cdot \sigma_{\mathrm{distance}}}. \tag{6.3}$$

An analytic proof for the validity of the geometric mean method for straight tracks can be found in [C+05]. An outcome of a simulation study of the geometric mean method for curved tracks is shown in figure 6.8(b). It is clearly visible, that the geometric mean is the correct choice for the calculation of the resolution. Especially in the outer rows, this method improves the resolution, more details can be found in [Jan08]
The most single point resolution results presented in chapters 9 and 10, have been determined for the χ^2 fit with PRF correction. Only in two cases a comparison of the resolution values of the different reconstruction methods are made, which yields a better understanding of the methods and allows a judgment on the quality of the results.

Chapter 7

Motivation for GEM Studies

Tracking plays an important role in the International Linear Collider (ILC) environment and has to fulfill ambitious requirements. The particle flow concept relies strongly on tracker information, since the energy of charged particles is determined from momentum measurements performed in the Time Projection Chamber (TPC). In addition, measurements of the specific energy loss in the TPC can be used for particle identification.
This thesis presents studies of Gaseous Electron Multipliers (GEMs). They are used as amplification devices in TPCs and compete with so called MicroMEGAS. The following sections introduce the challenges for TPCs and GEMs as motivation for the research work presented in the subsequent chapters.

7.1 A TPC as Main Tracking Detector

The choice of a time projection chamber as main tracking device is advantageous in many terms. Probably the best argument for a TPC is the excellent pattern recognition capability. The huge number of measured three dimensional space points (hits) – in the ILD of the order of 200 – allows for a precise reconstruction of trajectories and high resolution tracking. The large radius of the TPC allows to discriminate tracks in the inner region by starting the track reconstruction at the outer radius. This approach provides reliable track information up to very high multiplicities in dense jets and ensures a high reconstruction efficiency, which is needed for the particle flow concept. A silicon tracker provides better single point and double track resolution – of the order of 15-40 µm single point resolution for the CMS silicon tracker [CMS09]. But the large number of hits in a TPC compensates the moderate single point resolution and allows a good momentum resolution. In a silicon detector the material budget allows only very few detector layers and thereby pattern recognition suffers. Another difficulty of silicon detectors is the alignment, since every layer is able to provide a very good resolution but has to be aligned precisely with the other layers and other sub-detectors to achieve the desired level of precision.
In figure 7.1(a) the polar angle acceptance anticipated for the ILD using a TPC and

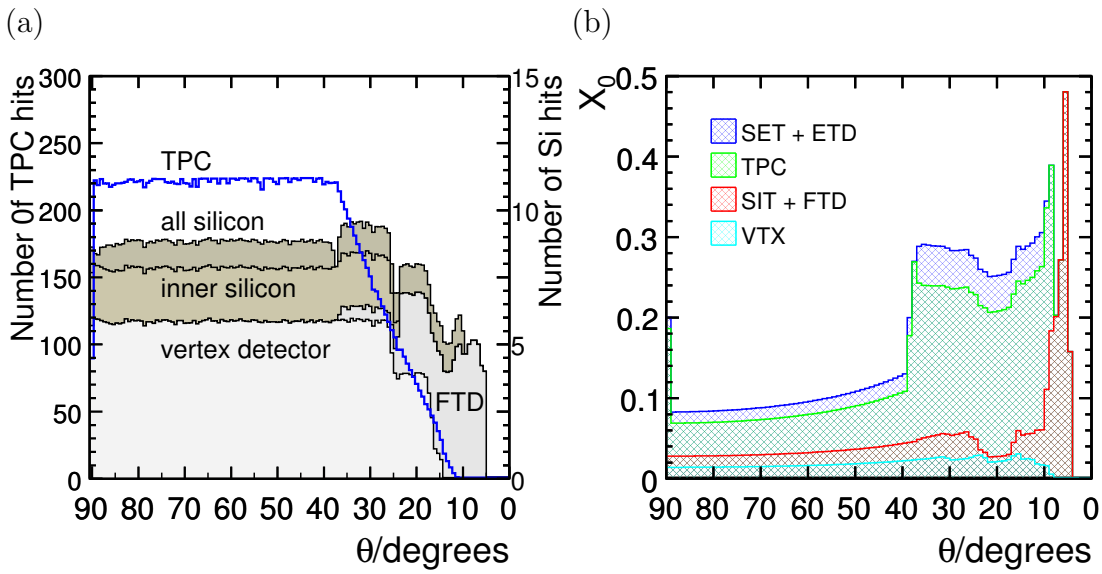

Figure 7.1: (a) Number of hits as function of polar angle θ of ILD tracking system. The left y axis describes the number of TPC hits, while the right one counts hits from all silicon detectors [LOI09]. (b) Material budget of the tracking system in fractions of a radiation length [LOI09].

additional tracking detectors is shown. The whole tracking system is designed to cover almost the full solid angle to ensure a good detector performance for precision measurements. The TPC is able to provide the full number of hits down to $\theta = 37\,^\circ$ and is able to add information to the track reconstruction down to roughly $\theta = 10\,^\circ$. A second very strong argument for the choice of a TPC is the small amount of dead material, since the whole chamber is only a gas filled cylinder built by lightweight composite materials. According to design requirements formulated in [LOI09], the material budget for walls and gas of the ILD TPC sums up to only 4 % of a radiation length X_0. This means a TPC as main tracking detector introduces the least possible amount of material in front of the calorimeters to ensure their best performance and allow for good photon and neutral hadron measurements. Little material keeps the number of hard interactions producing neutral particles, which have to be measured in the hadronic calorimeter, and the multiple scattering propability small. As already mentioned, a description of a lightweight large scale TPC prototype can be found in [Sch09]. In the same reference a simulation study is performed, in order to visualize the necessity of lightweight tracking structures. The analysis uses photons, electrons and pions originating from the interaction point, generated with energies from 500 MeV up to 20 GeV. The points of first hard interactions are shown in figure 7.2 in a side view of the ILD. Particle conversion or photon radiation are taken into account as such processes. Interactions inside the TPC are less critical than interactions in the mounting, because the fragments can be measured and so it is possible to reconstruct the initial energy and momentum. Of particular importance for the particle flow concept is the reduction of hard processes inside the TPC field cage

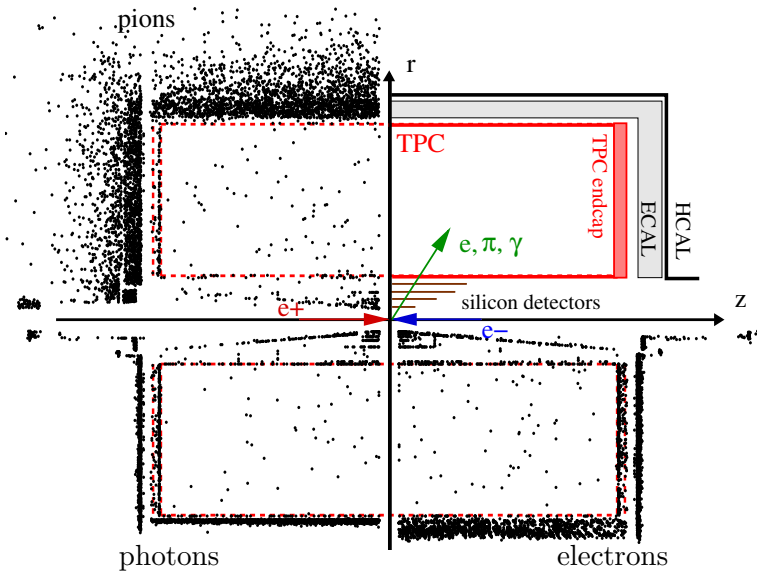

Figure 7.2: Simulated locations of first interactions in the rz-plane of photons, electrons and pions [Sch09].

and mounting structures. These distort the measurement in the calorimeters, since the amount of neutral particles is getting higher with each of these interactions and with it the jet energy resolution of the calorimeters is worsened. In order to reduce hard interactions as far as possible, a careful choice of materials with the smallest possible radiation length is necessary.
A third argument is, that a TPC is well suited to reconstruct so-called V particles, like Kaons [RB47], due to its good pattern recognition. These particles are long lived and therefore might decay inside the main tracker. In the case of decays of charged particles, characteristic kinks can be observed, since the particle changes its direction and momentum while decaying. If one of the daughter particles is neutral, only one track changing its direction can be observed. In the case of so-called V^0's, a neutral particle decays into two charged ones, which produce a signature of two suddenly occurring tracks forming a V. A study of the detection abilities for V particles in the ALICE TPC is presented in [Bon06]. Figure 7.3(a) shows a sketch of a charged Kaon topology, while figure 7.3(b) depicts the resulting efficiency of daughter particle detection as a function of the distance to the primary vertex. Only at distances larger than two meters – close to the outer diameter of the chamber – the efficiency starts to drop significantly.
Photons produce V^0 particles, when they convert to an electron positron pair. Since Higgs particles are able to decay into two photons, the ability to detect these converted photons is important for all active and future high energy physic detectors. Hence, a comparison between the ATLAS silicon tracker and the ILD TPC is described in the following, although this comparison is difficult, since the requirements for both detectors are very different. The ATLAS tracker has to deal with a bunch

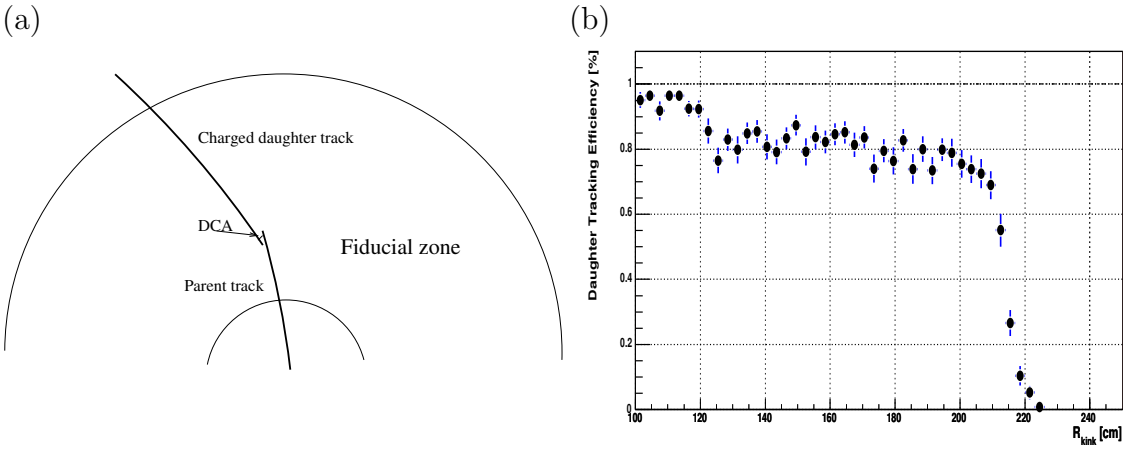

Figure 7.3: (a) Sketch of charged Kaon decays in the ALICE TPC [Bon06]. (b) Efficiency of daughter particle detection over distance to primary vertex [Bon06].

crossing rate of 40 MHz, needs to be able to withstand a lot of radiation and is older and shorter than a future ILD TPC. Nevertheless, some features of both trackers concerning converted photons are discussed in the following.
Compared to a silicon tracker, a TPC has two advantages in reconstructing such events. First, in a silicon tracker the conversion probability itself is much higher. In the ATLAS tracker at least one of the photons converts in 57 % of the $H \longrightarrow \gamma\gamma$ events [Fan09]. While in the ILD TPC only 15 % of the photons are converting according to a simulation study. This study was performed with the ILD detector model [Sch10b]. For this purpose, photons with energies between 50 GeV and 100 GeV were simulated with the ILD_00 Mokka program [Vog10] and the conversion probability is shown in figure 7.4(a). Second, at ATLAS the detection efficiency for the resulting electrons or positrons breaks down already at a distance of about 35 cm to the primary vertex as shown in figure 7.4(b). The efficiency of detecting conversion photons is found to be linearly decreasing with the conversion radius [Boh08]. As mentioned, a TPC produces less conversions and is able to detect the decay products also at larger radii (cf. figure 7.3(b)).
A fourth advantage of TPCs is particle identification achievable with the help of the specific energy loss dE/dx measured in the chamber. This capability is an additional bonus, since the ILD TPC is not optimized for this purpose, like for example the OPAL TPC. There, a pressure of 4 bar was applied in order to obtain the best possible separation power. Using the dE/dx information of the ILD TPC, Kaons and pions can be distinguished in a momentum range from 2-20 GeV [TESLA01a] and electron identification will be improved in comparison to the sole calorimetric information, in particular at low electron momenta. This topic is discussed in detail in section 7.5.
An advantage of silicon detectors is the readout speed. However, events in a TPC can be disentangled with the help of the track topology – following the track from

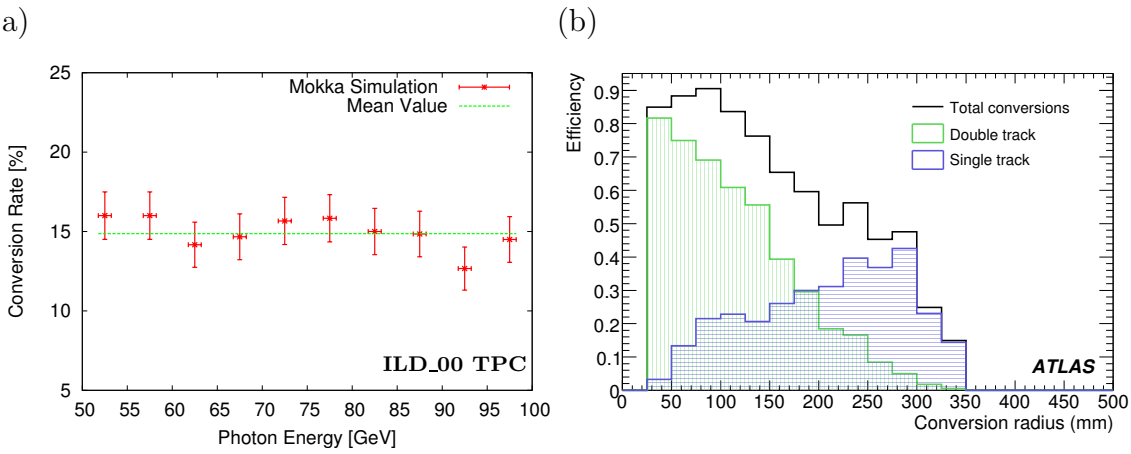

Figure 7.4: (a) Conversion probability of photons simulated with the ILD_00 Mokka model [Sch10b]. (b) Reconstruction efficiency of conversion electrons at ATLAS. Plotted over the conversion radius for events with one (blue) or two photons (green) converting. These photons have a transverse momentum of at least 25 GeV [Fan09].

the outer radius to the interaction point – or so-called time stamps, provided by the inner silicon detectors. A timing resolution of 2 ns should be possible [TESLA01a]. In the ILC environment, where a TPC has to deal with many superimposed events, these time stamps are important, although the number of tracks per event is relatively small compared to the LHC environment of the ALICE TPC. There, the TPC has to deal with signal occupancies of 40 % at the innermost and 15 % at the outermost radius [ALICE00] due to heavy ion collisions. The occupancy caused by beam induced background from an ILC bunch train was studied for the ILD TPC in [Vog08] and accounts to less than 0.1 %, which is negligibly small.

7.2 The Endcap Challenge

Due to the fact that all important components are located in the endplates, their design needs special attention. At the same time the concentration of components at the endcaps allows easy access for maintenance. Nevertheless, the ALEPH experience told the TPC community to be prepared to give also access to the field cage itself [ALEPH06]. In 1999 somebody had to enter the TPC, since a carbon fiber shortened two field strips. With the help of a small person and a vacuum cleaner the problem was eliminated.
The material budget of the ILD TPC endplate has to be as small as possible and is designed to be 15 % of a radiation length. This a quite high value, but the advantage of a TPC is, that all the material is concentrated in the endplates and not inside the tracker itself. A current estimate of the LCTPC collaboration [Set09] plans 3.5 % X_0 for amplification, readout and the endplate itself, 9 % X_0 for electronics and cables and 2.5 % X_0 for the cooling. The average total radiation length of the

whole tracking system as estimated for the ILD letter of intent is shown in figure 7.1(b). Critical is the polar angle region below $\theta = 40\,^{\circ}$, which is the location of the endplates. There the plans include, that the amount of material of all sub-detectors sums up to almost a third of one radiation length. Therefore still some effort has to be put into the design of a lightweight TPC endplate in order to reach the envisaged goal of 15 % X_0. About $10\,m^2$ on each side need to be instrumented with the least possible amount of insensitive area. In particular the mounting of amplification devices, readout planes and electronics including a cooling system is challenging.
In order to achieve this goal, electronics have to be small and have to provide a good performance with the least possible noise per channel. Since many channels have to be covered, not much space is available and total power consumption and heat dissipation becomes the most critical topic. For this reason power pulsing schemes, which are adapted to the bunch train structure, are developed at the moment. These schemes make the design even more challenging. For the readout two options are possible, either analog or digital readout techniques. Analog readout works with pad planes, segmented copper plated surfaces serving as anode. In this case amplitude information is used and amplification and digitization devices are mounted on the back side of the anode. More details can be found in [Mus09]. At the current status of detector development a trend to digital techniques can be observed. A very large amount of channels provides binary information for each channel. A digital silicon sensor chip readout for TPCs, capable to resolve single electron clusters due to the high granularity of the readout surface, requires much more channels than the analog readout and has the electronics installed directly on the backside, more details can for example be found in [Che09].
Micro pattern gas detector devices are proposed to serve as electron amplification stage inside the TPC. So far they were never used in a large scale TPC, but only in small prototypes. HERA-B [HERA-B00], and COMPASS [A$^+$02], were and are using the largest GEMs with roughly $30 \times 30\,cm^2$. Hence, the coverage of $10\,m^2$ is a new and challenging task. Especially, the mechanical design for a mounting with the least possible gaps is difficult. In the design for the ILD TPC endplate, a partition in concentric rings, subdivided in modules is planned. A sketch is shown in figure 7.5. For tests of these modules an endplate for the Large TPC Prototype (LP) built within the LCTPC collaboration was produced, which is a cutout of the endcap for the ILD TPC. This LP anode is also visible in figure 7.5 on the right hand side and in figure 6.1(b) on page 51. The chosen material for the LP endplate is aluminum, which is stable but introduces much material. For a later ILD endcap new materials, like composites made of honeycomb paper and glass fiber reinforced plastic (GRP) or carbon fiber, need to be tested. The LCTPC collaboration is facing this issue at the moment. The segmentation of the actual and thereby also the future anode is done via the mentioned circular rings, resulting in a module size of $25 \times 18\,cm^2$.

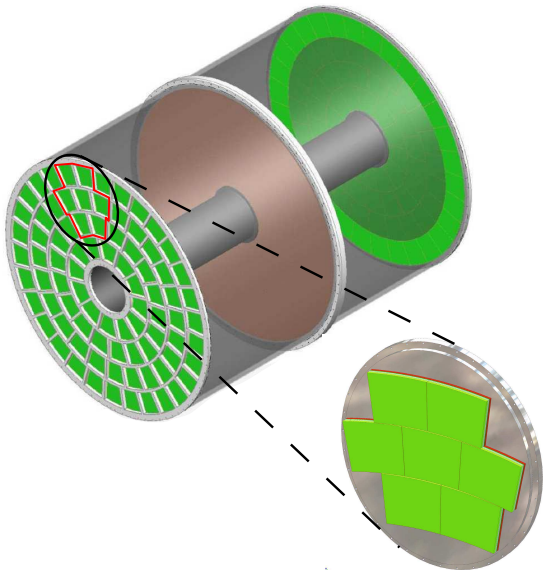

Figure 7.5: Schematic view of the ILD TPC with its envisaged endplate. The already used LP endplate is a cutout of the future design [LOI09, Die09].

7.3 GEMs versus MicroMEGAS

The micro pattern gas detector technologies were introduced in section 3.3.5. They have the potential to replace older amplification techniques – like wires – because only with MPGDs the ambitious goals, mentioned in table 6.1 on page 52, can be realized. Especially the good single point resolution and the absence of $\overrightarrow{E} \times \overrightarrow{B}$ effects makes MPGDs a good choice. This section outlines some differences between two of the possible amplification devices.
Both can be used with analog and digital readout systems. GEMs can be used in stacks of two or three foils, which provides many parameters for optimization of the assembly. One advantage of GEM stacks is their low discharge probability and their intrinsic ion feedback suppression, of the order of a few per mill [Lot06, BBSV03]. The back drifting ions form so-called ion discs during an ILC bunch train and distort the field homogeneity [Kra08]. Therefore, the ion feedback should be as small as possible. It is defined as fraction of back drifting ions divided by the number of electrons collected on the anode. In the ideal case, the ion feedback f_I should be of the order of $1/G_{eff}$. This would mean, the same amount of back drifted ions and primary electrons in the drift region. MicroMEGAS do also suppress ions generated during the gas amplification process, but cannot compete with stacked GEMs in this aspect. In order to reach the per mill level, they have to be operated with very small drift fields of the order of a few ten volts per centimeter. In consequence, the achieved gain is small. Parameters for optimization of the ion backflow in MicroMEGAS are the gap size between mesh and anode and the hole pitch. Increasing the gap and decreasing the pitch yields better values of f_I. More details can be

found in [Che09]. In addition, MicroMEGAS have a higher discharge risk. If a trip occurs, it happens always directly to the anode, especially for the pixel chip readout an additional safety coating is needed to prevent it from destructive discharges.
An advantage of MicroMEGAS used in combination with pixel readout is the narrow signal width. At the same time this is a drawback, if MicroMEGAS are used with an analog pad readout, where the signal width – better the amount of hit pads – is crucial for a good single point resolution. To deal with this problem so-called resistive layers are used. They are put directly on top of the anode and have a high resistivity to spread the charge signal over the pad plane. This effect allows for larger pads compared to setups without a resistive foil. The resulting advantage is, that less electronics channels and with it less material is needed. In addition, less heat is produced due to fewer channels. One problem of using resistive foils is the single point resolution in z, since the signal propagation in the foil is very slow compared to the drift of electrons. This results in a difference in time measurement in the center and on the edges of the broadened charge cloud. Another difficulty is the double track separation. In [Bal08] it is shown, that the ability to separate two tracks depends only on the pad size. If the pads are too large, there is no visible dip in the pulse structure, which is required to distinguish pulses from two different tracks. Hence, further studies of resistive foils have to be performed, in order to find an optimum of spread to have on the one hand not too much channels and on the other hand be able to obtain sufficient z resolutions and track separation.
Another advantage of MicroMEGAS structures is their compact design. The amplification stage is directly and solidly connected with the readout plane. For InGrids the alignment of the pixel readout is thereby intrinsically guaranteed and the mesh has a defined position. No external support structure, which introduces a non instrumented area, is needed. The mesh only rests on its pillars. Since the amplification of MicroMEGAS happens in the gap between mesh and anode plane, it has to meet accurate requirements in order to provide an uniform gain. But with the right choice of gas, it is possible to become almost independent from the distance between mesh and anode. In contradiction, the electron multiplication by GEM foils happens inside the foil. The distances between the foils and the anode are not critical for the single GEM gain but influence the extraction efficiencies, which are also part of the effective gain.

7.4 Momentum Resolution

To determine momenta of particle tracks the polar angle θ with respect to the beam axis and their transverse momenta – in the rϕ-plane – are measured. A transverse momentum can be calculated with the help of the curvature κ (or the radius) of the track caused by a magnetic field via Lorentz forces:

$$p_T[\text{GeV}] \approx 0.3 \cdot r[\text{m}] \cdot B[\text{T}] \tag{7.1}$$

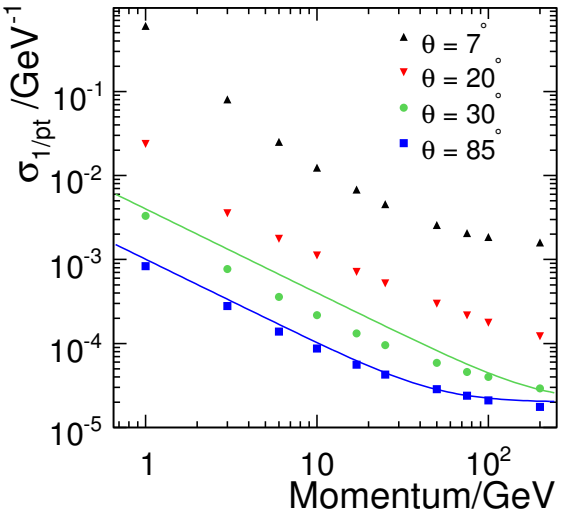

Figure 7.6: Simulated momentum resolution for muons with fixed polar angles in ILD. Shown are reconstructed points for different angles and parametrizations (solid lines) determined with the help of formula 7.3 and with $a = 2{\cdot}10^{-5}\,\mathrm{GeV}^{-1}$, b $= 1{\cdot}10^{-3}\,\mathrm{GeV}^{-1}$ [LOI09].

$$\mathrm{p} = \mathrm{p_T}/\sin\theta. \tag{7.2}$$

For high precision physics measurements at the ILC an excellent momentum resolution for charged particles is required. The designated goal of $\delta(1/\mathrm{p_T}) \leq 2 \cdot 10^{-5}\,\mathrm{GeV}^{-1}$ [LOI09] for the complete tracking system at 3.5 Tesla is one order of magnitude more precise than in all previous detectors.
The momentum uncertainty can be parametrized like:

$$\frac{\delta \mathrm{p_T}}{\mathrm{p_T}^2} = a \oplus \frac{\mathrm{b}}{\mathrm{p_T} \cdot \sin\theta}. \tag{7.3}$$

Where parameter a describes the error of the curvature measurement, while b stands for the uncertainty caused by multiple scattering.
ILD simulation studies with full reconstruction were performed in order to learn something about the necessary momentum resolution at the ILC. The above mentioned parametrization of the resolution was used. Muons at fixed polar angles and different momenta were generated and the achievable momentum resolution is analyzed. Results can be seen in figure 7.6. Parameters a and b are assumed to be: $a = 2 \cdot 10^{-5}\,\mathrm{GeV}^{-1}$ and $\mathrm{b} = 1 \cdot 10^{-3}\,\mathrm{GeV}^{-1}$ and are used to calculate limits shown as solid lines in figure 7.6, the points depict the reconstructed resolutions. Two polar angles are of special interest. $\theta = 85\,^\circ$ depicts the region where the full lever arm of the complete tracking system is available. Here, the reconstructed simulation points stay below the parametrization and the asymptote for high momenta is at

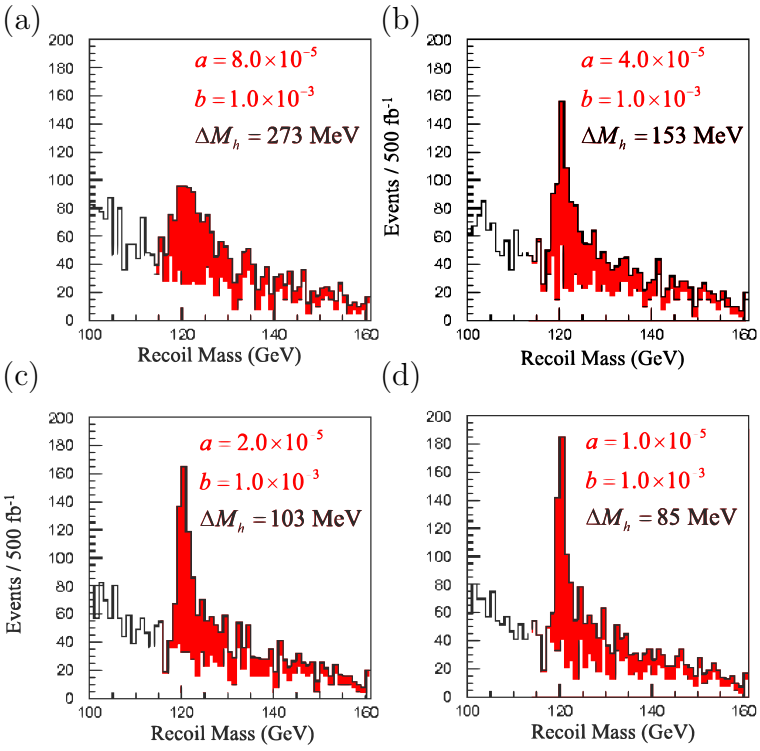

Figure 7.7: Simulation of Higgs recoil mass for different parametrizations of the momentum resolution [ILC07].

the envisaged value of $\delta(1/p_T) = 2 \cdot 10^{-5}\,\mathrm{GeV}^{-1}$. The other polar angle is given by $\theta = 30\,^\circ$, where the SET cannot contribute any longer to the measurement. But also in this case, the simulated result is better than the parametrization. This study did not account for possible mis-alignments of sub-detectors.
In order to reach this level of precision in $\delta(1/p_T)$, a very good alignment of the involved sub-systems – vertex detector, inner and outer silicon detectors and TPC – has to be ensured. Only the combination of different methods yields such a precise alignment. First, running at the Z^0 pole and measuring well determined muon tracks. Second, using a laser system, which feeds tracks into the detector and third using information of a highly resolved field map of the magnetic field.
One of the reason for such ambitious aims is for example the measurement of the Higgs recoil mass at the ILC. The simulated process is Higgs-strahlung $e^+e^- \longrightarrow ZH$ with subsequent decay of the Z into a muon pair [ILC07]. This channel allows for a measurement of the Higgs-strahlung cross section at the ILC, which is important for branching ratio determination (cf. section 2.1). The muons in the final state can be measured very precisely in the ILD detector. With the knowledge of the Z^0 mass and the center-of-mass energy the Higgs recoil mass can be measured independent from the Higgs decay channel. In figure 7.7, results of a simulation study with $500\,\mathrm{fb}^{-1}$ at a center-of-mass energy of 350 GeV and an assumed Higgs mass of 120 GeV are

shown. Four different assumptions are made for the momentum resolution, again parametrized with a and b. It can be seen, that with better resolution the Higgs peak becomes more prominent and the uncertainty on the mass and the cross section decreases. Here an eightfold improvement of the momentum resolution (from figure 7.7(a) to 7.7(d)) yields the same significance as a ten times higher luminosity [Jar07]. At least a momentum resolution of $\delta(1/\mathrm{p_T}) \leq 2 \cdot 10^{-5}\,\mathrm{GeV}^{-1}$ should be reached in the tracking system. The deduced requirement on the single point resolution in the TPC is explained in the following.
The TPC alone has to meet the goal of $\delta(1/\mathrm{p_T}) \leq 9 \cdot 10^{-5}\,\mathrm{GeV}^{-1}$ at 3.5 T [LOI09]. Using the Gluckstern formula [Glu63]:

$$\frac{\delta \mathrm{p_T}}{{\mathrm{p_T}}^2} = \frac{\sigma_\mathrm{T}}{\mathrm{L}^2} \cdot \frac{1}{0.3\mathrm{B}} \cdot \sqrt{\frac{720}{\mathrm{N}+4}} \tag{7.4}$$

the momentum resolution can be translated into single point resolution σ_T ($\equiv \sigma_{\mathrm{r}\phi}$), which is measurable in prototypes. B denotes the magnetic field, L the track length and N the number of equidistant space points reconstructed on the track. Of particular importance is the proportionality to the single point resolution and the number of space points. With a good resolution and many hits a good momentum resolution is achievable. This formula depicts again the difference between a TPC and a silicon tracker. The single point resolution of a silicon detector is much butter, but a TPC compensates this drawback with more space points N. For the ILD TPC 200 hits per track will be available. With a track length of the order of the TPC radius of 2 m and a magnetic field of 3.5 T a single point resolution of 100 µm (modulo track angle ϕ) over the whole length of the camber is required in order to reach the envisaged goal.
Another motivation for a very good momentum resolution is the measurement of the effective center-of-mass energy with the help of muon pair production and radiative returns to the Z boson. At LEP such measurements were performed, but only angular information from the leptons were used, since a direct muon momentum measurement was not able to add information. With the envisaged resolution of the ILD TPC this will be possible and the determination of E_{cm} can be improved to values of $\Delta\mathrm{E}_{cm} \approx 20\,\mathrm{MeV}$ by pushing the curvature error down to $2 - 3 \cdot 10^{-5}$ [ILC07].

7.5 Particle Identification with dE/dx

In order to determine reliable dE/dx measurements the detector has to fulfill stability requirements, quality cuts for the accounted hits are used and corrections are applied. Some of these needs are explained here, more details can be found in [H+92]. In the same reference, it is mentioned that the distinction of particles in the relativistic rise requires a stability of the energy loss measurement of the order of 1 %. Electronics gain has to be under control to assure accurate dE/dx measurements, however more crucial for this purpose is the stability of the gas gain. It

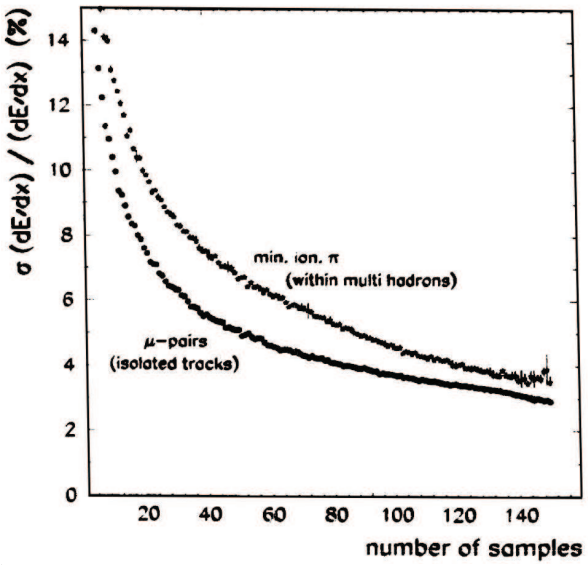

Figure 7.8: At OPAL measured relative dE/dx resolution as function of number N of hits. N is the number of samples used to calculate the truncated mean [H$^+$92].

is controlled by the gas density and therewith by the temperature stability and a sufficient flux, which compensates for small leaks. High voltage settings need to be stable during operation as well, to allow for a stable gas gain.
A precise knowledge of the effective gain of the amplification structure is required. Hence a gain map is needed, where the distribution of effective gain is described for the whole readout area. Variations of a few percent from one region to another do not cause problems, because they are small compared to variations of the primary ionization, which can be of the order of 50 percent. Such effects can be calibrated with the help of Z^0 pole runnings for instance. More important is the stability of the mean value of the effective gain over the whole anode. If this is not provided, tracks in different regions are amplified differently and therefore the dE/dx determination results in different values. LEP experience tells that variations smaller than $0.1\,\sigma_{\mathrm{dE/dx}}$ are tolerable to allow for precise physics analyses relying on dE/dx measurements [Hau09], although already variations of the order of 5 % $\sigma_{\mathrm{dE/dx}}$ are visible in the data.
The most important quality cut for hits, used to determine an energy loss measurement, deals with double tracks. In a dense jet environment signals are overlapping, therefore only hits with no other hits inside a distance of the order of the double hit resolution are accepted (3 mm in the rϕ-plane at OPAL [H$^+$92], 2 mm at ILD [LOI09]). Also in z direction no pulses with double structure are allowed to be used for dE/dx measurements. Another criterion was at OPAL [H$^+$92], that on tracks, crossing sector boundaries of the jet chamber, only hits were taken into account, which had a sufficient distance of 2 mm to this boundary. Corrections for the individual hits and also some track parameters have to be applied before dE/dx

information can be determined. They are derived from physics data, for example muon pair production. All corrections are described in detail in [H$^+$92]. Most important are corrections for electronics, multiple hits, saturation effects as well as track length and curvature, staggering, cross talk and gas gain.
After all this cuts and corrections a sample of N hits per track are left. In order to determine the energy loss a method called "truncated mean" is used. For it, the tails at low and high values of the Landau-like distribution are cut away, which is sensible since the tails are caused by δ-electrons and do not contain information for dE/dx measurements. To determine the truncation values an optimization of the resolution $\sigma_{\mathrm{dE/dx}}$ is performed. The dependence of $\sigma_{\mathrm{dE/dx}}$ on the number N of hits is shown in figure 4.2(b). The data – taken with OPAL – were fitted and the following dependence was determined:

$$\frac{\sigma(\mathrm{dE/dx})}{(\mathrm{dE/dx})} \propto \mathrm{N}^{-0.43}. \tag{7.5}$$

For a perfect Gaussian an exponent of -0.5 is expected, the difference is caused by the truncated mean method. It gives the Landau distribution a Gaussian-like shape, but it is obviously not a perfect Gauß function. The same exponent of -0.43 was also determined for the MARK II wire drift chamber [WFOW79].
The resolution depends – as mentioned – on N, but additionally on the effective sampling length ℓ and on the gas mixture. The sampling length ℓ is defined as product of absorber thickness and gas pressure. This means with a higher pressure and a careful choice of gas, better resolutions can be achieved. OPAL used a pressure of 4 bar in the jet chamber, however for the ILD a reduction of the amount of material in front of the calorimeters seems to be more crucial. Less pressure allows a mechanically less rigid field cage and reduces the amount of gas molecules. The dE/dx capabilities of the ILD TPC are accepted as they are, since a significant overpressure – improving the particle identification – would contradict the optimization efforts for a good spatial resolution and a small fraction of a radiation length for the wall structures.
In the letter of intent for the ILD [LOI09] an envisaged dE/dx resolution of 5 % is quoted for the TPC. Such good resolution has to be required to ensure high separation power for physics analyses performed at the ILC. Not $\sigma_{\mathrm{dE/dx}}$, but this separation power D is the figure of merit. It is defined as the distinctness of the separation of particle A from particle B [Hau96]:

$$\mathrm{D} = \frac{\frac{\mathrm{dE}}{\mathrm{dx}}(\mathrm{A}) - \frac{\mathrm{dE}}{\mathrm{dx}}(\mathrm{B})}{\sigma(\frac{\mathrm{dE}}{\mathrm{dx}})_{\mathrm{A,B}}}. \tag{7.6}$$

Here $\sigma(\frac{\mathrm{dE}}{\mathrm{dx}})_{\mathrm{A,B}}$ is the average dE/dx resolution of particles A and B, while the variables in the enumerator stand for the measured mean energy loss of both particle species. In figure 7.9 results of a simulation study of the separation power are shown. The analysis presented in [TESLA01a] uses TESLA parameters and assumes an uncertainty of 0.2 – 0.3 % due to calibration.

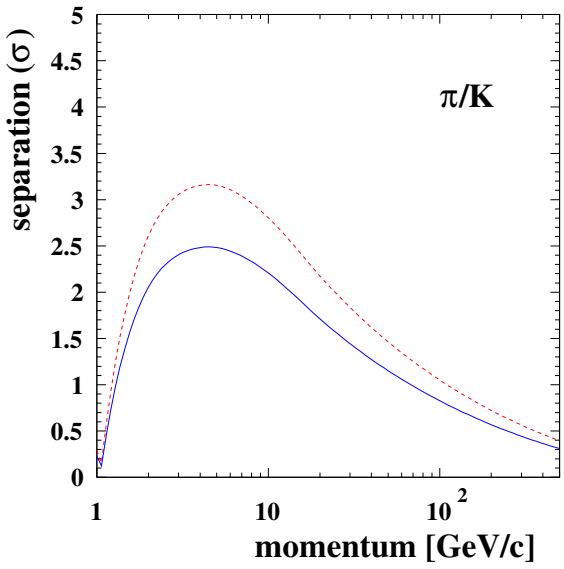

Figure 7.9: Simulated separation power D between Kaons and pions over particle momentum. The solid line is for tracks in jets, while the dashed one depicts values for isolated tracks [Hau06, TESLA01a].

To emphasize the importance of the separation power a PhD thesis recently finished at DESY is cited here. In [Sch09] a SUSY simulation study for ILD is presented, which aims to identify low energetic pions ($E_\pi < 45\,\text{GeV}$) in order to measure τ polarization. The dE/dx measurement is used in this analysis for particle identification of pions and gives an important handle for background suppression. A cut on the separation power is introduced in order to separate electrons from pions. Then a weighting of events is applied, according to their probability being identified as pions.

7.6 Track Reconstruction Efficiency

In principle the tracking efficiency depends on the single hit efficiency and track finding and fitting algorithms. A TPC with a good reconstruction algorithm and pattern recognition provides intrinsically a high tracking efficiency due to the large amount of measured space points, $\mathcal{O}(200)$. The tracking efficiency depends also on the polar angle since pattern recognition becomes more difficult with fewer reconstructed hits, if a track leaves the TPC through the endplates. But with additional sub-detectors like the forward tracking detector, which is part of the silicon detectors, the efficiency can be recovered even in the forward region. The tracking efficiency is crucial for the particle flow algorithm, as it can be read from equation 3.2 on page 19. Using this concept, momenta and with it energies of charged particles are measured in the tracking system. The momentum resolution is very good compared to the energy resolution of the calorimeter system. But the efficiency has

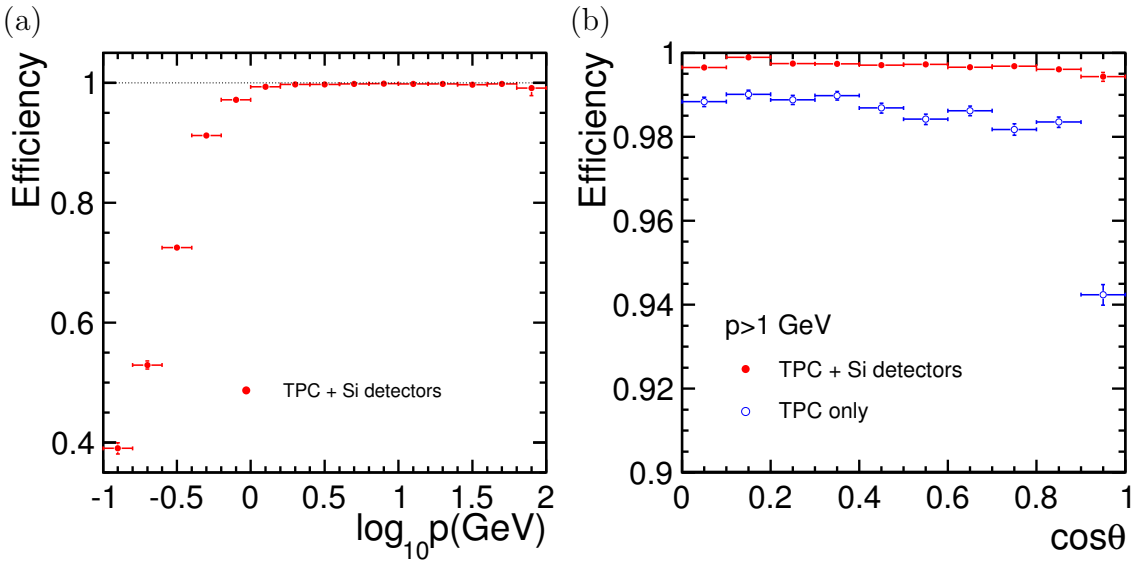

Figure 7.10: Tracking efficiencies at ILD as function of (a) momentum [LOI09] and (b) polar angle [LOI09].

to be excellent as well, since about 60 % of the information relies on the tracking detectors.
A simulation study to determine tracking efficiencies for ILD is presented in [LOI09]. $t\bar{t} \rightarrow 6$ jets events at 500 GeV center-of-mass energy are generated for this analysis. At least four hits are required including decays and V^0 particles. The resulting efficiency is shown in figure 7.10(a) as function of the particle momentum. For more than 1 GeV the value reaches almost 100 %. In figure 7.10(b) the reconstruction efficiency as a function of the polar angle is shown for tracks with $p > 1$ GeV. The combined tracking system has an efficiency of more than 99.5 % except in the bin of smallest polar angles. Not considered in this study are machine backgrounds. In [Pet07] another study is presented, which shows that the tracking efficiency does not suffer from an background occupancy of 1 %. Only for larger occupancies of the order of 3 % an effect becomes visible. However, beamstrahlung photons, electron-positron pairs and neutrons induced by the beam are calculated to sum up to an occupancy of only 0.1 % [Vog08].

7.7 GEM studies for the ILD TPC

This section gives a short summary of the motivation chapter and explains the role of the work presented in the scope of this thesis for the ILD TPC research.
For the ILD a TPC is chosen as main tracking detector. Developing an endplate for this chamber is challenging since many readout channels and amplification structures have to be accommodated on a large surface with the least possible amount

of material. Two different MPGD devices – MicroMEGAS and GEM – compete to be used as amplification technique on this endplate. The main features of a TPC are tracking efficiency, momentum resolution and particle identification capabilities. For the particle flow approach a highly efficient tracking with an excellent momentum measurement is required, since the energy information for charged particles is determined with its help. Another strong reason for an outstanding momentum resolution is the Higgs recoil mass measurement. In addition, many analyses, like SUSY studies, require a good separation power of particles by means of dE/dx measurements. Since the particle flow concept relies on the tracker information for charged particles, the tracking efficiency is crucial for the ILD.
In this thesis three different analyses of GEM related topics are presented. The matter of comparative GEM studies, presented in chapter 8, is the choice of GEM foils for future applications, at first in LP modules and later on for the endplate of the ILD TPC. Described are comparative effective gain and energy resolution studies of GEM foils produced by different manufacturers. The effective gain performance of GEMs is interesting, since a minimal gain is required by the used readout electronics and the high voltage system has to be adopted to these requirements. A GEM producing larger effective gains at lower voltages, allows for example less voltage at the cathode, which is easier to realize. The energy resolution is of importance, since the quality of the energy – respectively charge – measurement is directly related to the achievable dE/dx resolution.
An aspect of effective gain variations in GEM detectors, which was not studied up to now, is the spatial uniformity of the amplification structure. GEMs need to be as flat as possible to avoid large gain inhomogeneities in the sensitive area. Height profiles of GEMs are measured and the impact of not perfectly flat foils on the detector performance is analyzed and presented in chapter 9. Especially the influence of gain variations on dE/dx measurements is analyzed using simulated tracks passing a bent amplification structure. In addition, the influence of gain variations on the single point resolution and the impact of bent GEMs on the drift field quality in a TPC are analyzed. The motivation for GEM profile studies is to decide, whether a flat mounting and quality control concerning this flatness is needed.
In chapter 10, the development of a new mounting for GEMs in TPCs is described. It is studied, whether the chosen design of a GEM support structure does cope with the requirements for an ILD TPC endplate. The mechanical challenges are the coverage of a large area with the least possible amount of material and a very flat mounting of the GEM foils. The requirements for physical quantities are described above. In particular the impact of the new mounting on single point resolution, tracking efficiency and dE/dx resolution are analyzed, using cosmic muon data recorded with a TPC prototype.

Chapter 8

Comparative GEM Studies

In this chapter, GEMs with different characteristics are compared concerning their effective gain and energy resolution. First, the different GEM foil types and the measurement assembly are introduced. Second, the calculation of the effective gain is described and the sources of uncertainty and the comparability of the results are discussed. Third, the results are interpreted according to the characteristics of the GEMs. Finally, the energy resolution is discussed and a short summary is given.

8.1 Different GEM Types

The parameters of all available GEM foils – as specified by the manufacturers – are summarized in table 8.1. From the CERN Gas Detector Development group [GDD10a] standard GEMs and some with an enlarged pitch of 225 µm were tested. The US American company Tech-Etch [Tec10, S$^+$07, BTH06] produces GEM foils with the same characteristics as standard CERN GEMs. In addition, multiplier foils manufactured in Japan were tested. The latter are produced in a different way, developed by the company SciEnergy [Sci10]. The substrate for these foils is not polyimide, but a liquid crystal polymer (LCP) and the holes have cylindrical shapes, produced by a new laser-plasma procedure. Two types of these foils with different substrate thickness were available, one with the standard thickness of 50 µm and another with a 100 µm thick substrate.
In figure 8.1 microscopic pictures of the five different GEM foil types are shown. For each foil, two hole diameters and distances in x and y between the holes were measured.

8.2 Measurement Assembly

For the effective gain measurements, the small TPC prototype – introduced in chapter 6 – was used. The whole assembly is described in the following sections, including chamber, electronics and radioactive source.

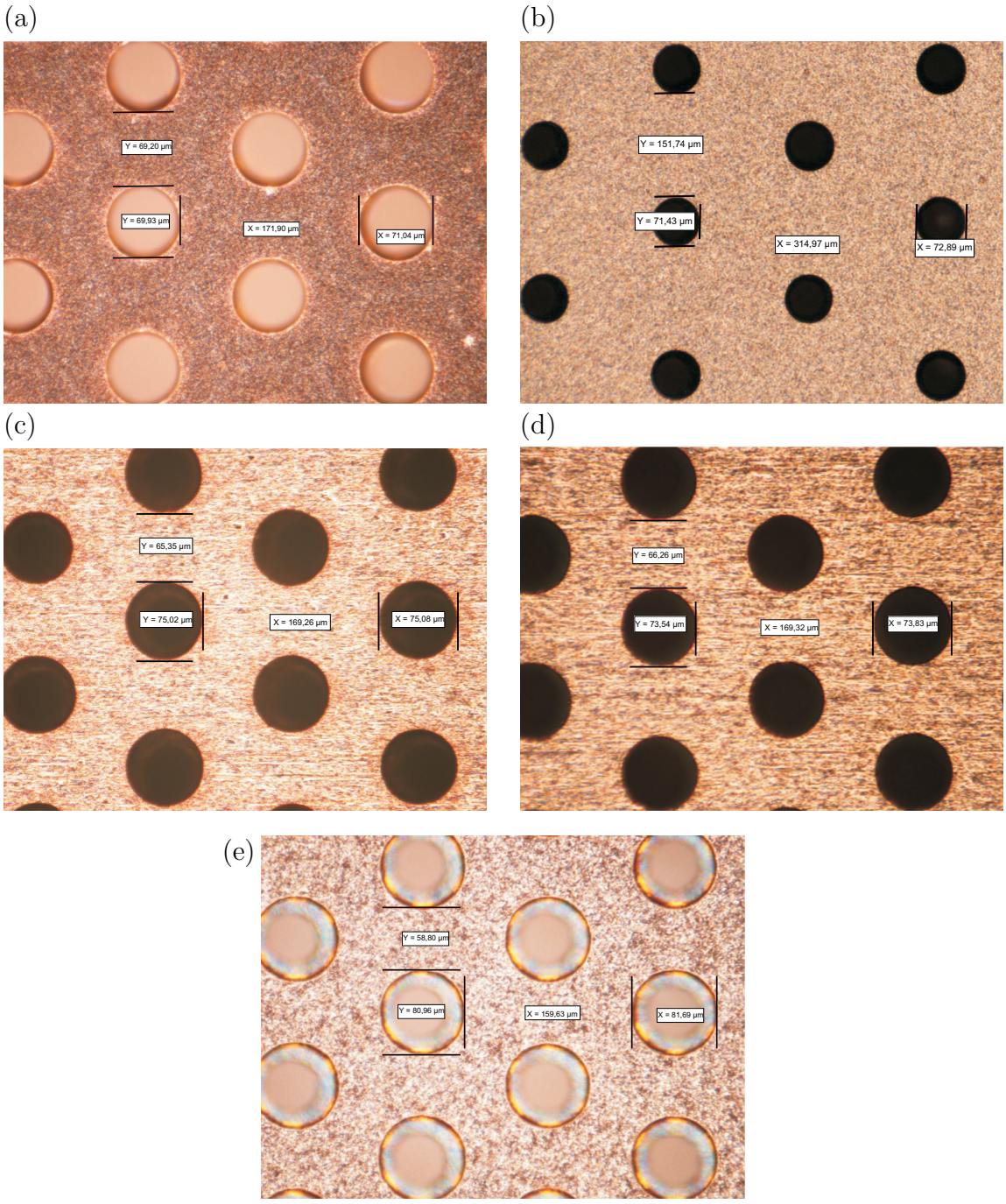

Figure 8.1: Microscopic pictures of different GEM types. (a) Standard CERN GEM, (b) CERN GEM with 225 µm pitch, (c) SciEnergy GEM, (d) SciEnergy GEM with 100 µm substrate thickness and (e) Tech-Etch GEM. Hole diameters and distances are measured with the kind help of Alexander Titze, DESY FEC group.

manufacturer	substrate material	thickness [µm]	pitch [µm]	hole shape	hole diameter inner/outer [µm]
CERN	polyimide	50	140	double conical	50/70
CERN	polyimide	50	225	double conical	50/70
Tech-Etch	polyimide	50	140	double conical	50/87
SciEnergy	LCP	50	140	cylindrical	70/70
SciEnergy	LCP	100	140	cylindrical	70/70

Table 8.1: Characteristics – as specified by the manufacturers – of the different GEM types, used to study effective gain and energy resolution.

8.2.1 Chamber

In the small TPC prototype a double GEM stack is installed below a cathode with a ^{55}Fe source mounted on top. A sketch of this setup can be found in figure 8.2. The anode consists of a copper clad printed circuit board (PCB) with one large pad of $30 \times 30\,\mathrm{mm}^2$. This unsegmented anode is surrounded by a copper area with outer dimensions of $100 \times 100\,\mathrm{mm}^2$, which is called anode ring.
The drift distance was set to 20 mm and as counting gas in the chamber, TDR gas (93 % argon – 5 % methane – 2 % carbon dioxide) was used. Fields and voltages across the GEM foils were applied via a voltage divider, 250 V/cm for the drift field and 1 kV/cm for transfer and induction fields. In order to gain a better homogeneity of the drift field, so-called field rings were used. They have been supplied with voltages according to their increasing distance to the cathode. The GEM voltages were varied between 340 V and 426 V by exchange of the resistors in the divider chain. In order to protect the GEMs in case of a trip, each GEM was connected via a 10 MΩ resistor to a multi channel power supply.
The comparative measurements in the following use a double GEM setup with a standard CERN GEM at position two and the different analyzed GEM types at position one. The measurements are labeled according to the changed GEM in the first position.

8.2.2 Electronics

The charge signals from the unsegmented anode were preamplified by a trans-impedance preamplifier and afterwards digitized with a charge to digital converter (QDC). No external trigger is available for measurements with radioactive sources, therefore a gate was produced using the signals themselves. For this purpose, the signal was doubled. From one of these resulting signals a digital gate was produced to start the read out of the QDC. The width of this gate had to be adapted to the width of the signals from the ^{55}Fe source. The other channel remained unchanged, but was delayed 20 ns and then fed into the QDC in order to extract the charge information of the signal.

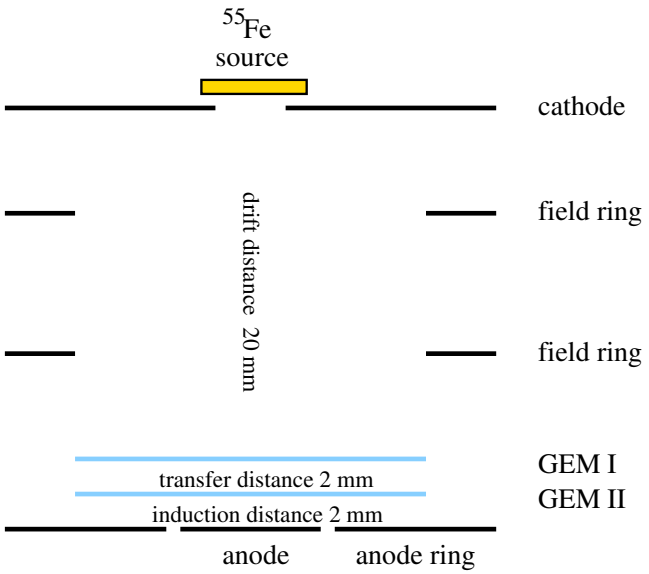

Figure 8.2: Sketch of small TPC prototype assembly, not to scale.

8.2.3 Iron-55 Source

In order to calibrate detectors and obtain information of effective gains, well known radioactive decays with characteristic spectra are used. In the small TPC prototype a ^{55}Fe source is used to generate a charge signal. The instable iron isotope – with a half life time of 2.73 years – captures an electron from its K shell and transforms into stable and excited manganese:

$$^{55}\mathrm{Fe} + \mathrm{e}^- \longrightarrow {}^{55}\mathrm{Mn}. \tag{8.1}$$

The ^{55}Mn is excited since an electron in the K shell is missing. Disexcitation via an electron coming from the L shell is the most probable process with 24.4 % [PDG06]. During this process monoenergetic photons with 5.9 keV are set free. A term scheme of the complete process can be seen in figure 8.3(a).
For the detection of these photons in a TPC, it is important to know the further processes occurring in argon. The three possibilities are listed and explained below. In all cases a photo effect of the 5.9 keV photon with the argon atoms takes place. The electrons on the K shell of argon have a binding energy of 3.2 keV, consequently these electrons obtain a kinetic energy of 2.7 keV, which they loose via ionization in the gas. The resulting gap in the K shell can be filled by two different processes [Kra79]:

1. photo effect with K shell electron: $W_{kin} = 2.7\,\mathrm{keV}$
   Auger effect: $W_{kin} = 3.2\,\mathrm{keV}$
   probability: 80 %
2. photo effect with K shell electron: $W_{kin} = 2.7\,\mathrm{keV}$
   K-L fluorescence: $W_{\gamma} = 2.9\,\mathrm{keV}$

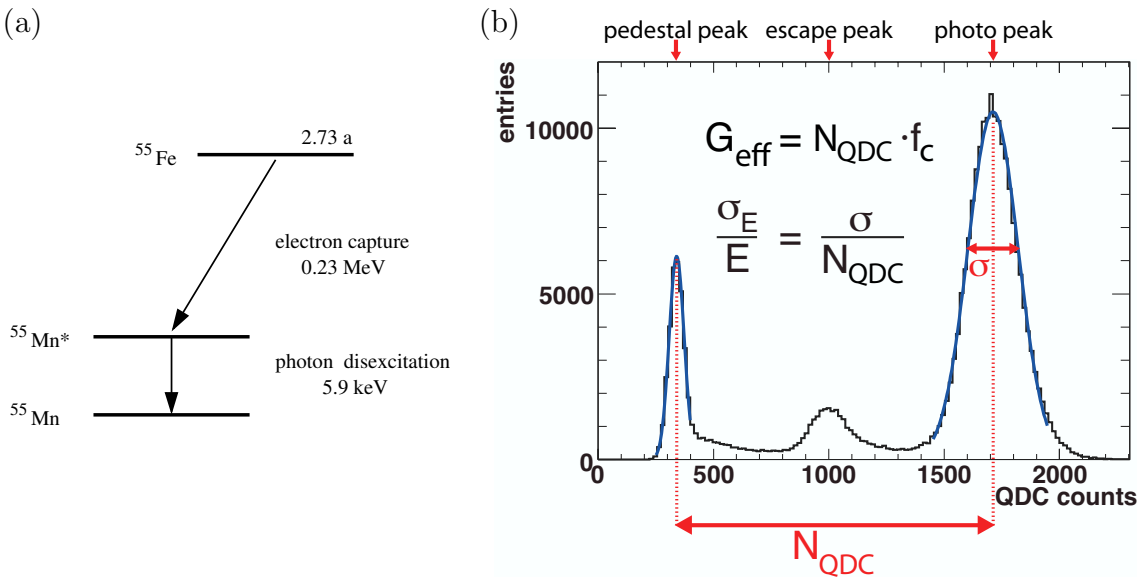

Figure 8.3: (a) Term scheme of ^{55}Fe decay. (b) Spectrum of ^{55}Fe source with pedestal, escape and photo peak. It is obtained with an double CERN GEM setup at 386 V across both GEMs.

Auger effect:	$W_{kin} = 0.3\,keV$
probability:	16 %

A third but unlikely, possibility is a photo effect with an L shell electron, subsequently followed by an Auger effect [Kra79]:

3. photo effect with L shell electron: $W_{kin} = 5.6\,keV$
   Auger effect: $W_{kin} = 0.3\,keV$
   probability: 4 %.

One way to fill the free space in the K or L shell is the Auger effect. It can be explained by an electron from a higher shell falling down to the K or L shell. The energy, which is set free during this process is transferred to an electron of the outer shell. This electron becomes able to leave the atom and to ionize the counting gas. A so-called photo peak develops in case 1 and 3, when the full energy of 5.9 keV is used to ionize the gas. The averaged number of generated electrons per decay is 234, since the mean energy needed to produce an electron-ion pair in argon mixtures – as used in TPCs – is W = 25.2 eV [Che09].
The K-L fluorescence – occurring in case 2 – produces high energetic photons, which have a large absorption length. This results in an undetected escape of theses photons from the detector. Consequently, only the 3 keV of the photo and Auger effect can be measured. The developing peak is called escape peak. It consists of 119 electrons and occurs in 16 % of the events.
In figure 8.3(b) a typical ^{55}Fe spectrum, as measured with the small TPC prototype, is shown. The escape and photo peaks are visible as second and third peak, while the first one is the so-called pedestal peak, which is explained in the next section.

8.3 Effective Gain Measurement

Measurements of the effective gain of a GEM structure can be performed with the help of a calibrated assembly and the knowledge of the primary ionization of a radioactive source. In particular, the amplification factor has to be understood. Other calibration methods with radioactive gases or lasers are possible as well (cf. [Leb02, E$^+$01]), but are not used in this thesis.

8.3.1 Effective Gain Calculation

Starting point for the calculation of the effective gain, observed in the small TPC prototype, are the recorded ^{55}Fe spectra as shown in figure 8.3(b). The position of the photo peak serves as measure for the effective gain. This position has to be corrected for the pedestal, which gives the calibration of the QDC spectrum and defines the zero line. Due to digitization techniques, the zero level of the analog signal is not identical with the zero in the digital scale, which causes a pedestal peak not at the zero position of the spectrum. In order to calibrate the spectra, the pedestal is not cut out via a discriminator threshold. Having the pedestal in each spectrum, allows an individual correction of the data. Therefore, the mean position of the pedestal peak is subtracted from the mean positions of the signal peaks.
The exact positions of pedestal, escape and photo peak are determined by Gaussian fits. One example is shown in figure 8.3(b), the corrected photo peak position is depicted with N_{QDC}. For the calculation of the effective gain, this position is multiplied with a constant factor, described in equation 8.11 and explained in detail in the next sections. To determine an effective gain for one data point, the averaged photo peak position N_{QDC} of a whole measurement series is taken. Such a series contains about ten to twenty measurements with 100,000 to 250,000 events each. This means that for a single measurement point many spectra were taken in order to enlarge the statistics and to reduce the sensitivity to small distortions. The variation of the photo peak position within one measurement series is taken as systematic uncertainty on N_{QDC} in the effective gain calculation. The treatment of other sources of uncertainties is described at the end of this section.
In the following, the determination of the effective gain is described, starting with the calibration of the used preamplifier.

Preamplifier Calibration

For the calibration of the used preamplifier, a well defined amount of charge is injected. A sketch of the charge injector device can be seen in figure 8.4(a). It consists of two capacitors in series with a voltage divider in front of them. In order to reduce the systematic uncertainty arising from the capacitor components, two capacitors with 1 pF each were chosen instead of one with $C = 0.5\,\text{pF}$. Details about the uncertainties can be found at the end of the section. The resistor R_0 is

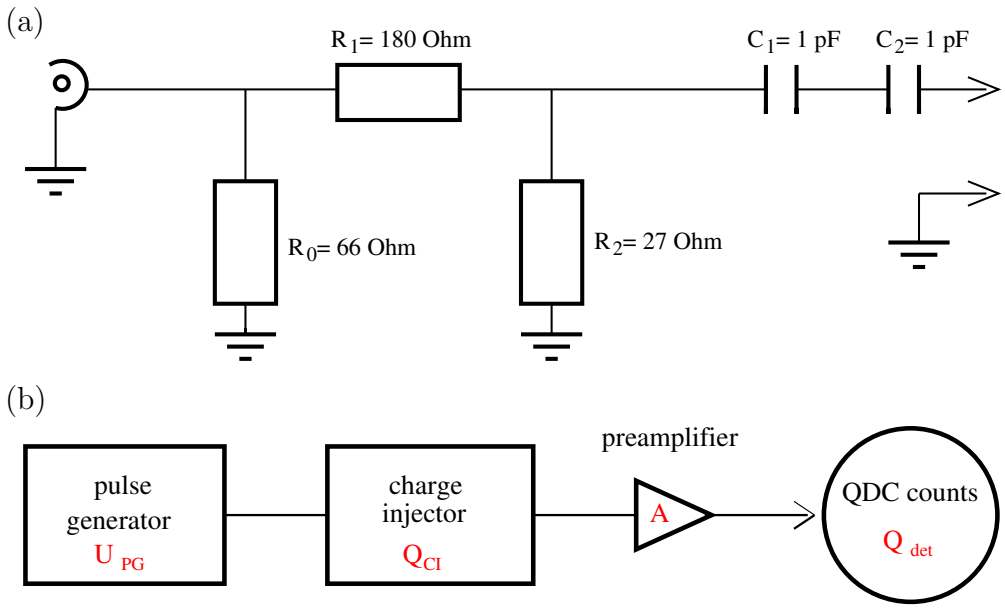

Figure 8.4: Sketch of (a) the charge injector device, and (b) of the charge injector assembly used for the calibration of the preamplifier.

used in order to terminate with the correct resistance. The voltage applied on R_2 is the same as on the parallel connected capacitance, which defines the amount of charge Q_{CI} produced by the charge injector. It can be calculated like:

$$Q_{CI} = U_{PG} \cdot C_{eff}, \tag{8.2}$$

where U_{PG} denotes the total voltage applied by a pulse generator. The effective capacitance C_{eff} is calculable via the voltage divider and the total capacitance C_{all} (0.5 pF):

$$C_{eff} = \frac{R_2}{R_1 + R_2} \cdot C_{all}. \tag{8.3}$$

In figure 8.4(b) a sketch of the whole calibration setup is shown. In order to calibrate the preamplifier, its amplification constant A had to be measured. For this purpose a known amount of charge Q_{CI} was injected into the device and the resulting amplified charge was measured. The charge was produced using a well defined voltage step produced by a pulse generator, which served as input for the charge injector. The charge Q_{det}, detected with the QDC device, can be calculated using the known charge per QDC count for this device:

$$Q_{det} = N_{QDC} \cdot 50\,\mathrm{fC/count}, \tag{8.4}$$

where N_{QDC} depicts the pedestal corrected peak position in QDC counts. Finally, the amplification constant A can be determined as:

$$A = \frac{Q_{det}}{Q_{CI}} = \frac{N_{QDC} \cdot 50\,\mathrm{fC/count}}{U_{PG} \cdot C_{eff}} = a \cdot \frac{50\,\mathrm{fC/count}}{C_{eff}}. \tag{8.5}$$

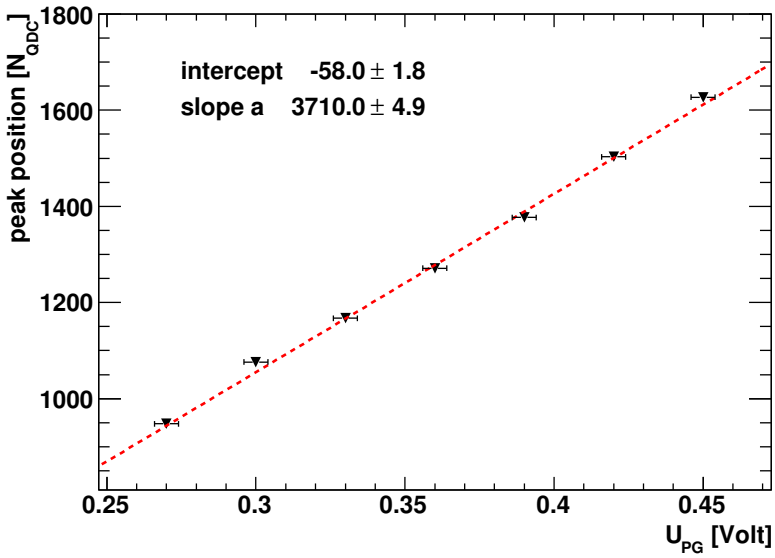

Figure 8.5: Calibration of preamplifier. Peak positions are shown as function of the pulse generator voltage.

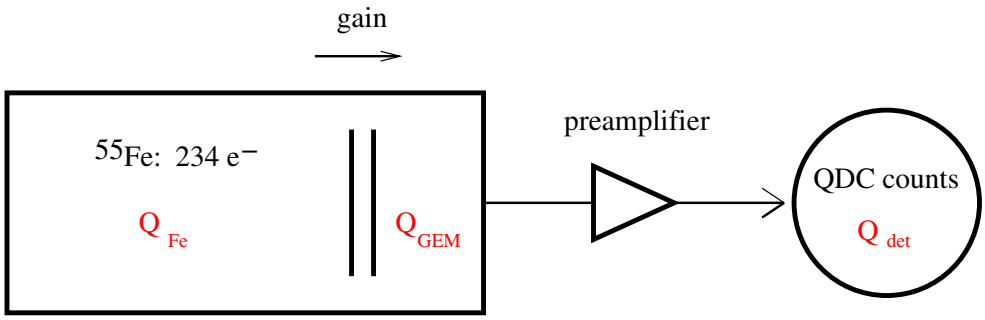

Figure 8.6: Illustration of the gain measurement assembly with the small TPC prototype.

Here $a = \mathrm{N_{QDC}}/\mathrm{U_{PG}}$, denotes the slope of the calibration curve. It is determined by a straight line fit to the measurement points shown in figure 8.5.

Gain Calculation

Figure 8.6 shows an illustration of the setup for the measurement of effective gains with a TPC prototype. A definition of the effective gain $\mathrm{G_{eff}}$ can be written as:

$$\mathrm{Q_{Fe}} \cdot \mathrm{G_{eff}} = \mathrm{Q_{GEM}} \Leftrightarrow \mathrm{G_{eff}} = \frac{\mathrm{Q_{GEM}}}{\mathrm{Q_{Fe}}}, \tag{8.6}$$

where $\mathrm{Q_{Fe}}$ describes the charge deposited by a ^{55}Fe source. Since ^{55}Fe produces on average 234 electrons in argon [Che09], it can be calculated to be $234 \cdot \mathrm{e} = 0.037\,\mathrm{fC}$.

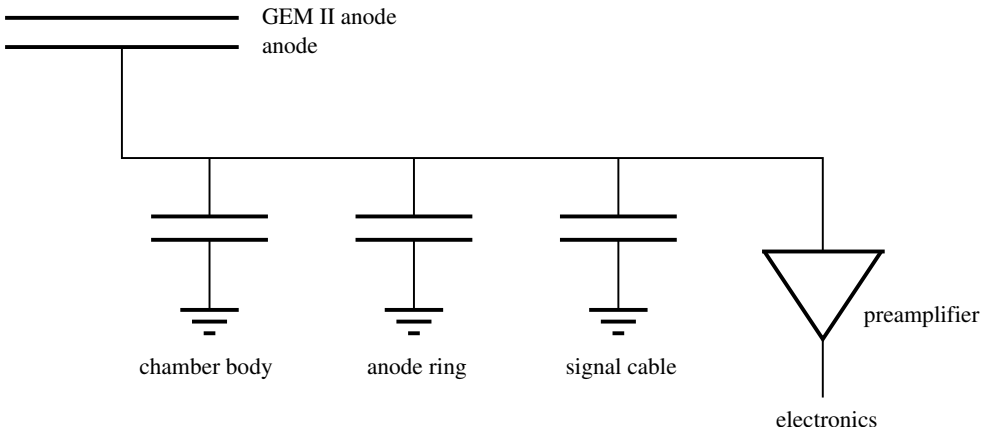

Figure 8.7: Equivalent circuit diagram for the charge propagation in the gain measurement setup. The capacities of chamber body and anode ring were simulated, the signal cable capacitance was measured and the impedance of the preamplifier is given in [Yar84].

Q_{GEM} denotes the charge after amplification by the GEMs.
During the year 2008, measurements with very small effective gains were observed. The reason for this result was a double sided copper anode, which formed a parallel plate capacitor. Hence, most of the produced charge was stored inside the chamber, instead of being amplified. As a consequence the anode was exchanged by one with only one copper clad surface. The captaincies between the anode and the other components of the assembly were simulated using a program for simulation of electrostatic problems, which makes use of finite element methods (CST-EM STUDIO [CST10]). In the simulated setup the aluminum body of the chamber itself, the anode and its ring, the cable from the chamber to the preamplifier and the preamplifier itself were considered to calculate a capacitance matrix, an equivalent circuit diagram of the setup is shown in figure 8.7. The matrix was used to extract the efficiency of the charge collection to the preamplifier as described in the following. The simulated capacitance values C were transformed to impedance values Z via:

$$Z = \frac{1}{2\pi\nu C}, \tag{8.7}$$

where the frequency ν was determined from the ^{55}Fe signal rise time to be $\nu = 40\,\mathrm{MHz}$. The capacitance of the signal cable was measured and the impedance of the preamplifier is $100\,\Omega$ [Yar84]. The ratio of the total impedance compared to the impedance of the single components gives the amount of charge, which is stored in the single parts of the setup. All values are summarized in table 8.2. The efficiency of the charge readout ϵ_C is therefore defined as:

$$\epsilon_C = \frac{Q_{preamp}}{Q_{GEM}} = 0.319. \tag{8.8}$$

Systematic uncertainties for this value are taken into account as described in the next section.

component	capacitance C [pF]	impedance Z [Ω]	impedance ratio $Z_{total}/Z_{component}$	charge collection efficiency [%]
chamber body	0.2	19409.1	1.1	0.2
anode ring	4.6	865.0	23.6	3.7
signal cable	80.0	49.7	410.6	64.2
preamplifier	—	100.0	204.2	31.9

Table 8.2: Capacitance, impedance and charge collection efficiency of the components of the gain measurement setup.

The detected charge Q_{det} (cf. figure 8.6), which is collected with the QDC, is related to the charge reaching the preamplifier Q_{preamp} via the amplification factor A, which describes the strength of the amplification:

$$Q_{det} = Q_{preamp} \cdot A. \tag{8.9}$$

Using equations 8.8 and 8.9, the effective gain can be reformulated as:

$$G_{eff} = \frac{Q_{det}}{A \cdot \epsilon_C \cdot Q_{Fe}}. \tag{8.10}$$

With the help of equations 8.4 and 8.5, describing Q_{det} and A, this can be transformed to:

$$G_{eff} = N_{QDC} \cdot \frac{C_{eff}}{a \cdot \epsilon_C \cdot Q_{Fe}}, \tag{8.11}$$

where N_{QDC} is the measurable quantity determined from the ^{55}Fe spectra, while the second term is constant and can be calculated from the preamplifier calibration.

Uncertainty Treatment

Associated uncertainties of all quantities in equation 8.11 are discussed in this section. The statistical uncertainty of the photo peak position N_{QDC} is given by the precision of the mean value of the fitted Gauß curve. This uncertainty is below one per mill for each measurement and is therefore neglected in the following.
More important are the sources of systematic uncertainties, which are summarized in table 8.3 and are described in detail in the following according to their occurrence in formula 8.11.

- The systematic uncertainty originating from the position N_{QDC} of the photo peak for one measurement point is determined from the data set at this specific GEM voltage. N_{QDC} is calculated as arithmetic mean of the corrected photo peak positions. The variation of the photo peak position in the single spectra in comparison to the averaged position is taken as systematic uncertainty. $\sigma_{N_{QDC}}$ is found to be up to 4 %.

variable	value and systematic uncertainty	systematic uncertainty in %	convoluted uncertainty sources
N_{QDC}	$700 \ldots 2500$	up to 4.1 %	
C_{eff}	$65.2\,\mathrm{fF} \pm 11.5\,\mathrm{fF}$	17.7 %	C_{all}, $\frac{R_2}{R_1+R_2}$
a	3710.0 ± 4.9	0.1 %	
ϵ_C	0.319 ± 0.067	21.1 %	C, ν, Z
Q_{Fe}	$234 \cdot e \pm 7 \cdot e$	3.0 %	n_e

Table 8.3: Systematic uncertainties for the effective gain. Each quantity is listed with quantitative uncertainty and comprised sources of uncertainties.

- The effective capacitance of the charge injector is needed for the preamplifier calibration. For the uncertainty determination of C_{eff}, the tolerances of the resistors and foremost the capacitors are used. The capacities have a tolerance of 25 % each, which is the reason to use two in series. This configuration allows to reduce the uncertainty on the combined capacity C_{all} to 17.68 %. Since the tolerances on the resistors are negligable in comparison, the Gaussian error propagation yields $\sigma_{C_{eff}} = 17.7\,\%$.

- The slope a of the preamplifier calibration curve is also needed for the effective gain calculation. σ_a is obtained from a linear fit to the calibration curve shown in figure 8.5. With an uncertainty of about one per mill, a is a negligible source of uncertainty.

- The dominant systematic uncertainty arises from the charge collection efficiency ϵ_C, which is taken from simulation studies. The capacitances from anode to chamber body and the anode ring, mentioned in table 8.2, are assumed with an relative uncertainty of 9 %, estimated from the discrepancy between analytical calculations of parallel plate capacitors and simulation results of these values. For the capacity of the signal cable, several measurements were performed and the resulting variation of 7.5 % is assigned as systematic uncertainty. The impedance of the preamplifier is known with an accuracy of 6 % [Yar84]. The uncertainty on the frequency ν is estimated from the ^{55}Fe signal shape – as observed on the oscilloscope in various measurements – to be 10 %. Using error propagation, σ_{ϵ_C} sums up to 21.1 %.

- The charge deposited by the ^{55}Fe source depends on the number of electrons produced by the 5.9 keV photon. In argon this number n_e corresponds to 234 electron-ion pairs per photon. The uncertainty on n_e can be described using the Fano factor F:

$$\sigma_{n_e} = \sqrt{F \cdot n_e}. \tag{8.12}$$

  In [Che09] the Fano factor was measured – with the help of MicroMEGAS – to be $F = 0.21 \pm 0.06$. The electrons of the escape peak in ^{55}Fe spectra were

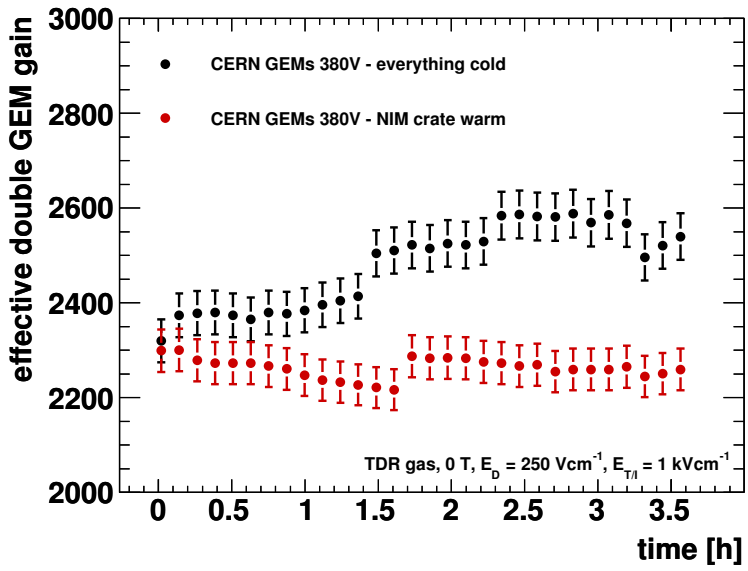

Figure 8.8: Effective gain development as a function of time after switching on the electronics. Only uncorrelated uncertainties are shown here.

counted on a pixel readout device in an argon-isobutane (95 % – 5 %) mixture. This mixture is similar to TDR gas, which is used for the measurements discussed here. The measured Fano factor translates into an uncertainty on the number of produced electrons of 3.0 %, which corresponds to a charge of 234 ± 7 electrons.

The fraction in equation 8.11 has large uncertainties. Most of them are correlated since they affect each measurement point in the same way leading to an uncertainty of the absolute normalization. The variation of the effective gain measurements in figure 8.9 is very small compared to the size of the errors. This shows that the whole setup is not suitable for high precision measurements of absolute values but allows reliable comparative measurements of effective gains.
The resulting uncertainties on the effective gain are calculated individually for each measurement point in the following diagrams. For this purpose, the averaged photo peak positions N_{QDC} and the variations in the corresponding data sets $\sigma_{N_{QDC}}$ are needed.

8.3.2 Time Dependence of Effective Gain Measurements

The characteristics of the electronics in this assembly change with time after switching on due to warming of the components. To investigate this effect, two measurement series using a double GEM stack with standard GEMs were performed as depicted in figure 8.8. The chosen voltages across both GEMs were 380 V. The assembly contains the QDC, the power supply for the preamplifier and a NIM crate, which contains the gate production via a discriminator. In one case, all parts were

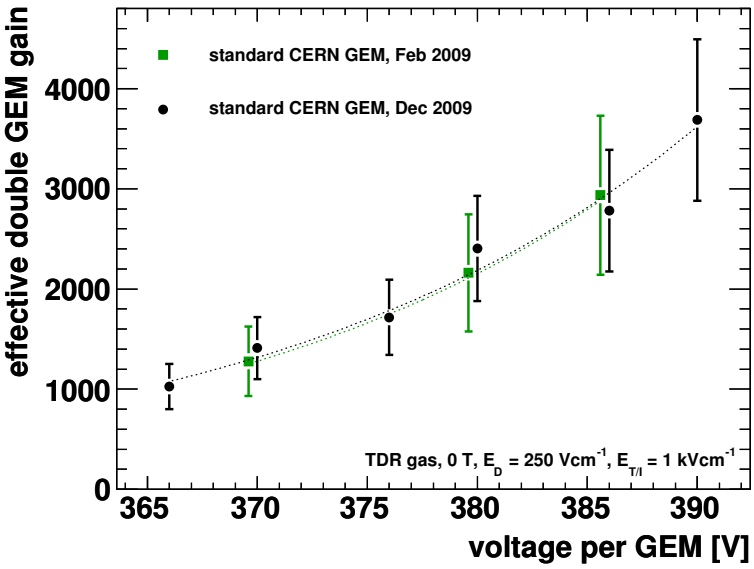

Figure 8.9: Effective gain of standard CERN GEMs as a function of GEM voltages. Two measurements with identical setup performed within a year are shown. The error bars denote the systematic uncertainties, voltages are plotted with a slight shift for better visibility. The dotted lines denote exponential fits to the data points.

switched on immediately before the measurement. The result shows a significant increase of the effective gain with time, even some steps are visible. In figure 8.8 only the uncorrelated uncertainties – estimated to be 1.95 % at this voltage – are shown. The steps can be explained within the error bands, but most likely the reason for these jumps has to do with the discriminator. Hence, a second measurement was performed with an already warm discriminator and then all steps vanish but one. Although in the second data series a decrease of the effective gain is notable, the effective gain measured with a warm discriminator is much more stable compared to the first measurement.
To avoid such effects of the electronics in the data, all parts of the assembly were kept switched on between all measurements taken in December 2009. This includes not only the NIM crate, but also the power supply for the preamplifier, the preamplifier itself and the QDC device. Otherwise, an additional systematic uncertainty would have been necessary in order to account for these effects.

8.3.3 Effective Gain Results

In figure 8.9, effective gains for two measurements with identical setups with CERN GEMs are compared, only systematic uncertainties are shown. The data sets were recorded using a double GEM stack consisting of two standard GEMs. The measurements were performed at the beginning and end of the year 2009. In between, the whole setup was disassembled and rebuilt and one of the GEMs was needed to be replaced. The results show almost perfect agreement and prove the reproducibility

of the effective gain measurements. Effective gains of 1000 to roughly 3500 can be achieved with the field settings mentioned in section 8.2.1. Since the effective gain is exponentially increasing with the GEM voltages, an exponential function is fitted to the data points in this and all following figures.

8.3.4 Comparison with Gain Parametrization

In order to obtain a handle for the quality of the determined effective gain results, a comparison of the measured values to an existing parametrization – described in the following – is performed.
To describe the charge transfer coefficients of GEM foils, electrostatic calculations were used to parametrize collection efficiency, single GEM amplification and extraction efficiency [Sob02]. Extensions of the model, necessary to match the experimental data, are introduced in [Lot06]. In this study, current measurements in a triple GEM TPC prototype were performed and analyzed in order to adjust the parametrization of the effective gain.
As input for this parametrization serve $2 \cdot N_{GEM} + 1$ parameters. The voltages across each GEM and the electrical field strengths for drift, transfer and induction fields. In addition, a collection of parameters for the gas and the magnetic field is required. In order to apply the parametrization to the data presented here, the effective gain – provided only for a triple GEM setup – was adapted to a double GEM assembly. This is possible, since the effective gain of a GEM stack factorizes in a product of effective single GEM gains. In consequence, the product over three GEMs – as shown in equation 5.11 on page 43 – was reduced to a product of two GEMs.
The comparison of measured values and parametrization in [Lot06] works well for the electron collection and extraction efficiencies, especially for the field ratios used in the small TPC prototype in this thesis. In figure 8.10, the single GEM gain at a magnetic field strength of 4 T is shown. The overall agreement between the experimental data and the parametrization is good, showing deviations only for GEM voltages below 200 V and voltages above 350 V. 385 V per GEM is the highest value used for the parametrization, while the comparative GEM studies presented here, were performed at GEM voltages between 340 V and 426 V. The validity of the parametrization in the region above 370 V is not proven, but a qualitative comparison is possible.
In figure 8.11(a), the parametrization describes the shape of the measured gain curves quite well. However, the mean value is too high in normalization by almost a factor two. For the uncertainty of the parametrization "a few ten percent" are mentioned in [Lot06]. With an assumed uncertainty of 30 % for the parametrization [Lot10], the error bands overlap. Part of the difference in normalization arises from different laboratory temperatures during the measurements. The parametrization in [Lot06] was taken at temperatures of $T = 25° \pm 3°$ and an atmospheric pressure of $p = 1023\,\text{hPa}$, while the compared measurements from December 2009 presented in this thesis are recorded at $T = 19° \pm 3°$ and $p = 1021\,\text{hPa} \pm 3\,\text{hPa}$. In [Kam05],

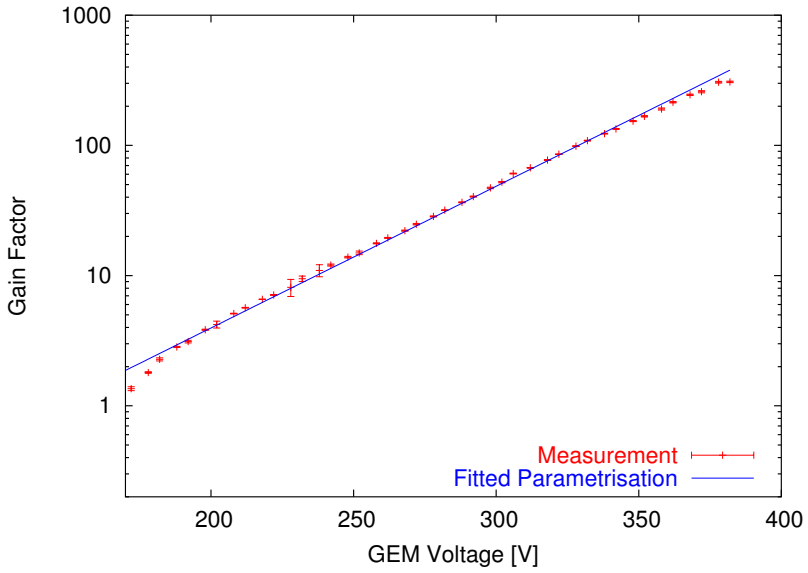

Figure 8.10: Single GEM amplification at 4 Tesla as a function of GEM voltages compared to the parametrization. Error bars are enlarged by a factor five [Lot06].

the correlation between effective gain and temperature is given with:

$$G_{\text{eff}} \sim e^{b \cdot \frac{T}{p}} \tag{8.13}$$

where the constant b is determined by a fit to measured data to be 47.6 mbar/K [Kam05]. Using the values above, yields a scaling factor of 0.77 for the parametrization, which is not able to describe the complete deviations, but changes the picture as it can be seen in figure 8.11(b).
From the comparison of measured effective gain values and parametrization, the conclusion can be drawn that the used setup produces – abandoning the normalization uncertainty – sensible values.

8.3.5 Comparability of Measurements from 2008 and 2009

Measurements performed in summer 2008 [Bec08], show a systematic shift to higher effective gain values. Data sets from 2008 and 2009 are compared in figure 8.12. The data points from 2008 show significant higher effective gains.
During the reassembly in February 2009 it turned out that the anode surface, which was used in [Bec08], was bent towards the lowest GEM surface. This anode consists of a plastic plate with a copper clad PCB glued on top, which serves as sensitive area. The bending was of the order of 1 mm, but no detailed quantification was performed. Assuming a bending of one millimeter, this reduces the induction distance by a factor two, from 2 to 1 millimeter. The induction field is applied through the resistor chain and was not adapted, which means the field would be twice as large as assumed in [Bec08].

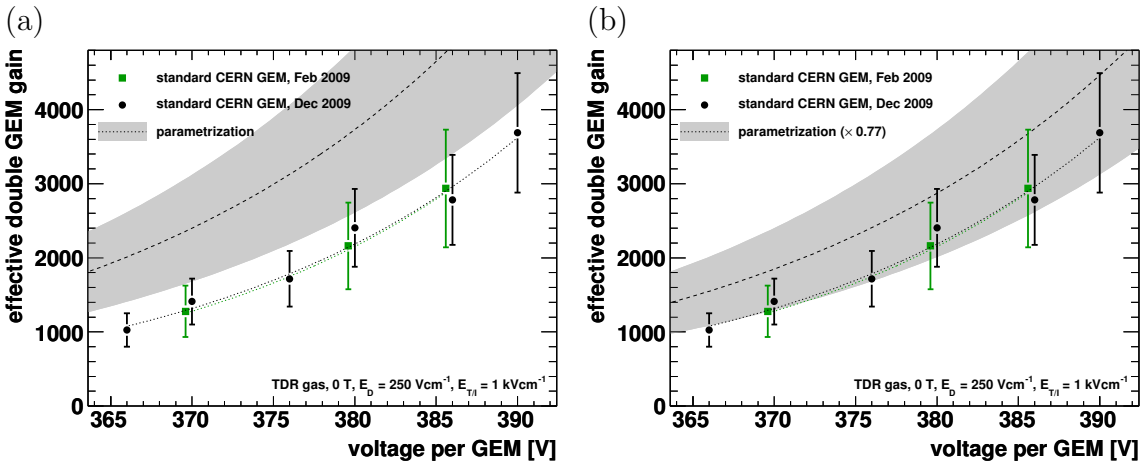

Figure 8.11: Effective gain of standard CERN GEMs and its parametrization as functions of GEM voltages. The dotted lines depict exponential fits to the effective gain values. In figure (b) the parametrization is scaled to account for temperature differences.

In order to support the above mentioned assumption, a measurement set with reduced induction distance and a flat anode was performed in December 2009. The induction distance was reduced to 1.5 mm – due to mechanical reasons the reduction to 1 mm was not possible – and the results are also shown in figure 8.12. It turns out, that due to the corresponding induction field of 1.33 kV/cm, the measured effective gain is shifted towards the measurements with the bent anode. However, the difference between the data of 2008 and 2009 is even larger and the anode needs to have been bent by more than 0.5 mm. The measurement results support the assumption of a deflection of 1 mm. These results are endorsed by calculations with the parametrization of the effective gain. An increase of the field by about a factor 2.2 yields effective gains with differences as observed between 2008 and 2009 data. Translated into the induction distance, the gap between last GEM surface and anode was reduced to 0.9 mm instead of 2 mm.
Due to this problem, all following comparisons of effective gains of different GEM types are just given with relative gain values. An interpretation of absolute values of the determined effective gains is not possible for the 2008 measurements.

8.4 Comparison of Effective Gains

A comparison of effective gains of all available GEMs – listed in table 8.1 – is shown in figure 8.13. The achievable effective gains differ for the various GEM types. All GEM foils differ in at least one geometrical parameter. In order to gain more information for the interpretation of the results, an electrostatic simulation of the field configurations inside the GEM holes was performed and is described in the following. Afterwards the effective gains of the different GEM foils are compared and discussed in detail.

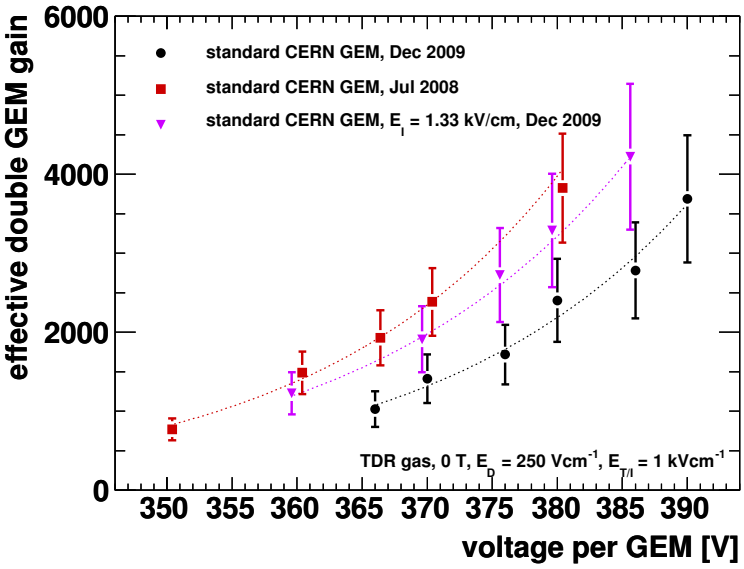

Figure 8.12: Effective gain of CERN GEMs as a function of GEM voltages, compared to a data set of 2008 and a measurement with reduced induction distance and higher induction field. Exponential fits to the data points are shown as well.

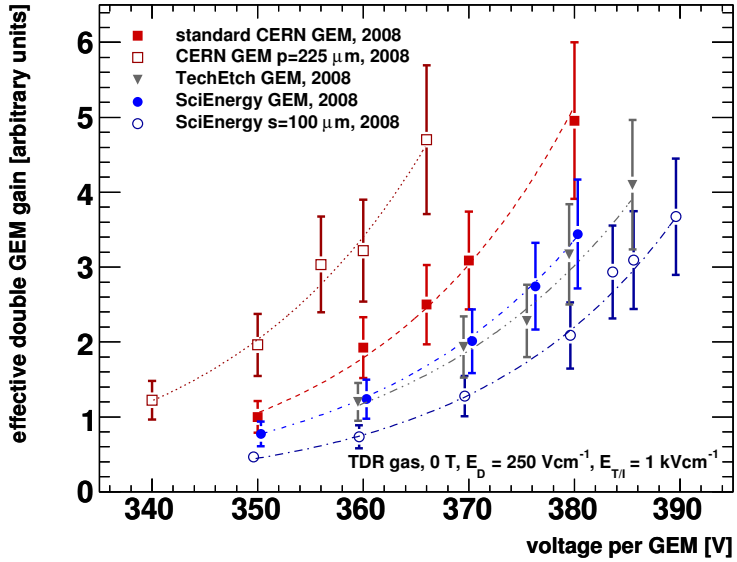

Figure 8.13: Comparison of effective gains of different GEM types. The gain is given in arbitrary units and exponential functions are fitted to the data. In the legend the geometrical parameters, which are differing from the standard values, are mentioned. The pitch is described by p, while s depicts the substrate thickness.

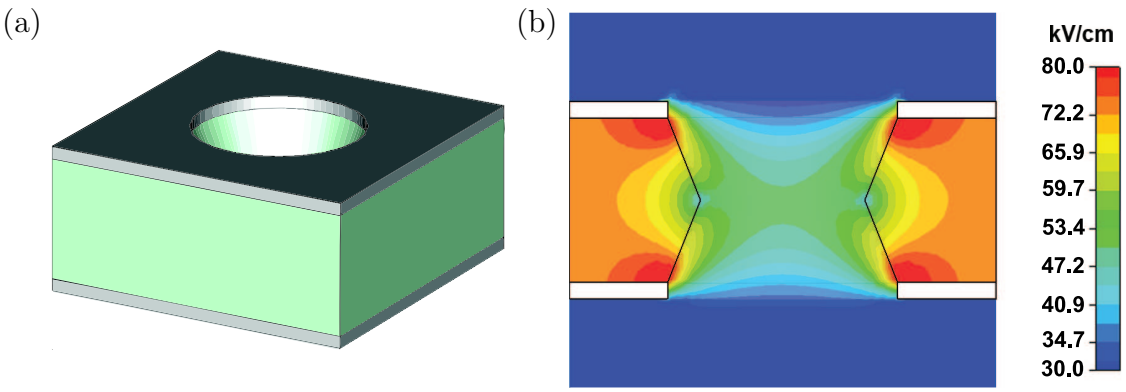

Figure 8.14: Model for simulation of electrical field inside GEM holes. (a) The geometry of the hole model – cathode and anode are not visible. (b) Resulting field strengths, cut through the hole. The field in the central part of the hole agrees with the analytically calculated field strength of 53.7 kV/cm.

8.4.1 Simulation of GEM Hole Fields

To model the electrical fields inside a single GEM hole, CST-EM STUDIO [CST10] was used. This field defines the GEM gain, which has to be multiplied with collection and extraction efficiency to determine the effective gain of a GEM foil.
A block around one hole with a cathode above and an anode below the hole (cf. figure 8.14) was modeled. The voltage applied across the GEM is in all models 370 V. The potentials were applied such that the GEM hole experience a field of 2.5 kV/cm into cathode and 10 kV/cm into anode direction. The geometrical parameters and the material were chosen according to the specific GEM, which was simulated. The boundary conditions are adjusted such that the anode and cathode limit the fields in z direction, while no normal components of the field are allowed in the xy plane. This allows the reduction of the model to one single hole. Cuts through the GEM hole are defined for the analysis of the results. In figure 8.15, these cuts are illustrated. In figures 8.16 and 8.17, the results of the finite element method simulations of electrical fields inside GEM holes are shown. The lines in the diagrams follow the cuts through the GEM holes, whereas the solid black lines always go through the center of the hole and the dotted blue ones through the outer edge.
The interpretation of these plots is explained exemplary for figure 8.16(a) – a standard CERN GEM hole. To cross check the simulation the averaged field strength in the hole can be calculated analytically with equation 5.4 on page 40. Using the parameters for standard CERN GEMs, a field of $E_{hole} = 53.7\,kV/cm$ is obtained. The validity of the simulation can be confirmed by the resulting fields of about 50 kV/cm in the center and 60 kV/cm on the edge of the hole (cf. figure 8.14(b) and figure 8.16(a)). The asymmetric shape of the field far outside the holes ($z < -100\,\mu m$ and $z > 100\,\mu m$) can be explained by the fields applied above and below the GEM. In the region of $z > 0$ a drift field of 2.5 kV/cm is applied, while the transfer field below the GEM is 10 kV/cm.

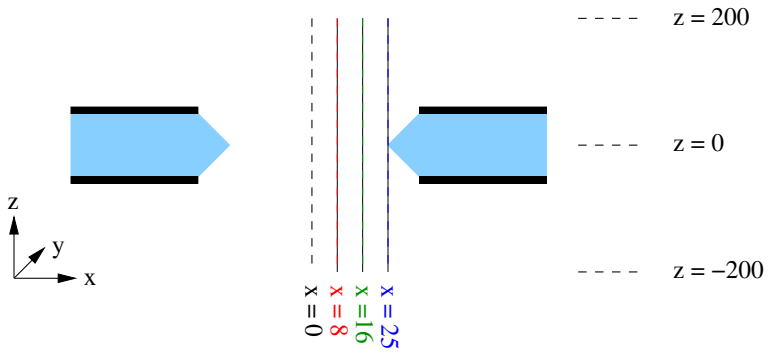

Figure 8.15: Cuts through GEM hole for field simulation. The given coordinates in micrometers correspond to a standard CERN GEM with an inner hole diameter of 50 µm. Sketch not to scale.

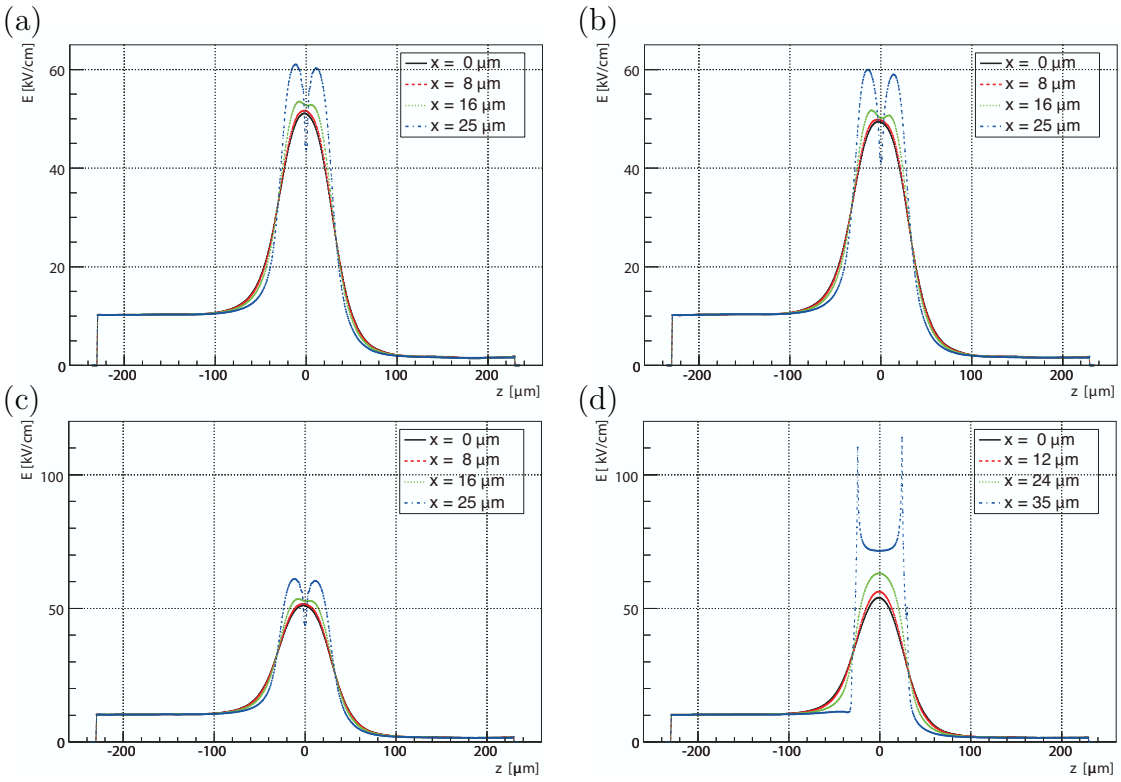

Figure 8.16: Simulated electric fields inside the holes of different GEM types. The applied GEM voltage is 370 V and the geometrical parameters can be found in table 8.1. (a) Standard CERN GEM, outer hole diameter 70 µm and (b) Tech-Etch GEM, outer hole diameter 87 µm. (c) equals (a) but is shown on another scale for comparison of standard CERN GEMs (double conical holes) with (d) GEMs with cylindrical holes.

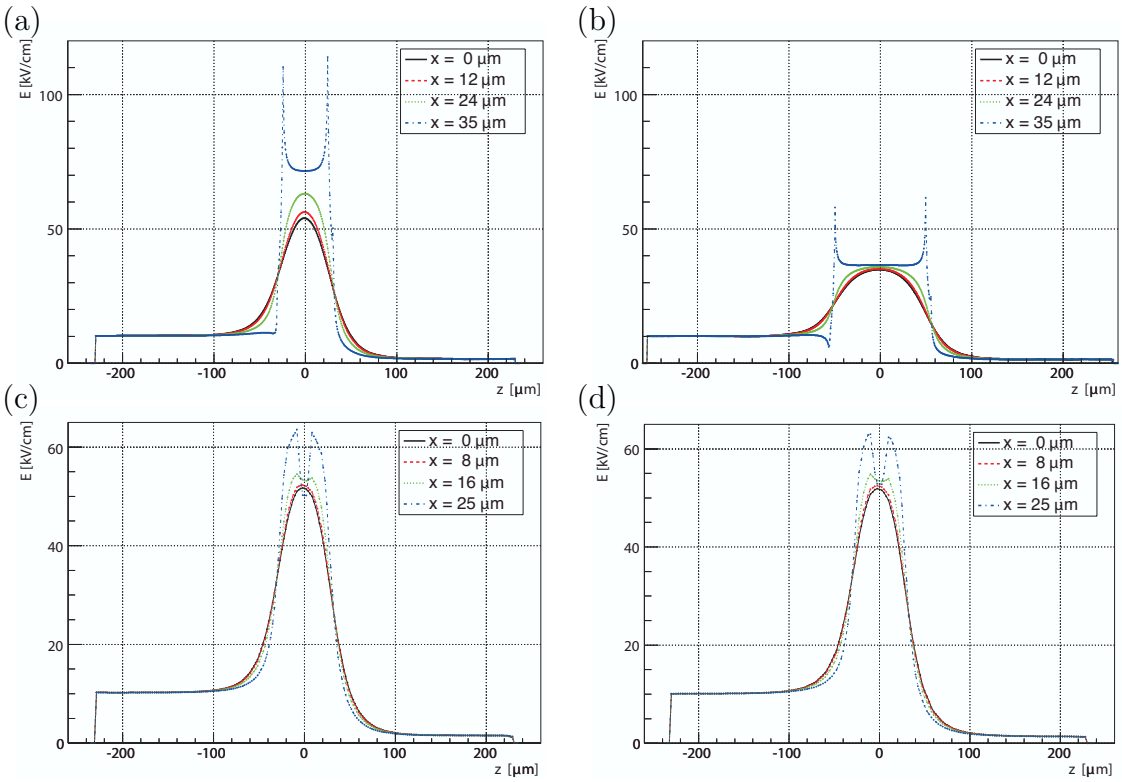

Figure 8.17: Simulated electric fields inside the holes of different GEM types. The applied GEM voltage is 370 V and the geometrical parameters can be found in table 8.1. (a) GEM with 50 µm substrate, (b) GEM with 100 µm substrate, (c) simulation of an array with nine holes, standard CERN GEM, pitch 140 µm and (d) simulation of an array with nine holes, standard CERN GEM with pitch 225 µm.

The peculiar shape of the curves on the hole edge (dotted blue lines) was already observed in [B+99]. At the metal-insulator interface the field shows a steep increase – also visible in figure 8.14(b) – which causes spikes in the field curves.

8.4.2 Interpretation of Effective Gain Results

The effective gains of all GEM types are compared pairwise in order to investigate the influence of the different geometrical parameters on the amplification behavior. In order to make the differences better visible and give the possibility to quantify the effects, the exponential curves fitted to the measurement data in figure 8.13 are extracted and normalized to the curve for the standard CERN GEM. The result is shown in figure 8.18.

Influence of Optical Transparency

The standard CERN GEM and the Tech-Etch GEM are produced in a similar way and most of the parameters are identical. Only the hole diameter in the copper

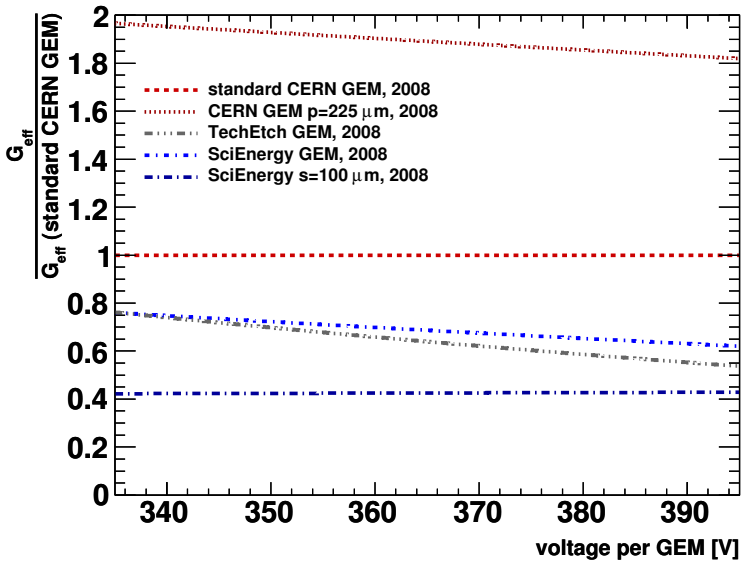

Figure 8.18: Comparison of effective gains of different GEM types relative to standard CERN GEM. The fit functions obtained from figure 8.13 are normalized to the fit of the standard CERN GEM. In the legend geometrical parameters, which are differing from the standard values, are mentioned. The pitch is described by p, while s depicts the substrate thickness.

coating is different, 70 µm for the standard CERN GEM compared to 87 µm for the Tech-Etch GEM. Hence, the optical transparency is different (see formula 5.1 on page 38). Since the extraction efficiency is directly proportional to $1/\tau_{opt}$, the extraction efficiency of the Tech-Etch GEM is lower by 34 % with respect to the CERN GEMs. Collection efficency and single GEM gain should be the same for both GEM types. In figure 8.16(a) and (b) the simulation results for the electric fields of these GEMs are shown, indicating that both fields – and by this the single GEM gains – are almost identical, only a small decrease caused by the slighlty larger outer hole diameter of the Tech-Etch GEM is visible. Due to the difference in the extraction efficiency, the effective gain of the Tech-Etch GEM should be at 66 % of the standard CERN GEM, as confirmed in figure 8.13 and in figure 8.18.
In addition, a measurement with a CERN GEM with enlarged pitch was performed. The resulting effective gain is higher than for the standard GEMs. Again, this fact can be explained by the optical transparency. A higher pitch yields a smaller τ_{opt} and therefore a higher extraction efficiency. To obtain an estimate about the single gain, an array of nine holes on two GEM surfaces with different pitches were modeled and the results are shown in figures 8.17(c) and (d). Since the hole fields depicted in these figures and therefore the single GEM gains stay at the same level and are not influenced by the pitch, the effective gain of the 225 µm pitch GEM should be due to the different optical transparencies 2.5 times larger than the standard CERN GEM effective gain. In figure 8.18 an averaged factor of about 1.9 is readable, which is only 76 % of the expected value.

The reason for this deviation is not clear, since the collection efficiency for both GEM types should be close to 100 % due to the applied field ratio (cf. figure 5.5 on page 43). The hole field and with it the single GEM gain of the GEM with enlarged pitch is also not changed compared to the standard CERN GEM. Hence, only a different extraction efficency remains as possible explanation. Besides the above mentioned considerations, it can vary due to impreciseness in the production process causing varying pitches or hole diameters of this specific GEM. These variations of the optical transparancey could yield a smaller effective gain.

Influence of Hole Shape and Substrate Material

In the comparison of the standard CERN GEM and the SciEnergy GEM with a substrate thickness of 50 µm, hole shape, material of the substrate and manufacturing technique play a role. For a GEM with cylindrical hole shape, the parameters in equation 5.4 on page 40 are different compared to foils with double conical holes. In [Sob02] they are given for cylindrical holes with a =169.27 cm^{-1} and b = 0.055. The resulting hole fields of $\mathrm{E_{hole,dcon}} = 52.2\,\mathrm{kV/cm}$ and $\mathrm{E_{hole,cyl}} = 61.6\,\mathrm{kV/cm}$ and the ratio $\frac{\mathrm{E_{SciE}}}{\mathrm{E_{CERN}}} = 1.18$ match with the simulated hole fields in figures 8.16(c) and (d). There, a standard CERN GEM with double conical holes is compared to one with cylindrical holes. The simulated substrate material is the same as for the standard CERN GEM. Therefore, the effect of the cylindrical holes is directly readable from the figures. In the center of the hole the field strength is almost identical, whereas for the cylindrical holes the gradient to the hole edge is much steeper. The averaged effective gain should be higher, which cannot be confirmed by the experimental data depicted in figures 8.13 and 8.18. The conclusion can be drawn, that the insulator material and potentially the manufacturing process have an influence on the effective gain as well.
Another explanation might be the hole diameter, which is for the measured holes rather 75 µm than the specified 70 µm (cf. figure 8.1(c) and (d)), yielding a higher optical transparency of the SciEnergy GEM. However, only two holes were measured and the effect would explain only a decrease in gain of about 12 %. Taking this effect and the hole shape into account the ratio of the effective gain of SciEnergy GEM to CERN GEM is expected to be $\mathrm{G_{SciE,thin}}/\mathrm{G_{CERN}} = 1.05$.

Influence of Substrate Thickness

From the SciEnergy company two GEMs with different substrate thickness were available. A simple method to estimate the differences is to compare the fields developing in the holes, assuming parallel plate capacitors. With E = U/d and the parameters for the SciEnergy GEMs, a field ratio of $\mathrm{E_{thick}}/\mathrm{E_{thin}} = 0.55$ is obtained. This ratio is confirmed by simulation results for the thin and the thick SciEnergy GEMs, with a distance of 24 µm to the hole center (cf. green lines in figure 8.17(a) and (b)). In the more central part of the hole, the field ratio for these GEMs is smaller and it is larger on the outer edge. The experimental data shown in

GEM type	considered factors	$G_{eff,exp}$ (norm. to CERN)	$\langle G_{eff} \rangle$	ΔG_{eff} [%]	$G_{eff,exp}$ (norm. to SciE.)	$\langle G_{eff} \rangle$	ΔG_{eff} [%]
CERN	–	1.00	1.00	–	–	–	–
CERN, p=225µm	τ_{opt}	2.59	1.89	27	–	–	–
Tech-Etch	τ_{opt}	0.66	0.64	3	–	–	–
SciEnergy	τ_{opt}, shape	1.05	0.69	34	1.0	1.0	–
SciEnergy, s=100µm	τ_{opt}, shape, s	0.57	0.43	25	0.55	0.62	13

Table 8.4: Comparison of normalized expected and measured effective gains for different GEM types. Given are the geometrical values, considered for the expected gain, the expected effective gain $G_{eff,exp}$, the mean value for the measured gain $\langle G_{eff} \rangle$ as obtained from the fitted exponential functions and the deviation of the measured from the expected values ΔG_{eff}. For the influence of the substrate thickness s, a second normalization to the thin SciEnergy GEM is presented in addition.

figure 8.18 can be quantified with an average ratio of 0.62, which is in reasonable agreement with the expectations. For the comparison with the standard CERN GEM, an expected ratio of $G_{SciE,thick}/G_{CERN} = 0.57$ can be calculated, considering the hole shape, thickness and slightly different optical transparency. The observed ratio is given with 0.43.

Summary of Effective Gain Results

The measured effective gains are interpreted by means of geometrical parameters of the GEM foils. The results are summarized in table 8.4. All five GEM types are presented with the parameters – optical transparency, hole shape and substrate thickness – which were used to interpret the specific measurement result. In order to allow an overview, the measured effective gains are normalized to the effective gain of the standard CERN GEM. For this purpose, the exponential functions fitted to the effective gain curves from figures 8.13 and 8.18 are averaged over the whole GEM voltage range and are depicted with $\langle G_{eff} \rangle$. The expected effective gain values $G_{eff,exp}$ are calculated as described in the previous sections.
The result for the Tech-Etch GEM can be fully explained by the optical transparency. The effect of the substrate thickness of the SciEnergy GEMs is well understood with an deviation of only 13 %. More difficult is the influence of the used substrate material, illustrated by only 66 % accordance to the standard CERN GEM. Also the results of the CERN GEM with large pitch deviate by 27 %. But overall it has to be stated, that the approach of explaining the behavior of effective GEM gains with geometrical parameters works quite well. Remaining differences may arise from variations in the production precision of the particular analyzed GEMs or in the case of the SciEnergy GEMs in effects caused by the LCP substrate.

8.5 Energy Resolution

The energy resolution is a measure which is of particular importance in a high energy physics detector. In a TPC the energy resolution is interesting for dE/dx measurements, since it quantifies the precision of dE, while the dx measurement is depending on track properties. There, mainly curvature and angle of the track to readout pad is important. As already mentioned, the Fano factor describes the uncertainty on the number of electron-ion pairs produced through ionization. Hence, the energy resolution cannot be better than:

$$\frac{\sigma_{\mathrm{E}}}{\mathrm{E}} = \frac{\sigma_{\mathrm{n_e}}}{\mathrm{n_e}} = \frac{\sqrt{\mathrm{F} \cdot \mathrm{n_e}}}{\mathrm{n_e}}. \tag{8.14}$$

Since a ^{55}Fe source produces 234 electrons in argon, the best achievable energy resolution can be calculated as $\sigma_{\mathrm{E}}/\mathrm{E} = 3\,\%$.
With the help of the recorded spectra, the energy resolution in the small TPC prototype can be measured. The ratio of peak width $\sigma_{\mathrm{N_{QDC}}}$ and peak position $\mathrm{N_{QDC}}$ (cf. figure 8.3(b)) defines the energy resolution:

$$\frac{\sigma_{\mathrm{E}}}{\mathrm{E}} = \frac{\sigma_{\mathrm{N_{QDC}}}}{\mathrm{N_{QDC}}}. \tag{8.15}$$

The uncertainty on this value is obtained by error propagation. Again the statistical uncertainty is below 0.5 % and can safely be neglected. The systematic uncertainties are estimated via the variations of $\mathrm{N_{QDC}}$ within one measurement series, as already explained for the uncertainty of effective gain measurements.
From equation 8.15 a correlation of effective gain and energy resolution can be deduced. The energy resolution is anti proportional to the effective gain, which is proportional to $\mathrm{N_{QDC}}$. The width $\sigma_{\mathrm{N_{QDC}}}$ is of the same order for all measurements. Hence, a correlation of:

$$\frac{\sigma_{\mathrm{E}}}{\mathrm{E}} \sim \frac{\mathrm{c}}{\mathrm{G_{eff}}} + \mathrm{d} \tag{8.16}$$

can be assumed, with c and d being free parameters.
The measurements performed during the year 2008 showed for some GEM foils an unexpected behavior of the energy resolution. This resolution increased from a certain value of effective gain on. One reason could be, as explained in [Bec08], a pedestal structure looking like an underlying box over the whole range of the spectrum. Especially for the thick SciEnergy GEM this effect was observed. Therefore, measurements with this GEM were repeated in December 2009. No additional pedestal was visible in these measurements, so that reliable energy resolutions were determined and are later on presented in figure 8.20. Another source for the unexpected behavior could be an inappropriate choice of the gate length for the QDC. To investigate the influence of the gate length a measurement series with the thick SciEnergy GEM with 400 V applied across the GEMs was performed end of 2009.

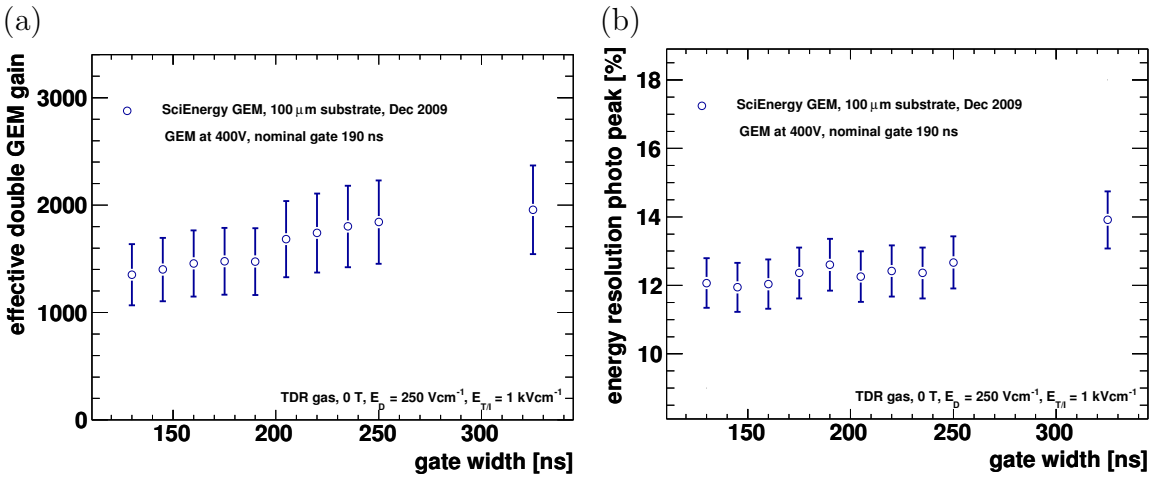

Figure 8.19: Studies of the influence of the gate length with the thick SciEnergy GEM at 400 V across the GEM foils. (a) Effective gain against gate length. (b) Energy resolution as a function of gate length.

The results are shown in figure 8.19. The signal length was measured on the oscilloscope to be 170 ns. Since the gate has to reach the QDC 20 ns in advance – in order to trigger the signal – the proper choice for the gate length is 190 ns. Below these 190 ns, the effective gain goes down with decreasing gate width as shown in figure 8.19(a). With a too short gate, not all charge is collected into the QDC. In contrast to a too wide gate, where overlapping events start to become more probable and therefore the collected charge is larger. The energy resolution in figure 8.19(b) shows also a tendency to larger values for wider gates. Since both measures, which are needed for the determination of the energy resolution, are influenced by the gate width, it has to be under careful control. This means, that the width of the gate has to be adapted to the signal width for every single measurement.
As a consequence, only results of energy resolution measurements performed in December 2009 under controlled circumstances are shown here. In figure 8.20, the energy resolutions of these measurements show an hyperbolic behavior with the effective gain, following equation 8.16. The results are similar for the three different GEMs. In figure 8.20(b), the same data points are shown with fitted hyperbolic functions and an enlarged effective gain range. For the effective gain used in this measurements, energy resolutions of 20 % down to 10 % are determined. The energy resolution seems to be almost independent from the GEM type. It is visible in figure 8.20(b), that energy resolutions of 9 % to 8 % would be possible in the limit of large effective gains. The energy resolution achieved with this setup, is similar to the typical values presented in [S$^+$07, A$^+$02, B$^+$03]. In these references a definition via Full Width Half Maximum (FWHM) of the iron peaks is used. These FWHM values of 18 % to 24 % at effective gains of several thousand are competetive, to the ones determined in this thesis.

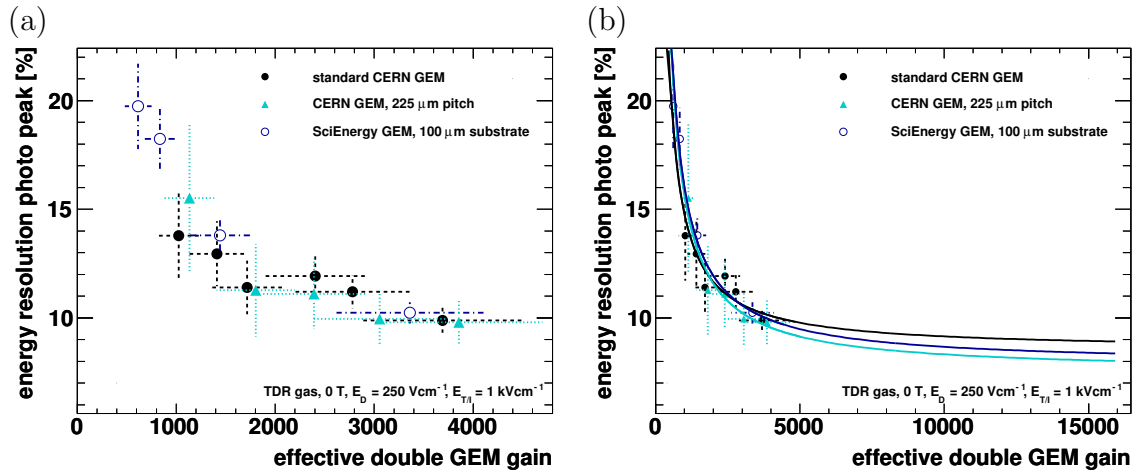

Figure 8.20: (a) Energy resolution of different GEM foils as a function of effective gains, (b) hyperbolic curves are fitted to the data points and the effective gain range is enlarged. All measurements were performed in December 2009.

8.6 Results of Comparative Studies

This chapter illustrates that the used assembly is well suited for comparative measurements of effective GEM gains, given that all sensitive measurables are under control. It is not suitable for precision measurements of absolute effective gain values. The electronics has to warm up before measuring and the gate length and the electric fields need to be controlled carefully. In order to become sensitive to absolute values, better capacitors and a better known charge injection efficiency to the preamplifier is necessary to reduce the systematic uncertainties.
A comparison of the parametrization of effective GEM gains to the measurement shows a good agreement in shape with the curves, but a difference in the absolute normalization, which is however within the assumed uncertainties of the parametrization and the measurements.
The relative comparison of the GEM foils from different manufacturers concerning their effective gain shows the behavior expected from the geometry for the CERN GEMs and the Tech-Etch GEM. The optical transparencies are able to explain the differences. The SciEnergy foils use a different substrate material and hole shape. The field simulations for double conical and cylindrical holes alone are not able to describe the measured performance differences. However, the effects cannot be disentangled, since both parameters – hole shape and material – can only be changed together. The relative comparison of the thick and thin SciEnergy GEM foils is consistent with the expectations. The thick foil produces lower gains at the same voltage due to the smaller hole fields.
The comparison of the energy resolution shows the expected improvement towards larger values of the gain and the achieved resolution of down to $\sigma_E/E = 10\,\%$ is compatible with the results of previous studies.

In summary it can be stated, that the highest effective gain values are achieved with CERN GEMs with enlarged pitch of 225 µm, while the energy resolution is independent from the characteristics of the GEM foils.

Chapter 9

GEM Profile Studies

Very important characteristics of GEM foils are the effective gain and its stability, since these quantities are essential for dE/dx measurements. In [YRS$^+$03, A$^+$02, S$^+$07], measurements of the uniformity and stability of the effective gain are presented for small double and triple GEM detectors. The results show spatially distributed gain deviations of about 20 % in the sensitive area. Intrinsic effective gain variations due to production processes are of the order of 5 % [Rop09].
The analysis presented in this chapter concentrates on the geometry of GEMs and its impact on the effective gain. For this purpose, several GEM surface profiles have been measured and the effective gain parametrization has been used for studies of the effect of deflected GEMs – which are not perfectly flat – on dE/dx measurements. In addition, studies of the influence on the single point resolution and the drift field quality are presented.

9.1 Profile Measurement

In the scope of this thesis, a method has been developed to measure surface profiles of GEM foils in order to study the effects of non uniform amplification structures. The height of many space points on the foil surface have been measured with the help of a laser device. Eight available GEMs have been scanned semi-automatically with over 10,000 points per GEM surface.

9.1.1 Measurement Assembly

The measurement assembly consists of the laser device, a movable xy table and the GEM mounting, which are described in the following. In the next section the determination of the surface profiles via a pattern recognition algorithm is explained.

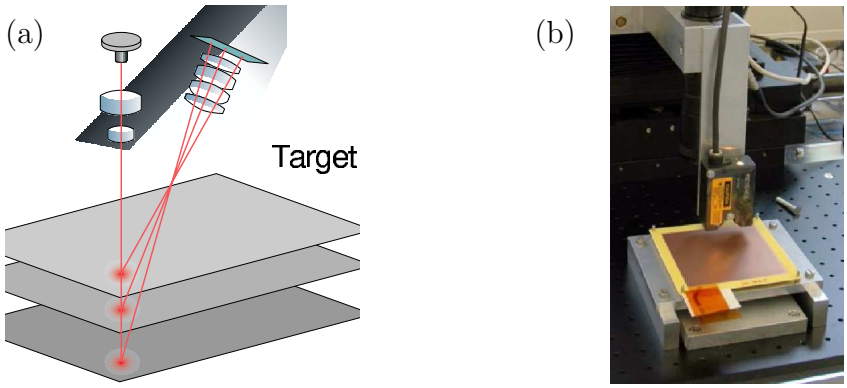

Figure 9.1: (a) Sketch of the measurement principle of the displacement sensor [Key08]. (b) Assembly on the xy table. The measuring head is fixed, while the table with the mounted GEM moves.

Measuring Device

A charge coupled device (CCD) laser displacement sensor – LK-G10 [Key08] – has been used to measure the surface profile of several GEM foils. The sensor works with a laser diode, based on a triangulation principle, sketched in figure 9.1(a). The optical path length is measured via the reflected laser light, which is focused by four lenses to a linearized CCD element. Each lens has a very small aberration, which allows to measure the distance of the object to the measuring head. It is done via the position of the light on the CCD, from which the entrance angle and the distance can be determined. The device has been chosen because of its small light point diameter of 20 µm and the accuracy of 1 µm [Key08]. The measuring head is built in a die cast case to assure a sufficient stiffness for measurement stability.

xy Table

The laser diode was installed above a GEM, which was mounted on a movable xy table (cf. figure 9.1(b)). The table was moved with a velocity of 1 mm/s on a meandric path over the GEM foil as sketched in figure 9.2(a). The inner area of a GEM frame is $104 \times 104\,\mathrm{mm}^2$, while the sensitive surface is $100 \times 100\,\mathrm{mm}^2$. In order to distinguish between foil surface and frame, the motion along the x axis had a length of 108 mm, followed by a movement in direction of the y axis of 1 mm and again 108 mm back along the x axis to the left edge. After this, a 1 mm step down was performed and the procedure started from the beginning until the whole surface was scanned. During the whole process the laser diode took data with a rate of 1 Hz. This yielded about one z measurement per square millimeter. In figure 9.2(b) the measured heights are shown as function of time. A step is visible every time the laser hits the frame, which is 0.5 mm thick.

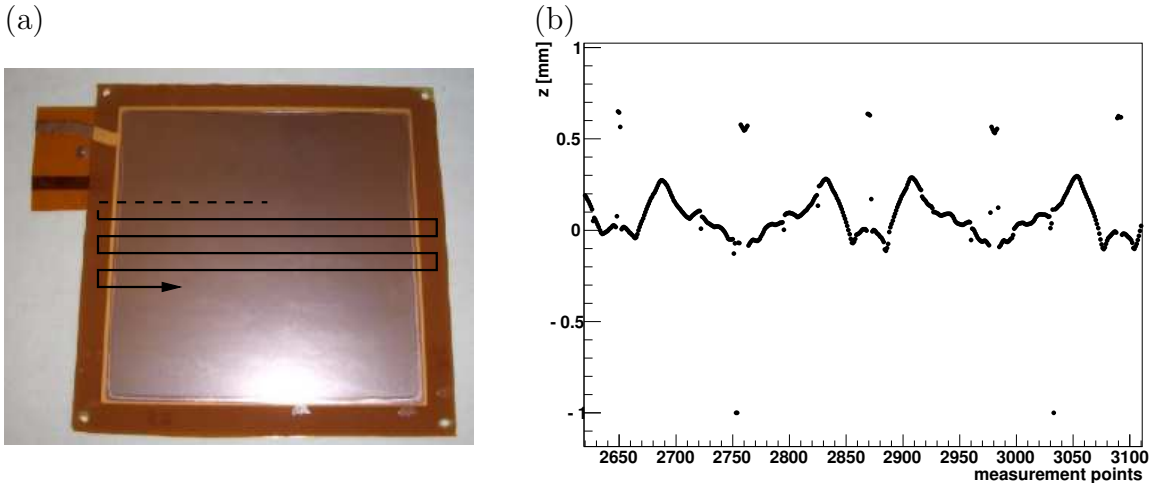

Figure 9.2: (a) Illustration of the path of the laser diode on the GEM surface, (b) measured z values for this track over four rows. The values above 0.5 represent points on the frame, the GEM surface is in between and symmetric around this reversal points. When no measurement was possible, e.g. due to holes, the value is set to -1.

GEM Mounting

The GEMs are stretched in either a glass fiber reinforced plastic (GRP) or a ceramics frame. For the measurement they were mounted on top of the table onto four screws with spacers and nuts, like in the TPC prototypes at DESY.
On the xy table, the GEMs had to be positioned horizontally beneath the laser device, although in a TPC they would be mounted vertically. This could explain that many of the measured GEMs seemed to sag in the middle. Deflections in an upright position remain to be checked. However, the measurements presented here can serve as an upper limit for the bending of GEM foils.
The behavior of GEM profiles while the voltages on the electrodes in a GEM stack are ramped up, has to be analyzed in future studies. Considerations about this topic can be found in section 9.6.

9.1.2 Pattern Recognition

The output of the laser device was a list of z values as a function of time, as shown exemplary in figure 9.2(b). In the context of this analysis, a pattern recognition has been written to transform the measured values to three dimensional GEM surfaces models.
For few points no measurement was possible, due to undefined reflection of the laser light in holes of the GEM. These values have been set to -1, like e.g. point 2752 and 3033 in figure 9.2(b). These outliers have been removed by averaging the height of the neighbor points. In the pattern recognition, the steps onto the 0.5 mm high frames on the left and right edges have been employed to identify the individual

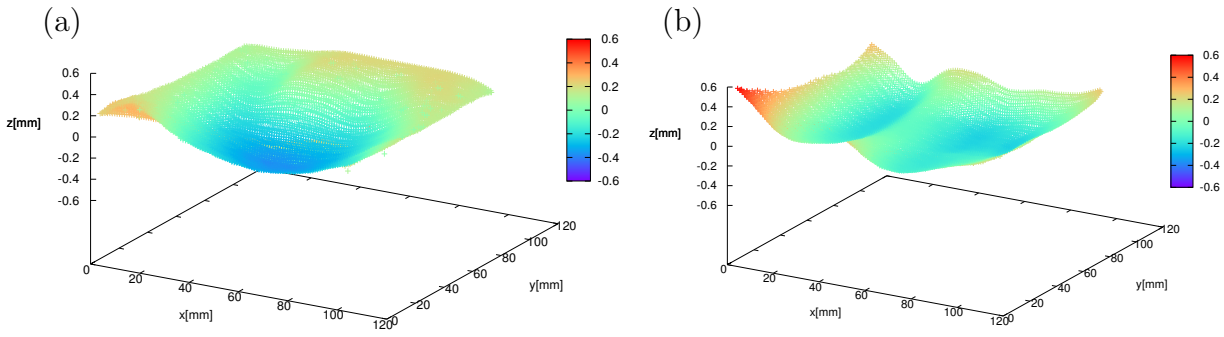

Figure 9.3: Measured GEM profiles: (a) shows a CERN GEM framed in a ceramics frame also shown in figure 9.4(g), (b) SciEnergy GEM as shown in figure 9.4(f).

rows. Looking by eye, the symmetry around the frame measurements can easily be seen (e.g. around point 2870 in figure 9.2(b)). Therefore, a search for symmetric areas has been performed in order to determine the reversal points. With the help of the known distances of 108 mm between these turning points, x and y coordinates have been assigned to the measured z values. The GEM surfaces originating from this pattern recognition are presented in the next section.

9.1.3 GEM Surface Profiles

In figure 9.3, two measured GEM surfaces are shown exemplary, after having applied the pattern recognition on their data sets. All eight measured GEM profiles are summarized in table 9.1 and in figure 9.4 with a common z axis range. The measured sample consists of six GEMs in standard GRP frames, one of them from the SciEnergy company, and two GEMs framed with a ceramics instead of GRP frame. Besides the material this frame is not different from the GRP frames, like the one which is shown in figure 9.2(a). A number is assigned to the standard CERN GEMs in order to distinguish them.
For the GEMs with ceramics frame and the one with the thicker foil of SciEnergy (100 µm substrate) another method of stretching than the usual was used. Instead of heating the GEM before gluing the frame onto the foil [GDD10b], the GEM was flattened by under-pressure. For this purpose the GEM foil was laid on an aluminum plate with holes and a vacuum pump sucked the foil onto the plate. Judging the two procedures by means of the resulting height differences over the GEM, the new method does not yield an obvious improvement.
The eight measured profiles in figure 9.4 show variations of z values between 384 µm and almost 1 mm, namely 922 µm. In table 9.1 all GEMs are listed with their maximal height difference Δz. All observed structures in the xy-plane are of the order of some millimeters, mostly more than ten. Hence, the gradients of the profile variations changes rather smooth and the sagging in the middle dominates most profiles.

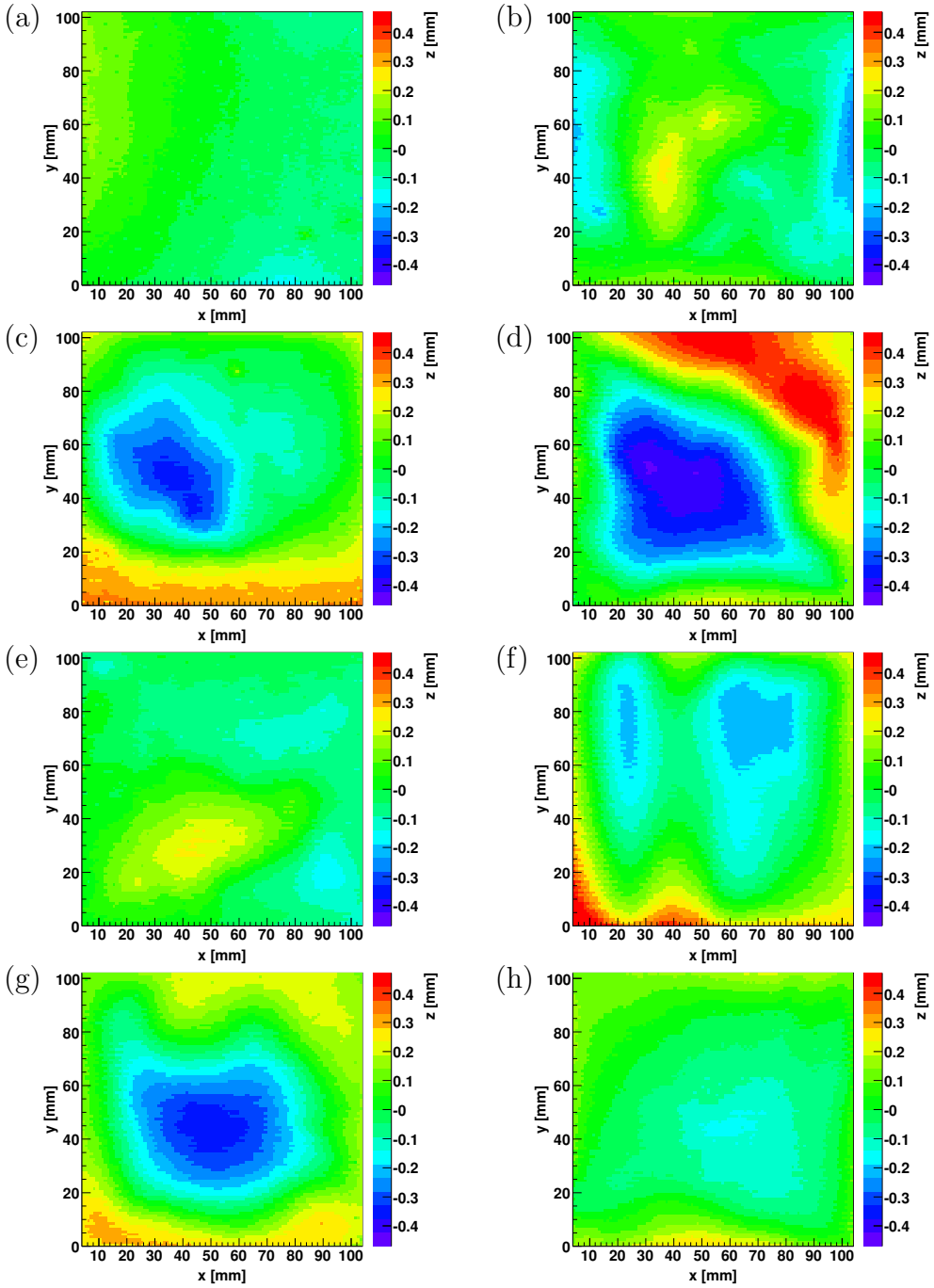

Figure 9.4: Measured GEM surface profiles and their maximal height difference Δz.
(a) CERN GEM 7 – Δz: 384 µm, (b) CERN GEM 17 – Δz: 523 µm,
(c) CERN GEM 18 – Δz: 733 µm, (d) CERN GEM 26 – Δz: 922 µm,
(e) CERN GEM 27 – Δz: 434 µm, (f) SciEnergy GEM – Δz: 921 µm,
(g) CERN GEM in ceramic frame – Δz: 690 µm and
(h) CERN GEM ceramic frame, pitch: 225 µm – Δz: 448 µm.
GEMs (a)-(f) are framed in GRP frames, (g) and (h) have ceramics frames.

manufacturer & identifier	pitch	thickness of substrate	frame material	framing method	maximal Δ z
CERN 7	140 µm	50 µm	GRP	warm	384 µm
CERN 17	140 µm	50 µm	GRP	warm	523 µm
CERN 18	140 µm	50 µm	GRP	warm	733 µm
CERN 26	140 µm	50 µm	GRP	warm	922 µm
CERN 27	140 µm	50 µm	GRP	warm	434 µm
SciEnergy	140 µm	100 µm	GRP	vacuum	921 µm
CERN ceramic	140 µm	50 µm	ceramic	vacuum	690 µm
CERN ceramic pitch	225 µm	50 µm	ceramic	vacuum	448 µm

Table 9.1: Characteristics and height differences Δz of the eight measured GEM surface profiles.

The impact of the deflections on dE/dx measurements, single point resolution and drift field quality is discussed in the following.

9.2 Simulation of Effective Gain

In order to study the effect of bent GEMs, the effective gain of a triple GEM stack is simulated spatially resolved, with a segmentation of 1 mm in x and y direction. The measured GEM surface profiles are utilized in the parametrization of effective gains [Lot06], which was introduced in chapter 8. Here, it is used – in contrast to chapter 8 – for a triple GEM setup with voltage settings, for which the parametrization is perfectly valid. The results of the effective gain simulation are used to estimate the impact of the deflections on dE/dx measurements.
At first, only the eight GEM surface profiles can be employed as input for the parametrization. However, the statistics is increased by mirroring the measured profiles around the x and y axis, as shown in figure 9.5. Including the mirrored profiles a sample of $24 \times 23 \times 22 = 12,144$ combinations of triple GEM stacks can be analyzed. In order to study, whether a quality control of GEMs is sensible, a second sample, containing only the four flattest GEMs, is analyzed. The parameters for the simulation are chosen such, that they correspond to measurements of cosmic muons with the medium size TPC prototype at DESY. The used gas is P5, which consists of 95 % argon and 5 % methane. As voltage across each GEM, 325 V are applied and the fields are set to 90 V/cm for the drift, 1.5 kV/cm for both transfer fields and 3 kV/cm for the induction field. The studies are performed for a magnetic field of 4 T.
In order to account for deflections of the GEMs, the effective gain is calculated in geometrical bins of the sensitive area of the amplification structure. The distances between the GEMs are calculated individually for each bin, based on the measured profiles. Afterwards, the known voltage of each GEM allows to recalculate the fields

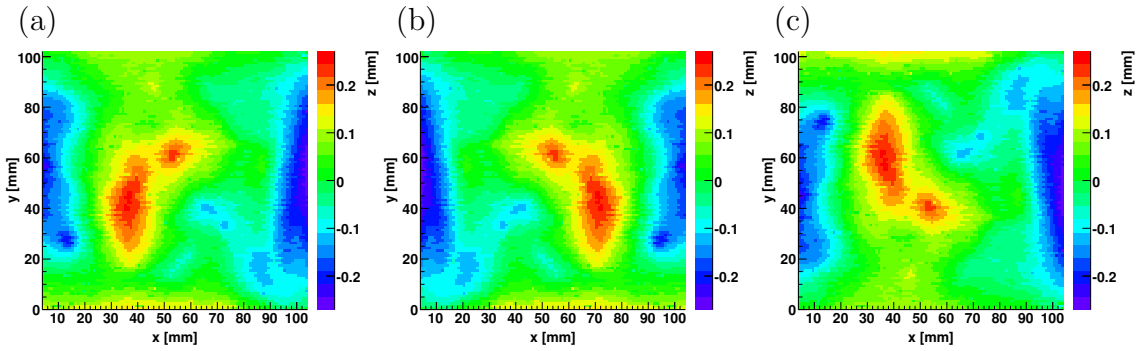

Figure 9.5: (a) Measured GEM profile, (b) same profile mirrored around the y axis and (c) mirrored around the x axis.

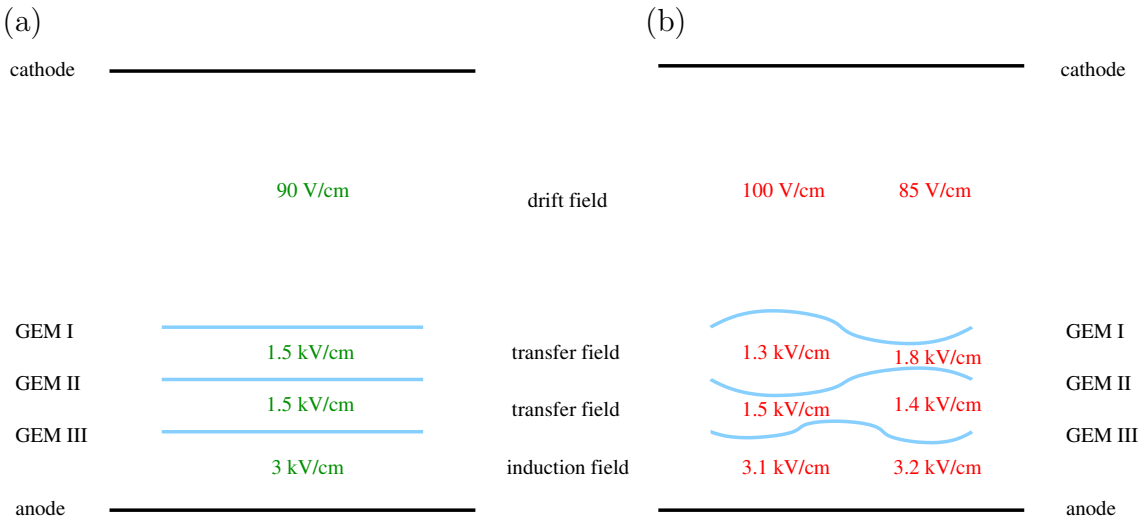

Figure 9.6: Illustration of electric field determination used for the gain calculation. The nominal values are calculated on the basis of (a), while the bent GEMs are considered as shown in (b). The distances between the bent GEMs determine the local fields.

and with these the effective gain for the actual distance. In figure 9.6 a sketch of this procedure is shown.

Effective Gain Maps

The effective triple GEM gain distribution is shown in figure 9.7. Every entry in figure 9.7(a) represents one of the $1 \times 1\,\mathrm{mm}^2$ bins of the gain structure in all 12,144 GEM stack combinations. The values shown in figure 9.7(b) are averaged for each bin. The distributions are normalized to the nominal gain, which is calculated with the nominal settings mentioned above under the assumption of perfectly flat GEM foils.
In the case of flat GEMs, the normalized effective gain would be represented by a delta function at 1.0. The mean value of the distribution, shown in figure 9.7(a), is

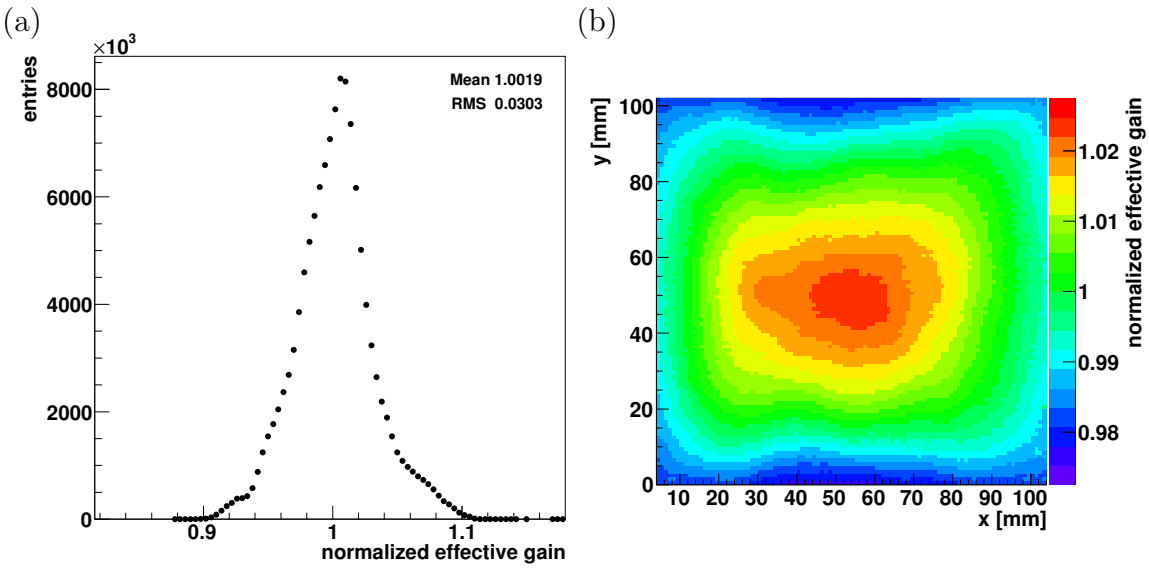

Figure 9.7: (a) Deviations of the effective gain from the nominal value at 4 Tesla. (b) The same deviations in the readout plane, with a binning of $1 \times 1\,\mathrm{mm}^2$.

1.002 with a root mean square of 3.03 %.
The shape of the effective gain distribution in figure 9.7(b) can be explained from the used GEM set, since most of the GEMs are sagging in the middle (cf. figure 9.4). Combination of the different mirrored profiles in a triple GEM stack leads to a rather symmetric shape. In a GEM stack – described by such a gain map – the sagging yields higher effective gains due to the decreased induction distance and therefore a higher field. Deviations on the edges of the profiles may be averaged out by the rotation of the profiles, but in the middle the sagging may be overestimated in exchange. It is assumed that in total, a realistic distribution of gain variations is described by this gain map.
To study the influence of the deflections on the dE/dx measurement, the mean effective gain per readout pad is needed, since the dE/dx determination is based on hit information, which consists of pad-wise charge depositions. Therefore, the profiles are averaged to bins of the size of the planned ILD TPC anode pads. In figure 9.8(b), the normalized effective gain using bins of $1 \times 6\,\mathrm{mm}^2$ is shown. This coarser binning yields the same mean value with a slightly smaller RMS of 3.01 %, which is simply explainable by the larger bins. The results of an analog calculation using a sample with only the four flattest GEMs are shown in figures 9.9 and 9.10. For the mean of the distributions a value of 1.001 with an RMS of 1.8 % is calculated. The underlying distribution, which broadens figure 9.7(a) and 9.8(a) vanishes.

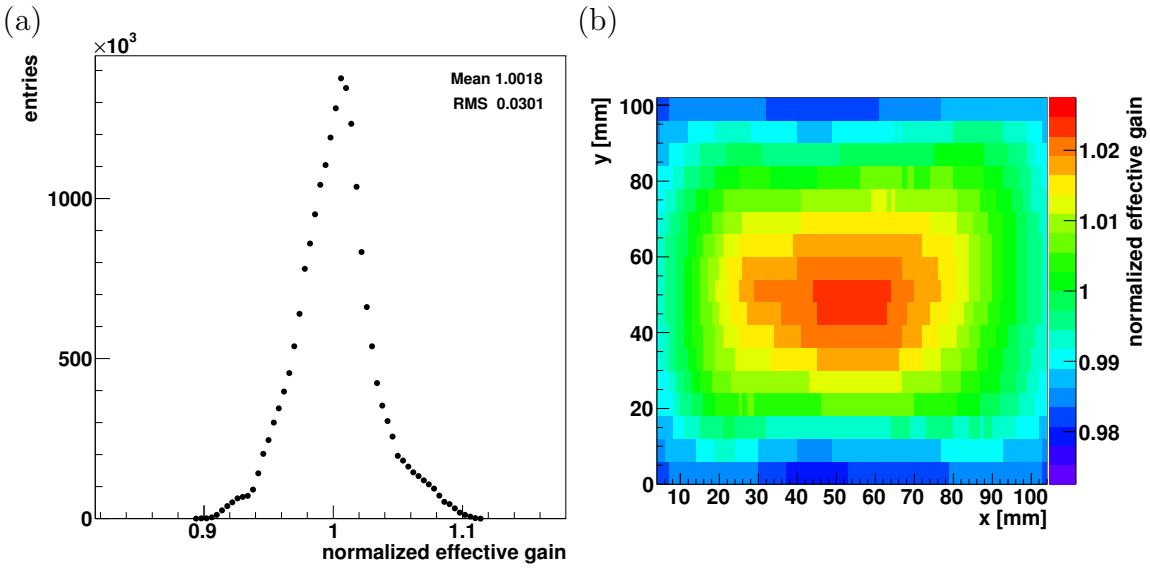

Figure 9.8: (a) Deviations of the effective gain from the nominal value at 4 Tesla. (b) The same deviations in the readout plane, with a binning of $1 \times 6\,\mathrm{mm}^2$.

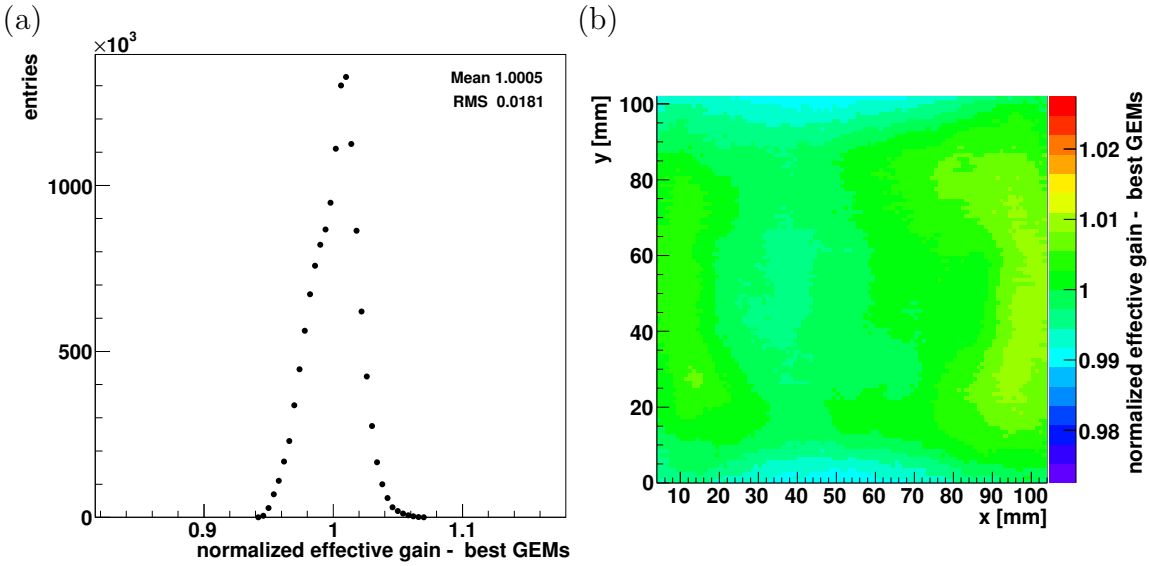

Figure 9.9: (a) Deviations of the effective gain from the nominal value at 4 Tesla. (b) The same deviations in the readout plane, with a binning of $1 \times 1\,\mathrm{mm}^2$. Only the four flattest GEMs are used in this sample.

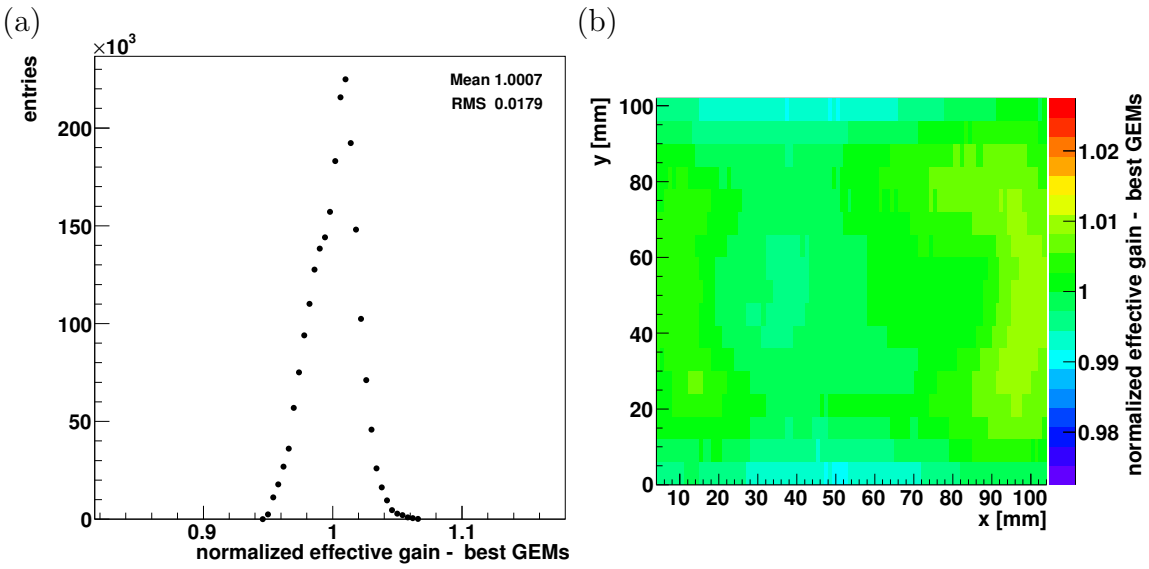

Figure 9.10: (a) Deviations of the effective gain from the nominal value at 4 Tesla. (b) The same deviations in the readout plane, with a binning of $1 \times 6\,\mathrm{mm}^2$. Only the four flattest GEMs are used in this sample.

9.3 Influence on dE/dx Measurements

To determine the influence of effective gain variations on dE/dx measurements, tracks using the calculated effective gain maps have been simulated. For this purpose, straight line tracks connect each bin in the lower row in figure 9.8(b) with each pad in the topmost row, forming $98 \times 98 = 9604$ tracks. In every row, the hits are assumed to consist of three pulses, which means they are three pads wide. The effective gains of all 51 bins per track (17 rows $\times$ 3 pads) are averaged and the resulting effective gain for the track is filled in a histogram, which is shown in figure 9.11. The RMS of 0.27 % is a measure for the stability of the gain for tracks in different regions of the sensitive area. In order to get a more detailed overview, the tracks are split into nine samples corresponding to different regions on the readout surface. The regions are sketched in the upper left corners of figures 9.12(a)-(i). These regions are obtained by subdividing the area in three parts, left, middle and right. Tracks are defined from the upper left to all three lower regions. The same is done for the upper middle and right part. The resulting track-wise effective gains are shown in figure 9.12, the mean and RMS values are summarized in table 9.2. Tracks crossing the middle region of the sensitive area are amplified stronger compared to tracks going straight along the left or right edge. This is a consequence of the gain map in figure 9.8(b), where the central region is characterized by the highest effective gains. Looking at figures 9.12(a) and (i), it turns out that the tail towards lower mean gains in figure 9.11 originates from straight tracks along the edges, while tracks fully crossing the central region produce narrow distributions with small RMS values (cf. figures 9.12(c), (e) and (g)).

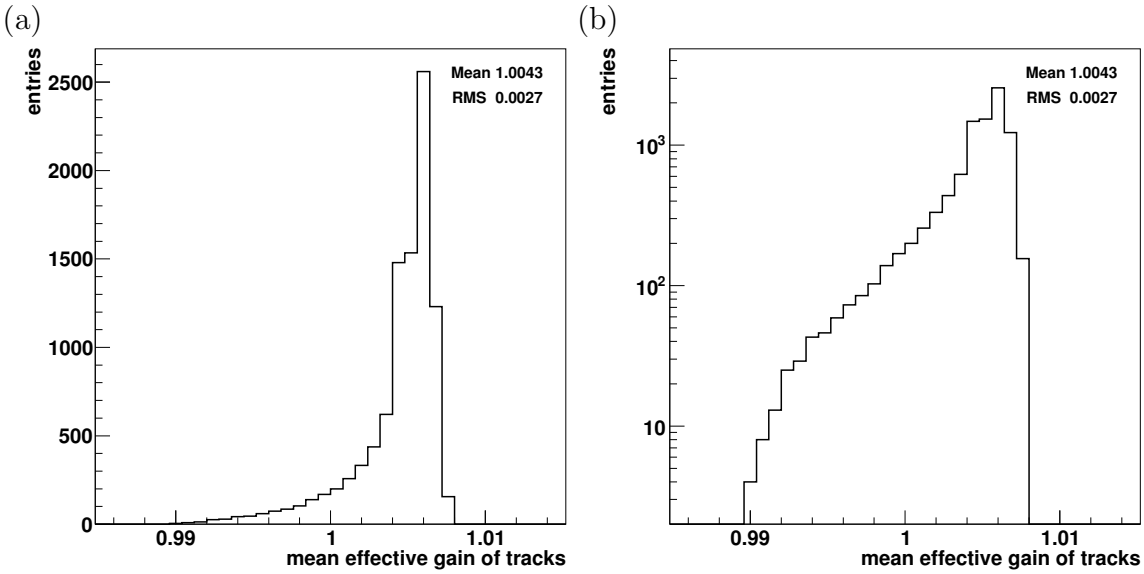

Figure 9.11: (a) Distribution of mean values of effective gain for tracks over the whole readout area, based on the effective gain map of the full sample (cf. figure 9.8(b)).
(b) Same distribution with logarithmic y axis.

	all GEMs		flattest GEMs	
region	mean value	RMS	mean value	RMS
left−left	1.001	0.36 %	1.000	0.15 %
left−mid	1.005	0.12 %	0.998	0.07 %
left−right	1.007	0.05 %	1.000	0.07 %
mid−left	1.005	0.10 %	0.997	0.05 %
mid−mid	1.006	0.06 %	0.998	0.10 %
mid−right	1.006	0.12 %	1.001	0.08 %
right−left	1.006	0.07 %	0.999	0.09 %
right−mid	1.004	0.14 %	1.001	0.13 %
right−right	1.000	0.30 %	1.004	0.16 %

Table 9.2: Normalized effective gain and RMS for tracks crossing the GEM stacks in different areas (cf. figure 9.12). The RMS denotes the fluctuation of the effective gain of tracks within the corresponding region. Two gain maps – one with all eight measured GEMs and one with only the four flattest – are listed here.

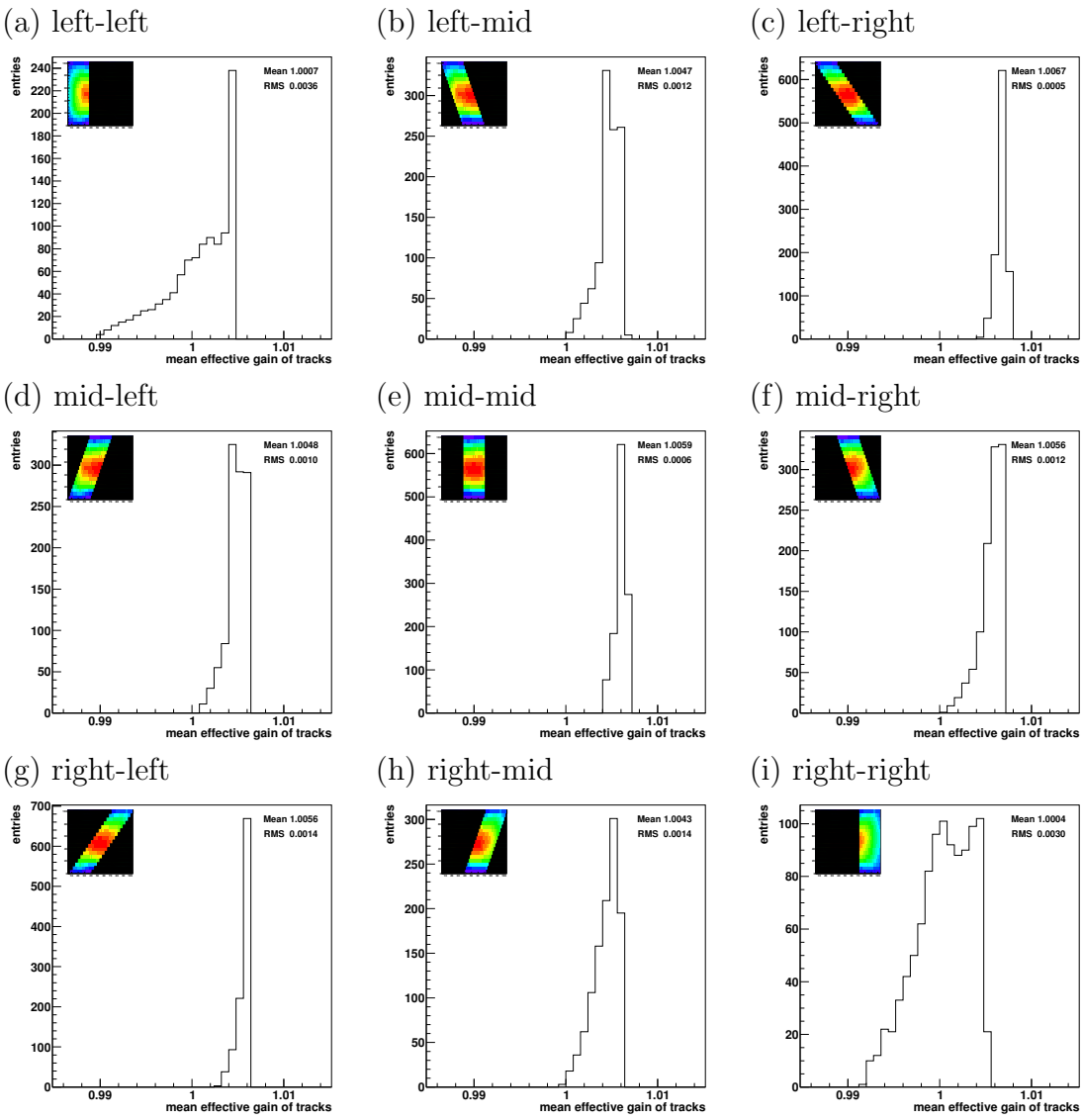

Figure 9.12: Distribution of mean values of effective gain for tracks in different areas of the readout plane. The region of the tracks is sketched in the upper left corners. For the calculation of the gain map all eight measured GEM profiles are used.

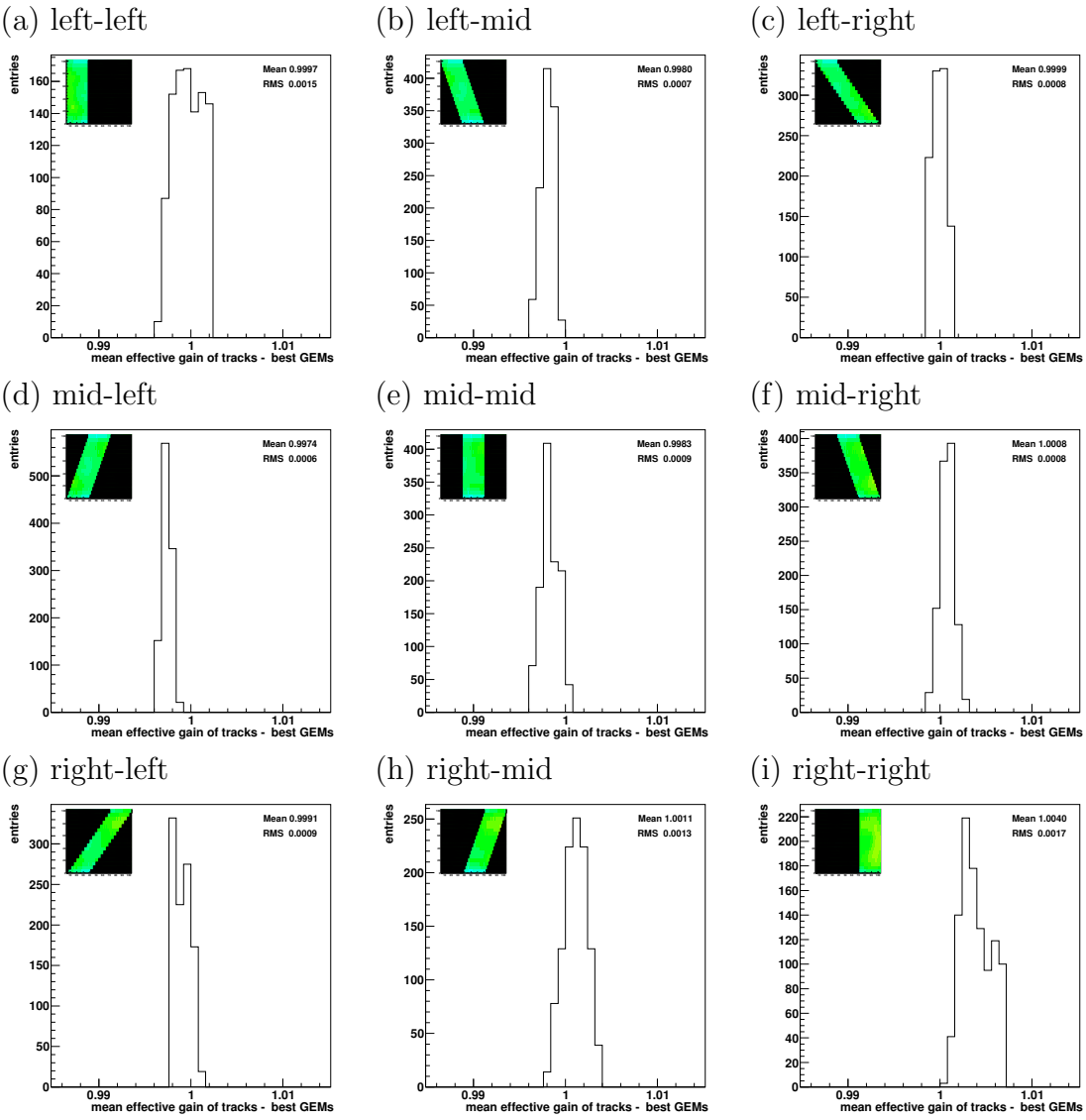

Figure 9.13: Distribution of mean values of effective gain for tracks in different areas of the readout plane. The region of the tracks is sketched in the upper left corners. For the calculation of the gain map only the four flattest GEMs are used.

While the RMS values in table 9.2 indicate that the effective gain fluctuations for tracks within one single region are not problematic, a comparison of the mean values in table 9.2 shows fluctuations of the average effective gain for tracks of up to 0.7 %, depending on the region. Gain instabilities of that size may cause problems for dE/dx measurements, since at most $0.1\,\sigma_{\mathrm{dE/dx}}$ are tolerable for precision analyses using particle identification, as explained in section 7.5. In the case of the ILD, with an envisaged $\sigma_{\mathrm{dE/dx}}$ of 5 %, this value would translate to an allowed instability of the mean effective gain of at most 0.5 %. Better would be a stability of the order of $0.05\,\sigma_{\mathrm{dE/dx}}$ [Hau09]. This makes it necessary to eliminate the effective gain variations via calibration in order to allow a reliable dE/dx measurement throughout the whole readout plane. In addition, for a dE/dx measurement in the ILD TPC, tracks of a length of the order of ten times more than the 10 cm provided by the prototype will be employed. This fact may allow the averaging of the effect caused by gain variations, which could lead to moderate instablities of the gain per track.
The same study has been repeated using only the four flattest GEM foils. The results are shown in figure 9.13 and are summarized in table 9.2. It turns out that the situation is much less critical for this gain map (cf. figure 9.10(b)). The deviation of the mean value of the tracks in different regions is with 0.4 % tolerable. However, a flatness measurement of GEM foils is advisable to guarantee a good dE/dx performance.

9.4 Influence on Single Point Resolution

To obtain an estimate of the influence of deflected GEMs on the single point resolution, studies with data recorded with the medium size TPC prototype were performed. A part of the effective gain map – shown in figure 9.8(b) – is used as calibration map for a measurement run with cosmics at a magnetic field of 4 T using P5 gas and a non-staggered pad plane. With this calibration, artificial disturbances due to gain inhomogeneities are introduced, which could influence the data reconstruction. The size of the part of the gain map, which is employed as calibration map, is defined by the size of the pad plane. It has 12 sensitive rows and 48 columns and is chosen as shown in the lower left corner of figure 9.14(a). From this gain map, calibration factors between 0.97 and 1.03 have been derived. The calibration algorithm of MultiFit applies this factor pad-wise to the charge information. Subsequently, the data are reconstructed without modifications of the usual procedure. A short introduction into reconstruction methods has been given in section 6.5. More detailed descriptions of the reconstruction methods and the used software can be found in [Die06, Jan08].
For the calculation of the single point resolution, only tracks, which fulfill the track selection cuts – listed in table 9.3 and described in detail in [Jan08] – are taken into account. The most important cut is a phi angle confinement of $|\phi| < 0.1$ rad. The determined single point resolution is compared to a resolution obtained from

variable	requirement
number of tracks	$n_{tracks} = 1$
number of hits	$n_{hits} = n_{rows}$
x region	$2.54\,mm < x_{hit} < 59.06\,mm$
curvature	$\lvert \kappa \rvert < 0.02\,mm^{-1}$
inclination in yz-plane	$\lvert \theta \rvert < 0.45\,rad$
inclination in xy-plane	$\lvert \phi \rvert < 0.1\,rad$

Table 9.3: Cuts for single point resolution determination.

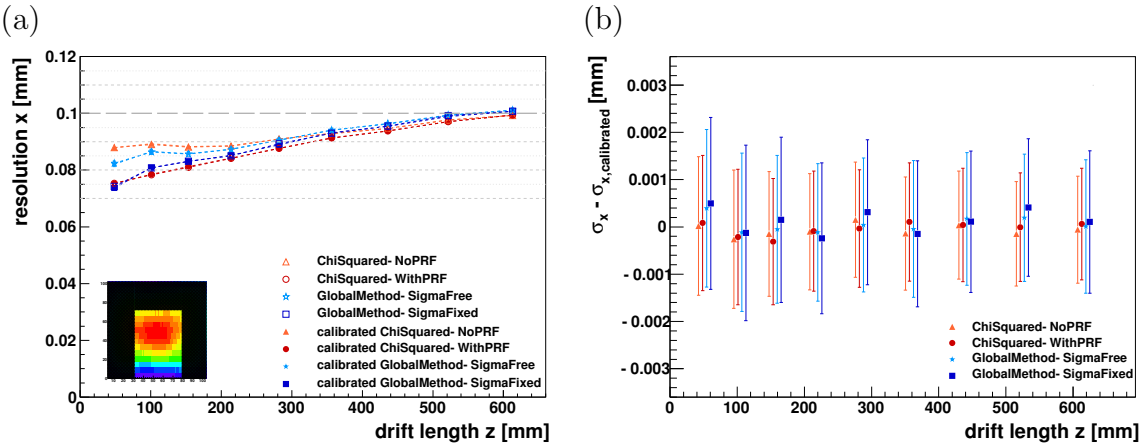

Figure 9.14: Influence of the calibration on single point resolution. (a) All reconstruction methods with and without calibration. (b) A differential diagram for better visibility of variations. The errors in this diagram are obtained from error propagation.

the same data set without additional calibration. Although the latter measurement set contains implicitly a gain map which originates from the GEMs built into the TPC prototype, a relative comparison is possible. There is no possibility available to determine this gain map from the data.
In figure 9.14(a), the obtained single point resolution is shown for different reconstruction methods as a function of the drift length with and without the applied calibration. The single point resolution is below 100 µm over the hole drift length of 67 cm. As mentioned in section 7.4, the design goal for the ILD TPC corresponds exactly to this 100 µm. Although the distribution has to be extrapolated to a drift length of 2 m for the ILD TPC, the resolution seems to be feasible.
For better visibility of the results, in figure 9.14(b) the differences between calibrated and uncalibrated points are depicted. The discrepancies are very small – within the errors consistent with zero. The global fit method seems to be slightly more sensitive to the gain variations. But overall, the influence of effective gain variations of about 3 % on the single point resolution is negligible.

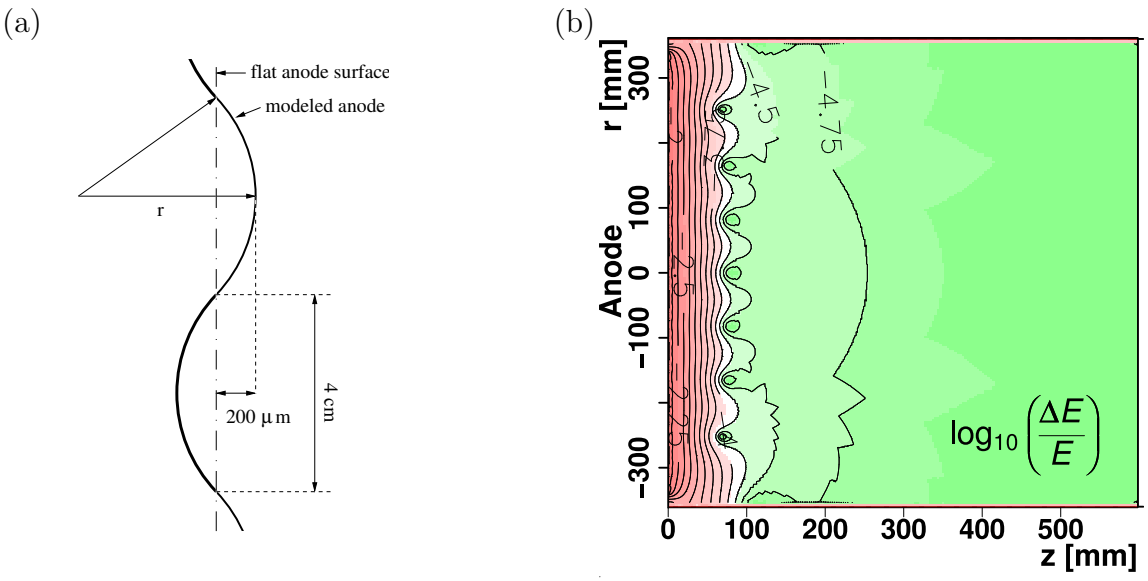

Figure 9.15: (a) Sketch of anode deflections for simulation. (b) Field quality with deflected anode. The contour lines have a distance of 0.25 and the green areas mark regions in the chamber, where the required field quality is reached [Sch10b].

9.5 Influence on Drift Field Quality

To simulate the influence of GEM deflections on the drift field quality, an existing CST-EM model of the drift field in the large prototype – introduced in chapter 6 – was modified [Sch09, Sch10b]. Since the amplification structure does not exist in this model, the anode has been assumed to be bent with periodic structures of the order of 200 µm in both directions. The expansions in the anode plane are set to 4 cm corresponding to the typical structure dimensions in the measured height profiles. An illustration of the anode model is shown in figure 9.15(a). The resulting relative field deviations are depicted in figure 9.15(b). Shown is $\log_{10}(\Delta E/E)$ for a chamber cross-section in rz, where E denotes the nominal electric field strength and ΔE its variation. Deviations of $\Delta E/E = 10^{-4}$ can be tolerated in order to reach the design goal for the single point resolution of $\sigma_{r\phi} < 100\,\mu m$. It is visible that in the first 80 mm after the anode, distortions above this limit occur. Close to the anode, distortions as large as $10^{-2.25}$ are calculated. In [Sch09] studies with a tilted cathode were performed. The result of these studies shows field distortions over a range of 200 mm in z direction, but the maximal distortions – of the same order as for the deflected anode – only occur in the outer corners of the field map.
In order to get a better handle to interpret the obtained results, tracks were simulated in the electric field caused by the deflected anode and a magnetic field. More details about this simulation studies can be found in [Sch10a]. The deviations of the reconstructed tracks from the true position is calculated, the resulting residuals are shown in figure 9.16. For a magnetic field of 4 T, the residuals are all smaller than 25 µm, however the magnetic field is needed to achieve tolerable results. Without

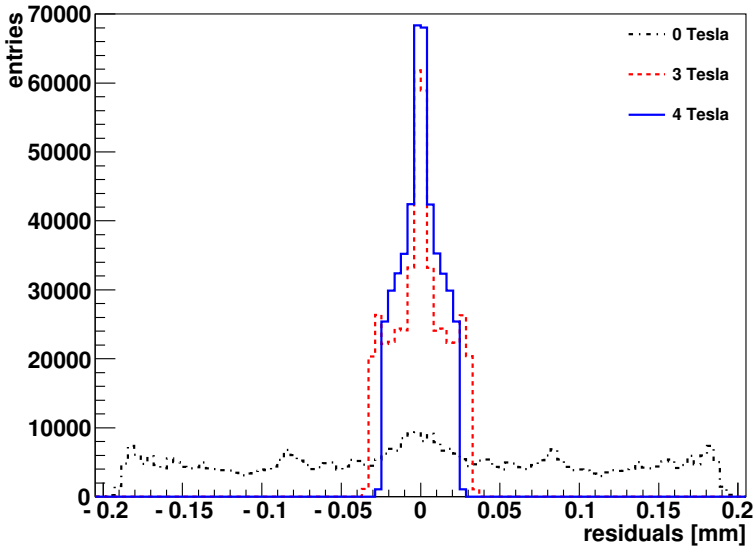

Figure 9.16: Residuals of reconstructed, simulated tracks going through an electric field distorted by deflected GEMs.

magnetic field, the residuals can become quite large. In the LOI for the ILD detector a single point resolution of better than 100 µm for the rϕ-plane is required. Assuming the residuals for a magnetic field of 4 T as systematic uncertainty, the following calculation can be performed:

$$\sigma_{r\phi} \rightarrow \sqrt{\sigma_{r\phi}^2 + \sigma_{res}^2} = \sqrt{(100\,\mu m)^2 + (25\,\mu m)^2} = 103.1\,\mu m. \tag{9.1}$$

This estimate gives a relative deviation of 3.1 % for the single point resolution assuming the GEMs to be deflected by ± 200 µm. This deviation is still close to the design goal formulated in the LOI, but it indicates that the flat mounting of the amplification structures is an important aspect to reach the challenging performance goals. Especially, since the systematic effects on the single point resolution are adding up. For example a tilted axis – described for the LP in [Sch09] – or an influence of ion discs in the chamber – described in [Kra08] – have to be considered. Altogether, the deviation of the single point resolution reaches about ten percent.

9.6 Time Dependence of Effective Gain

Calibration is a possibility to get rid of gain inhomogeneities, provided that the gain distributions shown in figure 9.8(b) and 9.10(b) are stable with time. A study of the behavior of GEM profiles with an applied potential is not in the scope of this thesis, but will be analyzed in future. It may happen, that a bending develops caused by increasing charge on the surfaces of the GEM foils. Such time dependent effects would make the calibration of the effective gain in a GEM based TPC much more difficult.

9.6.1 Force Estimation

A rough estimation of the electrical forces between the GEMs is presented in the following. In order to estimate an upper limit, the force between the last GEM surface and the anode is calculated as force in a parallel plate capacitor with the help of:

$$F = \frac{1}{2}\epsilon_0 A \left(\frac{U}{d}\right)^2, \tag{9.2}$$

where A denotes the area of the GEM, ϵ_0 is the dielectric constant, U stands for the potential difference and d depicts the distance. The resulting electrical force is F = 3.98 mN, which can be transformed to a mass of 0.4 grams pressing on the GEM foil surface. A GEM foil itself without mounting has a mass of roughly 2 grams, which is not much compared to the arising electrical force. But the foils are supported by their mounting and therefore the influence of the forces occurring during ramping up and down the voltages have to be studied. In addition, the effect of upright positions of the GEMs should be analyzed in future research.

9.6.2 Calibration Strategies

Effective gain variations over the readout surface of a TPC endplate can be reduced by selecting flat GEM foils and ensuring a plain mounting, but cannot be avoided completely. Remaining variations require a calibration of the effective gain. Other effects like field distortions can be calibrated in a similar way.
Different techniques to calibrate effective gains within a TPC are possible, for example using a radioactive ^{55}Fe source as described in detail in chapter 8. This method is usually used for prototypes. A technique applicable to large scale TPCs is to use radioactive gas like meta-stable krypton-83 [E$^+$01]. This gas produces five electron peaks between 9.4 keV and 41.6 keV and has the advantage, that it can be distributed via the existing gas system, during dedicated calibration runs. An additional advantage is the coverage of the whole readout area, which is necessary in order to obtain complete gain maps.
For energy calibration at running colliders, the well known decays of Z^0 bosons can be used as described in [LEP93]. Other important parameters, which have to be calibrated are the drift velocity and the field distortions. The uncertainty on these measurables determine the momentum resolution capabilities in a TPC. For this purpose, typically laser beams are used. Such a calibration method for prototypes is described in [Bal08] and an application of a laser in the STAR TPC at RHIC can be found in [Leb02].
All calibration strategies work with the same principle, the initial energy is known and the detector response is measured. This allows for precise and reliable measurements of the TPC, which can be used for instance for particle identification via dE/dx measurements.
Since most of the calibration processes cannot be applied during run time of a col-

lider, only variations which are stable over time can be calibrated. In the case of effective gain variations – discussed in this chapter – every effect, which yields deviations on short time scales, has to be avoided. Assuming that at least half of the gain variations shown in figure 9.8(a) and quantified with an RMS of 3.01 % are stable over time, they can be calibrated. If this is possible and the RMS of the remaining variations is of the order of 1.5 %, a similar picture as for the studies with the four flattest GEMs without calibration would result (cf. figure 9.10(a)). These kind of effective gain distributions do not cause problems for dE/dx determination. Nevertheless, a mounting scheme providing the flattest possible GEM installation improves the feasible level of precision. An analysis of effective gain variations during voltage ramping is an important topic for future GEM TPC research in order to decide, whether time dependent effects occur at all.

9.7 Results of GEM Profile Studies

A measurement procedure for GEM height profiles has been developed and the obtained data are analyzed in this chapter. The profiles are determined with GEM foils lying horizontally beneath the measurement device. In this setup, sagging cannot be avoided, hence the results should be interpreted as an upper limit.
Simulation studies with the help of a parametrization of the effective gain of a GEM stack allow to estimate the impact of deflected GEMs on the dE/dx resolution. Deviations of mean values of the effective gain for tracks in the sensitive area are above the limit, which is expected to be uncritical for dE/dx determination. Hence, a quality inspection concerning the flatness of the GEM mounting is important.
The effect of the profiles on the single point resolution has been judged by applying the obtained gain map as calibration onto a cosmic muon data set. This effect is very small and can safely be neglected.
A finite element calculation of the electric field caused by a deflected anode shows that the field homogeneity suffers. However, the effect of the obtained drift field quality on the single point resolution is small but it emphasizes again the importance of a flat mounting of the GEM foils, since it is not the only effect, which has to be considered.
Under the assumption that the deflections of the GEMs are not time dependent, calibration of the effects will be possible. For this reason, calibration strategies for an ILD TPC have to be thought of carefully, in order to reach the ILD design goals.

Chapter 10

Studies of a Grid GEM TPC with Cosmic Muon Data

In this chapter, the development and design of a grid GEM structure is presented. First, a short motivation and the requirements for a GEM mounting in a large scale TPC are mentioned. And second, details of the design, material budget and flatness of grid GEMs are described.
The influence of the grid mounting on track reconstruction and single point resolution is studied, using cosmic muon data recorded with a medium size TPC prototype. For this purpose, the data reconstruction is investigated step by step: starting on pulse level, subsequently looking at hit properties like single hit efficiencies and ending with track based quantities, including the impact on the single point resolution. In addition, implications on tracking efficiency and dE/dx determination are presented. At the end of the chapter, considerations about the design of a GEM support structure for future applications are described.

10.1 Requirements for GEM Mounting

For the large prototype of the LCTPC collaboration and later on for the ILD TPC a new way of mounting of GEM foils is necessary in order to provide a large area coverage and to reduce the amount of insensitive material inside the detector. Up to now, the support of GEMs in small prototypes is realized with Glass fiber Reinforced Plastic (GRP) frames. These frames are used on top and bottom of the foil. They have each a thickness of 0.5 mm. A photograph of a framed GEM can be seen in figure 9.2(a) on page 109, a technical drawing of the frame in figure 10.2(a). The width of the frames is typically 10 mm, which causes an intolerably large amount of insensitive material between GEMs in larger readout areas.
The development of a new support structure has to meet some requirements, which are described in the following. First of all, the structure has to be capable to be used on large readout areas. Hence, a self supporting structure with possibly no or only very small gaps in between GEMs would be favorable. Second, flatness shall be

(a) (b) (c)

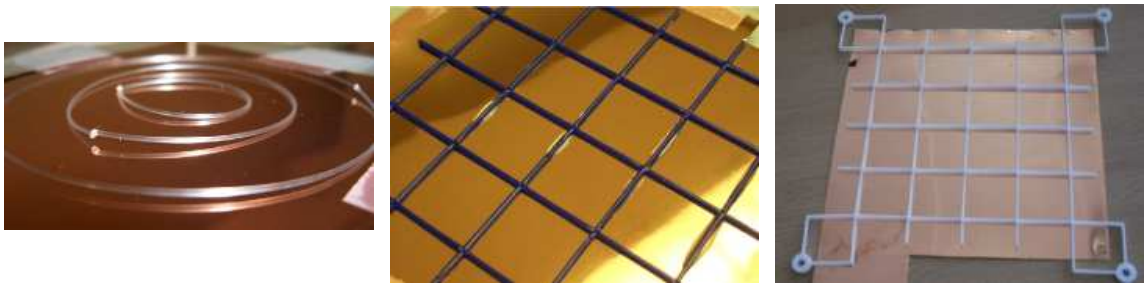

Figure 10.1: History of GEM support structure. (a) Nylon threads, (b) rapid prototyping grid – ABS polymer, 1 mm bars – and (c) polyamide (PA 12) grid – 0.5 mm bars.

provided by the structure, since variations of the effective gain have to be minimized, in order to allow for reliable dE/dx measurements, as described in chapter 9. Third, the material of the mounting should be minimized and has to sum up to the least possible percentage of a radiation length.

10.2 Ceramics Grid GEM

The development of a new GEM support structure – documented in figures 10.1(a)-(c) – started with nylon threads, but those could not be processed in a precise way. In the early phase, the idea of a grid structure came up and first tests were performed with rapid prototyping of polyamide grids. The problems of these materials were production precision and rigidity, which could not be provided. Finally, ceramics was found to be a very promising material candidate.
For the latest development stage, presented here, an aluminum oxide ceramic (Al_2O_3) is used as support structure [ANC10]. Aluminum oxide is very stiff, an excellent insulator and machinable by laser cutting. A technical drawing of the grids, which were produced to fit in the medium size TPC prototype at DESY, can be seen in figure 10.2(b). The advantage of a grid is the almost edgeless mounting, which provides the possibility to mount two grid modules next to each other with a very small gap of dead material in between.
Width and height of the bars is 1 mm. The restriction to the ratio 1 : 1 for width and height is given by the production process. The ceramic is produced by sintering and the grid is cut out afterwards with the help of a laser. The heat produced by this laser while cutting a 1 mm thick plate is dissipated in the material. If the width of the remaining structure would be smaller than one millimeter, this heat causes cracks in the structure. In order to achieve a width of only 1 mm, but a height of 2 mm, which is needed to provide sufficiently large transfer gaps in the GEM stack, two grids were glued on top of each other.
The outer dimensions of the grid are chosen to match with $10 \times 10\,\mathrm{cm}^2$ GEM foils and the mounting environment of the medium size TPC prototype. A triple grid

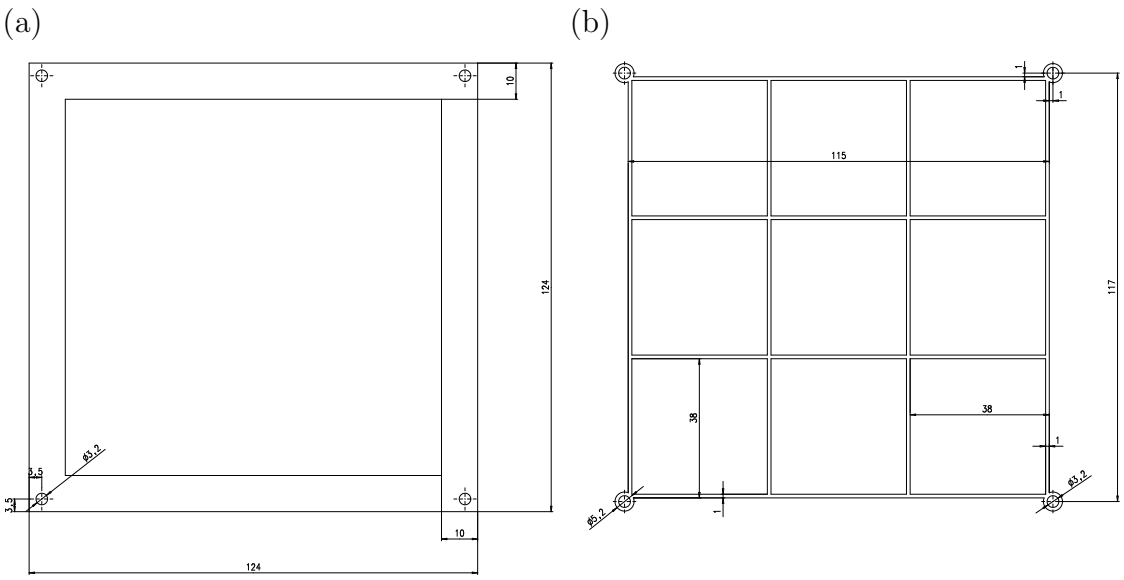

Figure 10.2: (a) Technical drawing of the GRP frame, so far used for GEM mounting. Two 0.5 mm thick frames are glued on both sides of a GEM foil. (b) Drawing of ceramics grid developed in the scope of this thesis, the thickness of the grids used in the triple GEM stack is 2 mm. All measures are given in millimeters. Drawings by [Heg10].

GEM stack was produced by gluing GEM foils directly onto grids with a two-component epoxy resin glue (polybond EP 4619/3 [PT10]). A stretching via heating of the foils – as used for framed GEMs – is not necessary, which permits the mounting structure to be thin, since no mechanical forces have to be absorbed by them. In the end, the stack is build by a structure of 'GEM foil – grid – GEM foil – grid – GEM foil'. A picture of this grid GEM stack can be seen in figure 10.3(b) and figure 6.5(b) on page 58. The glue was only applied on the outer frame of the grid, not in the sensitive area of the GEM foil, in order to avoid effects caused by glue sucked into the holes of the GEM.
The position of the grid support structure relative to the pad plane is shown in figure 10.5(a). In each row, pads 9, 10 and pads 39, 40 are covered partly by the vertical grid bars. This corresponds to the following x coordinates measured from the left side of the sensitive area of the pad plane: the left vertical bar can be found between 11.3 mm and 12.3 mm, while the right one covers the region from 49.3 mm to 50.3 mm. The horizontal bars are positioned in row four and nine of the pad plane in the medium size TPC prototype. Rows three and ten are adjacent to the rows covered by the horizontal structures. The grid is in particular very close to row ten, visible in figure 10.5(a).
In a large scale TPC, the horizontal bars will follow the curvature of the pad rows, while the vertical bars will be arranged radially.

(a) (b)

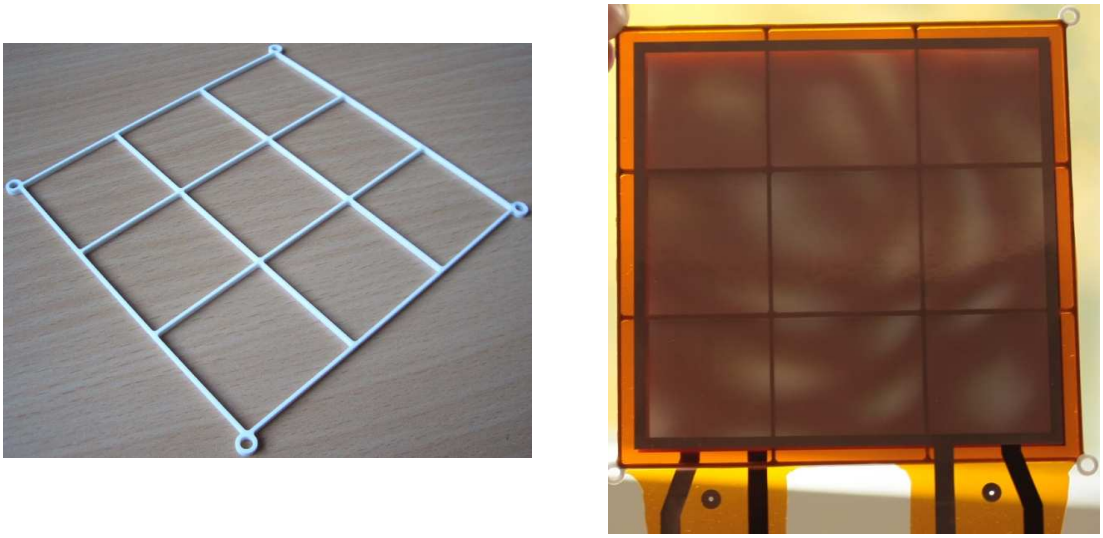

Figure 10.3: (a) Ceramic grid for GEM mounting and (b) grid GEM structure.

Material Budget

The radiation length of aluminum oxide can be calculated to $X_0 = 7.0\,\text{cm}$ which has to be compared to $X_0 = 19.4\,\text{cm}$ for glass fiber reinforced plastic [PDG06]. GRP shows a better performance in this aspect, but the stiffness of the ceramic grid allows the surface of the support structure to be built by a factor five smaller compared to the GRP surface of the mounting frames. This results in a larger solid angle region without dead material inside the detector. Another support structure, the pillars of InGrid MicroMEGAS [Che09], cover almost five times more area than the ceramic grids, if the same size of sensitive area is assumed. This means, that a track going through the support structure, sees a larger fraction of radiation length in the case of the grid mounting, but the probability to hit the support structure at all is significantly smaller compared to MicroMEGAS or GRP framed GEMs.

Flatness

Besides the reduction of dead material, the grid structure has an advantage in terms of stiffness. The mounting can be performed in a more precise way and the flatness of GEMs can be improved using a grid mounting. In figure 10.4, two height profiles of grid GEMs are shown. They are obtained the same way as described in chapter 9 and show deviations in height like the flattest framed GEMs (cf. figure 9.4 on page 111). Especially the sagging in the middle is avoided by the grid structure, but care is indicated, as can be seen in figure 10.4(b). This profile is worse than the other, which is a consequence of an imprecise gluing. On two positions the glue connection was lost and the foil stuck out a little bit. This reveals the importance of a careful

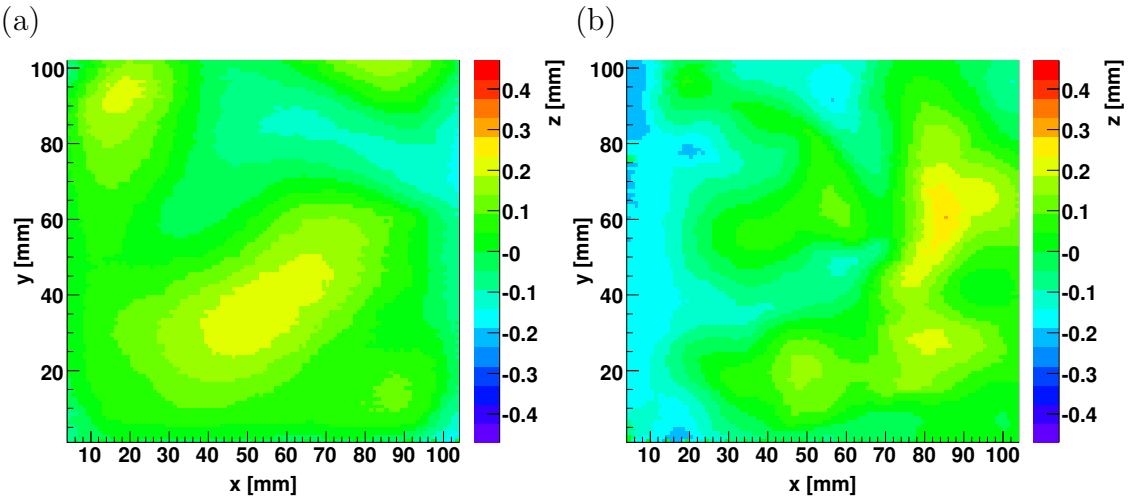

Figure 10.4: Grid GEM height profiles from both surfaces of the triple GEM stack. The maximal height differences are (a) $\Delta z : 385\,\mu m$ and (b) $\Delta z : 514\,\mu m$.

handling of the GEM stacks, during the gluing as well as during the assembly and disassembly into and out of a TPC.

10.3 Grid Influence on Pulse Level

In the following sections, an analysis of grid GEM TPC data is performed in order to obtain qualitative and quantitative results about the influence of the grid support structure on the track reconstruction. The cosmic muon data are taken with a medium size TPC prototype at DESY in a magnetic field of 4 T. As counting gas P5 is used, it consists of 95 % argon and 5 % methane. More details about the measurement setup can be found in section 6.4.2.
First of all, pulse quantities are studied. Pulses are charge depositions on one single pad, which are stored as a sequence of several charge slices in time. The time bins correspond in the used setup to slices in z direction.

10.3.1 Number of Pulses per Pad

An easy way to study characteristics of a measurement run is to plot two dimensionally the number of pulses per pad, as shown in figure 10.5. In figure 10.5(a) a direct comparison of the position of the grid and the number of pulses is depicted, while in figure 10.5(b) the whole pad plane can be seen. Four dead pads are visible and the "shadowing" of pads by the grid elements decrease the pulse reconstruction. The traces of the vertical bars of the grid structure are eye-catching. The horizontal bars are also visible, but much less noticeable. Although the width of the ceramic grid bars is only 1 mm – compared to 7 mm pad height – it turns out, that two pad rows are affected by each horizontal bar. The lower bar is positioned at the edge of

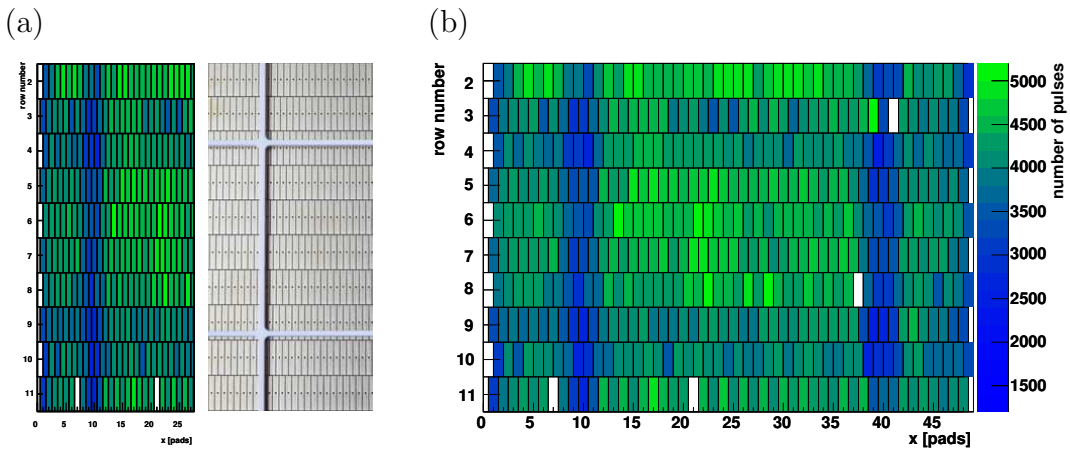

Figure 10.5: Number of pulses on the pad plane. (a) Comparison with photograph, (b) whole pad plane. Dead pads are visible as white pads in the rows three, eight and eleven. Row one and twelve are also in the sensitive area of the GEM foils, but not connected due to a finite amount of available readout channels.

row nine and influences also row ten. And even though the upper horizontal bar is situated in the middle of row four, nevertheless less pulses are counted in row three in comparison to the uncovered rows. The reason for less reconstructed pulses can be explained by the pulse shape, described in the following.

10.3.2 Charge per Pulse

Since primary ionization is a highly statistical process, it does not make sense to judge single pulse shapes – charge as function of time bins. Hence, averaged pulse shapes are shown in figure 10.6(a). Three curves are depicted, describing an uncovered, a partly covered and a covered pad. It can be seen, that the averaged pulse height is reduced by more than a factor of two from not covered to covered pad, while the reduction to the partly covered pad is about 10 %. The latter fact is interesting and indicates in comparison with the strongly decreased number of pulses in these partly covered and adjacent pads – visible in figure 10.5(b) – that a treshold effect appears. Only a small reduction of charge but at the same time a large reduction of the number of pulses yields the conclusion, that many pulses with low charge are cut away. The threshold for pulses in the measurement run analyzed here, was set to seven ADC counts. The grid reduces the charge deposited on the corresponding pads and especially on the partly covered pads, consequently many small pulses are not able to pass the threshold anymore.
In figure 10.6(b), the pulse charge sum per pad is shown. Besides the dead pads, it is clearly visible that only narrow regions in x are collecting less charge due to the vertical grid bars. The influence of the horizontal structures is also well visible and in addition, on rows three and ten less charge is collected. This is most probably due to a prevention of the charge cloud spread in vicinity of the grid structures,

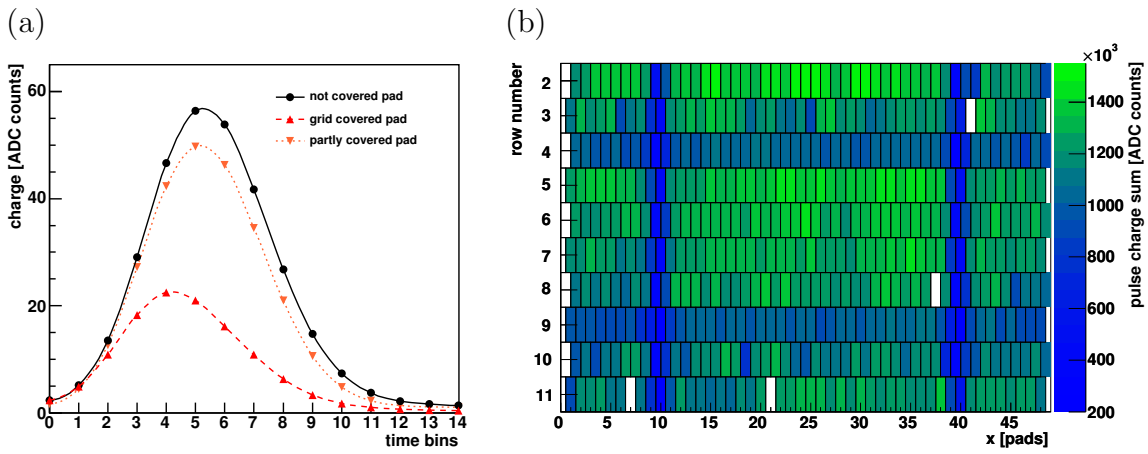

Figure 10.6: Charge per pulse in ADC counts. (a) Averaged pulse shapes for three pads – not covered, partly covered and grid covered – shown are the ADC counts as function of the time bins. (b) Pulse charge sum on the readout pads.

which is certainly also true for vertical structures. Another reason for the reduced charge could be an electrical charging effect of the grid structure itself, which needs to be studied in future analyses.
The charge distribution per pulse is shown in figure 10.7. Depicted are three different regions of the x axis. The first region includes the whole width of the pad plane, the second is limited to regions without vertical grid bar and a third at the position of the vertical grid bars. The shape of the distribution for the whole pad plane and the region, where the grid bars are cut out, are almost identical. In the region, which is covered by the vertical grid bars, the distribution shows a small but well visible shift towards lower pulse charge values.
On pulse level, the grid structure causes less pulses with less charge in the covered regions. This influence is passed on to the hit level, since hits are clusters of pulses.

10.4 Grid Influence on Hit Level

Pulses are combined row-wise to hits, which are three dimensional space points. Some hits are produced through noise, but most of them are linked to a track deposited by a traversing particle – in this case muons. In the used setup, hits consist mostly of three pulses. The x coordinate of these hits is obtained by a center of gravity method folded with a pad response correction. Besides the charge and position, foremost the single hit efficiency is analyzed, while the influence of vertical and horizontal grid bars on hit quantities are studied separately.

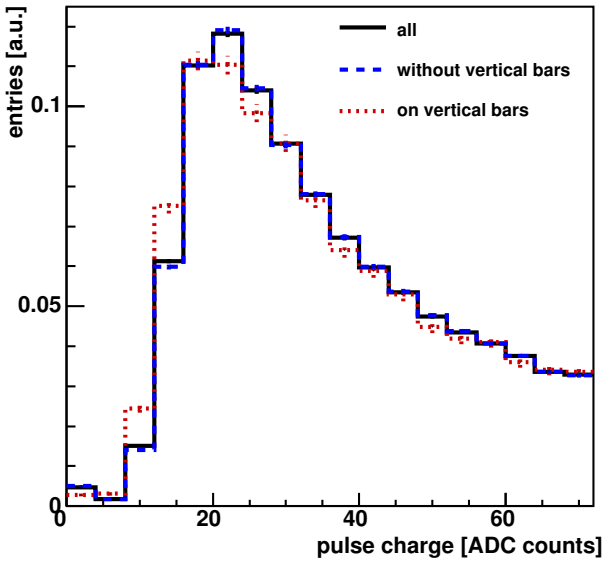

Figure 10.7: Grid influence on pulse charge for different regions along the x axis. One region covering the whole pad plane, one including only regions without vertical grid bar and one at the position of the vertical grid bars. The distributions are shown normalized. For pulse charge values larger than 70 ADC counts, the curves are behaving equally.

10.4.1 Number of Pulses and Charge per Hit

The number of pulses per hit plays an important role in the track reconstruction, since the precision of the position determination depends on it due to charge sharing. The more the charge is spread on many pads, the better the hit and by it the track reconstruction and the single point resolution.

Horizontal Bars

For the determination of the impact of the horizontal grid bars, the pad plane rows are subdivided in three groups. Row four and nine are directly covered by a bar, as it can be seen in figure 10.5. The second group consists of rows three and ten. They are adjacent to the grid covered rows and as seen for the pulses also influenced by the structure. All other rows build the third group, which serves as reference. These rows are not covered by horizontal bars and show no signs of an influence by the grid.
The number of pulses per hit and the uncertainty on the x coordinate of hits are shown in figure 10.8. A tendency towards less pulses per hit is visible for the adjacent rows and a clear effect for the grid covered rows can be seen as expected. The ratio of three to two pulse hits is significantly smaller. Hits with less pulses result in larger uncertainties on the hit position in x, visible in figure 10.8(b). The discrete value at the right end of the spectrum corresponds to one pulse hits. These get assigned the uncertainty given by pad width divided by the square-root of twelve – according to

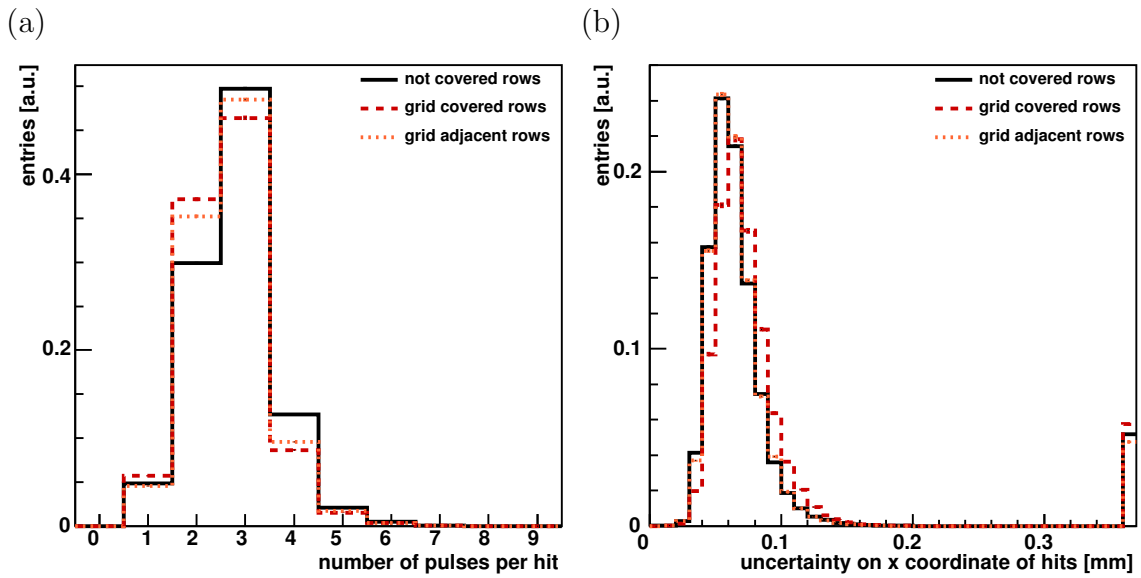

Figure 10.8: Influence of horizontal grid bar on (a) number of pulses per hit and (b) uncertainty on x coordinate of hits. Both distributions are shown normalized to the total number of entries.

the error of a rectangular distribution – which can be calculated to 0.37 mm. The uncertainties of the other hits are significantly larger for the grid covered rows.

Vertical Bars

In order to study the effect of the vertical grid bars, four neighboring regions are defined around the bars, having a width of 1.27 mm each, according to the width of the readout pads. The regions are illustrated in figure 10.9(a). The y axis range is restricted to the area in between the horizontal bars. In order to prove the reliability of such small strips of the pad plane, the number of pulses per hit of a small reference region with the same width of 1.27 mm – lying in the middle of the pad plane – are shown in figure 10.9(b). The reference region is compared to a distribution obtained in a large area of the pad plane, which is not affected by the grid structure. It can be seen, that the shapes of the distributions are in very good agreement.
In figure 10.10(a), the distribution of the number of pulses per hit for the four neighboring regions with different distances to the grid bar are shown. In all regions most of the hits consist of three pulses. For the region closest to the grid, the shape is significantly different, having much more hits with only one or two hits and less with three or four. The hits within the region with three pads distance to the vertical bar show the same behavior as in the reference region. But already the distributions of hits with a distance of only one or two pads have a shape very similar to the reference region.
The same effect is visible in figure 10.10(b), where the charge distribution in ADC counts per hit is shown. The shape of the distribution for hits in the region next

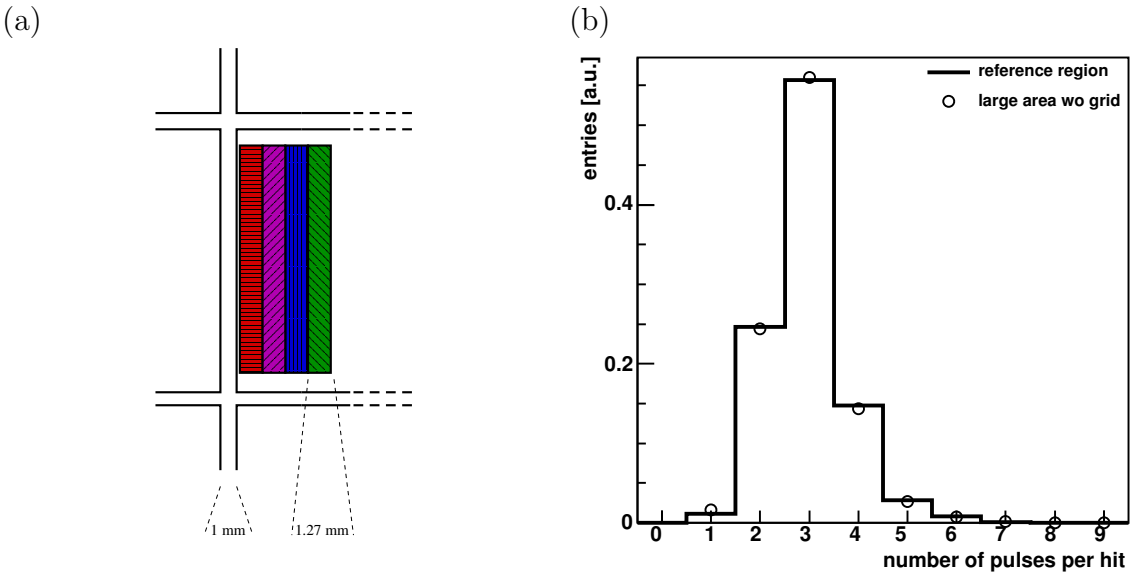

Figure 10.9: (a) Sketch of the neighboring vertical regions used for comparative studies of the influence of vertical grid bars. Each region has a width of 1.27 mm. (b) Normalized distribution of the number of pulses per hit for a reference region compared to the normalized distribution for a large region in between the grid bars.

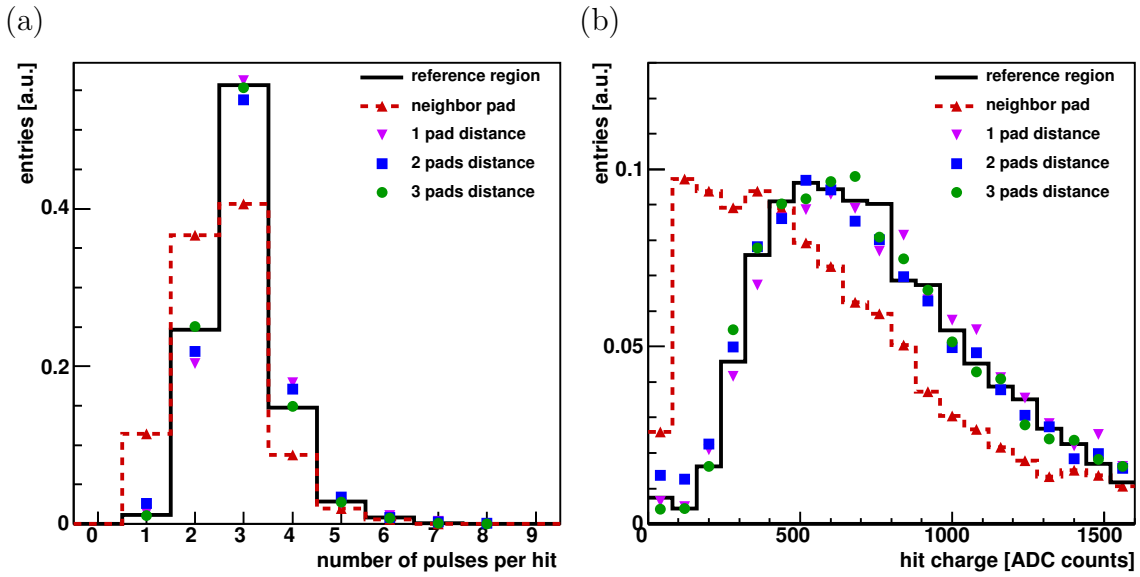

Figure 10.10: (a) Number of pulses per hit and (b) hit charge for the reference region, compared to regions with different distances to a vertical grid bar. All distributions are normalized to the number of entries.

to the grid bar differs significantly from the others. Less charge is deposited close to the grid, which is inherited from the pulses. A kind of shadowing effect takes place there, which is caused by a restriction of the charge cloud diffusion due to the grid structure. It may be that an electric charging of the grid surface amplifies this effect, which should be studied in future analyses.

10.4.2 Distribution of Hits

In the following, observations of hit positions are described in order to get an impression of effects visible on the pad plane. Therefore, distributions of all hits and of hits which are part of tracks are analyzed to prepare the single hit efficiency determination, which is explained in the next section.
The x position of hits is obtained via a center of gravity method using pulses linked to this hit [Die06, Jan08]. In addition, the pad response function is evaluated to correct for errors of the center of gravity method.
In figure 10.11(a), the x position of all hits in the grid GEM data sample are shown. The bin width is chosen such that each pad is represented by two bins in order to avoid binning effects due to the staggering of the pad plane – every second row is shifted by half a pad pitch. The obvious dips are caused by the vertical grid bars. The resulting gaps are three bins respectively one and a half pad or 1.9 mm wide, which is a bit more than the 1 mm wide grid. Spikes in the adjacent bins point to a shifting effect. Hits are not reconstructed at the position of the grid bar but shifted to the left or right due to missing pulses. In the very first and last bin less entries are visible, which is an effect of the staggered pad plane. Since the bins have half pad widths, only in every second row these border bins are filled. At the edges of the pad plane, more hits are reconstructed, which is a well known effect caused by tracks, traversing at the edge of the pad plane and therefore depositing only a part of the charge on the sensitive area. A detailed description of this edge effect can be found in [Die06]. Apart from the vertical grid bars and the edges, the distribution is flat, although fluctuations of single bins are quite large.
In figure 10.11(b), the same distribution is shown, but only for hits belonging to tracks with at least six hits. Less hits are plotted in this diagram with respect to figure 10.11(a), due to the requirement of at least six hits per track and the fact, that the track requirement avoids noise hits in the sample. At the same time, this reduces the fluctuations of the single bins. The distribution is decreasing towards small and high x values due to less reconstructed tracks at the edges of the pad plane. Tracks, which pass only a small part of the sensitive volume are not selected, since they usually produce less than six hits on the pad plane.
For tracks having a hit in each of the rows, the distribution of hit positions is shown in figure 10.12(a). The picture changes in many aspects. The spikes vanish, the gaps become broader and more dips originating from dead pads show up. The dip around $x = 25.4\,\text{mm}$ is caused by the dead 21st pad in row eleven at this position. Since most of the tracks have a small inclination angle ϕ, the influence of the dead pads is

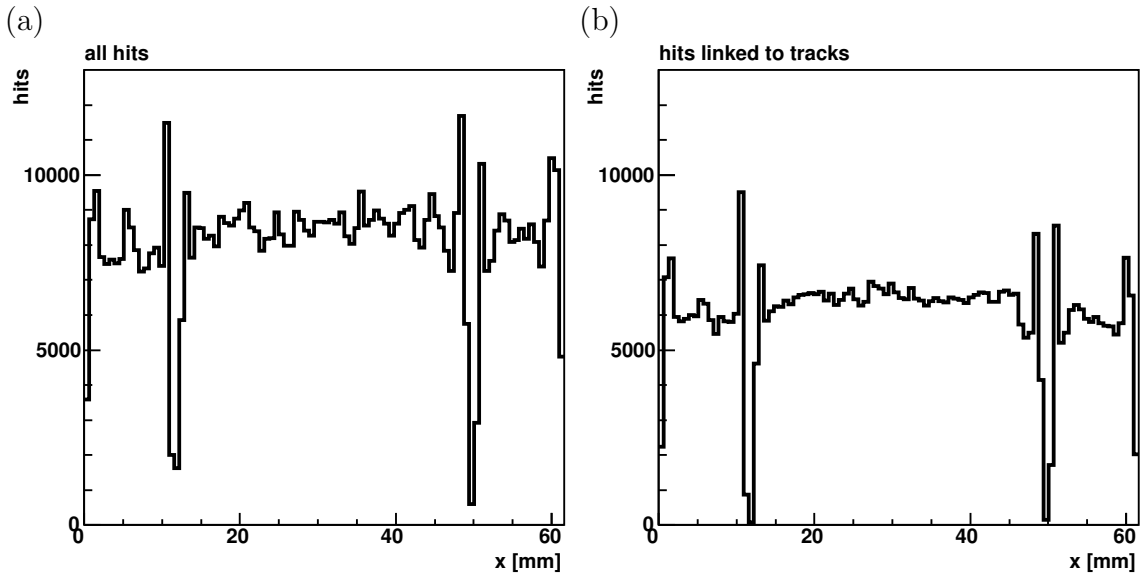

Figure 10.11: (a) Hit positions in x for all hits and (b) only for hits belonging to a track. Each bin corresponds to half a pad width.

visible vertically above and below them. The distribution of the inclination angle ϕ of the tracks is shown in figure 10.12(b). Most of the tracks cross the sensitive area under a relatively small angle, very few reach a tilt of $\phi = 10°$. If a track is crossing one of the vertical bars of the support structure and if no hit is reconstructed for this row, the track does not enter the sample with ten hits required. As a consequence, all other hits of this track are also not plotted in figure 10.12(a), causing broader gaps around the vertical bars. The width of these gaps can be estimated, taking the angle ϕ and the height y of the sensitive pad plane into account:

$$\Delta x = y \cdot \sin\phi, \tag{10.1}$$

where y is given to 77 mm and Δx denotes the distance in x between the hits in the first and last row. 95.5 % lie within the 2σ region of $-7.12° < \phi < 7.12°$. Using this angle a Δx of 9.5 mm can be calculated, which is in good agreement with the width of the broader gaps visible in figure 10.12(a).
Analyzing hit positions of tracks with different numbers of hits yields a good overview of the effects of the support structure. However, also edge effects and peculiarities caused by dead pads have to be accounted. A two dimensional distribution of the number of hits of all tracks without any requirements on the minimum number of hits is shown in figure 10.13(a). This is the same distribution as shown integrated over y in figure 10.11(a). Visible are the vertical grid bars, which influence three to four bins each. The four dead pads can be seen (cf. figure 10.5) due to less hits reconstructed on their positions and the earlier described edge effect is visible as well. In contrast to the vertical bins, the horizontal ones are not visible in this figure.

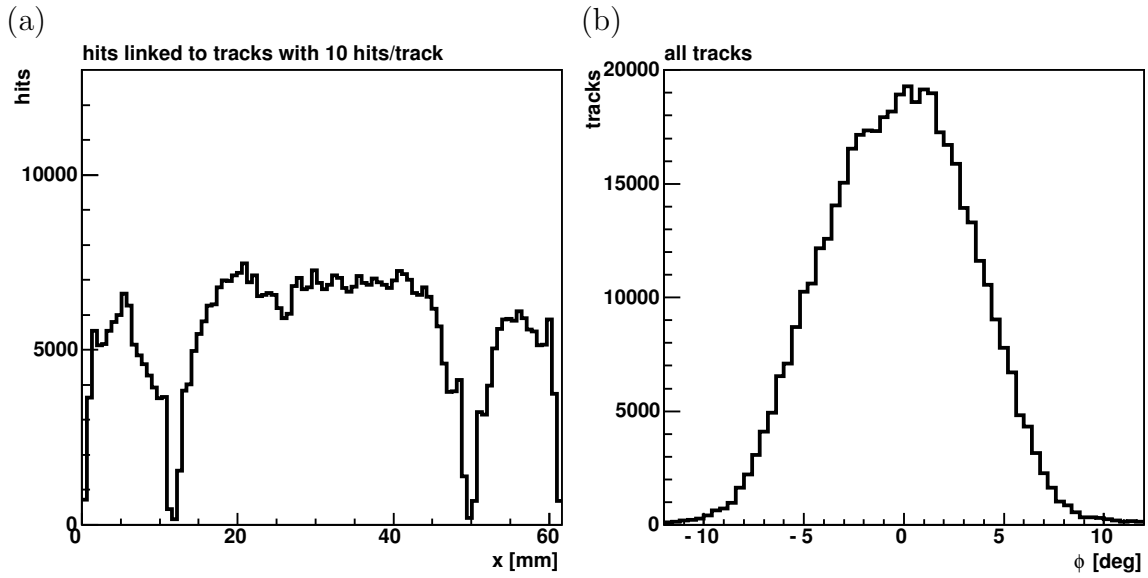

Figure 10.12: (a) Hit positions in x for hits belonging to tracks with ten hits per track. Each bin corresponds to half a pad width. (b) ϕ angles of these tracks.

To figure 10.13(b) contribute only hits belonging to tracks with ten out of ten hits. A fraction of 76 % of all tracks are reconstructed with exactly ten hits. The main difference to figure 10.13(a) is that the number of hits decreases towards the edges, as already seen in figure 10.11(b).
For figure 10.13(c) exactly nine hits per track are required. These tracks are well suited to study the effect of dead pads and vertical grid bars. The dead pad in the middle of the bottom row causes an obvious cone of tracks pointing to it, visualizing the region, which is influenced by a single pad and the given angular distribution. In principle the same holds for the other three dead pads, but they coincide with the vertical support structure bars. Around their position a significant amount of nine hit tracks is concentrated, originating from events in which the structure prevents that a hit is reconstructed and assigned to the track in the corresponding row. As additional effect, an increasing number of hits on the very edges of the pad plane are visible. These hits belong to tracks, which do not pass the full sensitive area. The effect becomes even more eye-catching for the tracks with less than nine hits, as shown in figures 10.13(d)-(f).
Losing one hit due to a crossing of one of the grid bars is not critical, since the track can still be reconstructed without any problems. The impact on the tracking efficiency and the single point resolution is presented later in this chapter. More important are tracks, where more than one hit is lost. This does not happen in the prototype, since the angular acceptance is too small to register tracks running over both vertical bars. In a large scale TPC this would become possible, although a larger number of hits will be reconstructed there and the effect becomes less important. For the dE/dx determination at OPAL, a resolution of 5 % was achieved with

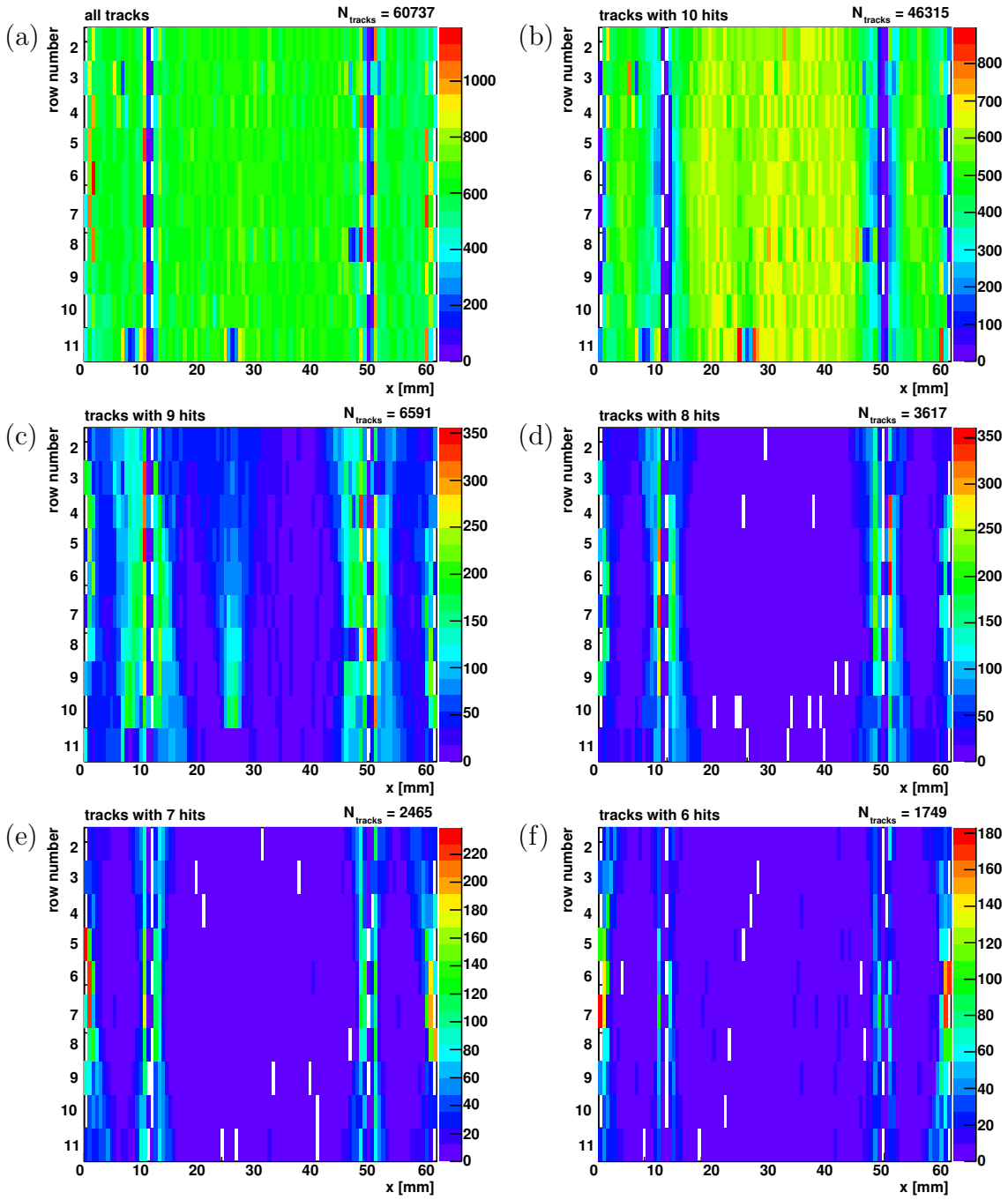

Figure 10.13: Two dimensional hit positions of tracks with different numbers of hits on the pad plane for (a) all reconstructed tracks, (b) tracks with ten out of ten hits, (c) tracks with nine hits, (d) tracks with eight hits, (e) tracks with seven hits and (f) tracks with six hits. The binning in x refers to half a pad width, in y to the pad height of 7 mm and the color coding shows the occurrence of hits in bins, no entries are indicated by white bins.

less than 50 % of the at most available hits, this fact can be seen in figure 7.8 on page 74. In consequence, about 100 hits will be needed at the ILD TPC. Assuming the pattern recognition can still be performed appropriately, the loss of hits due to a grid mounting is expected to be negligible. Some design considerations for large readout modules are mentioned at the end of this chapter.
In order to estimate the effect of the support structure in the prototype setup, the number of tracks with eight or less hits are added. They sum up to 13 % of all reconstructed tracks. Tracks with six hits – shown in figure 10.13(f) – represent only 3 % of all tracks. Almost all of these tracks leave the sensitive volume sidewards and the effect of the grid bars alone becomes negligible. Taking into account, that for tracks with more hits the edge effect occurs as well, 3 % of the tracks are assumed to have less than ten hits due to the edge effect. This leads to the rough estimation that 10 % of all tracks are influenced by the vertical grid bars in a way, that they could influence the track reconstruction, since more than one hit is missing. However, this is only true for exactly these conditions, namely the distance of the vertical bars and in particular the narrow ϕ distribution of the tracks. In a large scale physics environment, much less tracks will be affected in a significant way. In addition, the effect can be further reduced by accounting for it in the design of the endplate, as it is done for the ILD TPC, where the readout modules are planned to be staggered.

10.4.3 Single Hit Efficiencies

Another measure for the influence of the grid mounting is the single hit efficiency, which quantifies, whether a hit is reconstructed or not. Since ten rows per track are available, a fit through reconstructed hits can be used to calculate the expected position of a hit for each row.
In order to decide, whether a hit is on the awaited position, the residual for the hit is evaluated. As a reference a measurement run is used, which was recorded with framed GEMs without a support structure in the sensitive area. The distribution of residuals for the reference run is shown in figure 10.14. 99 % of the hits are inside the range of one pad width centered around zero ($-0.635\,\mathrm{mm} < x < 0.635\,\mathrm{mm}$). Hence, a hit is counted as reconstructed if the distance between fitted and real hit position is less than half a pad width: $\mid x_{\mathrm{fit}} - x_{\mathrm{hit}} \mid < 0.635\,\mathrm{mm}$.
In order to obtain row-wise hit efficiencies, the data are reconstructed twice. First, with the row, which shall be inspected, taken out of the reconstruction as illustrated in figure 10.15(a). In this case for each of the remaining nine rows a hit is required in the track reconstruction. This monitor sample is called 9/9 in the following. The second sample uses all ten available rows, whereas at least nine hits are required. This sample is called 9/10 (cf. figure 10.15(b)) and can be used to check, whether hits are reconstructed in the row, which was ignored in the monitor sample 9/9.
To ensure, that identical tracks are compared, in addition to the event number the slope and intercept of the tracks have to be the same. The selection cuts for the single hit efficiency determination are summarized in table 10.1. Using these tracks,

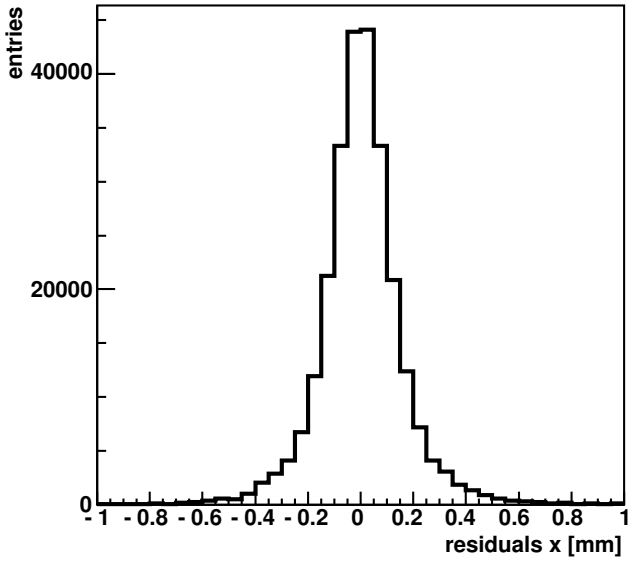

Figure 10.14: Residuals in direction of the x axis of all hits for a reference run without GEM support structure in the sensitive area.

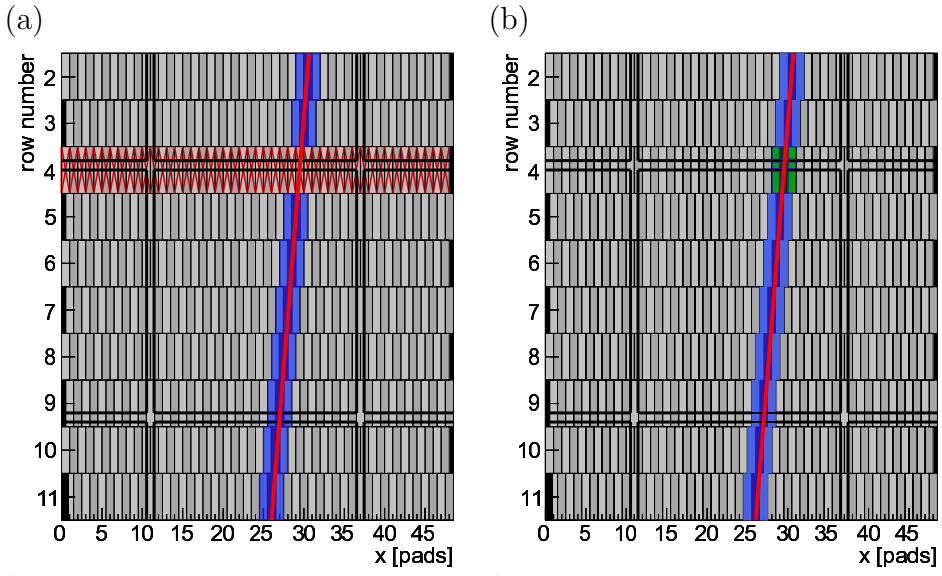

Figure 10.15: Illustration of reconstruction for single hit efficiency determination of the fourth row. (a) Sample 9/9: row four is taken out of the reconstruction, nine out of nine hits are required. (b) Sample 9/10: all rows are used in the reconstruction, at least nine hits are required. At the green position a hit is searched for the efficiency determination.

selection cuts for single hit efficiency			
slope	$\mid s_{9/9} - s_{9/10} \mid$	$<$	0.05
x intercept	$\mid I_{9/9} - I_{9/10} \mid$	$<$	1.0 mm
hit position	$\mid x_{fit} - x_{hit} \mid$	$<$	0.635 mm

Table 10.1: Cuts for tracks used for single hit efficiency determination.

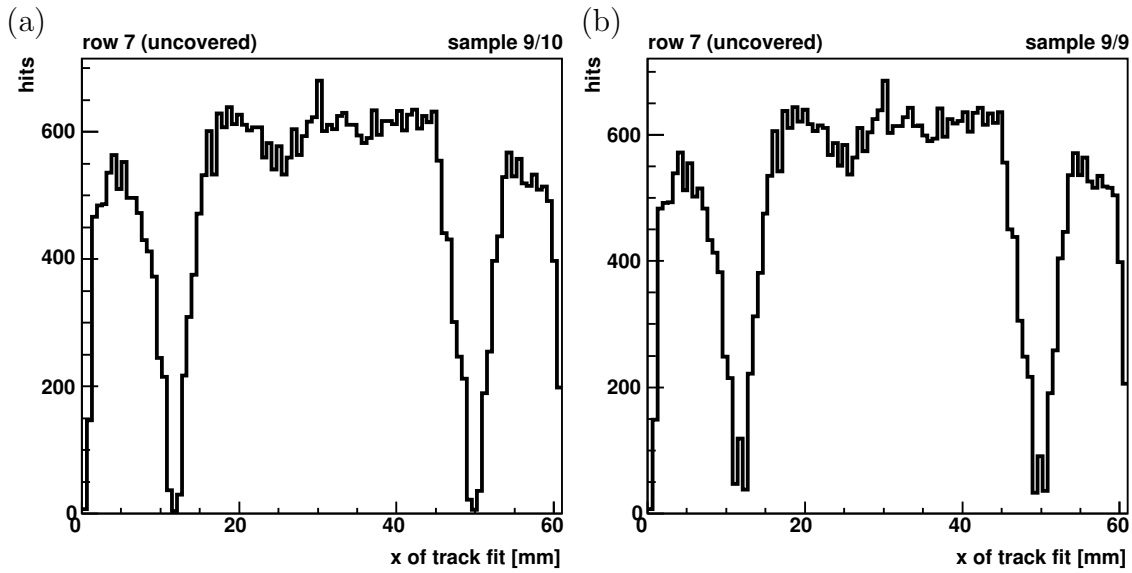

Figure 10.16: Hit positions as obtained from the track fit parameters for the single hit efficiency determination in an uncovered pad row. The bin width corresponds to half a pad pitch. (a) Hits of sample 9/10 as function of the x coordinate and (b) same distribution for monitor sample 9/9. In both histograms only hits contribute, which pass the selection criteria from table 10.1.

the single hit efficiency per row can be calculated. The track fit parameters are taken from the 9/9 sample and the 9/10 sample is searched for a hit in the inspected row. If a hit exists, its position is allowed to differ at most by half a pad pitch, as explained above. The procedure is applied to all tracks in the data set and the number of hits in both samples is plotted for each row as a function of the x coordinate.
In order to determine single hit efficiencies as a function of x, the histogram for sample 9/10 – shown in figure 10.16(a) – is divided by the one for the monitor sample 9/9 – visible in figure 10.16(b). The resulting single hit efficiency as a function of x for the uncovered row seven can be found in figure 10.17(a). The uncertainties are calculated with the help of Bayes theorem and the model of binomial distribution, more details about this method can be found in [Pat03]. The pure numerical value for the efficiency is obtained by dividing the numbers of hits by each other. For row seven a single hit efficiency of 98.363 % is determined. Both vertical grid bars influence three bins each. In these regions the efficiency drops significantly. But only three bins or 1.9 mm – less than two times the grid width – are influenced by

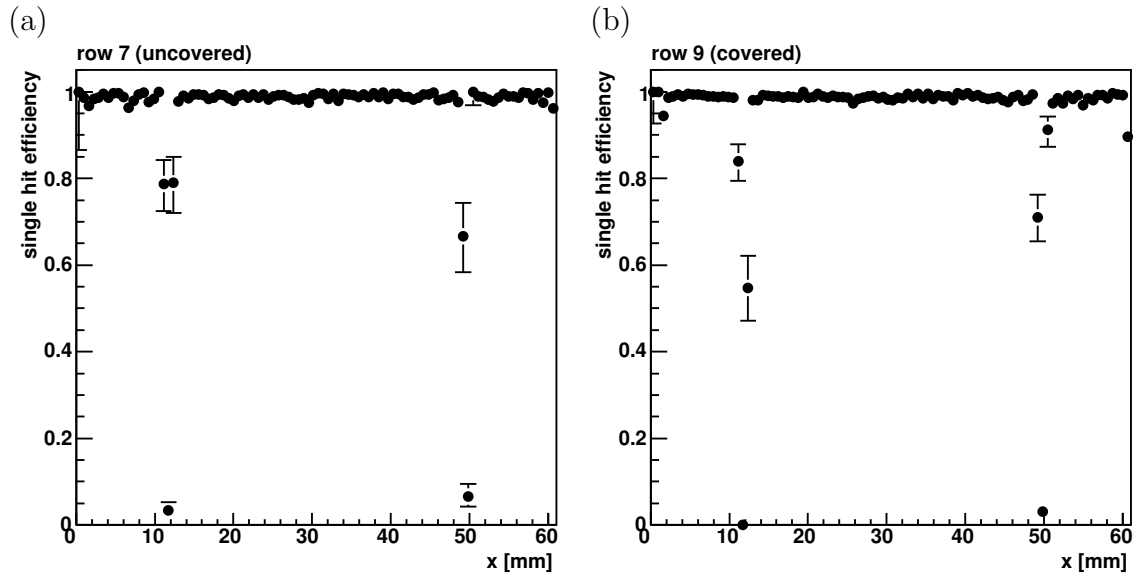

Figure 10.17: Single hit efficiencies for (a) the horizontally uncovered row seven and (b) row nine, covered by the lower horizontal grid bar.

the vertical structures. However, for a future application, the least possible number of vertical bars should be used.
The single hit efficiency for row nine – covered by one of the horizontal grid bars – is shown in figure 10.17(b). With 98.114 % the efficiency is not noticeable lower than for row seven. An overview over all row-wise single hit efficiencies as a function of the row number is given in figure 10.18 and the values are summarized in table 10.2 with their statistical uncertainties. It turns out, that the horizontal grid bars do not cause any decrease in these efficiencies. However, two effects are visible. First of all, the upper and lower rows – in figure 10.18 on the left and right – show a clear decrease in efficiency. Due to the long lever arm, the residuals in the topmost and bottom row become larger, as it can be seen in figure 6.8(b) on page 61. This yields a higher probability that the hit fails to fulfill the cut on the distance between reconstructed hit and fitted hit position. Hence, the single hit efficiency in these rows is smaller. A second effect, which is clearly visible in figure 10.18(b) is caused by dead pads. Row three and eight contain one, row eleven even two, dead pads. These cause less or shifted reconstructed hits, leading also to a drop in the single hit efficency. Row eleven is affected by both effects, which explains the relatively low efficiency of 92.756 %.
As a consequence, the single hit efficiency shown in figure 10.18 is not flat but, as expected, no influence of the horizontal support structure is visible, since the bars cover only one seventh of a pad row. The distribution is bent, due to different effects overlaying each other. In order to reduce these influences and to be able to draw a clear conclusion about the impact of the horizontal bars of the GEM support structure, a set of cuts – summarized in table 10.3 – is applied to the tracks.

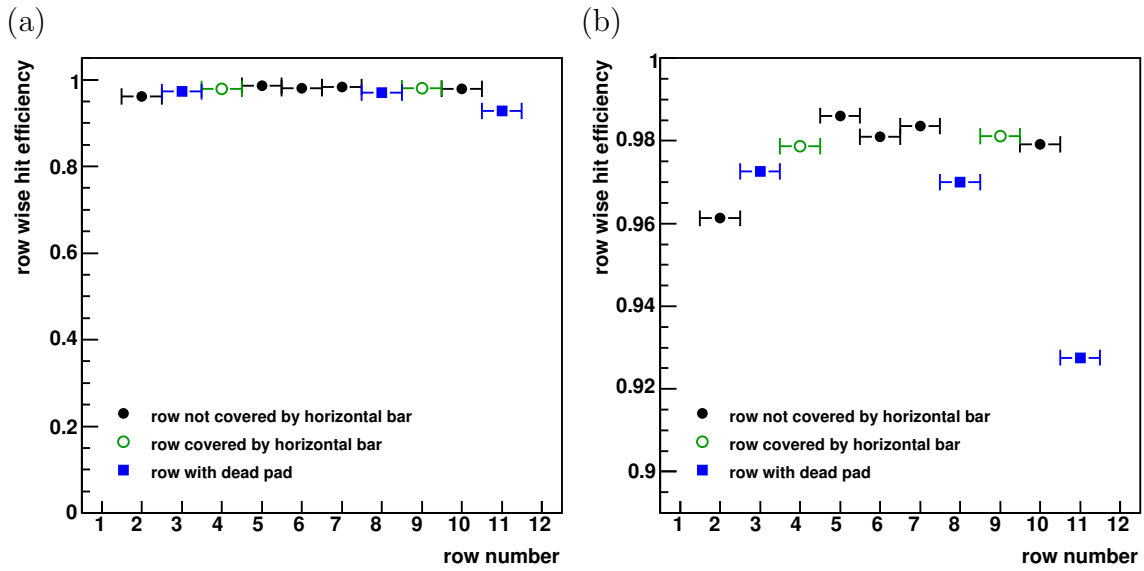

Figure 10.18: (a) Row-wise single hit efficiencies determined from the studies of hit efficiencies plotted over x direction, (b) same plot with zoom in the efficiency range on the y axis.

row	single hit efficiency [%]
2	$96.126\ ^{+0.089}_{-0.090}$
3	$97.255\ ^{+0.075}_{-0.076}$
4	$97.875\ ^{+0.066}_{-0.067}$
5	$98.609\ ^{+0.054}_{-0.055}$
6	$98.092\ ^{+0.063}_{-0.064}$
7	$98.363\ ^{+0.058}_{-0.059}$
8	$97.004\ ^{+0.078}_{-0.079}$
9	$98.114\ ^{+0.062}_{-0.063}$
10	$97.921\ ^{+0.065}_{-0.066}$
11	$92.756\ ^{+0.118}_{-0.119}$

Table 10.2: Row-wise single hit efficiencies.

track selection cuts	
inclination	$\mid \phi \mid < 0.05\,\mathrm{rad}$
inner region w/o dead pads	$18.5\,\mathrm{mm} < I_x < 43.1\,\mathrm{mm}$
intercept z	$3.0\,\mathrm{mm} < I_z < 633.0\,\mathrm{mm}$
z in bottom row	$3.0\,\mathrm{mm} < z_b < 633.0\,\mathrm{mm}$
curvature	$\mid \kappa \mid < 0.001\,\mathrm{mm}^{-1}$

Table 10.3: Track selection cuts used for single hit efficiency determination to ensure that tracks are well measured and fully contained in the sensitive area.

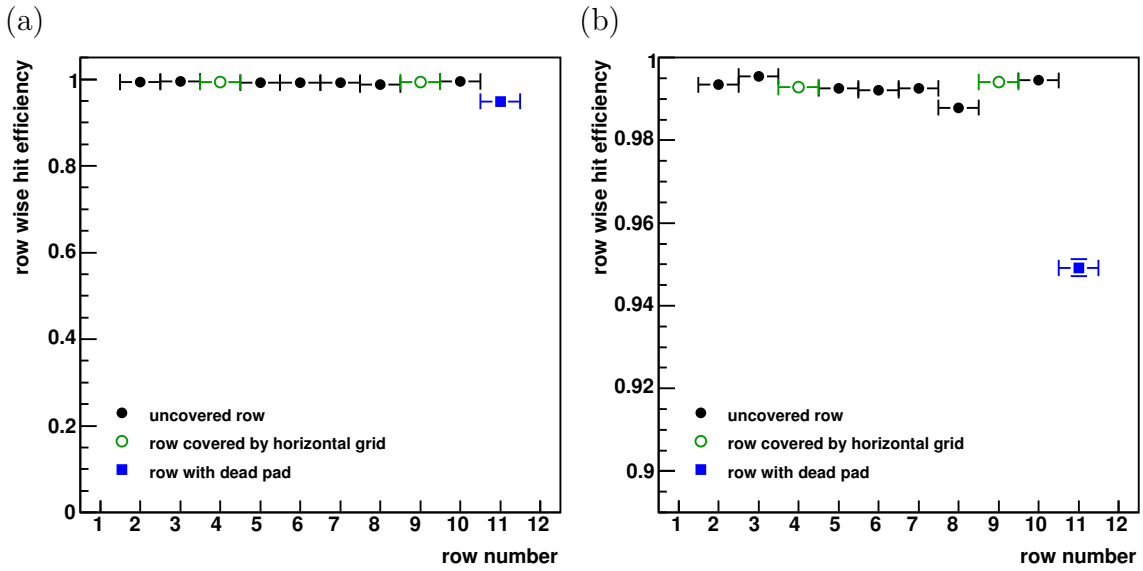

Figure 10.19: Single Hit Efficiency as function of rows after all applied cuts. (b) Flat efficiency distribution, only the last row has a lower value due to the remaining dead pad.

Two cuts are applied to restrict the studies to the region in between the vertical bars: the inclination angle ϕ has to be less than 0.05 rad and the x intercept of the tracks is restricted to $18.5 < I_x < 43.1$ to eliminate the influence of the vertical bars and the dead pads in row three and eight. One of the dead pads in row eleven is removed as well, the other one – in the middle of the x region – remains in the analyzed area. Removing also this pad, would cause a strong decrease in statistics. A cut on the z coordinate rejects tracks, which are leaving the chamber through the anode or cathode respectively. Finally, a cut on the curvature κ is introduced, to avoid tracks leaving the sensitive volume due to their curvature.
Using only tracks, which fulfill all above mentioned cuts, the single hit efficiency distribution is almost flat, as can be seen in figure 10.19. Only statistical uncertainties are plotted in the figures. A coarse estimation of the systematic uncertainties was determined by varying the track quality selection cuts. These variations lead to systematic uncertainties of the order of 0.2 %. They do not account for systematic uncertainties originating from other sources, like for example the used electronics.

However, assuming this systematic uncertainty of 0.2 %, the variations in figure 10.19 can be explained and no impact of the horizontal grid bars is visible. Only the remaining dead pad in row eleven decreases the efficiency significantly.

10.5 Grid Influence on Track Level

In this section, the impact of horizontal and vertical grid structures on residuals and distances and consequently the single point resolution is described. At the end, some considerations about the influence on tracking efficiency and dE/dx determination are presented.

10.5.1 Distance and Residual

Residuals and distances of hits describe the space between a found hit and the corresponding fitted track. In the case of residuals, the actual hit is excluded from the fit, while for distances the hit is included in the fit. Residuals and distances are used to calculate the single point resolution – which is presented in the next section – with the help of the geometric mean method described in chapter 6.

Vertical Bars

In figure 10.20(a), the distribution of the residuals is shown for the reference sample and the four regions next to the vertical grid bar as explained in section 10.4.1. Only the distribution for the adjacent pad deviates significantly from the reference. The small differences for the other distributions originate from fluctuations, which are also visible when comparing the reference distribution to a distribution obtained from a large part of the sensitive area without grid, as shown in figure 10.20(b). In contrast to the other distributions, the one for the adjacent region is not symmetric around zero, the maximum is shifted towards positive values of x and a tail in the negative part is present. The influence of the grid structure is, that hits are pushed away from the bars during the reconstruction. Since only the regions to the right of the grid bars are analyzed, the asymmetry can be explained. The residual distribution of all other regions are symmetric, which confirms again, that the influence of the grid affects only the directly adjacent pads.
The same observations can be made for the distance distribution, shown in figures 10.21(a) and 10.21(b). Since the specific analyzed hit is used for the fit during the distance calculation, the fit is pulled towards the actual hit. In consequence, the distribution of distances is narrower than residual distributions.

Horizontal Bar

In figure 10.22(a), the uncertainty on the x coordinate of hits is shown for rows covered by horizontal grid bars, not covered by grid and not covered but adjacent

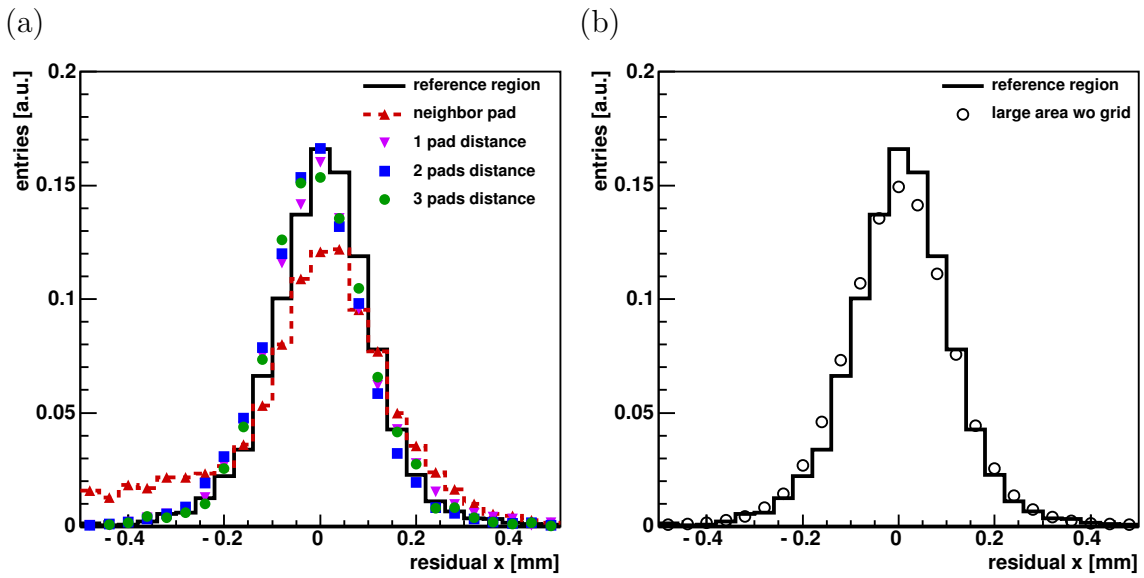

Figure 10.20: (a) Grid influence on hit residuals in x direction, compared are regions with different distances to a vertical grid bar. (b) Comparison of hit residuals in x direction for the reference region with a large region in between the grid bars. All distributions are normalized to the number of entries.

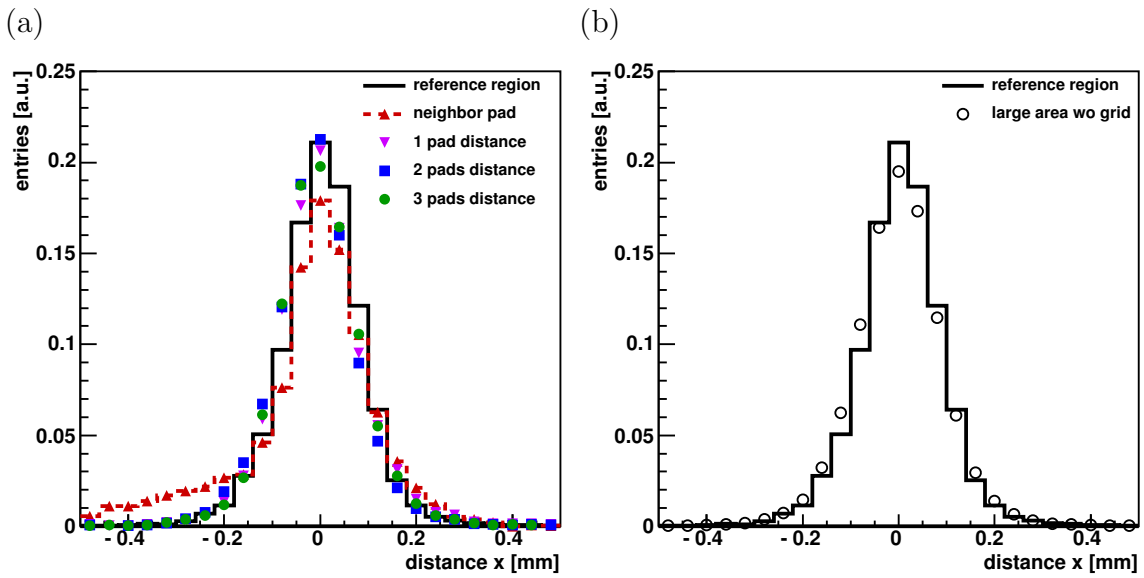

Figure 10.21: (a) Grid influence on hit distance in x direction, compared are regions with different distances to a vertical grid bar. (b) Comparison of hit distance in x direction for the reference region with a large region in between the grid bars. All distributions are normalized.

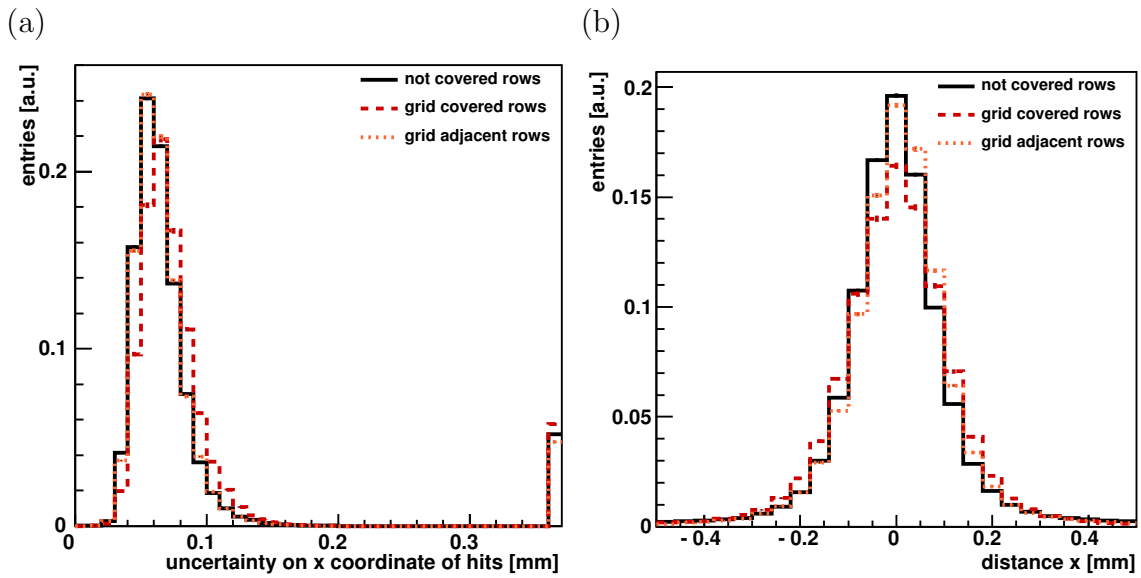

Figure 10.22: Influence of horizontal grid bar on (a) the uncertainty on x coordinate of hits and (b) the hit distance in x direction. The distributions are normalized.

to a row with horizontal bar. This values are directly related to the distance. The uncertainty on the position is larger in a grid covered row. Consequently, the hit gets a smaller weight during the fitting procedure and is not able to pull the fitted track into its direction as much as a hit with a smaller uncertainty. Distributions of the distances for hits in the same rows are shown in figure 10.22(b). As expected, the distances get larger for adjacent and grid covered rows.

10.5.2 Single Point Resolution

The single point resolution is an observable of particular importance in tracking detectors. It translates into the momentum resolution of a large scale TPC and gives a handle to judge the performance.
In figure 10.23, a reference run with a frame GEM setup is compared with the grid GEM measurement. Both measurements were performed in a magnetic field of 4 T and with the identical GEM settings. The tracks are selected according to the cuts summarized in table 9.3 on page 121.
The differences in the single point resolution between both measurements are small – about 5 µm – which is in the range of run to run variations. The single point resolution stays below 100 µm almost over the whole drift length of the prototype. The global fit method with free sigma shows a significantly better performance for the grid GEM setup, in particular at drift lengths below 200 mm. The reason was studied and the differences arise from the sensitivity of this method to the noise level. The reference run has a higher noise level and consequently the method produces

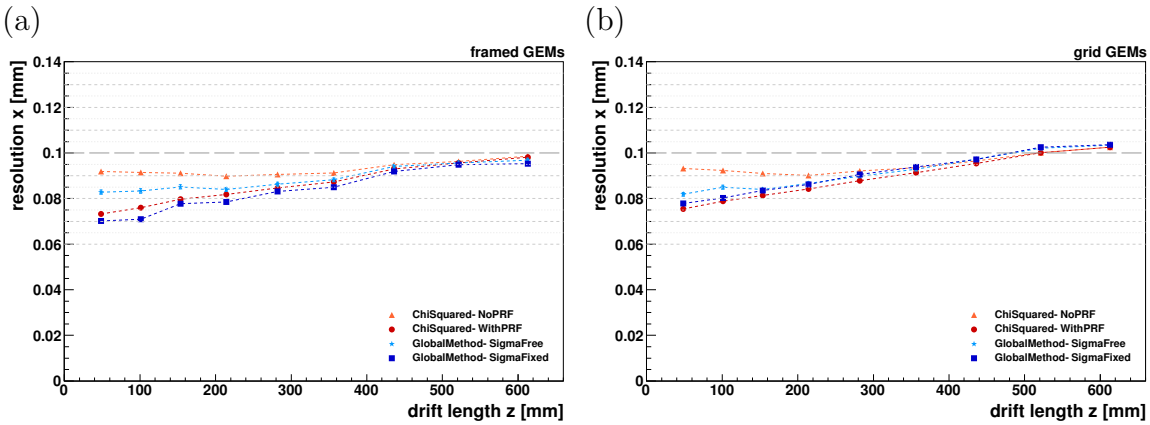

Figure 10.23: Single point resolution as function of the drift length for (a) a reference data set and (b) a grid GEM data set. Both sets were taken with the same field configuration and ten out of ten hits were required.

worse results. A detailed study of the behavior of the global fit method with free sigma can be found in [Die06].

Horizontal Bar

To draw a conclusion about the influence of horizontal structures on the single point resolution, the effects of horizontal and vertical bars have to be disentangled. Hence, a harder cut on the x coordinate of hits is made to exclude the outer regions with the vertical bars. With $15.3\,\text{mm} < x_{\text{hit}} < 46.3\,\text{mm}$ a safety margin of 3 mm to the vertical bars is established. For a detailed understanding of the impact of horizontal coverage, a comparison of row-wise single point resolutions is presented in figure 10.24. The χ^2 method using a pad response correction was used to calculate this resolutions. A very clear distinction can be made between the single point resolution in the grid covered and the not covered row, almost 20 µm difference can be observed over the full drift length. The two grid adjacent rows show different results. The one closer to the horizontal bar – row ten, cf. figure 10.5(a) – is much more influenced than row three, whose results are only slightly worse than those of the two reference rows.
A comparison of the single point resolution over all rows, but with the restricted x region can be seen in figure 10.25(a). The results clearly show that the horizontal bars have no influence on the complete measurement in terms of the single point resolution.

Vertical Bar

To illustrate the influence of vertical bars on the single point resolution, two sets of different regions of x are compared in figure 10.25(b). One set including the x ranges around both vertical grid bars, while the other contains two reference areas

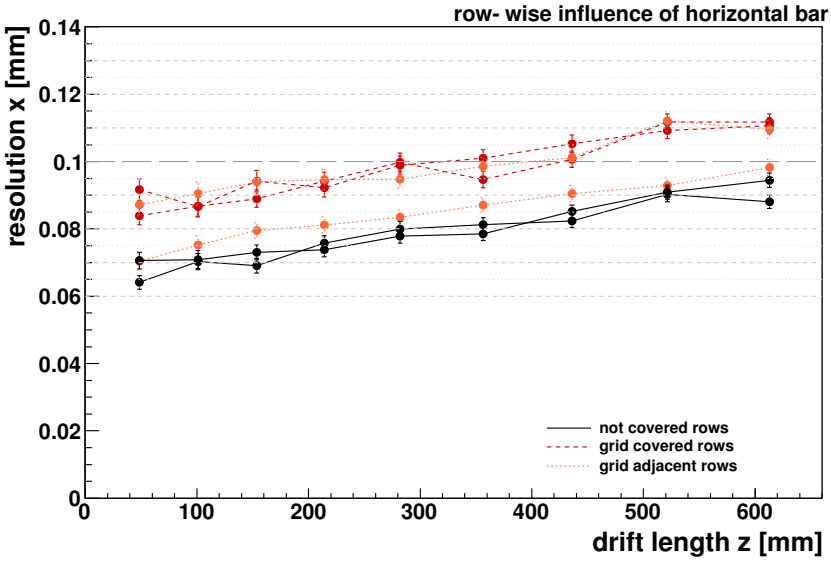

Figure 10.24: Influence of horizontal grid bar on single point resolution deduced by the χ^2 method with pad response correction. Shown are single point resolutions as function of the drift length for six individual rows, two for each case mentioned in the legend. An impact of the vertical bars is avoided via a cut on the inner x region ($15.3\,\mathrm{mm} < x_{\mathrm{hit}} < 46.3\,\mathrm{mm}$).

of the same width, but not covered by a vertical bar. Each area has a width of 8.62 mm: 1 mm for the bar itself and three pads to the left and to the right. The width of the areas is defined by the need to be close to the vertical bar in order to be sensitive to the effects and to be wide enough to have large enough statistics to gain reliable results without large statistical fluctuations. Furthermore, a certain width is needed to avoid an intrinsic ϕ cut in addition to the phi requirement from table 9.3. For this comparison, tracks with at least six out of ten hits are used, since by a requirement of ten hits an implicit improvement of the situation would be made, because the vertical grid is influencing the hit reconstruction. Requiring ten hits, would mean that tracks influenced by the grid are excluded from the data sample. A clear difference for the reference and the grid covered regions is visible. The deviations develop from 10 µm at short drift distances to almost 20 µm at the very end of the chamber. In the case of the covered regions, less statistics is available increasing the uncertainties on the single point resolution.

Result

To summarize the effect on the single point resolution, it can be stated, that the overall resolution is not affected in a critical way. The impact of the vertical bars is as expected larger, compared to the one from the horizontal structures, which is negligible. For a large scale TPC, where many hits per track are available, hits close

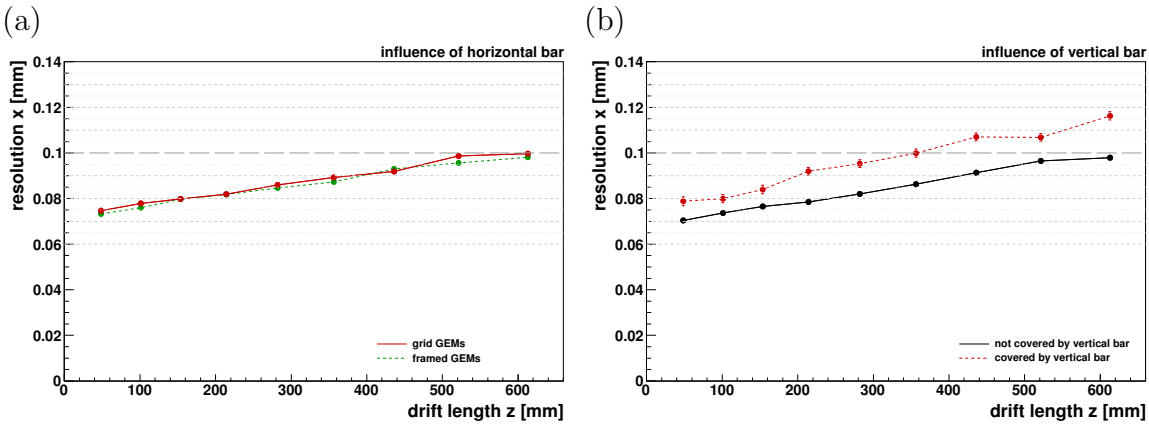

Figure 10.25: (a) Influence of horizontal grid bars on single point resolution as a function of the drift length. The region in x is restricted to $15.3\,\mathrm{mm} < x_{\mathrm{hit}} < 46.3\,\mathrm{mm}$. (b) Single point resolution for regions covered by a vertical grid bar: $7.49\,\mathrm{mm} < x_{\mathrm{hit}} < 16.11\,\mathrm{mm}$ or $45.59\,\mathrm{mm} < x_{\mathrm{hit}} < 54.11\,\mathrm{mm}$ and two x ranges: $15.00\,\mathrm{mm} < x_{\mathrm{hit}} < 23.62\,\mathrm{mm}$ or $25.00\,\mathrm{mm} < x_{\mathrm{hit}} < 33.62\,\mathrm{mm}$, where no vertical bar is shadowing the pad plane.

to support structures can safely be taken out of the track fit and with it out of the single point or momentum resolution determination.

10.5.3 Tracking Efficiency and dE/dx Determination

Tracking efficiencies cannot be determined with the prototype assembly used in this thesis, since no external reference for the tracks is available. Such studies will become possible with the large prototype setup, described in chapter 6, since the infrastructure of this prototype setup includes silicon detectors, which are able to provide two reference points, before and after the TPC volume. With the help of these reference hits, a tracking efficiency of the TPC in between can be determined. Experience at ALEPH showed, that the tracking efficiency for isolated particles traversing the full radius of the TPC was almost 100 % [A+91]. For particles in jets with momenta of at least 1 GeV the tracking efficiency is quoted with 98.6 %.
The analysis presented here, shows that only the vertical bars have an influence on the hit reconstruction in a way, that hits close to the structure are not linked to the corresponding track. All tracks need to have a sufficient number of hits on their way through the chamber, to ensure high tracking efficiencies for the ILD TPC. Hence, in particular straight tracks with a large transverse momentum passing along a sector boundary or support structure bar, require a careful design of staggered readout modules and grid support structures. A track with a transverse momentum of $p_T = 100\,\mathrm{GeV}$ in a magnetic field of 3.5 T has a radius of about 95 m. With this small curvature, the track stays over a length of 87 cm on a 1 mm wide strip, for example a module border or a grid bar. Taking into account one adjacent pad of 1.27 mm width on both sides of a vertical grid structure, the track would follow this region for 1.64 m – almost the whole ILD TPC radius. Although 100 GeV

transverse momentum are pretty much, such considerations emphasize the necessity of a sophisticated design for the TPC endplate. Radially aligned gaps in the instrumentation have to be avoided.
For dE/dx determination, quality cuts on the hits have to be applied, as described in section 7.5. These cuts account for various effects and construction of the chamber. In particular sector boundaries have to be cut out. For the grid support structure, additional geometric cuts have to be introduced. In order to obtain precise information, vertical and horizontal bars have to be taken into consideration, since both influence the measured charge per hit. However, to ensure reliable dE/dx information for particle identification in the ILD TPC, much fewer than all 200 maximal available space points will be necessary. At OPAL, at least 25 % of all available hits were required for the truncated mean method [H$^+$92]. A somewhat larger fraction of hits may be needed in the ILD TPC, since the OPAL jet chamber was with an overpressure of 4 bar designed for a particular good dE/dx performance, which enhanced the quality of the single measurements at the expense of a larger fraction or radiation length inside the calorimeters.

10.6 Summary of Grid Influence

In order to give a prospect for the design of a future GEM mounting module, the impact of horizontal and vertical grid bars – as determined from cosmic muon data recorded with a TPC prototype at DESY – are summarized in the following. Subsequently, some thoughts about a possible advanced grid layout are presented.

10.6.1 Influence of Horizontal Support Structures

On pulse level, the influence of the horizontal bars is only visible by a slightly smaller number of pulses in rows covered by a grid bar or grid adjacent rows caused by a threshold effect. Hits in rows covered by a horizontal bar consist more often of two instead of three pulses, causing a slightly larger uncertainty on the x coordinate of the hit position. The single hit efficiency is not affected, since the bars cover only one seventh of the total pad height. Due to the larger uncertainties on x_{hit}, also the distribution of the distance between hit position and track fit becomes broader compared to uncovered rows. A comparison of row-wise determined single point resolutions shows differences of up to 20 µm for uncovered rows to rows covered by horizontal bars. Depending on their distance to the grid bar, the adjacent rows show also a declined single point resolution compared to the uncovered rows. The single point resolution for all rows – excluding the areas around the vertical bars – does not suffer. Compared to a reference run – taken with GRP framed GEMs – almost no deviations are visible.
The tracking efficiency is assumed to be not influenced by the horizontal bars, since no hits are lost. For dE/dx determination, quality cuts will be necessary to reject

hits from rows, which are covered by either horizontal or vertical bars, since both have an impact on the charge deposition.

10.6.2 Influence of Vertical Support Structures

The vertical grid bars cause less pulses and a decreased charge per pulse in the accordant x regions. On hit level, the impact can be seen in several quantities. Comparing the number of pulses per hit and the hit charge, it can be deduced that the influence expands to one pad on both sides of the 1 mm wide bar. The hit positions show, that almost no hits are reconstructed in gaps of about two millimeter width. While in the adjacent region of half a pad pitch more hits are found. The reason for this is that hit positions are shifted due to the grid into the direction of the neighboring pad. An investigation of the underlying effect, which may be caused by an electric charging of the grid surface, should be performed in future analyses. As a consequence of the vertical bars, the single hit efficiency drops significantly in these regions of about two millimeter width around the vertical structure.
About ten percent of the tracks in the used setup – defined by the cell size of the grid and the narrow inclination angle ϕ spectrum – loose more than one hit due to the vertical structure. This indicates the necessity of a good staggering scheme of the modules and support structures for the ILD TPC, in order to achieve a good tracking efficiency also for tracks with a large transverse momentum. Distances and residuals recover normal shapes, as soon as the hits have more than one pad distance to the vertical grid bars. Close to the bars, the single point resolution is up to 20 µm worse compared to reference regions not influenced by vertical bars. The impact on the charge information, which is used to obtain dE/dx values, is large and geometrical cuts have to be introduced, in order to ensure reliable particle identification via dE/dx measurements.

10.6.3 Design of an Advanced Grid Structure

Several mechanical aspects have to be considered for the design of a second generation of the grid support structure. The cell size is a matter of optimization of provided flatness of the GEM foils versus the material budget and dead areas introduced into the detector. This material budget can be further reduced by using grids with smaller height and width, provided that the difficulties in the production can be solved. Such thin grids could be used to ensure the flatness of the GEM foils, whereas the required transfer distances between the GEMs can be provided by spacers, which are only installed in the corners of the structure. In addition, the gluing process and GEM design can be improved, to make it possible to glue the foils onto every grid bar. This is likely to further improve the flatness of the GEM foils.
The analysis of the impact of horizontal and vertical structures shows, that the vertical bars are much more critical and that a design with the least possible number

of vertical – or in a large chamber, radial – bars should be favored. In addition, the design and placement of the modules relative to each other is very important. A staggering scheme especially for the radial bars becomes important to ensure also for high p_T tracks a sufficient number of precise hits.

Chapter 11

Summary & Conclusions

Analyses of characteristic GEM properties and the development and testing of a grid GEM support structure are presented in this thesis. With a small TPC prototype assembly, comparative measurements of effective gains and energy resolutions have been performed. The setup is well suited for such measurements, although a determination of precise absolute effective gain values was not possible due to large overall normalization uncertainties. Within these large normalization uncertainties, the measurements can be reproduced by a parametrization of effective GEM gains. The comparison of measured effective gains of foils from different manufacturers is well understood, if the different geometrical parameters are taken into account. Only the influence of the insulator material cannot be disentangled from the influence of the hole shape, since the specific GEMs differ in both parameters at once. The energy resolution has been measured to be 10-20 %, which is compatible with previous studies. The differences between the measured foils are marginal in this respect. GEM foils produced by the CERN workshop have been found to provide in both aspects, effective gain and energy resolution, the best performance.
A procedure for height profile measurements of GEM foils has been developed. The resulting profiles, with maximum height differences between 380 µm and 920 µm, depending on the GEM, have been used to simulate effective gain maps. With these maps, the effects of gain variations have been analyzed. For simulated tracks, variations of the mean gain value of about 0.7 % have been determined. Such variations can become critical for dE/dx measurements, since for reliable dE/dx determination, variations of the averaged gain larger than 10 % of the dE/dx resolution $\sigma_{\mathrm{dE/dx}}$ have to be avoided. At the ILD a dE/dx resolution of 5 % is anticpiated, which would allow for variations of the mean gain of the order of 0.5 %. In order to reduce this effect, a careful choice of GEM foils is sensible. The impact of gain variations on the single point resolution determination is negligible. In addition, the influence of bent GEMs on the drift field quality has been simulated. The resulting field map contains field deviations $\Delta E/E$ of the order of $10^{-2.25}$, which is almost two orders of magnitude worse, than the envisaged field homogeneity of $\Delta E/E < 10^{-4}$. A translation of this result into a systematic uncertainty of 3 % on the single point resolution,

has shown, that also in this aspect a careful GEM quality control concerning their flatness is advisable.
A novel scheme to support and mount GEM foils inside a TPC has been developed, in order to be able to cover a large readout area with the least possible dead material. This structure is made of a ceramic grid glued in between the GEM foils. Ceramic is due to its electrical and mechanical properties a material, which is well suitable for applications in a TPC. It is a good insulator and on the same time very stiff. The material budget has been reduced compared to GRP mounting frames and a very flat mounting can be achieved, without stretching of the GEMs. The new support structure allowed for stable operation and has been successfully tested in a medium size TPC prototype.
In order to quantify the impact of the grid GEMs on the track reconstruction, cosmic muons have been recorded in a magnetic field of 4 T. The data analysis has shown that the influence of the ceramic grid will be visible in all steps of the track reconstruction, from pulse over hit to track level due to a reduction of the detected charge. However, the impact of horizontal and vertical bars – perpendicular and parallel to the long axis of a readout pad – has to be treated separately. Horizontal or pad perpendicular structures do not cause any problems. The hit efficiency is not affected at all, the single point resolution obtained with grid GEMs in between the vertical bars is competitive, only for dE/dx determination additional quality cuts will have to be introduced to ensure a reliable measurement. Vertical or pad parallel bars produce shifted hits in their immediate vicinity and, for about 10 % of the tracks, more than one hit has not been reconstructed due to the pad parallel structure. The single point resolution is worsened by up to 20 % around these structures and hits close to pad parallel bars have to be removed from dE/dx samples. However, in the end the benefits will outweigh these caveats and will help to improve track reconstruction and in particular dE/dx measurements in future GEM TPCs. The advantages of the grid support structure are the small amount of material, the achievable flatness without the need of stretching the foils, the almost edgeless module borders and the possibility to cover large areas without significant gaps. The developed grid mounting will allow for the step from small GEM applications for proof-of-principle studies to a large scale GEM TPC in modern high energy detectors like the ILD.

List of Figures

List of Tables

References

[4th09] *4th concept web site*, (2009), `http://www.4thconcept.org`.

[A+91] W. B. Atwood et al., *Performance of the ALEPH time projection chamber*, Nucl. Instrum. Meth. **A306**, 446–458 (1991).

[A+02] M. C. Altunbas et al., *Construction, test and commissioning of the triple-GEM tracking detector for COMPASS*, Nucl. Instrum. Meth. **A490**, 177–203 (2002).

[A+06] D. Attié et al., *Ongoing activities at Saclay*, (2006), EUDET-Memo-2006-10.

[AC80] W. W. M. Allison and J. H. Cobb, *Relativistic Charged Particle Identification by Energy Loss*, Ann. Rev. Nucl. Part. Sci. **30**, 253–298 (1980).

[ALEPH95] D. Buskulic et al. (ALEPH), *Performance of the ALEPH detector at LEP*, Nucl. Instrum. Meth. **A360**, 481–506 (1995).

[ALEPH06] C. Grupen, (ed.) et al. (ALEPH), *The ALEPH Experience – 25 years of memories*, (2006), `http://aleph.web.cern.ch/aleph`.

[ALICE00] G. Dellacasa et al. (ALICE), *ALICE technical design report of the time projection chamber*, (2000), CERN-OPEN-2000-183.

[ANC10] *ANCeram company web site – technical ceramics*, (2010), `http://www.anceram.com/3_keramik/produktbeschreibung_en.php`.

[B+64] V. E. Barnes et al., *Observation of a Hyperon with Strangeness -3*, Phys. Rev. Lett. **12**, 204–206 (1964).

[B+99] S. Bachmann et al., *Charge amplification and transfer processes in the gas electron multiplier*, Nucl. Instrum. Meth. **A438**, 376–408 (1999).

[B+02] S. Bachmann et al., *Discharge mechanisms and their prevention in the gas electron multiplier (GEM)*, Nucl. Instrum. Meth. **A479**, 294–308 (2002).

[B+03] P. S. Barbeau et al., *A first mass production of gas electron multipliers*, Nucl. Instrum. Meth. **A515**, 439–445 (2003), hep-ex/0304013.

[B+04] O. S. Bruning, (ed.) et al., *LHC design report. Vol. I: The LHC main ring*, (2004), CERN-2004-003-V-1.

[B+08] H. Blank et al., *Towards a Digital TPC for the LC*, (2008), EUDET-Memo-2008-43.

[Bal08] M. Ball, *Methods and results for calibration and track separation of a GEM based TPC using an UV-laser*, Phd thesis, Hamburg University, 2008, DESY-THESIS-2008-051.

[Bar09] B. Barrish, *GDE Report*, (2009), `http://ilcagenda.linearcollider.org/getFile.py/access?contribId=8&sessionId=2&resId=1&materialId=slides&confId=3461`.

[BBSV03] A. Bondar, A. Buzulutskov, L. I. Shekhtman and A. Vasiljev, *Study of ion feedback in multi-GEM structures*, Nucl. Instrum. Meth. **A496**, 325–332 (2003), physics/0208017.

[Bec08] J. Beck, *Gasverstärkungseigenschaften von GEM-Folien – in german*, diploma thesis, supervised by Lea Hallermann, Hamburg University, 2008, DESY-THESIS-2009-002.

[Bet33] H. Bethe, *Handbuch der Physik 24/1*, Springer, Berlin, 1933, p. 491.

[BGJW04] M. Ball, N. Ghodbane, M. Janssen and P. Wienemann, *A DAQ System for Linear Collider TPC Prototypes based on the ALEPH TPC Electronics*, (2004), LC-DET-2004-013.

[Bic06] H. Bichsel, *A method to improve tracking and particle identification in TPCs and silicon detectors*, Nucl. Instrum. Meth. **A562**, 154–197 (2006).

[BNL74] J. J. Aubert et al. (BNL, E598), *Experimental Observation of a Heavy Particle J*, Phys. Rev. Lett. **33**, 1404–1406 (1974).

[Boh08] M. Bohler, *Reconstruction of photon conversions in tau lepton decays in the ATLAS experiment*, diploma thesis, Hamburg University, 2008, DESY-THESIS-2009-013.

[Bon06] M. Bondila, *Detection of Charged Kaons Using the Decay Topology in ALICE TPC*, Phd thesis, University of Jyvaeskylaes, 2006.

[Bow95] C. Bowdery, (ed.), *ALEPH Handbook, Volume 1*, (1995), CERN 2nd edition.

[BTH06] U. Becker, B. Tamm and S. Hertel, *Test and evaluation of new GEMs with an automatic scanner*, Nucl. Instrum. Meth. **A556**, 527–534 (2006).

[C+86] D. F. Cowen et al., *Gating in the ALEPH Time Projection Chamber*, Nucl. Instrum. Meth. **A252**, 403–406 (1986).

[C+05] R. K. Carnegie et al., *Resolution studies of cosmic-ray tracks in a TPC with GEM readout*, Nucl. Instrum. Meth. **A538**, 372–383 (2005), physics/0402054.

[CCFT64] J. H. Christenson, J. W. Cronin, V. L. Fitch and R. Turlay, *Evidence for the 2 pi Decay of the k(2)0 Meson*, Phys. Rev. Lett. **13**, 138–140 (1964).

[CDF95] F. Abe et al. (CDF), *Observation of top quark production in $\bar{p}p$ collisions*, Phys. Rev. Lett. **74**, 2626–2631 (1995), hep-ex/9503002.

[Che09] M. A. Chefdeville, *Development of micromegas-like gaseous detectors using a pixel readout chip as collecting anode*, Phd thesis, University of Amsterdam, 2009.

[CMS08] R. Adolphi et al. (CMS), *The CMS experiment at the CERN LHC*, JINST **0803**, S08004 (2008).

[CMS09] The CMS Collaboration (CMS), *Commissioning and Performance of the CMS Silicon Strip Tracker with Cosmic Ray Muons*, (2009), 0911.4996.

[CST10] *CST web site*, (2010), `http://www.cst.com/Content/Products/EMS/Overview.aspx`.

[D095] S. Abachi et al. (D0), *Observation of the top quark*, Phys. Rev. Lett. **74**, 2632–2637 (1995), hep-ex/9503003.

[Die06] R. Diener, *Study of reconstruction methods for a time projection chamber with GEM gas amplification system*, diploma thesis, Hamburg University, 2006, DESY-THESIS-2006-040.

[Die09] R. Diener, *private communication*, (2009).

[DRW81] S. Dimopoulos, S. Raby and F. Wilczek, *Supersymmetry and the Scale of Unification*, Phys. Rev. **D24**, 1681–1683 (1981).

[E+01] V. Eckardt et al., *Calibration of the STAR forward time projection chamber with krypton-83m*, (2001), nucl-ex/0101013.

[EB64] F. Englert and R. Brout, *Broken Symmetries and the Masses of Gauge Boson*, Phys. Rev. Lett. **13**, 321–322 (1964).

[Fan47] U. Fano, *Ionization Yield of Radiations. 2. The Fluctuations of the Number of Ions*, Phys. Rev. **72**, 26–29 (1947).

[Fan09] Fang, Yaquan (for the ATLAS Collaboration), *Standard Model $H\gamma\gamma$ discovery potential with ATLAS*, (2009), 0910.2149.

[FF77] P. Fayet and S. Ferrara, *Supersymmetry*, Phys. Rept. **32**, 249–334 (1977).

[FGML73] H. Fritzsch, M. Gell-Mann and H. Leutwyler, *Advantages of the Color Octet Gluon Picture*, Phys. Lett. **B47**, 365–368 (1973).

[FLA10] *FLASH web site*, (2010), `http://flash.desy.de`.

[Gas09] *Gas properties studied at Saga University – web site*, (2009), `http://www-hep.phys.saga-u.ac.jp/ILC-TPC/gas/`.

[GDD10a] *Gas Detector Development Group web site*, (2010), `http://gdd.web.cern.ch/GDD/`.

[GDD10b] *GEM framing - Gas Detector Development Group web site*, (2010), `http://gdd.web.cern.ch/GDD/gemframing.html`.

[GHK64] G. S. Guralnik, C. R. Hagen and T. W. B. Kibble, *Global Conservation Laws and Massless Particles*, Phys. Rev. Lett. **13**, 585–587 (1964).

[GIM70] S. L. Glashow, J. Iliopoulos and L. Maiani, *Weak Interactions with Lepton-Hadron Symmetry*, Phys. Rev. **D2**, 1285–1292 (1970).

[Gin09] C. Ginsburg, *Global Cavity Database Report*, (2009), `http://ilcagenda.linearcollider.org/getFile.py/access?contribId=182&sessionId=29&resId=1&materialId=slides&confId=3461`.

[Gla61] S. L. Glashow, *Partial Symmetries of Weak Interactions*, Nucl. Phys. **22**, 579–588 (1961).

[Glu63] R. L. Gluckstern, *Uncertainties in track momentum and direction, due to multiple scattering and measurement errors*, Nucl. Instrum. Meth. **24**, 381–389 (1963).

[GM64] M. Gell-Mann, *A Schematic Model of Baryons and Mesons*, Phys. Lett. **8**, 214–215 (1964).

[God06] R. M. Godbole, *LHC-ILC synergy*, Acta Phys. Polon. **B37**, 1225–1236 (2006), hep-ph/0604230.

[Goe10] J. W. Goethe, *Faust. Der Tragödie erster Teil – english version translated by George Madison Priest*, (2010), `http://www.levity.com/alchemy/faust02.html`.

[GRRC96] Y. Giomataris, P. Rebourgeard, J. P. Robert and G. Charpak, *MICROMEGAS: A high-granularity position-sensitive gaseous detector for high particle-flux environments*, Nucl. Instrum. Meth. **A376**, 29–35 (1996).

[Gru99] M. Gruwe, *Gas Studies for a TPC of a detector for the future linear collider TESLA*, (1999), LC-DET-1999-003-TESLA.

[H+92] M. Hauschild et al., *Particle identification with the OPAL jet chamber*, Nucl. Instrum. Meth. **A314**, 74–85 (1992).

[Hau96] M. Hauschild, *Progress in dE/dx techniques used for particle identification*, Nucl. Instrum. Meth. **A379**, 436–441 (1996).

[Hau06] M. Hauschild, *dE/dx and Particle ID Performance with Cluster Counting*, (2006), `http://ilcagenda.linearcollider.org/materialDisplay.py?contribId=159&sessionId=10&materialId=slides&confId=1049`.

[Hau09] M. Hausschild, *private communication*, (2009).

[Heg10] F. Hegner, *private communication*, (2010).

[HERA-B00] T. Zeuner (HERA-B), *The MSGC-GEM Inner Tracker for HERA-B*, Nucl. Instrum. Meth. **A446**, 324–330 (2000).

[Hig64a] P. W. Higgs, *Broken Symmetries and the Masses of Gauge Boson*, Phys. Rev. Lett. **13**, 508–509 (1964).

[Hig64b] P. W. Higgs, *Broken symmetries, massless particles and gauge fields*, Phys. Lett. **12**, 132–133 (1964).

[IDAG09] I. D. A. Group (IDAG), *IDAG Report on the Validation of Letters of Intent for ILC detectors*, (2009), `http://ilcdoc.linearcollider.org/record/23970/files/`, ILC-REPORT-2009-021.

[ILC07] J. Brau, (ed.) et al. (ILC), *International Linear Collider Reference Design Report. 1: Executive summary. 2: Physics at the ILC. 3: Accelerator. 4: Detectors*, (2007), ILC-REPORT-2007-001.

[ILD09] ILD, *International Large Detector web site*, (2009), `http://www.ilcild.org`.

[JADE80] W. Bartel et al. (JADE), *Observation of Planar Three Jet Events in e+ e- Annihilation and Evidence for Gluon Bremsstrahlung*, Phys. Lett. **B91**, 142 (1980).

[Jan04] M. E. Janssen, *Auflösungsstudien an einer Zeit-Projektions-Kammer (TPC) mit GEM Gasverstärkungssystem – in german*, diploma thesis, Dortmund University, 2004, DESY-THESIS-2004-049.

[Jan08] M. E. Janssen, *Performance studies of a time projection chamber at the ILC and search for lepton flavour violation at HERA II*, Phd thesis, Hamburg University, 2008, DESY-THESIS-2008-011.

[Jar07] J. Jaros, *Experiments at the ILC*, (2007), `http://ilcagenda.linearcollider.org/getFile.py/access?contribId=8&sessionId=0&resId=0&materialId=slides&confId=1556`.

[K+03] M. Killenberg et al., *Modelling and measurement of charge transfer in multiple GEM structures*, Nucl. Instrum. Meth. **A498**, 369–383 (2003), physics/0212005.

[K+04] M. Killenberg et al., *Charge transfer and charge broadening of GEM structures in high magnetic fields*, Nucl. Instrum. Meth. **A530**, 251–257 (2004).

[Kak93] M. Kaku, *Quantum field theory: A Modern introduction*, (1993), New York, USA: Oxford Univ. Pr. 785 p.

[Kal60] R. E. Kalman, *A New Approach to Linear Filtering and Prediction Problems*, Transactions of the ASME-Journal of Basic Engineering **82**, (Series D): 35–45 (1960).

[Kam05] J. Kaminski, *Developing studies for a time projection chamber at the International Linear Collider (ILC)*, Phd thesis, Karlsruhe University (TH), 2005, IEKP-KA-2005-15.

[Key08] Keyence, *LK-G10 Manual*, (2008), `http://www.keyence.com`.

[KLM+05] J. Kaminski, B. Ledermann, T. Muller, S. Kappler and M. T. Ronan, *Study of various anode pad readout geometries in a GEM- TPC*, IEEE Trans. Nucl. Sci. **52**, 2900–2906 (2005).

[KM73] M. Kobayashi and T. Maskawa, *CP Violation in the Renormalizable Theory of Weak Interaction*, Prog. Theor. Phys. **49**, 652–657 (1973).

[Kra79] M. O. Krause, *Atomic radiative and radiationless yields for K and L shells*, Journal of Physical and Chemical Reference Data **Volume 8, Issue 2**, 307–327 (1979).

[Kra08] T. Krautscheid, *Simulationen zur Ionenrückdrift in einer Zeit-Projektionskammer am ILC – in german*, diploma thesis, Universität Bonn, 2008.

[L+07] X. Llopart et al., *Timepix, a 65k programmable pixel readout chip for arrival time, energy and/or photon counting measurements*, Nucl. Instrum. Meth. **A581**, 485–494 (2007).

[L397] M. Acciarri et al. (L3), *Measurements of mass, width and gauge couplings of the W boson at LEP*, Phys. Lett. **B413**, 176–190 (1997).

[L303] P. Achard et al. (L3), *Measurement of W polarization at LEP*, Phys. Lett. **B557**, 147–156 (2003), hep-ex/0301027.

[LCTPC09] Linear Collider TPC collaboration (LCTPC), *collaboration web site*, (2009), `http://www.lctpc.org`.

[Leb02] A. Lebedev, *A laser calibration system for the STAR TPC*, Nucl. Instrum. Meth. **A478**, 163–165 (2002).

[Leo94] W. R. Leo, *Techniques for Nuclear and Particle Physics Experiments: A how to Approach*, (1994), Berlin, Germany: Springer 368 p.

[LEP93] L. Arnaudon et al. (LEP, Energy Working Group), *Measurement of the mass of the Z boson and the energy calibration of LEP*, Phys. Lett. **B307**, 187–193 (1993).

[LEP04] *A Combination of preliminary electroweak measurements and constraints on the standard model*, (2004), hep-ex/0412015.

[LEP09] *LEP Electroweak Working Group and Tevatron Electroweak Working Group web site*, (2009), `http://lepewwg.web.cern.ch/LEPEWWG/`.

[LHC-LC06] G. Weiglein et al. (LHC-LC, Study Group), *Physics interplay of the LHC and the ILC*, Phys. Rept. **426**, 47–358 (2006), hep-ph/0410364.

[LOI09] International Large Detector web site (LOI), *ILD Concept Group: Letter of Intent*, (2009), `http://www.ilcild.org/documents/ild-letter-of-intent/LOI.pdf/view`.

[Lot06] S. Lotze, *Ion Backdrift Minimisation in a GEM -Based TPC Readout*, Phd thesis, RWTH Aachen University, 2006.

[Lot10] S. Lotze, *private communication*, (2010).

[Lux05] T. Lux, *Studies for a time projection chamber for the International Linear Collider and measurement of beauty cross sections in deep inelastic scattering at HERA*, Phd thesis, Hamburg University, 2005, DESY-THESIS-2005-019.

[LW92] T. Lohse and W. Witzeling, *The Time projection chamber*, Adv. Ser. Direct. High Energy Phys. **9**, 81–155 (1992).

[Max09] *Maxwell web site*, (2009), `http://http://www.ansoft.com/maxwell`.

[MP+08] G. A. Moortgat-Pick et al., *The role of polarized positrons and electrons in revealing fundamental interactions at the linear collider*, Phys. Rept. **460**, 131–243 (2008), hep-ph/0507011.

[Mus09] L. Musa, *Charge Readout Chip Development and System Level Considerations*, (2009), `http://ilcagenda.linearcollider.org/materialDisplay.py?contribId=1&materialId=slides&confId=3334`.

[Nyg74] D. R. Nygren, *The Time Projection Chamber: A New 4 π Detector for Charged Particles*, (1974), Paper published in the Proceedings of The 1974 PEP Summer Study, 5-30 Aug 1974, Berkeley, California.

[O+08] K. Ohmi et al., *Study for ILC Damping Ring at KEKB*, (2008), EPAC'08, 11th European Particle Accelerator Conference, 23- 27 June 2008, Genoa, Italy.

[Pat03] M. Paterno, *Calculating Efficiencies and their Uncertainties*, (2003), `http://home.fnal.gov/~paterno/images/effic.pdf`.

[PDG06] W. M. Yao et al. (PDG, Particle Data Group), *Review of particle physics*, J. Phys. **G33**, 1–1232 (2006).

[PDG08] C. Amsler et al. (PDG, Particle Data Group), *Review of Particle Physics*, Phys. Lett. B667, 1 (2008), http://www-pdg.lbl.gov/.

[Pet07] D. Peterson, *TPC digitization and track reconstruction: efficiency dependence on noise*, (2007), `http://www.lepp.cornell.edu/%7Edpp/linear_collider/images/talks/Peterson-LCWS07-SimRecon.pdf`.

[Pet09] D. Peterson, *LP endplate web site*, (2009), `http://w4.lns.cornell.edu/~dpp/linear_collider/LargePrototype.html`.

[PLUTO79] C. Berger et al. (PLUTO), *Evidence for Gluon Bremsstrahlung in e+ e- Annihilations at High-Energies*, Phys. Lett. **B86**, 418 (1979).

[PT10] *Polytec PT company web site – in german*, (2010), `http://www.polytec-pt.com`.

[RB47] G. D. Rochester and C. C. Butler, *Evidence fot the Existence of New Unstable Elementary Particles*, Nature **160**, 855–857 (1947).

[Rop09] L. Ropelewski, *private communication*, (2009).

[S+07] F. Simon et al., *Development of Tracking Detectors with industrially produced GEM Foils*, IEEE Trans. Nucl. Sci. **54**, 2646–2652 (2007), 0707.2543.

[Sau77] F. Sauli, *Principles of Operation of Multiwire Proportional and Drift Chambers*, (1977), CERN-77-09.

[Sau97] F. Sauli, *GEM: A new concept for electron amplification in gas detectors*, Nucl. Instrum. Meth. **A386**, 531–534 (1997).

[Sch06] O. Schäfer, *Ein Monitorsystem für Gasbasierte Detektoren am International Linear Collider (ILC) – in german*, diploma thesis, Universität Rostock, 2006.

[Sch09] P. Schade, *Development and construction of a large TPC prototype for the ILC and study of tau polarisation in stau decays with the ILD detector*, Phd thesis, Hamburg University, 2009, DESY-THESIS-2009-040.

[Sch10a] P. Schade, *Correction algorithm for TPC operation in inhomogeneous magnetic fields*, (2010), LC-NOTE in preparation.

[Sch10b] P. Schade, *private communication*, (2010).

[Sci10] *SciEnergy company web site – GEM foils*, (2010), `http://www.scienergy.jp/smash.html`.

[Set09] R. D. Settles, *private communication*, (2009).

[SiD09] *Silicon Detector web site*, (2009), `http://silicondetector.org/display/SiD/home`.

[SKam98] Fukuda, Y. et al., Super-Kamiokande (SKam), *Evidence for oscillation of atmospheric neutrinos* , Phys. Rev. Lett. **81**, 1562–1567 (1998), hep-ex/9807003.

[SLAC74] J. E. Augustin et al. (SLAC, SP-017), *Discovery of a Narrow Resonance in e+ e- Annihilation*, Phys. Rev. Lett. **33**, 1406–1408 (1974).

[SNO02] Q. R. Ahmad et al. (SNO), *Direct evidence for neutrino flavor transformation from neutral-current interactions in the Sudbury Neutrino Observatory*, Phys. Rev. Lett. **89**, 011301 (2002), nucl-ex/0204008.

[Sob02] B. Sobloher, *Simulationsstudien zu GEM-Folien für die Auslese einer TPC – in german*, diploma thesis, RWTH Aachen, 2002.

[SW64] A. Salam and J. C. Ward, *Electromagnetic and weak interactions*, Phys. Lett. **13**, 168–171 (1964).

[TASSO80] R. Brandelik et al. (TASSO), *Evidence for a Spin One Gluon in Three Jet Events*, Phys. Lett. **B97**, 453 (1980).

[Tec10] *Tech-Etch company web site*, (2010), `http://www.tech-etch.com`.

[TESLA01a] T. Behnke, (ed.), S. Bertolucci, (ed.), R. D. Heuer, (ed.) and R. Settles, (ed.) (TESLA), *TESLA: The superconducting electron positron linear collider with an integrated X-ray laser laboratory. Technical design report. Pt. 4: A detector for TESLA*, (2001), DESY-01-011.

[TESLA01b] R. Brinkmann, (ed.) et al. (TESLA), *TESLA: The superconducting electron positron linear collider with an integrated X-ray laser laboratory. Technical design report. Pt. 2: The accelerator*, (2001), DESY-01-011.

[UA183a] G. Arnison et al. (UA1), *Experimental observation of isolated large transverse energy electrons with associated missing energy at s**(1/2) = 540-GeV*, Phys. Lett. **B122**, 103–116 (1983).

[UA183b] G. Arnison et al. (UA1), *Experimental observation of lepton pairs of invariant mass around 95-GeV/c**2 at the CERN SPS collider*, Phys. Lett. **B126**, 398–410 (1983).

[Vog08] A. Vogel, *Beam-induced backgrounds in detectors at the ILC*, Phd thesis, Hamburg University, 2008, DESY-THESIS-2008-036.

[Vog10] A. Vogel, *ILD_00 model, Mokka database web site*, (2010), `http://www-flc.desy.de/ldcoptimization/tools/mokkamodels.php`.

[Voi04] B. Voigt, *A test setup for the investigation of charge transfer processes of a GEM based TPC*, diploma thesis, Hamburg University, 2004, DESY-THESIS-2004-014.

[Web03] M. Weber, *Simulationen zur Verwendung von GEM-Folien als Auslesemodul einer TPC – in german*, diploma thesis, RWTH Aachen, 2003.

[Wei67] S. Weinberg, *A Model of Leptons*, Phys. Rev. Lett. **19**, 1264–1266 (1967).

[WFOW79] A. H. Walenta, J. Fischer, H. Okuno and C. L. Wang, *Measurment of the Ionization Loss in the Region of Realtivistic Rise for Noble and Molecular Gases*, Nucl. Instrum. Meth. **161**, 45–58 (1979).

[WMAP09] E. Komatsu et al. (WMAP), *Five-Year Wilkinson Microwave Anisotropy Probe (WMAP) Observations:Cosmological Interpretation*, Astrophys. J. Suppl. **180**, 330–376 (2009), 0803.0547.

[XFEL10] European X-Ray Free-Electron Laser (XFEL), *web site*, (2010), `http://www.xfel.eu/en`.

[Yar84] R. J. Yarema, *A New Preamplifier for Particle Detectors*, (1984), FERMILAB-TM-1284.

[YRS+03] B. Yu, V. Radeka, G. C. Smith, C. L. Woody and N. N. Smirnoff, *Study of GEM characteristics for application in a MicroTPC*, IEEE Trans. Nucl. Sci. **50**, 836–841 (2003).

Danksagung

Seit Monaten hab ich mich darauf gefreut diese Danksagung zu schreiben, denn sie markiert den letzten Akt meiner Doktorarbeit und beendet eine Phase meines Lebens fast zehn Jahre nach dem Beginn meines Physikstudiums. Nach Abgabe der Arbeit und erfolgreicher Disputation möchte ich nun all den Menschen danken, die es mir ermöglicht haben, unbeschadet und sogar bereichert aus diesem Prozess der Promotion hervorzugehen.
Als Erstes ein Dank – der mit Worten allein nicht auszudrücken ist – an den Mann, der dafür sorgt, dass es Dr. Hallermann keine zwei Monate geben wird. Ohne dich wäre vieles in meinem Leben schwieriger und es würde das Wichtigste fehlen, Danke!
Einen herzlichen Dank an meine Eltern, Geschwister und den ganzen Rest der besten Familie, die ich kenne – zu der ich auch Steders zähle. Ihr habt mich immer bestärkt und mir das Gefühl gegeben, dass ich geliebt werde, obwohl ich den Elementarteilchen verfallen bin, Danke!
Vielen Dank an Beate Naroska, die mich begeistert hat für die Teilchenphysik und mich nach der Diplomarbeit in ihrer Gruppe an FLC verwiesen hat. Danke an Ties und Rolf für die Möglichkeit in diesem Umfeld zu promovieren, es hat Spaß gemacht! Und es wäre nicht so schön gewesen ohne all die Menschen in dieser Gruppe. Ich kann nicht alle einzeln nennen, besonders erwähnen möchte ich aber Matthias, Adrian, Peter, Ralf, Christoph und Ramona, die mir zu Freunden geworden sind. Matthias, der mich mit seinen geduldigen Erklärungen in die Welt der TPC eingeführt hat und mich für DoIt begeistert hat, Danke! Adrian, der immer ruhig und zuverlässig für alle Fragen – besonders im Bereich der IT-Tricks – eine Antwort wusste oder gefunden hat, Danke! Peter, der mir die Laborarbeit nahe gebracht und immer wieder bewiesen hat, dass Gewalt nur dann keine Lösung ist, wenn man zuwenig davon anwendet, Danke! Ralf, der mich in die Geheimnisse der MediTPC und die Tiefen der Datenanalyse eingeweiht hat, Danke! Christoph, der unserer Gruppe neuen Schwung und mir immer ein offenes Ohr und ehrliches Interesse geschenkt hat, Danke! Und Ramona, die uns alle wieder auf den Boden holt und einfach unersetzbar ist, Danke!
Für unentbehrliche Hilfe während der Laborarbeit möchte ich Sasha danken, der immer noch eine Idee hatte und nie zuließ, dass ich aufgab. Danke an Volker, der dafür gesorgt hat, dass während meiner letzten Messphase überhaupt so etwas wie ein Labor zur Verfügung stand und unermüdlich fehlendes Gas oder Werkzeug organisiert hat.
Auch Doktoranden haben Freizeit, deshalb vielen Dank an Alex, Wiebke, Ralf, Peter, Christoph, Regina, Shiraz, Roman, Jonathan und Hanna mit denen ich viel Spaß und Entspannung beim Bouldern, im Urlaub, bei Spiele- oder Fußballabenden und dem gemeinsamen Kochen hatte und in Zukunft häufiger haben werde. Thore und Leon samt Eltern haben mir vor Augen geführt, was wirklich wichtig ist im Leben, Danke!

Fürs Korrekturlesen dieser Arbeit und die hilfreichen Anmerkungen möchte ich Michael, Ralf, Christoph, Philip und Ties danken. Ein besonderer Dank geht an Rolf, der sich trotz seines sicher nicht ganz ruhigen Jobs die Zeit genommen hat als Gutachter zur Verfügung zu stehen. Vielen Dank auch an Philip, der sich durch die Übernahme des Zweitgutachtens verpflichtet gefühlt hat, mich wirklich zu betreuen, das ist keine Selbstverständlichkeit.
Danke an Johannes, der im Prinzip bereit war Disputationsgutachter zu werden und der sich dafür eingesetzt hat, dass das veränderte Komitee von der Uni akzeptiert wurde. Außerdem natürlich herzlichen Dank an Joachim Mnich, der trotz seines vollen Terminkalenders eingesprungen ist.
Danke an die Rehearsal Besucher und Ties, ohne euch wäre der Vortrag nicht so gut geworden. Besonderen Dank nochmal an Michael, deine Geduld hat mir die Punktlandung ermöglicht. Vielen Dank an alle Fragesteller, besonders Ron, Michael und Adrian, die extra angereist sind. Dafür möchte ich auch Bernhard, Mona, Sanna, Helga, Heinz und Marko danken, es war ein wunderschöner Tag. Danke, Sanna, du hast den Physikern gezeigt, was wirklich gutes Essen ist.
Zum Schluss möchte ich noch Madhu, Jan und Michael für die Gutachten zu meiner Bewerbung danken, die es mir ermöglichen weiterhin in diesem Feld, das mir wirklich etwas bedeutet, zu arbeiten.